Titre: Title:	Hybrid Metallo-Dielectric Waveguide Architectures and Technologies for THz Circuits and Systems
Auteur: Author:	Chunmei Liu
Date:	2024
Type:	Mémoire ou thèse / Dissertation or Thesis
Référence: Citation:	Liu, C. (2024). Hybrid Metallo-Dielectric Waveguide Architectures and Technologies for THz Circuits and Systems [Thèse de doctorat, Polytechnique Montréal]. PolyPublie. https://publications.polymtl.ca/62517/

POLYTECHNIQUE MONTRÉAL

affiliée à l'Université de Montréal

Hybrid Metallo-Dielectric Waveguide Architectures and Technologies for THz Circuits and Systems

CHUNMEI LIU

Département de génie électrique

Thèse présentée en vue de l'obtention du diplôme de Philosophiæ Doctor

Génie électrique

Décembre 2024

POLYTECHNIQUE MONTRÉAL

affiliée à l'Université de Montréal

Cette thèse intitulée :

Hybrid Metallo-Dielectric Waveguide Architectures and Technologies for THz Circuits and Systems

présentée par **Chunmei LIU**

en vue de l'obtention du diplôme de Philosophiæ Doctor

a été dûment acceptée par le jury d'examen constitué de :

Chahé NERGUIZIAN, président

Ke WU, membre et directeur de recherche

Elham BALADI, membre

Abdel Razik SEBAK, membre externe

DEDICATION

To my grandfather

ACKNOWLEDGEMENTS

I would like to express my heartfelt gratitude to my supervisor, Prof. Ke Wu, for his invaluable guidance and support throughout my research. His insights and encouragement have been instrumental in my development, and I deeply appreciate his mentorship. I would like to extend my sincere thanks to him for his unwavering support in my scholarship application. His encouragement and supporting throughout the process were invaluable. I truly appreciate his support in enabling me to attend numerous international conferences. His assistance provided me with many opportunities for networking and collaboration. I am grateful for his belief in the importance of these experiences for my academic and professional growth.

I wish to acknowledge with special thanks to the technical and administrative team at Poly-Grames Research Center, especially Jules Gauthier for hi invaluable advises on fabrication, Traian Antonescu for fabricating all alumina samples, assembling measurement kits and making very good pictures for publications, and Steve Dube for fabricating all fixtures, David Dousset for offering materials and connectors, and Maxime Thibault for support on the antenna measurements. I would like to express my heartfelt gratitude to Rachel Lortie for her supporting during my challenging times throughout my project. She consistently offered me kind words and comforting meals, always taking the time to talk with me patiently and making me feel truly warm. Her assistance has been invaluable in helping me navigate various challenges and administrative issues. I would also like to thank Jean-Sébastien Décarie for his support with IT.

I appreciate Prof. Chahé Nerguizian, Prof. Elham Baladi, and Prof. Abdel Razik Sebak serving as jury members of my Ph.D. examination committee and reviewing this thesis.

I would like thank all group members from Prof. Ke Wu for their valuable academic discussions and suggestions. I would like to thank Jie Deng for his helping on

simulation on twists, Dr. Pascal Burasa and Jianye Mai for their help on extensive measurements.

I would like to extend my thanks to all my friends, particularly Bengeng Cai, Qingtao Chen, Peng Chu, Yunjie Geng, Xiaoqiang Gu, Tongfeng Guo, Zhenzhen Li, Wentao Lin, Yunlong Lu, Yihong Su, Yingying Tian, Desong Wang, Yue Wu, Xiaoyi Wang, Kanglin Xing, Gaoming Xu, Jun Xu, Shuangshuang Xu, Wenwen Yang, Yifan Yin, Ben You, Yi Zhan, Yang Zhang, You Zhang, Ping Zhao, Dongze Zhen, Guichi Zhu, I've met in Montréal for their support throughout my journey. Each of you has played a significant role in enriching my life, whether through shared laughter, meaningful conversations, or simply being there during tough times. Your friendship has made my experience in this vibrant city truly unforgettable, and I am grateful for the moments we have shared and the memories we have created together.

I would like to thank Dr. Louis-Philippe Carignan for his invaluable support in fabricating the first prototype of my project, making a significant milestone in my research. His expertise in fabrication, materials, and measurement was instrumental in helping me troubleshoot some hidden issues, allowing my project to progress more smoothly. I always find our discussions to be inspiring and enriching, and I am truly grateful for his guidance throughout this journey. As a co-author, he consistently provides constructive suggestions and candid feedback, which greatly facilitates the review process. His insights not only enhance the quality of our work but also foster a collaborative atmosphere that encourages open dialogue and continuous improvement. I truly appreciate his ability to challenge us to think critically.

I am deeply grateful to my parents, sister, grandparents, and my aunts and uncles for their boundless love and care. Words cannot fully express how much I love them and how profound my gratitude is. My parents have consistently supported my important decisions, standing by me through every challenge. Their unconditional love and support have been a constant source of strength. Whenever I face difficulties in my projects or life, they are there to encourage me. My father often reminds me that I do

not need to be the best because, to them, I am already the best. Meanwhile, my mother's only concern is my happiness. Their unwavering support and belief in me inspire me every day, and I am truly fortunate to have them in my life. My sister is not just my sibling; she is my best friend. Our bond is built on trust and understanding. Whether celebrating our successes or navigating difficult times, we always uplift and encourage one another. I would like thank my grandfather, who taught me the importance of kindness and the value of having a beautiful heart. His wisdom and compassion have profoundly influenced my character and how I interact with others. Thank my grandmother for her unconditional love.

RÉSUMÉ

Les systèmes de communication et de détection sans fil à haute vitesse deviennent de plus en plus omniprésents. Aujourd'hui, tout autour de nous devient de plus en plus "intelligent" grâce aux technologies de communication et de détection sans fil omniprésentes, telles que les smartphones, les montres connectées, les systèmes de maison intelligente, les voitures intelligentes, etc. Alors que le nombre d'utilisateurs finaux des systèmes de communication sans fil augmente de manière exponentielle, le canal de communication devient saturé. Les communications de nouvelle génération sont devenues la clé pour surmonter les problèmes de communication sous-jacents. La solution THz (de 0.1 à 10 THz) est l'un des enjeux technologiques importants pour les futurs systèmes de communication et de détection. Bien que les bases théoriques fondamentales de la communication THz soient exactement les mêmes que celles des micro-ondes, de nombreux défis subsistent. L'un d'eux, par exemple, est lié au processus de fabrication qui influence fortement les performances des circuits. Un autre défi est lié à la perte de transmission, qui est généralement considérable aux fréquences THz. Par conséquent, de nouvelles architectures de transmission THz et des stratégies de développement technologique doivent être conçues et démontrées.

Ce travail commence par une investigation des guides d'ondes diélectriques non radiatifs intégrés au substrat (SINRD) pour la bande THz. L'une des propriétés remarquables du guide d'ondes SINRD est sa capacité à confiner les ondes électromagnétiques (EM) sans avoir besoin de parois latérales métalliques, même à des discontinuités abruptes. Avant d'explorer le confinement des ondes SINRD aux discontinuités, nous examinons d'abord le comportement modèle d'un simple guide d'ondes SINRD droit. Une étude paramétrique est réalisée, fournissant des orientations complètes pour la conception du guide d'ondes SINRD. Parmi divers matériaux diélectriques, tels que le saphir, le silicium et le substrat Rogers, l'alumine est choisie pour la démonstration en raison de sa rigidité, de sa résistance à la température et de son faible facteur de perte tangent. Des expériences approfondies sont menées pour

affiner le processus optimal de perçage laser. De plus, une approche de fabrication à double couche est explorée pour relever les défis de fabrication liés au perçage laser. Ensuite, les guides d'ondes intégrés au substrat (SIW) et les guides d'ondes diélectriques intégrés au substrat (SIDW), fabriqués à partir du même matériau, sont étudiés théoriquement et expérimentalement. Les résultats indiquent que le guide d'ondes SINRD offre des caractéristiques de transmission plus prometteuses que le SIW, mais présente des pertes plus élevées que le SIDW, nous incitant à poursuivre le concept proposé d'une architecture de guide d'ondes hybride.

L'architecture de guide d'ondes hybride vise à créer des circuits et des systèmes compacts à faible perte, en utilisant différents guides d'ondes adaptés à des blocs de construction spécifiques en fonction de leurs avantages. Dans ce cadre, le guide d'onde diélectrique non radiatif (NRD) est considéré comme un élément clé pour les blocs fonctionnels où des discontinuités peuvent se produire. Le guide d'ondes diélectrique (DW), qui est exempt de pertes de conducteur, est utilisé pour la transmission point à point. Avant de construire des composants fonctionnels, nous évaluons l'efficacité de couplage du guide d'ondes hybride droit en examinant trois conditions : l'appariement de la vitesse de phase, l'appariement des motifs de champ et l'appariement d'impédance. Nous démontrons la compatibilité des modes entre le mode LSM_{01} du guide d'ondes NRD et le mode fondamental E_{11} du DW. Cette compatibilité assure une connexion fluide à l'interface entre les deux guides d'ondes, évitant des transitions d'appariement encombrantes qui pourraient atténuer les avantages de l'architecture de guide d'ondes hybride. En conséquence, les ondes EM peuvent traverser l'interface avec une faible perte d'insertion, ouvrant la voie aux applications pratiques de l'architecture de guide d'ondes hybride.

Étant donné le couplage efficace entre les deux guide d'ondes, nous appliquons le guide d'ondes hybride à des applications, en commençant par les courbures de guide d'ondes hybrides. Le guide d'ondes NRD est utilisé uniquement dans les zones de courbure pour supprimer les fuites de rayonnement, tandis que le guide d'ondes diélectrique (DW) est

employé pour les interconnexions droites afin de minimiser les pertes conductrices associées aux couches métalliques. Pour garantir l'excitation du mode non-radiatif LSM_{01} dans le guide d'ondes NRD, un mode E_{11} polarisé horizontalement dans le DW est nécessaire. Avec l'assistance du guide d'ondes NRD, le rayon de courbure peut être réduit d'un facteur d'environ 10 par rapport aux courbures conventionnelles de DW, résultant en une structure compacte qui montre un potentiel significatif pour l'intégration. Cependant, la sélectivité inhérente du mode du guide d'ondes hybride et la conversion de mode dans la courbure NRD nécessitent que le chemin de courbure soit optimisé pour assurer la présence du mode LSM_{01} à la sortie de la section NRD, augmentant ainsi la complexité de conception et limitant la bande passante de fréquence.

L'architecture du guide d'ondes hybride est également utilisée dans les croisements, servant non seulement à supprimer les fuites de rayonnement à l'intersection, mais aussi à réduire la diaphonie entre deux guides d'ondes diélectriques (DW) intersectants. Le guide NRD est appliqué uniquement au niveau de la jonction, tandis que le DW est utilisé pour les sections droites connectant aux ports afin de minimiser les pertes conductrices. Cette combinaison crée une interface sélective au niveau du mode qui permet uniquement au mode LSM_{01} de passer. En supprimant le mode couplé LSE_{11} à la jonction, nous réduisons efficacement la diaphonie, améliorant ainsi la performance de transmission de chaque chemin de guidage.

Ce travail propose, démontre et vérifie que le guide d'ondes hybride, combinant les avantages du NRD et du DW, présente un grand potentiel pour les applications intégrées. Les circuits hybrides utilisant le DW pour des interconnexions fondamentales à faible perte et le NRD pour des éléments fonctionnels compacts sont particulièrement attrayants pour les systèmes THz à faible perte. L'architecture de guide d'ondes hybride métallique-dielectrique proposée pourrait devenir l'épine dorsale des futurs interconnexions, circuits intégrés et systèmes THz, entraînant des avancées significatives et une évolution dans la recherche et les applications THz.

ABSTRACT

High-speed wireless communication and sensing systems are becoming more and more pervasive. Today, everything around us is getting more and more “smart” because of the ubiquitous wireless communication and sensing technologies and applications such as smart phones, smart watches, smart home systems, smart cars, and so forth. With the number of end-users of wireless communication systems is increasing exponentially, the communication channel is getting congested. Next generation communications have become the key to overcoming the underlying communication issues. Terahertz (THz) solution (from 0.1 - 10 THz) is one of the important technological proponents and enablers for future communication and sensing systems. Even though the theoretical foundation of THz communication is the same as that for microwaves, there are many challenges in connection with its developments and implementations. One of them, e.g., is related to the fabrication process that highly influences the performance of circuits and systems. Another challenge is concerned with guided-wave or transmission loss that is usually considerable at THz frequencies. Therefore, novel THz transmission architectures and technology development strategies should be devised and demonstrated.

This work begins with an investigation of substrate-integrated non-radiative dielectric (SINRD) waveguide for THz band. One of the remarkable properties of the SINRD waveguide is its ability to confine electromagnetic (EM) waves without the need for metallic sidewalls, even at sharp discontinuities. Before delving into the SINRD wave confinement at discontinuities, we first examine the model behavior of a simple straight SINRD waveguide. A parametric study is conducted, providing comprehensive guidance for the design of SINRD waveguides. Among various dielectric materials, such as sapphire, silicon, and Rogers substrate, alumina is selected for demonstration due to its stiffness, temperature resilience, and notably low loss tangent. Extensive experiments are conducted to refine the optimal laser drilling process. Additionally, a double-layer fabrication approach is explored to address fabrication challenges related

to laser drilling. Afterward, substrate-integrated waveguide (SIW) and substrate-integrated dielectric waveguide (SIDW) made of the same material are studied theoretically and experimentally. The result indicates that the SINRD waveguide offers more promising transmission characteristics than the SIW, but exhibits higher loss than the SIDW, therefore inspiring us to devise and develop a new concept of hybrid waveguide architecture.

The proposed hybrid waveguide architecture aims to create low-loss, compact circuits and systems, by utilizing and combining different waveguides tailored to specific building blocks based on their advantages. In this framework, the NRD waveguide is considered a key component for functional blocks of circuits where discontinuities usually happen. On the other hand, DW, which is free from conductor losses, is deployed for point-to-point straight transmission. Before constructing functional components, we assess the coupling efficiency of straight hybrid waveguide by evaluating three conditions: phase velocity matching, field pattern matching, and impedance matching. We demonstrate mode compatibility between the longitudinal-section magnetic $(LSM)_{01}$ mode of the NRD waveguide and the fundamental E_{11} mode of the DW. This compatibility ensures a seamless connection at the interface between two waveguides, avoiding bulky and lengthy matching transitions that could greatly compromise the benefits of the hybrid waveguide architecture. As a result, EM waves can traverse the interface with a small insertion loss, paving the way for practical applications of the proposed hybrid waveguide architecture.

Given the effective coupling between the two waveguides, we apply the hybrid waveguide and demonstrate practical cases, starting with hybrid waveguide bends. The NRD waveguide is applied only at the bending areas to suppress the radiation leakage, while the DW is employed for straight interconnects to minimize conductor loss associated with metal layers. To ensure the excitation of the non-radiative LSM_{01} mode in the NRD waveguide, a horizontally polarized E_{11} mode in DW is required. With the support of the NRD waveguide, the bend radius can be shrunk by a factor of about 10

compared to conventional DW bend, resulting in a compact structure that shows significant potential for integration. However, the inherent mode selectivity of the hybrid waveguide and mode conversion in NRD bend necessitate that the bend path should be optimized to ensure the presence of the LSM_{01} mode at the exit of the NRD section, thus increasing design complexity and limiting the frequency bandwidth.

The hybrid waveguide architecture is also deployed in the development of crossovers, serving not only to suppress radiation leakage at intersection but also to reduce crosstalk between two intersecting DWs. The NRD waveguide is applied only at the junction, while the DW is used for the straight sections connecting to the ports so to minimize conductor loss. This combination creates a mode-selective interface at all four branches of the junction that allows only the LSM_{01} mode to pass through. By suppressing the coupled longitudinal-section electric $(LSE)_{11}$ mode at the junction, we effectively reduce crosstalk, thereby improving transmission performance of each through guiding path.

The work proposes, demonstrates, and verifies that the hybrid waveguide, combining the advantages of NRD waveguide and DW, holds great promise for integrated system development. Hybrid circuits utilizing DW for low-loss fundamental interconnects and NRD waveguide for compact functional elements are particularly attractive for THz low-loss systems development. The proposed hybrid metallo-dielectric waveguide architecture could become the backbone of future THz interconnects, integrated circuits and systems including antennas, driving significant advancement and evolution in THz research and applications.

TABLE OF CONTENTS

DEDICATION……. iii
ACKNOWLEDGEMENTS iv
RÉSUMÉ……..... vii
ABSTRACT ……..... x
LIST OF TABLES xvii
LIST OF FIGURES xviii
LIST OF SYMBOLS AND ABBREVIATIONS xxvii
LIST OF APPENDICES xxxi
CHAPTER 1 INTRODUCTION 1
1.1 Research background 1
1.2 Research objectives 2
1.3 Thesis outline 3
1.4 Research impact 6
CHAPTER 2 LITERATURE REVIEW 7
2.1 Planar metal guiding lines 7
2.1.1 Coplanar waveguides 7
2.1.2 Thin-film microstrip lines 8
2.1.3 Advanced material-based transmission lines 10
2.1.4 Planar Goubau lines 11
2.2 Metallic waveguides 12
2.2.1 Single-wire waveguides 12
2.2.2 Cylindrical waveguides 13
2.2.3 Rectangular waveguides 14
2.3 Substrate-integrated waveguides 19
2.3.1 General structure of SIWs 19
2.3.2 CMOS-based SIWs 20
2.3.3 SIWs on high-resistivity silicon interposer 21

2.3.4 SIWs on other advance materials 21
2.3.5 Air-filled SIWs 23
2.4 Dielectric waveguides 27
2.4.1 Ribbon waveguides 27
2.4.2 Polymer-cladding ribbon waveguides 27
2.4.3 Substrate-integrated ribbon waveguides (SIRW) 28
2.4.4 Rectangular dielectric waveguides 29
2.4.5 Dielectric image lines 30
2.4.6 Non-radiative dielectric waveguide 31
2.5 Conclusion 32
CHAPTER 3 ARTICLE 1: SUBSTRATE-INTEGRATED NON-RADIATIVE DIELECTRIC (SINRD) WAVEGUIDE FOR THZ INTEGRATED CIRCUITS AND SYSTEMS…….....34
3.1 Introduction 35
3.2 Performance of SINRD waveguide 37
3.2.1 Bandwidth of SINRD waveguide 39
3.2.2 Loss performance of SINRD waveguide 40
3.2.3 SINRD waveguide 44
3.3 Experiment 47
3.4 Conclusion 51
CHAPTER 4 ARTICLE 2: VERTICALLY STACKED DOUBLE-LAYER SUBSTRATE-INTEGRATED NONRADIATIVE DIELECTRIC WAVEGUIDES FOR THZ APPLICATIONS.....52
4.1 Introduction 53
4.2 Double-layer SINRD waveguide 55
4.3 Experiment 59
4.4 Conclusion 61

CHAPTER 5 ARTICLE 3: SUBSTRATE-INTEGRATED HYBRID METALLO-DIELECTRIC WAVEGUIDE ARCHITECTURE FOR MILLIMETER-WAVE AND TERAHERTZ APPLICATIONS 62
5.1 Introduction 63
5.2 Feasibility of substrate-integrated hybrid metallo-dielectric waveguide 65
5.2.1 SIDW and SINRD waveguide 65
5.2.2 Substrate-integrated hybrid metallo-dielectric waveguide 67
5.3 Back-to-back SIHMD waveguide 70
5.3.1 Proposed SIHMD waveguide architecture consisting of SIDW and SINRD 70
5.3.2 Comparison with SIHMD waveguide architecture consisting of SIDW and SIW 74
5.4 Discussion 75
5.4.1 Core width 76
5.4.2 Effective permittivity of perforated region 77
5.4.3 SINRD waveguide 78
5.5 Conclusion 80
CHAPTER 6 ARTICLE 4: HYBRID METALLO-DIELECTRIC WAVEGUIDE ARCHITECTURE FOR COMPACT LOW-LOSS THZ APPLICATIONS 81
6.1 Introduction 82
6.2 Hybrid metallo-dielectric waveguide 83
6.2.1 DW and NRD waveguide 83
6.2.2 Discontinuity-tolerant compact low-loss guiding 85
6.3 Experiment 87
6.4 Conclusion 89
CHAPTER 7 ARTICLE 5: CROSSTALK AND LEAKAGE SUPPRESSION BY MODE SELECTIVITY AND CONVERSION IN TERAHERTZ HYBRID METALLO-DIELECTRIC WAVEGUIDE CROSSOVER AND INTERSECTIONS 90

7.1 Introduction 91
7.2 Principle of HMDW crossover 92
7.2.1 Modes of DW and NRD waveguide 93
7.2.2 Mode conversion of NRD waveguide intersection 95
7.2.3 Mode selectivity of HMDW 96
7.3 HMDW crossover 98
7.3.1 Asymmetrical HMDW crossover 98
7.3.2 Symmetrical HMDW crossover 100
7.3.3 Simulation model of symmetrical HMDW crossover with material losses and feeding losses 102
7.4 Alternative validation strategy: two-port device with intersection 105
7.4.1 Unterminated tapered orthogonal waveguide arms 105
7.4.2 Two-port device with four intersections 107
7.5 Fabrication and measurement 110
7.6 Discussion 114
7.7 Conclusion 120
CHAPTER 8 CONCLUSION AND FUTURE WORK 121
8.1 Conclusion 121
8.2 Future work 124
REFERENCES 131
APPENDICES 156

LIST OF TABLES

Table 2.1 Table of rectangular waveguides 18

Table 2.2 Table of SIWs 25

Table 5.1 Parameters of demonstrated SIHMD waveguide architecture 71

Table 7.1 Important parameters of proposed HMDW with four intersections 111

LIST OF FIGURES

Figure 2.1 (a) CPW, (b) CPW with air-bridge, (c) air-filled cavity-back CPW ·····8

Figure 2.2 (a) Microstrip line, (b) thin-film microstrip line ·····9

Figure 2.3 Planar Goubau line ····· 11

Figure 2.4 (a) Parallel-plate waveguide, (b) metallic slit waveguide, (c) two-wire transmission line, (d) coaxial transmission line ····· 12

Figure 2.5 (a) Cylindrical metallic waveguide (MWG), (b) silver/PS-coated glass tube ····· 14

Figure 2.6 (a) E-plane split waveguide, (b) H-plane split waveguide····· 15

Figure 2.7 Process of on-wafer micromachined waveguide. (i) Deposit gold on a silicon wafer, (ii), photoresist form, (iii) deposit gold on entire surface, (iv) remove photoresist····· 15

Figure 2.8 SU-8 photoresist micromachining. (i) Silicon substrate, (ii)-(iv) form waveguide core, (v) deposit gold, (vi) assemble two pieces····· 16

Figure 2.9 Structure of SIWs ····· 20

Figure 2.10 (a) SIW on ABF/glass/ABF stack, (b) SIW on ABF on glass ····· 22

Figure 2.11 Integrated waveguide based on AAO membrane ····· 23

Figure 2.12 Air-filled SIW ····· 24

Figure 2.13 (a) Dielectric ribbon waveguide, (b) polymer-cladding ribbon waveguide, (c) substrate-integrated ribbon waveguide ····· 27

Figure 2.14 (a) Rectangular dielectric waveguide (RDW), (b) three-layer RDW, (c) hollow RDW····· 29

Figure 2.15 (a) Silicon-on-glass waveguide, (b) rib dielectric waveguide, (c) strip dielectric waveguide ····· 30

Figure 2.16 (a) Inserting image plane at middle of dielectric waveguide, (b) dielectric image line, (c) dielectric insulated image guide····· 31

Figure 2.17 (a) Non-radiative dielectric waveguide and first two non-radiative modes, (b) image non-radiative dielectric waveguide ····· 32

Figure 3.1 Model of SINRD waveguide. (a) Practical structure, (b) equivalent model. …… 37

Figure 3.2 Dispersion curves of the given SINRD waveguide example. h = 0.254 mm, w = 0.35 mm, w_a = 0.5 mm, ε_{r1} = 9.8, ε_{r2} = 3.2 …… 38

Figure 3.3 Parametric study of waveguide width w and effective relative permittivity of perforated region ε_{r2} on cutoff frequencies of SINRD waveguide …… 40

Figure 3.4 Loss performance of the LSM_{01} mode of SINRD waveguide at 260 GHz. (a) Core width w and (b) ε_{r2}. α_c, α_d and α_t are the conductor, dielectric and total loss, respectively …… 41

Figure 3.5 Simulated transverse electric field patterns of the LSM_{01} mode at 260 GHz. (a) SINRD waveguide with the width of w = 0.25 mm, (b) SINRD waveguide with the width of w = 0.35 mm …… 42

Figure 3.6 Design chart. (a) Average loss performance in dB/cm at 300 GHz, (b) bandwidth of the LSM_{01} mode in GHz …… 43

Figure 3.7 Loss performance of the given SINRD equivalent model operating in LSM_{01} mode, SIW and SIDW with the same materials and dimension. h = 0.254 mm, w = 0.35 mm, ε_{r1} = 9.8, ε_{r2} = 3.2 …… 44

Figure 3.8 (a) Structure of the designed SINRD waveguide, (b) the designed metallic housing with transitions and supporting base. Parameters: l = 10 mm, w = 0.35 mm, l_t = 3.5 mm. The total length of the metallic housing is 30 mm. The dimension of WR3-band rectangular waveguides used in simulation is 0.86 mm × 0.43 mm. The loss tangent of alumina substrate is about tan δ = 0.001. The conductivity of gold is $\sigma = 4.1 \times 10^7$ S/m. The metallic housing is made by aluminum with a conductivity of $\sigma = 3.8 \times 10^7$ S/m …… 45

Figure 3.9 Simulated electric field distributions at 260 GHz along the propagation direction. (a) At xoz plane (E-plane), (b) at yoz plane (H-plane) …… 46

Figure 3.10 Simulated transmission performance of the designed SINRD waveguide with length of l = 10 mm under different surface roughness …… 46

Figure 3.11 Fabrication process. (a) Metallization of hosting substrate (alumina), (b) laser drilling with a desired or designed air-hole pattern ····· 47

Figure 3.12 Photographs of the as-fired alumina-based devices under test. (a) SINRD waveguide, (b) SIW, (c) metallized via holes of the SIW waveguide, (d) SIDW 48

Figure 3.13 Measurement set-up of the device-under-test (DUT) in WR3-band using a PNA-X and VDI extenders ····· 48

Figure 3.14 Transmission performance of the designed SINRD waveguides in Figure 3.12 (a) ····· 49

Figure 3.15 Transmission performance of the designed SIW in Figure 3.12 (b). ···· 50

Figure 3.16 Total loss of the SINRD waveguide, SIW and SIDW ····· 51

Figure 4.1 (a) Manufacturing process and (b) 3D view of 10-mil single-layer SINRD waveguide ····· 54

Figure 4.2 Manufacturing process of vertically stacked double-layer SINRD waveguide. (a) Penetrating through two backside metallized 5-mil substrates separately, (b) flipping over one of the substrates and assembly the two layers together, (c) 3D view ····· 54

Figure 4.3 (a) Side view and (b) equivalent model of perforated double-layer substrate. Unit in mil ····· 56

Figure 4.4 Dispersion curves of SINRD waveguides, single-layer (dashed lines) and double-layer with air layer (solid lines with symbols). $h_1 = h_2 = 10$ mil, $w = 14$ mil, $\varepsilon_{r1} = 9.8$, $\varepsilon_{r2} = 3.2$, $\varepsilon_{r3} = 1$, $h_a = 1$ mil ····· 57

Figure 4.5 Transverse electric field patterns of LSM_{01} mode of (a) double-layer and (b) single-layer SINRD waveguides at 300 GHz. Unit in mil ····· 58

Figure 4.6 Air layer effect on higher-order PPW TE_1 mode ····· 58

Figure 4.7 Air layer effect on loss behavior of LSM_{01} mode. Loss tangent of alumina is tan $\delta = 0.001$, and conductivity of gold is $\sigma = 4.1 \times 10^7$ S/m ····· 59

Figure 4.8 Simulation model of double-layer SINRD waveguide. (a) The bottom layer of SINRD waveguide, (b) metallic housing with two 5-mil alumina layers inside for testing. Unit in mil ····· 60

Figure 4.9 Prototype of the proposed double-layer SINRD waveguide, bottom layer (left) and top layer (right) ····· 61

Figure 4.10 Transmission performance of the proposed double-layer SINRD waveguide ····· 61

Figure 5.1 (a) Existing hybrid waveguide architecture consisting of SIDW and SIW, (b) scheme of the proposed hybrid waveguide architecture consisting SIDW and SINRD waveguide ····· 64

Figure 5.2 Structures of (a) SIDW and (b) SINRD waveguide, equivalent models of (c) SIDW and (d) SINRD waveguide, simulated transverse electric field patterns of (e) E_{11}^{x} mode and (f) of LSM_{01}^{x} mode ····· 66

Figure 5.3 Dispersion curves of (a) SIDW and (b) SINRD waveguide. Parameters: h = 0.254 mm, w = 0.3 mm, ε_{r1} = 9.8, ε_{r2} = 3.2 ····· 67

Figure 5.4 (a) Phase velocities of SIDW and SINRD waveguide, (b) wave impedances of SIDW and SINRD waveguide ····· 68

Figure 5.5 (a) Equivalent model of SIHMD waveguide, (b) transmissions, (c) electric field distributions of SIHMD waveguide architecture at the *xoz* plane. (d) E_x^{11} mode at AA' (left) and LSM_x^{01} mode at BB' (right). Parameters: h = 0.254 mm, w = 0.3 mm, ε_{r1} = 9.8, and ε_{r2} = 3.2 ····· 69

Figure 5.6 (a) Layout of the proposed back-to-back SIHMD waveguide architecture, (b) metallic housing used to support the waveguide under testing. Parameters: l = 10 mm, w = 0.3 mm, l_t = 3.5 mm, l_n = 1.75 mm ····· 70

Figure 5.7 Simulated electric field distributions of the proposed back-to-back SIHMD waveguide architecture at 280 GHz. (a) Top view, (b) side view, (c) cross section of SIDW, E_{11}^{x} mode, (d) cross section of SINRD waveguide, LSM_{01}^{x} mode ··· 72

Figure 5.8 Photograph of the presented back-to-back SIHMD waveguide architecture under microscope ····· 72

Figure 5.9 Simulated and measured results of the presented back-to-back SIHMD waveguide architecture ····· 73

Figure 5.10 Simulated electric field distributions of the traditional back-to-back SIHMD waveguide architecture (SIDW and SIW) at 280 GHz. (a) Top view, (b) side view, (c) cross section of the SIDW, E_{11}^{y} mode, (d) cross section of the SIW waveguide, TE_{10}^{z} mode ····· 74

Figure 5.11 Comparison between the measured S-parameters of two SIHMD waveguide architectures ····· 75

Figure 5.12 (a) Equivalent model of the proposed back-to-back SIHMD waveguide architecture, (b) transmissions and reflections of the back-to-back SIHMD waveguide architecture with different SINRD width, (c) transmission of the back-to-back SIHMD waveguide architecture with different widths at 330 GHz. Parameters: h = 0.254 mm, w = 0.3 mm, l_n = 0.254 mm, ε_{r1} = 9.8, ε_{r2} = 3 ····· 76

Figure 5.13 (a) Width effect and (b) ε_{r2} effect on frequency response ····· 77

Figure 5.14 (a) Transmissions and reflection of SIHMD waveguide architectures with different SINRD length (w = 0.3 mm), (b) loss comparison between the SIDW and the SINRD waveguide, (c) conductivity effect on the conductor loss of SINRD waveguide ····· 80

Figure 6.1 Discontinuity-tolerant hybrid metallo-dielectric waveguide architecture. Two parallel metal sheets are added over the discontinuity to avoid radiation leakage. Here, w = 0.3 mm, h = 0.254 mm, l_m = 1 mm, w_m = 2.5 mm, R = 0.2 mm, l = 3 mm ····· 83

Figure 6.2 Dispersion diagram of DW and NRD waveguides: E_{11}^{x} and E_{11}^{y} modes of DW; LSE_{11}^{x}, LSM_{01}^{x} and LSE_{21}^{x} modes of NRD waveguide ····· 84

Figure 6.3 Transverse electric field patterns of the modes of interest for DW and NRD waveguide ····· 84

Figure 6.4 Simulated performance of the back-to-back guide shown at Figure 6.1 with and without metal layers over bends and the standard straight guide, for comparison ····· 86

Figure 6.5 Mode conversion loss of LSM_{01} mode to LSE_{11} over sharp bend with metallic patch on the bends and with a radius of R = 0.2 mm ····· 86

Figure 6.6 Cross-section electric field distribution at 280 GHz with two metal layers (left) and without metal layers (right) over the four 90° bends ····· 87

Figure 6.7 Simulation model of the back-to-back guiding waveguide (in blue) with four 90° bends placed on the base of the designed two-piece aluminum housing (in grey). The loss tangent of alumina substrate is set at tan δ = 0.001 in simulation. The conductivity of aluminum is $\sigma = 3.8 \times 10^7$ S/m ····· 87

Figure 6.8 Photograph of the alumina based guiding structure with bends, (b) picture of bends, (c) two pieces of the aluminum housing, base and cover, (d) photograph of the standard back-to-back straight waveguide. Unit in mm ····· 88

Figure 6.9 Comparison between measured and simulated results of the back-to-back guide with four 90° bends with/without metallic covering and standard back-to-back straight guide ····· 88

Figure 7.1 Hybrid metallo-dielectric waveguide (HMDW) crossover. Schematics of electric fields for LSM_{01}^{x} of the through NRD guide and E_{11}^{x} mode of the through DW and LSE_{11}^{z} mode of the orthogonal NRD guide are given ····· 93

Figure 7.2 Dispersion curves of E_{11}^{x}, E_{11}^{y} and E_{21}^{y} modes of DW; LSE_{11}^{x}, LSM_{01}^{x} and LSE_{21}^{x} of NRD waveguide with h = 0.254 mm, w = 0.28 mm and ε_r = 9.8. Inset: schematic of NRD waveguide. Dispersion curves circled by blue dashed circles are for DW, circled by orange dashed circles are for NRD waveguide ····· 94

Figure 7.3 Simulated performance of NRD waveguide junction. Inset: schematic of the NRD waveguide junction (center) and simulated electric field at 280 GHz (right). LSM_{01}^{x} mode is assigned at P1 ····· 96

Figure 7.4 Mode selectivity of HMDW architecture. (a) Mode compatibility between LSM_{01}^{x} mode and E_{11}^{x} mode, inset: electric field distribution inside HMDW architecture when LSM_{01}^{x} mode propagates along NRD guide, (b) mode incompatibility between LSE_{11}^{z} mode and $E_{11}^{z/y}$ mode, inset: electric field distribution inside HMDW architecture when LSE_{11}^{z} mode propagates in NRD guide ····· 97

Figure 7.5 (a) Simulated performance of the asymmetrical hybrid metallo-dielectric waveguide (AHMDW) crossover, inset: simulated electric field at 280 GHz when P1 is excited by LSM_{01}^{x} mode. (b) transmission performance of the through guide versus NRD stub length (orthogonal NRD guide length), (c) simulated performance when P3 is excited by E_{11}^{z} mode, inset: simulated electric field at 280 GHz ····· 99

Figure 7.6 Simulation of the symmetric HMDW crossover. (a) Model, (b) performance, (c) electric field of DWC (left, P1 is excited by E_{11}^{x} mode), NRDWC (middle, P1 is excited by LSM_{01}^{x} mode) and the proposed HMDWC (right, P1 is excited by E_{11}^{x} mode)) at 280 GHz. Symmetrical HMDW crossover is called SHMDWC in Figure 7.6 (b) legend for short, DW crossover is called DWC, NRD waveguide crossover is called NRDWC ····· 101

Figure 7.7 Loss of DW and NRD waveguide with a cross-section with h = 0.254 mm, w = 0.28 mm and ε_r = 9.8. The loss tangent of alumina is set as tan δ = 0.001, conductivity of metal layers (gold) is set as $\sigma = 4.1 \times 10^7$ S/m. The letters c, d and t refer to conductor, dielectric and total losses, respectively ····· 103

Figure 7.8 (a) Simulation model of the proposed crossover with supporting and feeding structure, (b) details of feeding port of the aluminum housing, unit in mm, (c) simulated performance, inset: simulated electric field of the crossover with (left) and without (right) metal layers over intersection when P1 is excited at 280 GHz ····· 104

Figure 7.9 (a) Simulation model of the proposed crossover with P3/4 unloaded (left) and with the orthogonal dielectric rod tapered at two ends (right), (b) performance of the through guide from P1 to P2 with the orthogonal dielectric guide loaded with wave ports, unloaded and tapered. h = 0.254 mm, w = 0.28 mm, $l_{nrd} = w_{nrd}$ = 1 mm, l_d = 2 mm, l_a = 2 mm. E_{11}^{x} mode is assigned ····· 106

Figure 7.10 Electric field distributions of two-port device intersected with tapered orthogonal dielectric rod with (left) and without (right) two metal plates at the intersection at 280 GHz. E_{11}^{x} mode is assigned at P1 ····· 107

Figure 7.11 (a) Simulation model of the presented back-to-back device with four intersections with metal plate covering, (b) exploded view of aluminum housing for enclosing the fragile alumina structure, (c) simulated transmission performance, (d) electric field of the two-port device with four cascading intersections covered by two metal layers (left) and not covered (right) at 280 GHz. The blue dashed line is the transmission between two reference planes indicted with red dot-dashed line in Figure 7.11 (a) without considering material losses. Four intersections only introduce 0.5 – 1.7 dB of structural loss (including leakage and reflection loss) from 272 GHz to 295 GHz with the assistance of metal layers ·····109

Figure 7.12 (a) Experimental prototype of two-port device with four intersections, (b) dimension details, (c) cover of aluminum housing for measurement, (d) assembled with the base of aluminum housing. Unit in mm ·····111

Figure 7.13 Comparison between measured losses (dashed red) and analytical losses (based on perturbation method) of aluminum rectangular waveguide with a designed dimension of 0.86 mm × 0.43 mm ·····113

Figure 7.14 Measured surface roughness profile of alumina substrate ·····114

Figure 7.15 Simulated and measured results of two-port device with four intersections covered by metal layers. Simulated results are based on a modified model with the measured size of the fabricated prototype in Figure 7.12·····114

Figure 7.16 Effect of width of the metal layers on the performance of the two-port device·····115

Figure 7.17 (a) Schematic of a potential displacement of alumina circuit inside the aluminum housing, (b) potential offset or rotation between the alumina circuit and the aluminum housing during measurement. Unit in mm ·····116

Figure 7.18 Offset effect of the alumina circuit in the aluminum housing on the simulated performance of the two-port device. (a) off_x, (b) off_z·····117

Figure 7.19 Tilt effect of the alumina circuit with respect to the aluminum housing on the simulated performance of the two-port device·····117

Figure 7.20 Effect of imperfect matching taper of the alumina circuit on the simulated performance of the two-port device ·····118

Figure 7.21 Simulated and measured results of two-port straight dielectric waveguide operating in E_{11}^{y} mode. ε_r = 9.8 and tan δ = 0.001 are used for alumina in the simulation ·····118

Figure 7.22 Comparison between the simulated results of the two-port device with rectangular and trapezoid shaped cross section and measured results ·····119

Figure 8.1 Structures (top) and electric field distributions (bottom) of dividers. (a) Y-shape dielectric waveguide (DW) divider, (b) DW divider with smooth bend transition, (c) compact DW divider, (d) hybrid metallo-dielectric waveguide (HMDW) divider·····124

Figure 8.2 (a) Image SINRD waveguide, (b) conductor loss of SINRD waveguide and iSINRD waveguide ·····125

Figure 8.3 LSE_{11} mode suppressor based on mode selectivity·····126

Figure 8.4 Mode conversion of NRD 90° bend·····126

Figure 8.5 Structures (top) and electric field distributions (bottom) of 90° bends. (a) DW bend, (b) HMDW bend without mode suppressor, (c) HMDW bend with mode suppressor·····127

Figure 8.6 Routing EM waves (a) with DW bends and (b) with NRD bends·····127

Figure 8.7 Flexible routing between multiple modules ·····129

Figure 8.8 Electric field distribution of multiple (a) DW crossovers, (b) NRD waveguide crossovers ·····129

Figure 8.9 3-D printing custommizable substrate ·····130

LIST OF SYMBOLS AND ABBREVIATIONS

3-D	Three-dimension
AAO	Anodic aluminum oxide
ABF	Ajinomoto build-up film
AFSIW	Air-filled substrate-integrated waveguide
AGC	Asahi Glass Company
AHMDW	Asymmetrical hybrid metallo-dielectric waveguide
ARC	Alumina ribbon ceramic
BCB	Benzocyclobutene
BEOF	Back-End-Of-Line
CMOS	Complementary metal-oxide-semiconductor
CNC	Computerized numerically controlled
COC	Cyclo-olefin copolymer
CPW	Co-planar waveguide
CSRR	Complementary split ring resonator
DIIG	Dielectric insulated image guide
DIL	Dielectric image line
DRIE	Deep reactive ion etching
DRW	Dielectric ribbon waveguide
DUT	Device under test
DW	Dielectric waveguide
DWC	DW crossover
E-	Electric-

EDM	Electric discharge machining
EM	Electromagnetic
FDM	Fused deposition modeling
GHz	Gigahertz
G-line	Goubau-line
HDPE	High-density polyethylene
HE	Hybrid electric
HFSS	High frequency structural simulator
HMDW	Hybrid metallo-dielectric waveguide
HMDWC	HMDW crossover
HMSIW	Half-mode substrate-integrated waveguide
HR-Si	High-resistivity silicon
IBM	International Business Machines
IC	Integrated circuit
iNRD	Image non-radiative dielectric
KMPR	Kathy M. P. R
LCP	Liquid crystal polymer
LSE	Longitudinal-section electric
LSM	Longitudinal-section magnetic
LTCC	Low temperature co-fired ceramic
MD	Metallo-dielectric
MEMS	Micro-electromechanical system
ML	Microstrip line
MLT	Multi-layer technology

mmW	Millimeter-wave
MRR	Microstrip ring resonator
MWG	Metallic waveguide
NRD	Non-radiative dielectric
NRDWC	NRD waveguide crossover
PCB	Printed circuit board
PGL	Planar Goubau line
PPWG	Parallel-plate waveguide
PS	Polystyrene
RDW	Rectangular dielectric waveguide
RWG	Rectangular waveguide
SAP	Semi-Additive Patterning
SHMDW	Symmetrical HMDW
SHMDWC	SHMDW crossover
SIC	Substrate-integrated circuit
SIDW	Substrate-integrated DW
SIHMD	Substrate-integrated hybrid metallo-dielectric
SIIG	Substrate-integrated image guide
SINRD	Substrate-integrated NRD
SIRW	Substrate integrated ribbon waveguide
SIW	Substrate-integrated waveguide
SLA	stereolithography
SLM	Selective laser melting
SLS	Selective laser sintering

SOG	Silicon-on-glass
SOLT	Short-open-load-through
SR	Surface ratio
TE	Transverse electric
TEM	Transverse electromagnetic
TFML	Thin-film microstrip line
THz	Terahertz
TM	Transverse magnetic
TSV	Through-silicon via
VDI	Virginia Diodes Inc.
UV-LIGA	Ultraviolet lithographic
WR	Waveguide rectangular

LIST OF APPENDICES

Appendice A 156
Appendice B 159
Appendice C 160
Appendice D 163

CHAPTER 1 INTRODUCTION

1.1 Research background

With the rapid development of THz technology, we foresee a vast deployment of high-performance wireless sensors and communication devices that will always be omnipresent and accessible. To support this, these wireless circuits and systems including antennas must be highly integrated to accommodate numerous components within limited spaces. In any wireless communication and sensing system, waveguide structures are essential elements, serving to build and interconnect functional blocks. However, traditional waveguides often pose challenges in space efficiency and are sensitive to losses—particularly at THz frequencies. Loss mechanisms vary based on geometry, frequency, and propagation mode.

Various waveguide types, such as microstrip lines (MLs), coplanar waveguides (CPWs), metallic waveguides (MWGs), and substrate-integrated waveguides (SIWs), have been utilized in wireless circuit and system designs. However, these conductor-based structures face significant challenges in the THz band due to pronounced frequency-dependent conductor losses, which stem from the finite conductivity of metals and possible field singularities along the propagation path. Additionally, surface roughness from fabrication further contributes to these losses at higher frequencies. In contrast, dielectric waveguides (DWs), commonly used in optical circuits and systems, offer significant promise for THz applications due to the absence of conductor losses. Yet, DWs are prone to radiation loss and mode conversion loss at discontinuities, necessitating smooth transitions that are challenging to implement in compact, integrated circuits and systems.

To address these challenges, early-developed non-radiative dielectric (NRD) waveguides present a compelling solution. These structures can be optimized for specific frequency bands, allowing longitudinal-section electric (LSE) and

longitudinal-section magnetic (LSM) modes to propagate through discontinuities without radiation. For integration, synthesized planar NRD waveguides—also known as substrate-integrated NRD (SINRD) waveguides—offer a metallized-via-free design that simplifies fabrication, which is essential for THz circuit and system development.

Each waveguide type brings distinct advantages and limitations, underscoring the need for innovative designs to shift the THz band paradigm while harnessing the strengths and advantages of various waveguide technologies. A promising solution lies in hybrid architectures that integrate diverse structures, combining metallic and dielectric waveguides in both open and closed configurations. This approach aims to optimize performance, reduce losses, and enhance the overall efficiency of THz integrated circuits and systems.

1.2 Research objectives

The primary objectives of this Ph.D. project are to propose, investigate, and demonstrate innovative waveguide architectures and technologies for THz circuit and system integration. This work is conducted through both theoretical analysis and experimental validation, with a focus on key factors including loss performance, efficiency, ease of fabrication, and structural compactness. The research specifically addresses the following aspects:

(1) Transmission performance and fabrication complexity: This research examines the transmission characteristics, fabrication complexity, and cost implications of various substrate-integrated circuits optimized for THz applications. A detailed analysis is conducted on SINRD waveguides, SIWs, and substrate-integrated dielectric waveguides (SIDWs) to identify topologies that achieve high performance while reducing manufacturing challenges. The objective is to pinpoint optimal designs that balance efficiency with fabrication simplicity and cost-effectiveness.

(2) Fabrication process development: Advancing and optimizing fabrication techniques are considered for producing high-performance, high-yield waveguide architectures.

This work is set to focus on enhancing precision, reliability, and repeatability in the manufacturing process, ensuring that the resulting waveguides meet the rigorous requirements for THz applications.

(3) Evaluation of hybrid waveguide architectures: Hybrid waveguides are investigated that integrate and explore different types of waveguides, such as metallic and dielectric structures, to leverage the unique advantages of each. This study will assess coupling efficiency, fabrication complexity, and structural simplicity, aiming to achieve minimal loss, cost-effectiveness, and optimal performance in THz integrated circuits and systems.

(4) Application of hybrid waveguide architectures: Hybrid waveguide designs are adapted for low-loss, compact THz integrated circuits and systems. This research includes practical demonstrations showcasing the implementation of these hybrid architectures in connection with various applications, highlighting their potential to achieve high-performance THz integrated circuits and systems.

1.3 Thesis outline

Chapter 1 provides an overview of the background, motivation, and objectives of this Ph.D. project on hybrid waveguide architectures and technologies for THz circuits and systems. It also presents the thesis structure, guiding the reader through the research and its contributions.

Chapter 2 reviews current THz transmission line technologies from an electrical perspective, including an examination of planar transmission lines, MWGs, SIWs, and DWs.

Chapter 3 focuses on SINRD waveguides operating in the WR3-band from 220 to 330 GHz, providing a theoretical analysis of key performance metrics, including cut-off frequency, dispersion, bandwidth, and attenuation. Solution to Maxwell's equations for supported hybrid longitudal-section electric (LSE) and longitudal-sention magnetic (LSM) modes propagation in the SINRD waveguide is obtained. Bounday conditions

at dielectric interfaces are applied to derive the transcentental equation determining the cut-off frequency for each mode. The loss performance of each mode is investigated using perturbation method. Guidance based on parametrical study is offered for optimizing waveguide design with respect to bandwidth and loss performance. Equivalent mode is used throughout the modal analysis and parametrical study. A back-to-back SINRD waveguide was designed and fabricated using a 0.254 mm as-fired alumina substrate. For comparison, SIW and SIDW structures operating in the same frequency band were also designed and fabricated with the same material. Measured results reveal that the SINRD waveguide exhibits lower loss than the SIW but higher loss than the SIDW. These findings highlight the potential advantages of hybrid waveguides that combine dielectric and metallic elements. The SINRD waveguide demonstrates superior transmission characteristics and a simpler fabrication process compared to the SIW, as it eliminates the need for metallized vias.

Chapter 4 presents a double-layer SINRD waveguide design. For achieving a wider bandwidth, the SINRD waveguide requires a larger dielectric constant contrast between the guiding core and the perforated region. This necessitates a dense air-hole perforation, which, however, can make the substrate fragile. Furthermore, heat from laser processing can damage the air-hole edges and metal surfaces, potentially compromising the SINRD waveguide's integrity. The proposed vertically stacked double-layer SINRD waveguide addresses these challenges by using two half-height substrates, each metallized only on the backside, with laser drilling beginning from the front. This configuration preserves the metal layers on the substrate backsides. Interestingly, a potential thin air layer between the stacked layers—which often degrades performance of multi-layer waveguides—has negligible effect on the SINRD waveguide's functionality. However, misalignment between the layers can introduce unwanted parallel-plate waveguide (PPW) modes, degrading transmission. Efforts to minimize misalignment are essential to enhance the transmission performance of this double-layer SINRD waveguide.

Chapter 5 introduces a substrate-integrated hybrid metallo-dielectric (SIHMD) waveguide architecture that combines SINRD and SIDW. The compatibility between the LSM_{01} mode of the SINRD waveguide and the E_{11} mode of the SIDW allows EM waves to traverse the interface between the two waveguides without the need for a matching transition. A back-to-back hybrid waveguide was designed and simulated, incorporating a SINRD section in the middle, flanked by two SIDWs at either end. Measurements from the fabricated prototype show strong agreement with the simulation results. For comparison, a second hybrid waveguide was constructed by replacing the SINRD section with an SIW. The results indicate that the hybrid architecture featuring the SINRD waveguide provides superior transmission characteristics while also simplifying the manufacturing process.

Chapter 6 presents the first application of the proposed hybrid metallo-dielectric waveguide (HMDW) architecture for developing compact, low-loss circuits. In this chapter, NRD waveguides are specifically employed for sharp bends to mitigate radiation loss. By incorporating two parallel metal layers to sandwich the dielectric waveguide bends, we can achieve radiation-free bends within a certain bandwidth. This design effectively reduces the bend radius by approximately tenfold with only a small increase in insertion loss. However, the operational bandwidth remains constrained due to mode conversion between the LSM_{01} and LSE_{11} modes at the NRD bends, as well as the mode selectivity inherent in the proposed hybrid waveguide architecture. To broaden the bandwidth, it is crucial to preserve the LSM_{01} mode throughout the NRD bends by integrating LSE_{11} mode suppressors.

Chapter 7 investigates the application of the proposed hybrid waveguide architecture in THz crossover configurations. In this configuration, NRD waveguide is employed at the intersection of two DWs to minimize radiation loss at the discontinuity and reduce crosstalk between the guiding paths. The mode conversion occurring at the NRD intersection, combined with the mode selectivity of the hybrid waveguide, facilitates this crosstalk reduction. Specifically, the E_{11} mode in the DW section is converted to

the LSM_{01} mode in the NRD and then reconverted to the E_{11} mode upon exiting the NRD guide. In the orthogonal NRD guide, both the LSE_{11} and LSM_{01} modes are excited. Notably, the coupled LSE_{11} mode in the orthogonal guide is unable to pass through the interface between the NRD guide and the DW due to mode incompatibility, which diminishes crosstalk. To better illustrate the advantages of the hybrid waveguide in mitigating crosstalk, multiple orthogonal guides are cascaded. Both simulated and measured results demonstrate that the NRD section significantly enhances the confinement of EM waves in the intended guiding direction.

Chapter 8 concludes the research presented in this thesis by summarizing the key findings and contributions of the hybrid metallo-dielectric waveguide (HMDW) architecture for THz circuits and systems. Additionally, this chapter outlines potential avenues for future research and development, highlighting areas where further exploration could advance the field.

1.4 Research impact

The impact of my research is far-reaching, influencing multiple facets of technological advancement. By developing hybrid metallo-dielectric waveguide architectures that optimizes THz transmission performance and enhances space efficiency, my work can address the high demand for more efficient, compact, cost-effective THz circuits, which are essential for the future high-speed wireless communication and sensing systems. The enhanced performance of THz circuits could lead to faster date rates, wider bandwidth, and more reliable communication links, which are essential for meeting the ever-increasing demand for date in next-generation technologies like 6G and beyond. By focusing on space efficiency and minimizing the footprint of THz circuits, this work enables the development of more compact systems, which are crucial for portable devices. The reduction in size also aids in the development of systems that are easier to integrate into wearable technologies, smart home devices, and autonomous vehicles. The involved manufacturing process in this research is cost-effective, making it more feasible for large-scale development in commercial and industrial applications.

CHAPTER 2 LITERATURE REVIEW

The THz frequency band, ranging from 0.1 to 10 THz, has emerged as a vibrant area of research over the past few decades. Scholars from both microwave and optical domains have extensively investigated THz sources, guiding mechanisms, and detection methods. Low-loss interconnects are crucial for achieving high-efficiency THz systems, as they alleviate demands on system power and detection sensitivity. Although THz transmission lines exhibit mechanistic similarities to established microwave and optical waveguides, they encounter unique challenges related to manufacturing and transmission performance. Recent advancements in fabrication processes aim to enhance production capabilities, while new materials are being explored to improve THz transmission efficiency. This chapter provides a comprehensive overview of THz waveguide technologies from an electrical perspective.

2.1 Planar metal guiding lines

2.1.1 Coplanar waveguides

In the early development of THz technology, scaled-down coplanar waveguides (CPWs) were commonly used for wave guidance, as illustrated in Figure 2.1 (a). However, transmission losses can become considerable due to conductor loss, dielectric loss, and Cherenkov-like radiation loss [1]. Research has shown that radiation loss becomes predominant above 200 GHz, exhibiting a quadratic dependence on frequency [1], [2]. To mitigate radiation loss, various strategies have been proposed, such as the use of air bridges (Figure 2.1 (b)) [3] and narrowing the ground plane [4].

Additionally, research detailed in [5] examined CPWs fabricated on low permittivity substrate. The findings indicate that a higher impedance transmission line on a thin, low permittivity substrate exhibits lower conductor and radiation losses. This increased impedance results in a weaker magnetic field around the conductor, thereby lowering the current density and, subsequently, the conductor loss. However, matching a high

impedance transmission line to the standard 50-Ω can pose challenges. In [6], a 50-Ω CPW was fabricated on a 30-um-thick benzocyclobutene (BCB) substrate with a relative permittivity ε_r= 2.42 and a loss tangent of tan δ = 0.007. This design achieved an attenuation constant of 2.7 dB/mm at 400 GHz and 3.5 dB/mm at 500 GHz. The low ε_r and tan δ of BCB contribute to a low dispersion behavior up to 1 THz. In [7], an air-filled cavity-back CPW (Figure 2.1 (c)) was presented, operating between 220 to 325 GHz. The sidewalls and ground plane are set to enhance the uniformity of the field distribution on the conductors, thereby reducing conductor loss. Additionally, the removal of dielectric material beneath the signal line further diminishes dielectric loss, resulting in a measured average loss of less than 0.12 dB/mm across the entire band of interest.

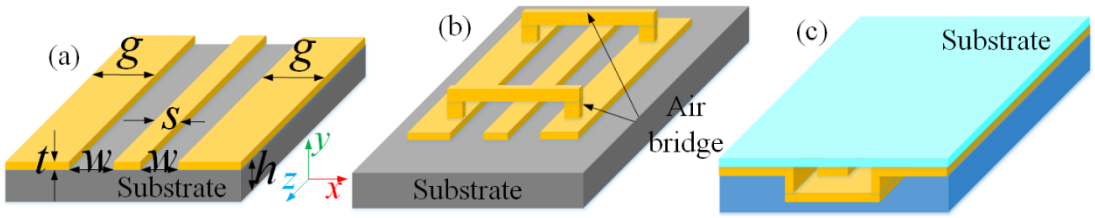

Figure 2.1 (a) CPW, (b) CPW with air-bridge, (c) air-filled cavity-back CPW

2.1.2 Thin-film microstrip lines

Microstrip lines (MLs) (Figure 2.2 (a)) on semiconductor wafer typically ranging from 100 to 500 um in thickness, featuring an extended ground plane on the backside, have been used for microwave and millimeter-wave (mmW) integrated circuits up to 100 GHz [8]. However, as the frequency increases, more energy becomes confined within the wafer, leading to higher transmission losses. Additionally, MLs exhibit significant dispersion as the operating frequency approaches the cut-off frequency of the dispersive higher-order slab modes supported by the grounded slab.

To solve this issue, one approach is to shift the dispersive higher-order modes to higher frequencies. In [9], a highly conductive cobalt silicide ground plane, with conductivity comparable to aluminum at room temperature, was buried 7 um beneath a 5-um-wide

aluminum ML on a high-resistivity silicon (HR-Si) wafer. The proposed ML exhibits lower dispersion within a 100 GHz bandwidth compared to conventional MLs.

Thin-film microstrip lines (TFMLs) (Figure 2.2 (b)) have been proposed based on a similar principle [10]. In this design, a scaled-down 2-um-wide aluminum ML with both the signal and ground conductors at the same side of the semiconductor wafer was fabricated. An 800-nm-thick SiO_2 layer with a high resistivity of approximately 10^{15} Ω·cm separated the signal and ground conductors. Another 500-nm-thick SiO_2 insulating layer was inserted between the ground plane and the semiconductor wafer. This configuration confines the electric field within the surface-mounted SiO_2 layer, reducing dielectric loss and geometric dispersion up to several hundred GHz. Moreover, the mode confinement within the top dielectric layer minimizes crosstalk, facilitating the development of highly integrated circuits.

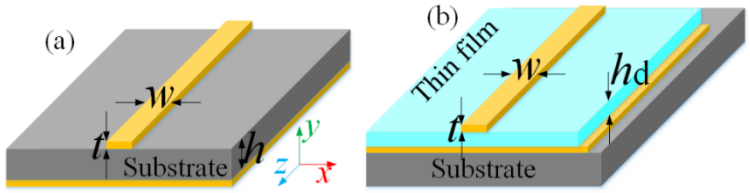

Figure 2.2 (a) Microstrip line, (b) thin-film microstrip line

Various polymers have been used for TFMLs operating in the THz band [11], [12], [13], [14], [15], [16], [17]. In [11], [12], a thin layer of polymerized cyclotene was employed as the dielectric layer between the signal and ground conductors of the TFML. The fabrication process began with the evaporation of an 800-nm-thick aluminum layer on a low-resistivity silicon wafer, which served as the ground conductor. Next, cyclotene from Dow Chemicals, with a ε_r of 2.7 and a tan δ of 0.015 (obtained through curve fitting), was spin-coated and cured. Following this, another 800-nm-thick aluminum film was deposited and patterned using a lift-off technique to create an 8-um-wide signal conductor. Samples with varying polymer thickness but a constant signal width were fabricated and measured to evaluate the impact of characteristic impedance on transmission performance. A 1.7-um-thick sample yielded an impedance of 35 Ω, while

a 5.4-um-thick one provided an impedance of 70 Ω. Both simulations and measurements revealed that the 35-Ω line exhibits about twice the attenuation of the 70-Ω line up to 1 THz. At frequencies below 100 GHz, conductor loss dominates. As the operating frequency increases, conductor loss increases with the square root of frequency ($f^{1/2}$), whereas dielectric loss increases proportionally. Therefore, dielectric loss becomes more significant, particularly for high-impedance lines due to the stronger electric field within the dielectric layer. TFMLs using BCB as the dielectric layer can achieve low dispersion with an acceptable attenuation up to 1 THz (4 dB/mm at 1 THz). In summary, isolating the signal conductor from semiconductor using a thin, low-loss dielectric film can improve the transmission performance of MLs, thereby enhancing the overall efficiency of circuits and systems. A similar technique has been applied to reduce losses of CPWs [18], [19].

2.1.3 Advanced material-based transmission lines

In studies [20], [21], a thin, large-panel glass interposer has been reported as a superior alternative to silicon and organic interposers due to its low cost, excellent surface finish, and dimensional stability. A “polymer on glass” process was employed to prevent glass from cracking, where polymer layers acting as stress buffers during cutting, thereby improving yield. These polymer layers also serve as adhesion layers for metallization, thus facilitating the manufacturing process. A 15-um-thick Ajinomoto build-up film (ABF) was laminated on both sides of a 100-um-thick EN-A1 glass substrate from Asahi Glass Company, creating a composite ABF/glass/ABF stack. Microstrip ring resonator (MRR) method was applied to characterize this stack, which has a stable ε_r of 4.72 ± 0.1 and a tan δ ranging from 0.004 to 0.015 across the 20 - 170 GHz band. ML and CPW were designed and fabricated on the stack using a Semi-Additive Patterning (SAP) process [22]. The 70-Ω CPW line exhibits an average attenuation of 0.055 - 0.50 dB/mm, the ML shows an average attenuation of 0.12 - 0.62 dB/mm within the characterized band. In [23], a 70-Ω ML was fabricated on an additional ABF layer

placed atop the ABF/glass/ABF stack, demonstrating comparable transmission performance to lines fabricated directly on the composite stack.

Ultrathin and flexible alumina ribbon ceramic (ARC) substrates from Corning Inc., known for their very low tan δ, have been used in mmW applications [24], [25], [26]. In one study [24], an 80-um-thick ARC was characterized using the MRR method, exhibiting a stable ε_r of about 10.12 and an exceptionally low tan δ varying from 0.000066 to 0.0013 over 3 - 170 GHz. ML and CPW on ARC were fabricated using the SAP process. The measured loss for a 50-Ω ML varies from 0.019 to 0.293 dB/mm, the loss for a 60-Ω CPW line ranges from 0.026 to 0.24 dB/mm within the characterized frequency band.

2.1.4 Planar Goubau lines

Another type of planar transmission lines, known as the planar Goubau line (PGL) shown in Figure 2.3 [27], [28], [29], [30], [31], [32], has gained significant attention for its low-loss performance in the THz band. The PGL is essentially the planar version of a dielectric-coated single wire [33], [34], [35], [36]. In [28], a 1-um-wide gold PGL was printed on the surface of a 450-um-thick crystalline quartz substrate with a ε_r of 4.5 and a low tan δ of 0.00011. An optimized CPW line was used to excite the non-radiating TM_{01}-like mode (Goubau mode). The estimated loss for the fabricated PGL is about 2.8 dB/mm at 140 GHz and 4 dB/mm at 220 GHz. In [37], [38], [39], [40], [41], ultrathin dielectric layers such as HR-Si and polyethylene terephthalate (PET) films were used to minimize substrate mode excitation, thus reducing radiation losses.

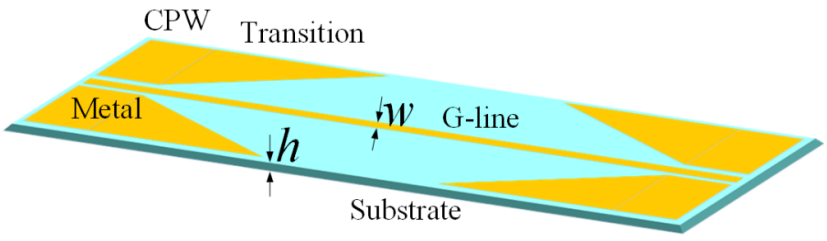

Figure 2.3 Planar Goubau line

2.2 Metallic waveguides

Metallic waveguides (MWGs), widely used in microwave applications, have been scaled down in size to effectively guide THz waves, for example, parallel-plates waveguides (PPWGs) [42], [43], [44], [45], [46], metallic slit waveguides [47], two-wire transmission lines [48], as shown in Figure 2.4 (a) - (c). These configurations are favored for THz pulse propagation due to their low dispersion and low loss. Coaxial transmission lines with a supporting dielectric spacer between the inner and outer conductors [49], [50] provide a full electromagnetic shielding.

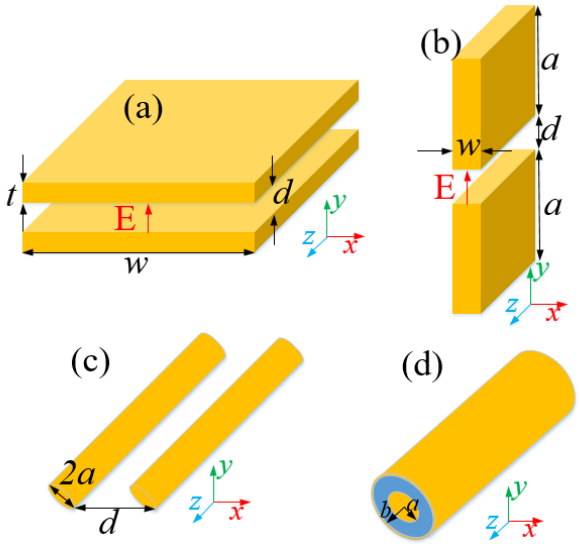

Figure 2.4 (a) Parallel-plate waveguide, (b) metallic slit waveguide, (c) two-wire transmission line, (d) coaxial transmission line

2.2.1 Single-wire waveguides

A single conductor with finite conductivity can guide surface wave propagation as initially described by Sommerfeld. The field associated with Sommerfeld's wave is loosely bound to the wire's surface and extends very far. As reported in [33], [34], [35], [36], a thin dielectric layer on the wire surface (Goubau line, also known as G-line) can considerably change the field extension without significantly affecting the phase velocity, making the G-line suitable for wideband signal propagation. However, a large

clearance around single-wire waveguides is required to avoid field perturbation and subsequent radiation, which limits their practicality in microwave applications. As frequencies up to the THz band, the field extension of the surface wave supported by single-wire waveguides becomes more manageable [36]. More importantly, their low-loss characteristics make them exceptional candidates for guiding THz waves [51], [52].

2.2.2 Cylindrical waveguides

Metallic waveguides (MWGs), which confine EM waves within an air core wrapped in metal, are free from radiation losses [53], [54]. Cylindrical and rectangular waveguides are discussed frequently, while elliptical waveguides are less popular [55]. In the case of a cylindrical waveguide (Figure 2.5 (a)) [56], TE_{01} mode has the lowest loss; however, exciting this azimuthally polarized mode can be challenging. TE_{11} mode, despite its higher loss, holds greater practical significance than the TE_{01} mode.

To reduce conductor loss, a thin dielectric layer can be added to the inner metallic wall, reducing the normal electric field at the metallic surface and then lowering conductor loss [57], [58], [59], [60], [61], [62], [63], [64], [65], [66]. Optimizing the thickness of the dielectric layer can suppress the TE_{01} mode meanwhile maintaining low transmission loss for the hybrid HE_{11} mode. In [60], a cylindrical hollow silver waveguide with a polystyrene (PS) coating on the inner wall has been presented, as shown in Figure 2.5 (b). A PS film was deposited over the inner silver layer of a 2.2-mm-diameter glass tube using a liquid-flow coating process [67], [68]. The silver layer, about 1 um thick, exceeds the skin depth for the operating band. This configuration with an optimal 8.2-um-thick PS film achieves a transmission loss of 0.95 dB/mm at 2.5 THz.

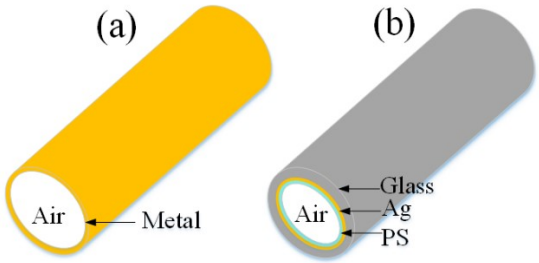

Figure 2.5 (a) Cylindrical metallic waveguide (MWG), (b) silver/PS-coated glass tube

Glass-based waveguides are fragile and lack flexibility, whereas plastic tubes offer enhanced flexibility [69]. In [70], polycarbonate (PC) was used to form a hollow tube. A copper film, with a thickness of 0.5 - 0.7 um, was deposited inside a 3-mm-diameter tube using electroless plating and liquid-phase chemistry process [71]. This design achieved a measured loss of about 3.8 dB/m at 1.89 THz. In [65], a bendable silver-coated acrylonitrile-butadiene-styrene (ABS) tube was used for low-loss transmission and imaging in the low THz band. Waveguides with different inner diameters (2.3, 3.2 and 4.2 mm) were investigated and fabricated. Experimental results indicated that the 4.2-mm-diameter waveguide has the lowest loss, measuring 0.71 dB/m and 1.41 dB/m at 100 GHz and 300 GHz, respectively. The 3.2-mm-diameter waveguide exhibits a better bendability. The loss can be further reduced by adding a thin low-loss dielectric film.

2.2.3 Rectangular waveguides

Rectangular waveguides, as shown in Figure 2.6, have found extensive applications in guiding THz waves. The main challenge is manufacturing. Traditional machining methods, such as computerized numerically controlled (CNC) milling and electric discharge machining (EDM), are often costly and time-consuming [72], [73], [74], [75]. In recent decades, micromachining techniques based on photolithography have emerged as a promising alternative due to their high precision.

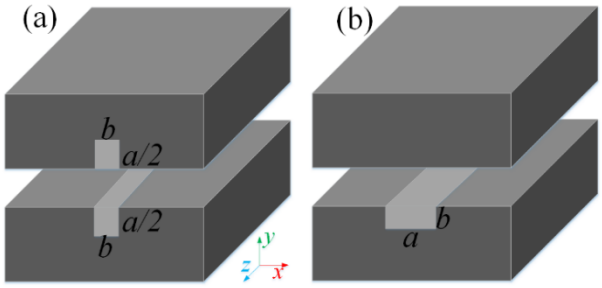

Figure 2.6 (a) E-plane split waveguide, (b) H-plane split waveguide

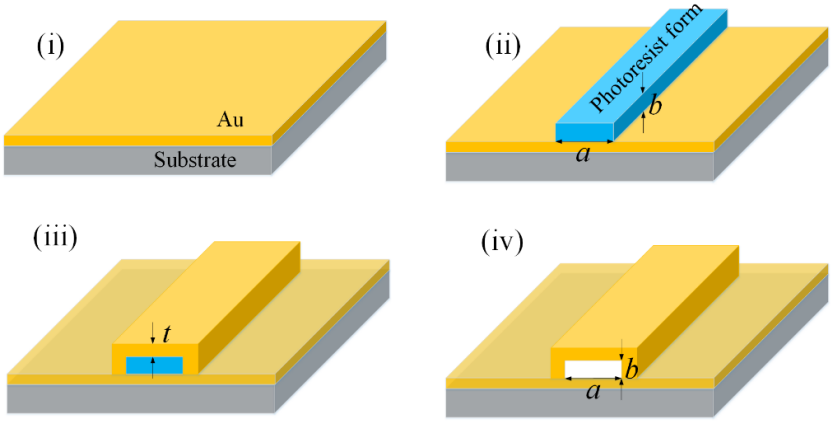

Figure 2.7 Process of on-wafer micromachined waveguide. (i) Deposit gold on a silicon wafer, (ii), photoresist form, (iii) deposit gold on entire surface, (iv) remove photoresist

In [76], an on-chip micromachined waveguide was developed. As shown in Figure 2.7, a titanium adhesion layer was first deposited, followed by a gold layer thicker than one skin depth of the operating band, on the surface of a semiconductor wafer. A thick photoresist layer, about 100 um in thickness, was then spin-coated on top of the gold layer, baked, exposed, and developed to form the desired waveguide shape. Another gold layer was deposited over the entire surface through evaporation and electroplating, reaching a total thickness of 50 um to increase strength. Finally, the photoresist was removed with acetone. The measured loss for this design ranges from 0.1 to 0.6 dB/mm within the 90 - 110 GHz band, which is relatively high because of the reduced height of the designed waveguide compared to a full-height waveguide. The thickness of the

photoresist limits the maximum achievable waveguide height, thereby restricting the optimal transmission performance.

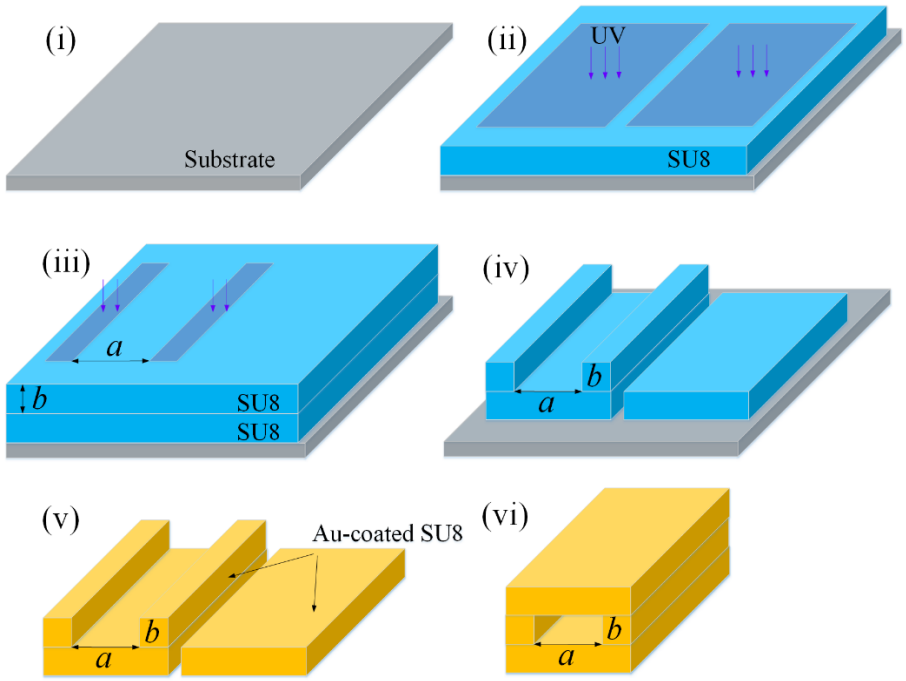

Figure 2.8 SU-8 photoresist micromachining. (i) Silicon substrate, (ii)-(iv) form waveguide core, (v) deposit gold, (vi) assemble two pieces

Advanced machining techniques have been developed to overcome the limitation of achievable aspect ratio. In [77], a waveguide with a cross-section of 2.54 mm × 700 um (half-height) was fabricated using SU-8 photoresist micromachining. The fabrication process is described in Figure 2.8. This design achieves a loss of 0.4 - 0.8 dB per guide wavelength over a frequency range from 75 to 110 GHz. In [78], an improved two-layer SU-8 photoresist micromachining technology was developed. The demonstrated WR3-band waveguide has a measured loss of 0.012 - 0.05 dB/mm, which is comparable to the performance of standard waveguides with an average loss of about 0.02 dB/mm.

Silicon wet etching has been employed to create rectangular waveguide operating in the WR10-band [79], achieving a measured loss of about 0.04 dB per wavelength at 100 GHz, which is comparable to commercial waveguides with a loss of about 0.024 per wavelength. Silicon deep reactive ion etching (DRIE) [80], [81], [82], [83], [84]

provides nearly vertical etched sidewalls and allows for more complex shapes. In [85], a waveguide operating in the 350 - 460 GHz band was presented, demonstrating an average loss of 0.086 dB/mm within this band. Numerous works have been done to enhance the performance of rectangular waveguides in the THz band by addressing issues such as misalignment and potential air gaps, decreasing sidewall slope, and reducing surface roughness. DRIE-based Si waveguides have reached a mature stage of development and show significant potential in THz applications.

An all-metal microfabrication technique based on ultraviolet-lithography (UV-LIGA) was developed in [86], [87], [88], [89]. This approach involves sputtering a seed layer onto a thick photoresist former patterned using LIGA, followed by electroplating to form the waveguide shell. Afterwards, the photoresist is removed to yield the shell. Although similar to the technique reported in [76], this method utilizes thick photoresist materials such as SU-8 [90], [91] and KMPR [89], making full-height waveguides possible. Also, this method can achieve a surface roughness as low as 30 nm, which is very crucial for improving the performance of THz waveguides. In [89], a full-height WR3-band waveguide was presented, with a measured loss of about 0.96 dB/mm.

Additive manufacturing, commonly known as 3-D printing, has gained popularity due to its cost-effectiveness and rapid prototyping. This technology enables the creation of complex structures through layer-by-layer material deposition. Various 3-D printing technologies are available, including fused deposition modeling (FDM), stereolithography (SLA) and selective laser sintering (SLS). The precision of 3-D printing largely depends on the nozzle [92]. FDM typically has a voxel size of $400\times400\times50$ um^3, which may be insufficient for producing THz prototypes. In [93], an E-plane split WR10-band waveguide was fabricated using the SLA featuring a voxel size of $50\times50\times50$ um^3. The inner wall of the 3-D printed plastic pipe was metallized by electroless plating process. The measured loss is about 0.036 dB per wavelength, which is comparable to that of commercial waveguides.

All-metal 3-D printing technology was developed in [94]. Selective laser melting (SLM) technology was used to melt Cu-155n powder to build waveguides. The performance of the 3-D printed waveguide is comparable to that of commercial waveguides in the E-band (60 - 90 GHz). However, performance degrades rapidly at frequencies above 100 GHz due to surface roughness, with bumps and leftover powder noted inside the waveguides. Post-polishing processes are needed to improve the propagating performance of metallic 3-D printed waveguides. The combination of SLM technology and these post-polishing processes can lead to high costs, making this method most suitable for creating complex structures that are difficult to achieve with traditional machining methods.

Table 2.1 Table of rectangular waveguides

Fabrication methods	Material of shell	Dimension	Frequency (GHz)	Loss	Ref.
CNC milling	Aluminum/brass	2.54 × 1.27 mm	70-116	0.004 dB/mm (Aluminum) 0.008 dB/mm (brass)	[72]
On-chip micromachining	Gold	1.84 × 0.1 mm	90-110	0.1-0.6 dB/mm	[76]
Two layer SU8 micromaching	Silver	864 × 432 um	220-325	0.012-0.05 dB/mm	[78]
Silicon micromachinned with KOH solution	Gold	2.54 × 1.27 mm	75-115	0.04 dB/λ at 100 GHz	[79]
DRIE (Silicon)	Gold	380 × 190 um	550-750	0.15 dB/mm at 600GHz	[82]
		864 × 275 um	220-325	0.02-0.07 dB/mm	[81]
		635 × 317.5 um	350-460	0.086 dB/mm	[85]
UV LIGA with KMPR resists	Nickel body with gold coating	864 × 432 um	220-325	0.042-0.126 dB/mm	[89]

All-metal micromachining	Copper	200 × 100 um	1300	N. A	[87]
3D-printing	Metal-coated plastic	2.54 × 1.27 mm	75-110	0,036dB/λg average	[92]
3D-printing	Cu-155n	3.03 × 1.55 mm	60-90	7.5dB/m	[94]
		1.73 × 0.82 mm	110-170	18.96 dB/m (50-mm length) 21.47 dB/m (100-mm length)	
		0.88 × 0.45 mm	220-325	120.92 dB/m (50-mm length) 96.12 dB/m (100-mm length	

2.3 Substrate-integrated waveguides

Air-filled MWGs are free from dielectric loss, but their bulkiness makes them unsuitable for integrated circuits. Moreover, integrating them with other planar circuits poses challenges. Although transitions between MWGs and planar circuits are feasible in the microwave regime, achieving such transitions in the THz band can complicate circuit design and degrade overall performance. In contrast, SIWs [95], [96] offer notable advantages for integrated circuits and systems. SIWs confine electromagnetic waves effectively between two metal layers and two rows of metallized via holes, providing enhanced shielding compared to MLs and CPWs.

2.3.1 General structure of SIWs

Figure 2.9 [95] illustrates the structure of SIWs. Two rows of plated through vias within a hosting substrate work as the sidewalls of a rectangular waveguide. The spacing between adjacent vias must be optimized to minimize radiation leakage and avoid electromagnetic bandgap effect within the band of interest. Meanwhile, the spacing must ensure the mechanical stability of the SIWs. For a given substrate, the cut-off frequency of the fundamental TE_{10} mode in SIWs can be precisely controlled by adjusting the distance between the two rows of plated through vias.

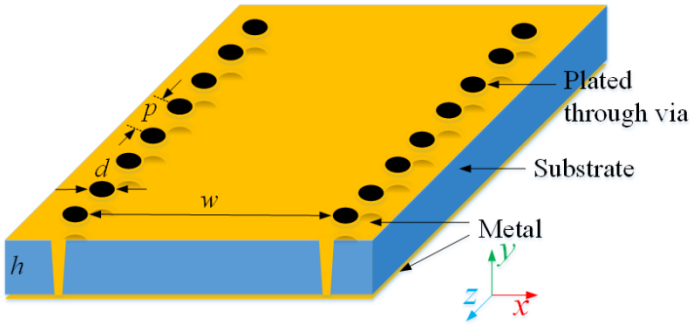

Figure 2.9 Structure of SIWs

2.3.2 CMOS-based SIWs

SIWs based on PCB process have been applied in microwave and mmW applications up to 100 GHz [96]. The operating frequency can be extended to 150 GHz using low-temperature co-fired ceramic (LTCC) process [97], and up to 360 GHz with micro-electromechanical systems (MEMS) process [98]. SIWs have been developed utilizing CMOS technology [99], [100], [101]. In [99], an SIW with a width of 560 um was designed on the thick dielectric layers and metallic layers provided by IBM 130nm CMOS process. Unlike other fabrication processes, the CMOS process restricts the use of large, continuous metal layers. Small slots were etched throughout the metal layers of the SIW, increasing conductor loss. Simulations indicate that the conductor loss is higher than the dielectric loss (using a model with a ε_r of 4.15 and a tan δ of 0.001) and radiation loss from these slots on the top and bottom metal layers.

In [102], [103], half-mode SIW (HMSIW) using CMOS technology was reported. To enhance impedance matching between a ML and the HMSIW, complementary split ring resonators (CSRRs) were etched onto the surface of the HMSIW. The measured loss of this design varies from 0.2 to 1.3 dB/mm from 120 to 220 GHz. In [104], a T-folding technique was used to reduce the footprint of the SIW, achieving a 30% reduction in size compared to a standard SIW. The simulated loss for this configuration is 2.41 dB/mm at 200 GHz.

Due to the limited thickness of the Back-End-Of-Line (BEOF) layers in CMOS technology, typically less than 10 um, SIWs with CMOS technology exhibit higher losses (2.4 dB/mm) compared to classical MLs (1 dB/mm) in the low THz band. Compared to 50-Ω MLs with a width under 10 um, the large footprint of SIWs, about half the guide wavelength, leads to higher costs.

2.3.3 SIWs on high-resistivity silicon interposer

SIWs based on other materials have been developed concurrently. Silicon, with a larger ε_r than silicon dioxide used in COMS BEOLs, allows for more compact waveguide design and is compatible with CMOS technology. In [105], a 70-um-thick HR-Si interposer was used to build an SIW interconnect in the D-band. A 2-um-thick silicon dioxide layer (ε_r = 3.9, tan δ = 0.0024) was used to isolate the top and bottom metal layers from the HR-Si interposer. Aluminum layers with a thickness of 2 - 3 um were used for metal layers. The sidewalls were formed using tungsten trenches (σ = 18.6 MS·m−1) achieved through a modified through-silicon via (TSV) technology. A prototype SIW with a cutoff frequency of 90 GHz was designed and fabricated. The measured loss ranges from about 0.4 to 0.6 dB/mm across the entire D-band, which is significantly lower than that of CMOS-based SIWs. Performance was improved by using a thicker substrate, resulting in a measured loss of 0.12 to 0.2 dB/mm in the 85 - 105 GHz band [106]. Other etching methods are also available for fabricating silicon-based SIWs [107], [108].

2.3.4 SIWs on other advance materials

Numerous studies have explored SIWs using advanced materials such as liquid crystal polymer (LCP). The electrical properties of LCP have been characterized in the D-band [109], with a ε_r of about 3.17 and a tan δ ranging from 0.0055 to 0.009. In [109], [110], a D-band SIW was fabricated using low-cost, low-loss raw LCP with a thickness of 50.8 um, achieving a measured average loss of about 0.8 dB/mm. In [111], polished LCP was used for an SIW prototype. The raw LCP was polished using a Logitech PM5

polisher, reducing the rms surface roughness to 0.17 um after 30-minute of polishing. This improvement in surface quality results in a loss reduction of 0.35 dB/mm.

In [112], an SIW operating in the WR10-band was fabricated on a 30-um-thick BCB layer (with a ε_r of 2.5 and a tan δ of 0.007 at 1 THz), achieving a measured loss of less than 0.5 dB/mm from 70 to 145 GHz. Simulations indicate that the BCB-based SIWs offer additional advantages in the WR5- and WR3-bands. Passive components and circuits can be designed within the interposer using BCB "above-IC" technology, facilitating the development of functionalized interposers.

In [113], an SIW operating in the D-band was proposed using the ABF/glass/ABF stack characterized in [21], as shown in Figure 2.10 (a). The measured loss of this design varies between 0.5 and 1 dB/mm across the D-band. In [23], an additional 87.5-um-thick ABF film was laminated on top of the metallized ABF/glass/ABF stack, as shown in Figure 2.10 (b), serving as the hosting layer for the SIW. Optec Femtosecond Laser was used to form vias in the ABF layer, and then SAP was used to define the top metal pattern of the SIW. The configuration achieves a measured loss of about 0.35 dB/mm in the D-band.

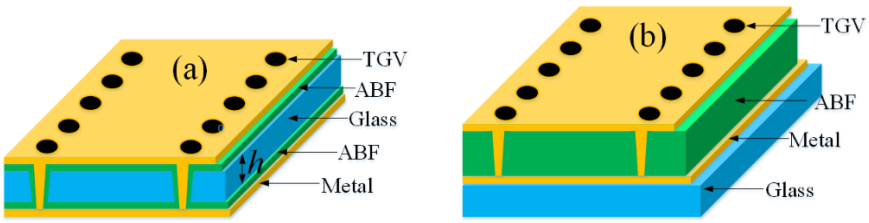

Figure 2.10 (a) SIW on ABF/glass/ABF stack, (b) SIW on ABF on glass

In [114], an SIW using an ARC substrate was reported. The SIW was fabricated on an 80-um-thick ARC with laser-drilled vias measuring 40 um in diameter. SAP process was used for metallization. The measured average copper thickness of the top and bottom metal layers is about 8 um. The measured surface roughness is about 70 nm, significantly smaller than the skin depth at the operating frequency band and much less than that of SIWs based on other substrates. The measured loss of this ARC-based SIW

is about 0.13 dB/mm from 75 to 110 GHz and about 0.15 dB/mm from 110 to 170 GHz. Its low loss, comparable to that of air-filled SIWs, is attributed to the substrate's low surface roughness and ultralow tan δ. These characteristics suggest that ARC-based SIWs have strong potential for applications up to 1 THz.

In [115], an integrated waveguide fabricated on a nanoporous anodic aluminum oxide (AAO) membrane was reported, offering a low-cost alternative manufacturing process for THz waveguides. The structure, illustrated in Figure 2.11, uses vertically aligned copper nanowires, selectively grown inside the nanopores of a 50-um-thick commercial nanoporous AAO membrane, to electrically connect the top and bottom metal layers. These nanowires, with a diameter of 40 nm and a center-to-center distance of 107 nm, provide an effective electrical connection between the two broadside layers while confining the EM waves inside the center waveguide. A 3-um-thick copper layer was deposited on the top and bottom surfaces by sputtering and then thickened through electrodeposition. The measured loss ranges from 0.5 to 0.8 dB/mm in the band of 75 - 110 GHz. Further polishing of the AAO membrane could improve transmission. In [116], carbon nanotudes were used to form the sidewalls of the SIW, providing another approach to confine THz waves.

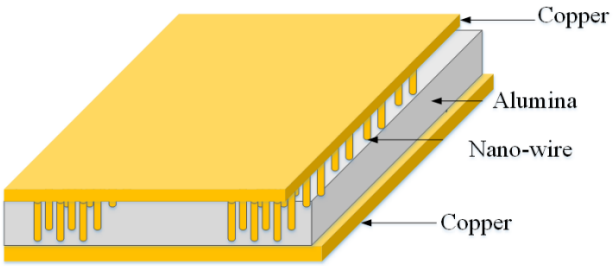

Figure 2.11 Integrated waveguide based on AAO membrane

2.3.5 Air-filled SIWs

An alternative approach to enhance the transmission performance of SIWs is the development of air-filled SIWs (AFSIWs) by removing the dielectric filling, thereby eliminating dielectric loss, as shown in Figure 2.12. Multi-layer technology (MLT) is essential for the fabrication of AFSIWs, requiring at least three layers: the top and

bottom substrates with one side metallized to form the broadside walls of the SIWs, and a middle layer to support the sidewalls [117]. In [118], an AFSIW in the D-band was reported. Solid sidewalls were created by the MLT PCB process. This design has a measured loss ranging from 0.07 to 0.08 dB/mm in the D-band. In [119], the measured loss was reduced from 0.34 to 0.13 dB/mm in the D-band by partially removing the Astra material from one of the dielectric core layers.

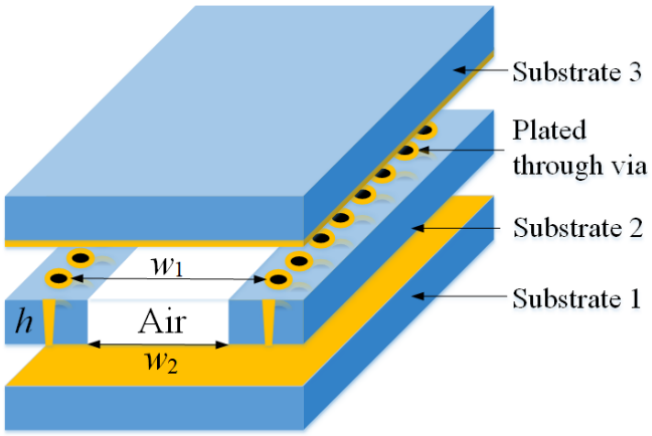

Figure 2.12 Air-filled SIW

Although SIWs offer advantages over traditional MWGs for integrated applications, they are prone to high losses, particularly in the THz band where conductor loss becomes considerable. The reduced height of SIWs, aiming at achieving compact system architectures, results in higher conductor loss than commercial full-height MWGs. The surface roughness of hosting substrates can dramatically increase conductor loss in the THz band. A performance comparison of SIWs based on various materials and technologies is given in Table 2.2.

Table 2.2 Table of SIWs

Technology or materials	Filled dielectric		Dimension (um)	Frequency range (GHz)	Loss (dB/mm)	Ref.
	ε_r	tan δ or resistivity ρ				
CMOS	4.5	0.001	560 × 11	160-220	2.35 simulated	[99]
	4.1	0.001	449 × 9.4	200-330	1.5 simulated	[101]
	N. A	N. A	300 × 11	110-220	1.2 (200 GHz)	[103]
	4.5	0.001	285 × 11 T-folding	180-220	2.41 (200 GHz) Sim.	[104]
Silicon	11.9	2-10 kΩ·cm	480 × 70	110-170	0.4-0.6	[105]
Silicon etched by KOH solution	11.9	0.7-1.3 kΩ·cm	560 × 300	77-110	0.2	[107]
DRIE	11.6	5 kΩ·cm	200 × 150	220-330	0.43 (325 GHz)	[108]
Liquid crystal polymer	3.17	0.0055-0.009	940 × 50.8	110-170	0.035	[111]
Benzocyclobutene	2.5	0.007 (1THz)	1550 ×30	70-145	Less than 0.5	[112]

Asahi Glass Company (AGC) ENA1 glass	4.6	0.009-0.015	900 × 100	110-170	0.5-1	[113]
Ajinomoto build up film (ABF)	3.3	0.0044 (5.8 GHz)	900 × 87.5	110-170	0.035	[23]
Alumina ribbon ceramic	9.94	0.0005-0.0006	634 ×80	110-170	0.155	[114]
Nanoporous alumina membrane	6.7	0.015	860 × 50	75-110	0.5-0.8	[115]
Carbon nanotubes air-filled waveguide	1	0	2700 × 110	81-86	0.5	[116]
Air-filled SIW PCB	1	0	1600×300	115-155	0.07-0.08	[118]
Partial air-filled SIW on glass	3.0	0.0017 (10 GHz)	2000 × 137	110-170	0.13dB	[119]

2.4 Dielectric waveguides

2.4.1 Ribbon waveguides

Dielectric waveguides (DWs) [120] show great potential for THz circuits and systems thanks to their low-loss performance. In [121], a 2-cm-wide ribbon waveguide made from high-density polyethylene (HDPE) with a thickness of 120 um was proposed for low-loss propagation in the frequency range from 0.1 to 3.5 THz. In [122], [123], ribbon dielectric waveguides with a high aspect ratio (a/b>10) and with a ε_r larger than 9, such as alumina, silicon, and sapphire, were proposed, as shown in Figure 2.13 (a). These wavegudies support surface wave modes, allowing only a small portion (about 10%) of EM waves to propagate inside the dissipative and dispersive materials, achieving ultralow loss transmission. As concluded in [124], at 300 GHz, silicon ribbon waveguide can achieve remarkably low dielectric absorption of only 0.15 dB/m, significantly outperforming quartz circular rods (5.5 dB/m), MWGs (15 dB/m), and MLs (150 dB/m).

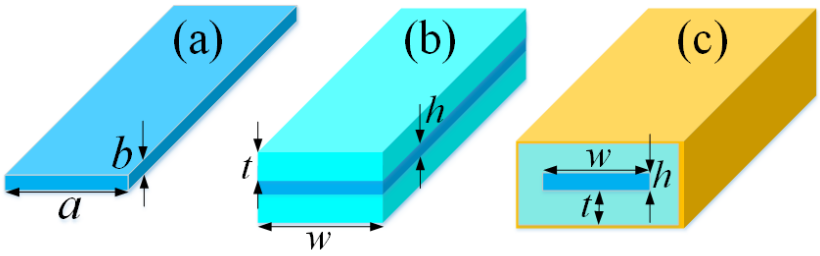

Figure 2.13 (a) Dielectric ribbon waveguide, (b) polymer-cladding ribbon waveguide, (c) substrate-integrated ribbon waveguide

2.4.2 Polymer-cladding ribbon waveguides

One issue of ribbon waveguides is that EM waves can easily detach from the surface when perturbations occur, causing radiation and limiting their use in integrated circuits and systems. In [124], to remedy this issue, two polymer coatings with a thickness of one-quarter of the free-space wavelength were added to sandwich the ribbon, as shown in Figure 2.13 (b). This approach aims to enhance wave confinement with a reasonable

expense of degraded transmission performance. For instance, the calculated attenuation constant for a 10:1 aspect ratio alumina ribbon coated with Teflon is about 0.2 dB/mm at 3 THz, whereas a bare ribbon theoretically has a much lower attenuation of 0.0006 dB/mm at 3 THz. Similar approache using new polymer-ceramic nanocomposite thin films has been reported in [125], [126], [127].

There is a trade-off between wave confinement and loss performance in ribbon waveguides. As suggested in [124], [127], bare ribbons are optimal for long, straight transmission, whereas polymer-coated ribbons are suitable for bends and other types of discontinuities in circuits. Consequently, a transition between bare and coated ribbons is needed. Since the transition starts in the region where the field is loosely bound, smooth transition is preferred. In [124], insertion losses of 0.22 and 0.3 dB were achieved using taper and inverted taper transitions, respectively, both with a length of $6\lambda_0$.

2.4.3 Substrate-integrated ribbon waveguides (SIRW)

In [128], [129], a hybrid waveguide structure combining the advantages of SIWs and ribbon waveguides, named as substrate-integrated ribbon waveguide (SIRW), as shown in Figure 2.13 (c), was proposed. This design features a cladded ribbon surrounded by metal. The center ribbon, made from alumina with a ε_r of 9.2 and a tan δ of 0.003, was encased in a cladding layer composed of VeroWhitePlus with a ε_r of 2.8 and a tan δ of 0.04 in the lower THz band [130]. This cladding was fabricated using 3-D plastic printing. Measurements indicate no significant different in loss between two waveguides of different lengths, demonstrating that the fabricated waveguides exhibit low loss from 100 to 500 GHz (about 0.15 dB/mm). The propagation loss can be further reduced by exploring alternative low-loss cladding materials [125] and employing different additive manufacturing processes.

2.4.4 Rectangular dielectric waveguides

As studied in [120], rectangular dielectric waveguides (RDWs) demonstrated in Figure 2.14 (a) support two types of hybrid modes, namely E_{mn}^{x} and E_{mn}^{y} modes. The cut-off frequencies and dispersion curves of the supported modes can be determined using the equations provided in [131], under the assumption that most EM waves are well confined within the dielectric core. Research in [132] indicates that RDWs with a square cross-section provide an optimal single-mode propagation. HR-Si substrates with thicknesses of 585 um and 385 um were used to form RDWs operating in the F-band (90 - 140 GHz) and G-band (140 - 220 GHz), respectively. DRIE was used to etch the HR-Si substrate and create the desired guiding core. HR-Si-based waveguides have been developed for chip-to-chip interconnects [133], [134], [135], [136], [137], [138], [139], [140], [141], [142], [143]. The PCB process provides a cost-effective manufacturing method for RDWs [144], [145] in the lower THz band (Figure 2.14 (b)). To further reduce dielectric loss, a hollow RDW (Figure 2.14 (c)) realized through multilayer PCB process was proposed in [146], achieving a measured loss of 0.028 dB/mm.

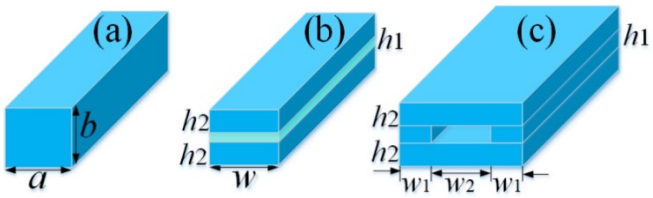

Figure 2.14 (a) Rectangular dielectric waveguide (RDW), (b) three-layer RDW, (c) hollow RDW

Freestanding DWs can be placed on or buried within another dielectric substrate [131] for integration. For example, Si waveguides supported by a glass layer, known as silicon-on-glass (SOG) waveguides, as shown in Figure 2.15 (a), have been developed for mmW applications [147], [148] and then extended into the THz band [149], [150], [151]. In [150], a suspended SOG waveguide was proposed to mitigate the high loss

associated with glass substrate. In this design, the Si-guiding channel is supported by periodic subwavelength Si beams. The measured insertion losses are about 0.028 and 0.021 dB/λ_0 over the frequency bands of 420 - 500 and 500 - 595 GHz, respectively. In [151], a U-shape SOG waveguide was proposed, achieving a measured loss as low as 0.026/λ_g within the frequency band from 0.9 to 1.08 THz. The guiding cores can be supported by perforated substrate with designed pattern, leading to substrate-integrated dielectric waveguides (SIDWs) [152], [153].

Various types of DWs with diverse geometries have been developed for the mmW and THz applications. These include dielectric rib waveguides (Figure 2.15 (b)) [154], [155], [156], strip dielectric waveguides (Figure 2.15 (c)) [157], [158], inverted strip dielectric waveguides [159], [160], [161]. Each design offers unique advantages in terms of wave confinement, propagation loss, and compatibility with other technologies, making them suitable for a wide range of applications in the mmW and THz bands.

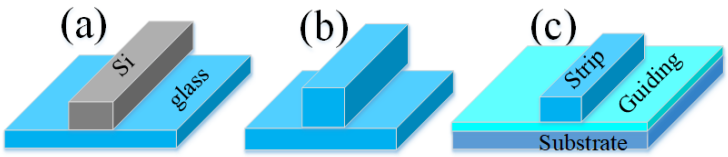

Figure 2.15 (a) Silicon-on-glass waveguide, (b) rib dielectric waveguide, (c) strip dielectric waveguide

2.4.5 Dielectric image lines

In [131], [162], a horizontally oriented grounding plane (mirror) was introduced to achieve single-mode operation in DWs for optical integrated circuits, also known as dielectric image lines (DILs). This concept has been successfully adapted for the microwave and mmW applications, as shown in Figure 2.16 (a) and (b). The metal layer not only isolates the dielectric guide from the circuits on the backside but also enables the integration of active components and aids in heat dissipation. In [163], a low-loss DIL was realized using 3-D printing, exhibiting a measured loss varying from 0.025 to 0.035 dB/mm in the WR5-band (135 - 225 GHz). Cyclo-olefin copolymer (COC) was

used as the 3-D printing material due to its low dissipation factor. In addition, its low ε_r results in larger waveguide dimension, easing the precision challenges for 3-D printing.

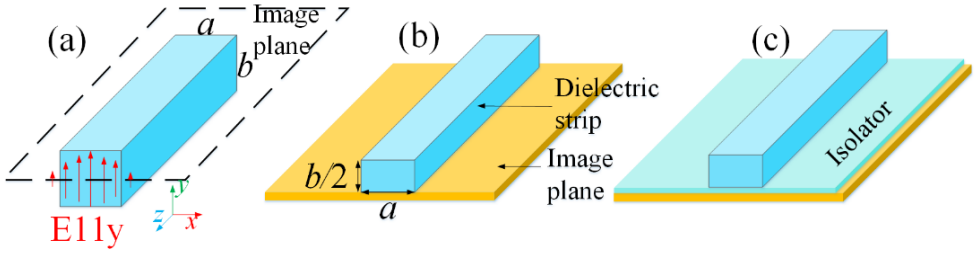

Figure 2.16 (a) Inserting image plane at middle of dielectric waveguide, (b) dielectric image line, (c) dielectric insulated image guide

To reduce additional conductor loss of DILs, an insulator with a lower ε_r than the guiding core can be inserted between the guiding core and the metal layer, resulting in a dielectric insulated image guide (DIIG) (Figure 2.16 (c)) [164]. Furthermore, leveraging the high-order E_{11}^{x} mode of DILs can be advantageous, as it has an attenuation constant that is nearly half that of the fundamental E_{11}^{y} mode [165].

Substrate-integrated image guides (SIIGs) have been demonstrated in the mmW band [166] and further extended to the THz band. In [167], [168], SIIG prototypes operating in the WR5- and WR3-bands were fabricated using alumina material with a ε_r of 9.6 and a tan δ of 0.006. The measured loss is about 0.0578 dB/mm in the band of 135 - 225 GHz and 0.1431 dB/mm in the band of 215 - 335 GHz.

2.4.6 Non-radiative dielectric waveguide

DWs, including DILs and DIIGs, suffer to radiation leakage [169]. To solve this issue, non-radiative dielectric (NRD) waveguides [170], [171], [172], [173], [174] have been proposed. An NRD waveguide consists of a center dielectric core sandwiched between two parallel metal layers, as shown in Figure 2.17 (a). The non-radiative frequency band is determined by the separation between these two metal layers. Their planar

counterparts, substrate-integrated non-radiative dielectric (SINRD) waveguides, belong to the SICs family [175], have also been developed [176], [177].

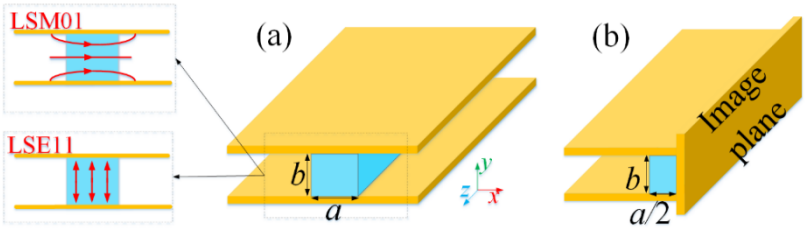

Figure 2.17 (a) Non-radiative dielectric waveguide and first two non-radiative modes, (b) image non-radiative dielectric waveguide

Although the NRD waveguides share a similar geometry with H-guides [178], their operating modes make them non-radiative. The first two non-radiative modes are LSE_{11} and LSM_{01} modes. The LSM_{01} mode, in particular, has gained more interest in the mmW range and shows great potential in the THz band due to its low conductor loss. However, its practical application in integrated circuits and systems is limited by mode conversion at discontinuities. In [179], a metal patch was etched on a thin Teflon substrate and then inserted in the vertical mid-plane of the dielectric strip to suppress the LSE_{11} mode, however, this could generate a quasi-TEM mode. A λ/4 choke structure was applied to suppress the quasi-TEM mode within the band of interest. In [180], [181], a filter-like pattern mode suppressor was proposed. Image NRD (iNRD) waveguide, as shown in Figure 2.17 (b), was proposed in [182] to suppress the LSE_{11} mode with an increase in conductor loss.

2.5 Conclusion

It is important to recognize that no single guide can be considered universally superior for all THz applications. For instance, MWGs with polished surface have lower loss compared to traditional planar transmission lines in the THz band, making them suitable for medium- and long-distance transmission. Their high power handling capacity and excellent thermal conductivity further enhance their appeal. However, their relatively

large guiding size and bulkiness can be disadvantages in integrated circuits, meanwhile integrating active components can be challenging. In contrast, CPWs excel in integration and are commonly used for short-distance transmission, such as on-chip interconnects. A significant drawback of CPWs is the radiation leakage at frequencies above 200 GHz, which can adversely affect circuits and systems performance. SIWs, which are synthesized planar versions of rectangular waveguides, adapt well to integration. However, in the THz band, SIWs become less suitable due to their high conductor loss. DWs can achieve very low loss by narrowing the guiding core, making them suitable for long-distance transmission, such as chip-to-chip interconnects. However, they require large clearance around the guiding core, limiting their use in compact integrated circuits and systems. Each guiding structure has its own strengths and drawbacks. Selecting the appropriate guiding structure for a specific situation is important.

CHAPTER 3 ARTICLE 1: SUBSTRATE-INTEGRATED NON-RADIATIVE DIELECTRIC (SINRD) WAVEGUIDE FOR THZ INTEGRATED CIRCUITS AND SYSTEMS

Chun-Mei Liu, Louis-Philippe Carignan, and Ke Wu

Published in *IEEE Transactions on THz Science and Technology,* vol. 13, no. 5, pp. 454-463

Publication date: July 26, 2023

Abstract: In this work, a theoretical and experimental investigation of substrate-integrated non-radiative dielectric (SINRD) waveguide is conducted in terahertz (THz) band. Parametric studied on operation bandwidth and transmission performance are studied. An alumina-based SINRD waveguide with a thickness of 0.254 mm is first demonstrated in WR3-band. The performance of the presented SINRD waveguide is then experimentally verified. The demonstrated SINRD waveguide has an average measured insertion loss of 3.5 dB (3 dB in simulation) from 240 GHz to 330 GHz. A substrate-integrated waveguide (SIW) with the same materials and dimensions has an average measured insertion loss of 5.5 dB (3 dB in simulation) over the same bandwidth. The metallized-via-free process of SINRD waveguide makes the low-cost manufacturing and low-loss performance more appealing than that of the well-known SIW with metallized via holes for applications in the development of THz integrated circuits and systems.

Index Terms: Low cost, metalized-via-free, packaging and shielding, substrate-integrated non-radiative dielectric (SINRD) waveguide, terahertz (THz) integrated circuits and systems, transmission performance.

3.1 Introduction

The performance of guided-wave structures is critical for the development of high-frequency distributed-element integrated circuits and systems, especially for the recently blossoming THz (0.1 - 10 THz) techniques and applications where the transmission performance should be delicately evaluated and optimized for design considerations. Hollow waveguides with inner coating [57], [59], [61], [66] have been widely studied in the THz thanks to their low-loss performance while operating in some specific modes; however, they are not suitable for integration design. Many popular and well-known planar-form transmissions, for example, coplanar waveguides [4], microstrip lines [52] and parallel-plate waveguides (PPWGs) [43] are not preferable for THz integrated circuits and systems because of their high conductor loss related to finite conductivity. In addition, parasite effects such as radiation loss or modal leakage related to surface-wave modes or parallel-plates waveguide modes introduced by discontinuities can degrade the performance of THz integrated circuits and systems. Moreover, difficulty of avoiding line-to-line parasitic coupling with narrow line width caused by strong magnetic fields should be considered in the design, which is detrimental to high-density circuit integration.

Dielectric waveguides (DWs) [120], [132], [144], [149], [183] have shown potential in the development of the THz band thanks to their conductor-loss-free property. However, the DWs, as well as the planarized substrate-integrated DWs (SIDWs) [152], generally suffer from inherent radiation loss and leakage problems when geometric discontinuities are involved. Substrate-integrated image guides (SIIGs) [166], [167], [184] with backside metalized helping to improve the isolation from backside circuits are also limited in compact circuit design because of the potential leakage introduced by surface waves supported by grounded dielectric slab [56]. Smooth transitions and additional shielding structures are always required to mitigate radiation and leakage loss and to suppress potential coupling problem between adjacent channels, resulting in low-density bulky and complex circuits.

Substrate-integrated waveguides (SIWs) [96], essentially the planar synthesis of rectangular metallic waveguides, have been widely studied and used in the development of microwave and millimeter-wave integrated circuits and systems. In this case, two rows of densely arranged metallized via holes can effectively replace metallic sidewalls to confine electromagnetic (EM) waves inside the guiding core even at discontinuities like conventional waveguides. However, the dielectric-filled metallic waveguides suffer from high conductor loss when the operating frequency is in the THz band [185], [186]. Moreover, the metallization process of via holes at THz frequencies is set to highly increase the manufacture complexity. Furthermore, the surface roughness of metallized via holes would contribute to the overall losses, which makes the SIWs solution unprofitable for THz integrated circuits and systems.

On the other hand, non-radiative dielectric (NRD) waveguides [170] were proposed, which allow sharp discontinuities while operating in non-radiative modes [174]. Especially, they exhibit low conductor loss when operating in their LSM mode [171], which offers an alternative and compromise solution for THz developments. Planarized NRD waveguides, namely substrate-integrated non-radiative dielectric (SINRD) waveguides [176], [177], [187], [188], have been proposed and developed for integrated circuits and systems. Standard lithography techniques are available to obtain metallic coating over the hosting substrate surface. Laser drilling can be used for locally removing the metalized substrate to create a guiding dielectric core. Compared to SIW counterparts with one row of metallized via holes at each side, SINRD waveguides get rid of the complex metallization process, which is critical and also essential for creating high-performance THz integrated circuits and systems at low cost.

In this work, an SINRD waveguide is presented and experimentally verified in WR3-band. The characteristics of the SINRD waveguide are theoretically analyzed. Parametric analysis is carried out, which facilitates THz design considerations of the SINRD waveguide. The effect of surface roughness is experimentally studied by comparing the transmission performance of two SINRD waveguides constructed on as-

fired and polished alumina substrates. Finally, a comparison between SIDW (non-metallized), SIW (metalized via holes/walls and surfaces) and SINRD waveguides (metalized surfaces) is performed. Metallized via hole/wall processes of SIWs have proven to be very lossy and unsuitable for THz integrated circuits and systems. Instead, surface metallization processes of SINRD waveguides are much easier to implement with reasonable sacrifices on transmission loss.

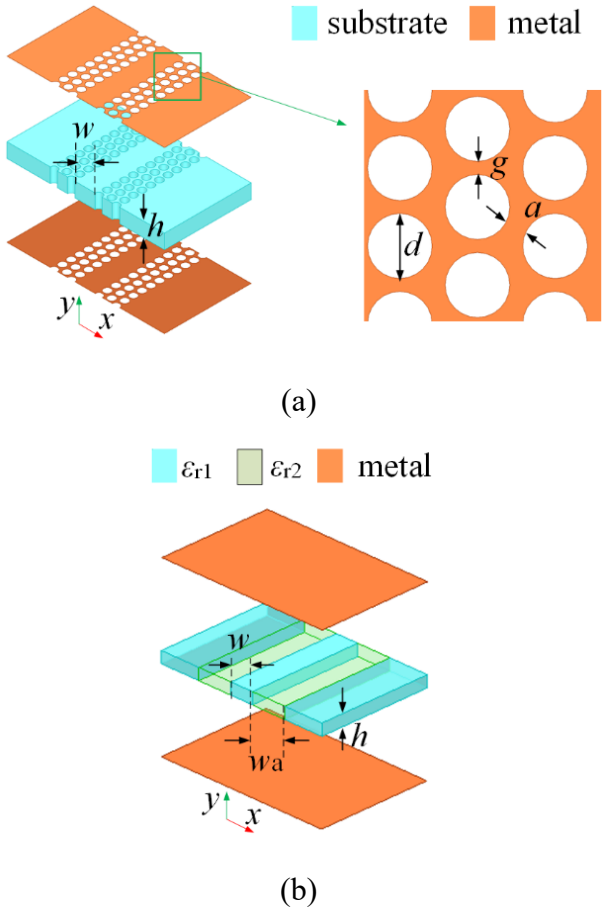

Figure 3.1 Model of SINRD waveguide. (a) Practical structure, (b) equivalent model

3.2 Performance of SINRD waveguide

The structure of SINRD waveguide is presented in Figure 3.1 (a). The hosting metallized substrate is bilaterally perforated by laser to create a guiding channel (with a larger permittivity than the perforated region). According to the effective medium theory [189], the perforated substrate can be equivalent to a substrate with a lower effective permittivity, as shown in Figure 3.1 (b). Same as NRD waveguide, the SINRD

waveguide supports two groups of non-radiative modes, namely LSE modes and LSM modes [188]. The cut-off frequencies and dispersion performances of the non-radiative modes supported by an SINRD waveguide can be obtained by numerically solving a set of transcendental equations obtained by applying the boundary conditions at the interfaces.

To create a desired large contrast in permittivity between the guiding core and surrounding region, substrates with a larger permittivity are preferred. On the other hand, the processing feasibility of a microstructure should be considered. Using planar substrates of relative permittivity much higher than 10 would result in a tiny microstructure in the THz band, which poses some low-cost fabrication challenges. The operating non-radiative band is approximately predetermined by the thickness and the permittivity of hosting substrate.

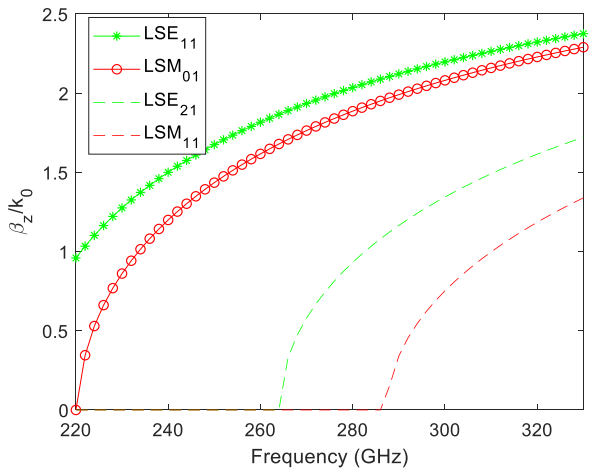

Figure 3.2 Dispersion curves of the given SINRD waveguide example. h = 0.254 mm, w = 0.35 mm, w_a = 0.5 mm, ε_{r1} = 9.8, ε_{r2} = 3.2

An alumina substrate with a relative permittivity of ε_{r1} = 9.8 and a thickness of h = 0.254 mm is considered here for WR3-band. The dispersion curves of an SINRD waveguide example are shown in Figure 3.2. The fundamental non-radiative mode is LSE_{11} mode. The second non-radiative LSM_{01} mode starts at 220 GHz. In most cases, the LSM_{01} mode attracts much attention thanks to its lower conductor loss. After selecting the hosting substrate, one needs to optimize the core width or the air-hole

perforation to garner a feasible structure with desired performance in terms of bandwidth and loss.

3.2.1 Bandwidth of SINRD waveguide

Ideally, the waveguide should be used in monomode over the operating frequency band to avoid a potential mode conversion between the operating mode and other undesirable modes. Here, the fundamental mode of the SINRD waveguide is the undesired LSE_{11} mode, followed by the desired LSM_{01} mode. The mode conversion between these two non-radiative modes is inevitable. However, the undesired LSE_{11} mode can always be converted back to the original LSM_{01} mode based on the coupling theory. Also, mode suppressor may be available [190], [191].

Once there are more than two undesired modes, the mode conversion becomes complicated. As shown in Figure 3.*2*, the first higher-order LSE_{21} mode appears after the LSM_{01} mode. Different conversion paths are required to convert different modes back to the original LSM_{01} mode, which will certainly cause some mode conversion losses. Therefore, the bandwidth of the SINRD waveguide is defined as the difference in the cut-off frequencies between the LSM_{01} mode and the higher-order LSE_{21} mode or the first higher-order parallel-plates waveguide (PPW) TE_1 mode terminating the non-radiative frequency band, depending on which of the two has a lower cutoff frequency.

A parametric study is carried out on the effect of core width and air-hole perforation effective permittivity on the cut-off frequencies. As shown in Figure 3.3, the cut-off frequencies of the LSM_{01} and LSE_{21} modes increase with decreasing the core width, leading to a narrow non-radiative bandwidth but a wider LSM_{01} mode bandwidth. However, further reducing the core width leads to poor field confinement and higher loss, which will be discussed later. The cut-off frequency of the TE_1 mode is determined by the thickness and effective permittivity of the perforated substrate. A lower effective permittivity of the perforated region of a given substrate (dense air-hole perforation) always yields a wider non-radiative bandwidth. Practically, dense air-hole perforation

is not advisable while considering structural stability. Also, lower effective relative permittivity ε_{r2} does not necessarily give wider bandwidth for the LSM_{01} mode if the bandwidth is terminated by the LSE_{21} mode. For a given core width, the ε_{r2} hardly influences the bandwidth since it synchronously affects the cut-off frequencies of the LSM_{01} and LSE_{21} modes.

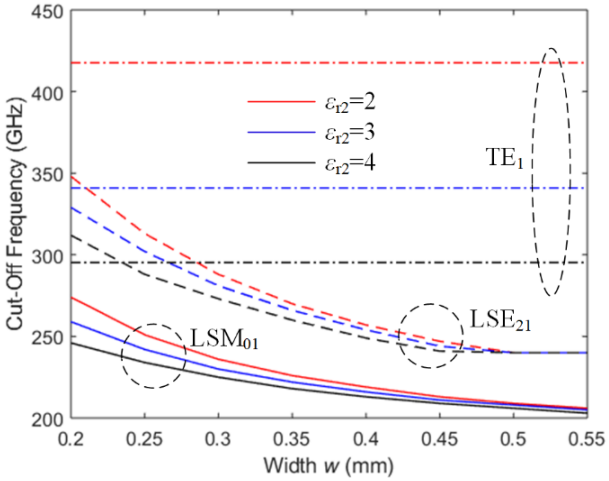

Figure 3.3 Parametric study of waveguide width w and effective relative permittivity of perforated region ε_{r2} on cutoff frequencies of SINRD waveguide

3.2.2 Loss performance of SINRD waveguide

The transmission loss of the SINRD waveguide is addressed here. The loss of SINRD waveguide is composed of conductor loss and dielectric loss, which can be calculated by a perturbation method [56], [192], as detailed in Appendice A. Here, gold with a conductivity of $\sigma = 4.1 \times 10^7$ S/m is used. The loss tangent of alumina is set as $\tan \delta = 0.001$.

As given in Figure 3.4 (a), the conductor loss decreases with increasing core width w. The reason is the change of electric field component E_y, shown in Figure 3.5. For the SINRD waveguide with a width of $w = 0.25$ mm, the E_y component is more pronounced near the metal layers, resulting in a higher conductor loss. For the one with a width of $w = 0.35$ mm, the electric field is almost parallel to the two metal layers, and is close to zero near the metal layers because of the boundary conditions, resulting in a lower

conductor loss. After $w = 0.35$ mm, the loss decrease eventually saturates. As discussed above, the ε_{r2} value slightly affects the LSM_{01} mode. It can be concluded that the ε_{r2} has a slight effect on the field distribution, then the loss performance.

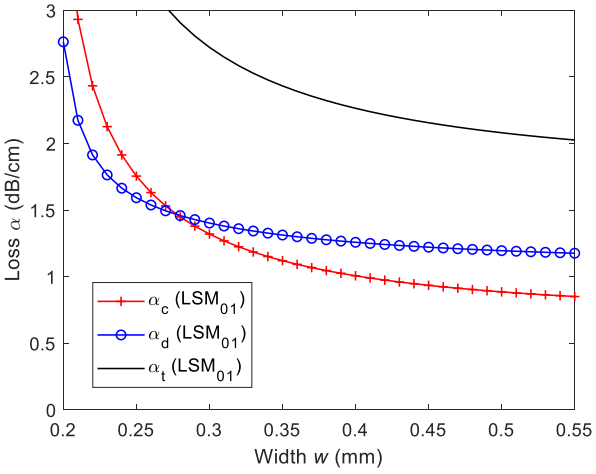

(a)

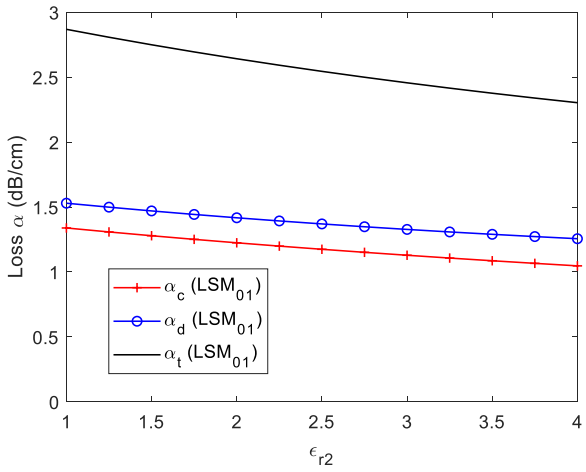

(b)

Figure 3.4 Loss performance of the LSM_{01} mode of SINRD waveguide at 260 GHz. (a) Core width w and (b) ε_{r2}. α_c, α_d and α_t are the conductor, dielectric and total loss, respectively

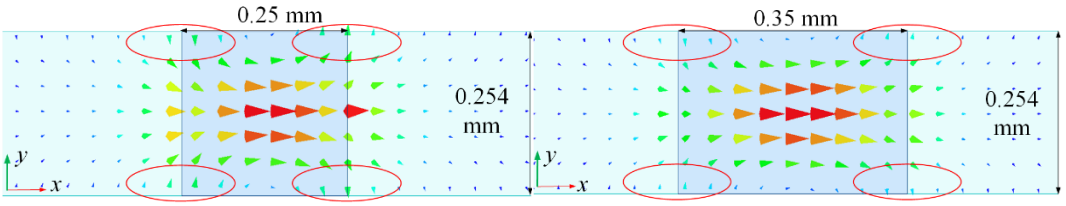

(a) (b)

Figure 3.5 Simulated transverse electric field patterns of the LSM_{01} mode at 260 GHz. (a) SINRD waveguide with the width of w = 0.25 mm, (b) SINRD waveguide with the width of w = 0.35 mm

Figure 3.6 summarizes the loss and bandwidth of the LSM_{01} mode as a function of the waveguide width w and the effective relative permittivity ε_{r2} at the perforated region. The loss of the SINRD waveguide converges to 2 dB/cm after w = 0.35 mm. The value of ε_{r2} hardly influences the loss performance of the SINRD waveguide when the width w is larger than 0.35 mm, which partially relieves the requirement for layer drilling precision. When the bandwidth is more concerned, one can obtain a wider one by narrowing the width with the cost of higher loss. Densely perforating the substrate to obtain a lower ε_{r2} results in a wider non-radiative bandwidth, however, not necessarily gives a wider bandwidth for the SINRD waveguide with a width of w = 0.35 mm since changing ε_{r2} only slightly shifts the cut-off frequencies of the LSM_{01} mode and the LSE_{21} mode. Moreover, dense perforation would increase the risk of fracture. A ε_{r2} lower than 3.2 might be required to avoid the TE_1 mode across the WR3-band [56].

The analytically calculated theoretical loss performance of SINRD waveguide, SIW and SIDW within WR3-band is shown in Figure 3.7. The SIDW has the lowest loss among the three because it is free from conductor loss. However, it suffers from the radiation leakage problem. The SIW and SINRD waveguide are favorable while considering the packaging and shielding in integrated circuits and systems. It suggests that the SIW waveguide has a better performance than the SINRD waveguide in terms of the theoretical total loss at lower frequency end, and the opposite at the higher frequency end, however, the SINRD waveguide will operate in the multimode region

including the higher-order LSE_{21} and LSM_{11} modes. While considering manufacturing complexity and high losses associated with the metalized via holes, the SINRD waveguides are preferred over the SIWs in the THz band.

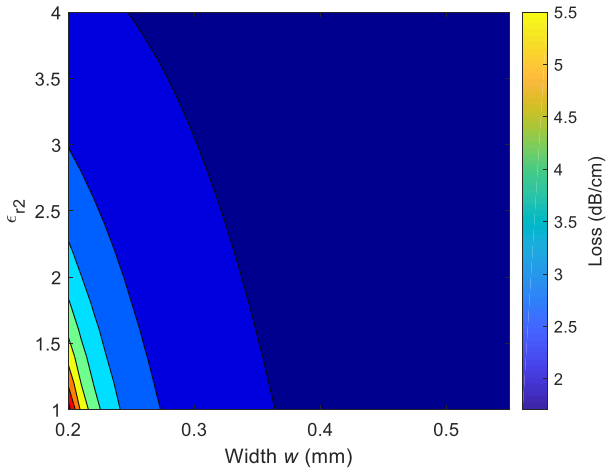

(a)

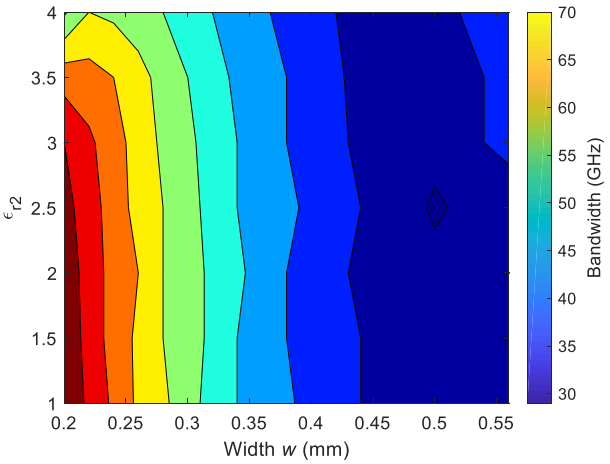

(b)

Figure 3.6 Design chart. (a) Average loss performance in dB/cm at 300 GHz, (b) bandwidth of the LSM_{01} mode in GHz

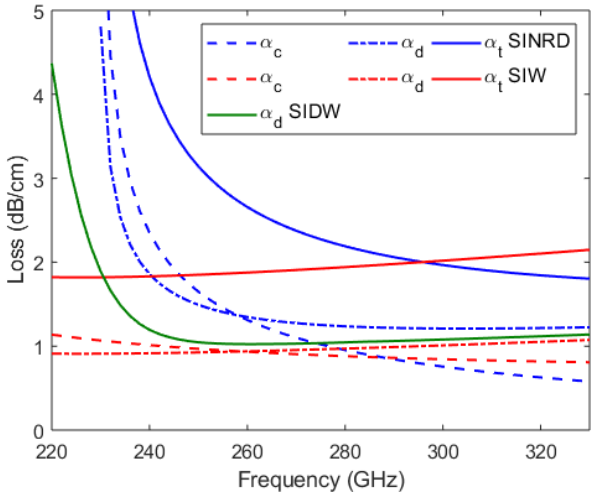

Figure 3.7 Loss performance of the given SINRD equivalent model operating in LSM_{01} mode, SIW and SIDW with the same materials and dimension. h = 0.254 mm, w = 0.35 mm, ε_{r1} = 9.8, ε_{r2} = 3.2

3.2.3 SINRD waveguide

An SINRD waveguide built on an as-fired alumina substrate with a relative permittivity of ε_{r1} = 9.8 and a thickness of h = 0.254 mm is demonstrated in WR3-band, as shown in Figure 3.8. The width of guiding core is w = 0.35 mm, the length of the SINRD is l = 10 mm. After selecting the hosting substrate, one needs to design the air-hole perforation pattern. The effective relative permittivity of the air-hole perforation in Figure 3.1 (a) with a period of $p = d + g$ = 0.15 mm, which is much smaller than the guided waveguide wavelength of about 0.35 mm to avoid bandgap in band of interest, and a wall thickness between two adjacent holes of g = 0.025 mm (fabrication limitation of laser drilling in our lab) is approximately set as ε_{r2} = 3.2 for the LSM_{01} mode according to the effective medium theory [189].

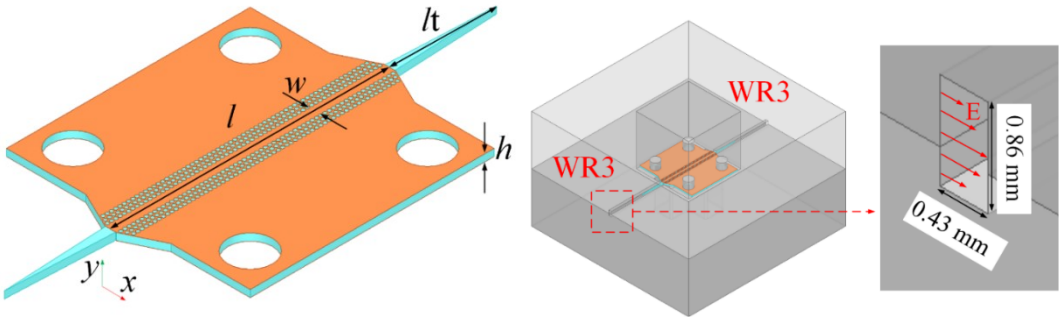

(a) (b)

Figure 3.8 (a) Structure of the designed SINRD waveguide, (b) the designed metallic housing with transitions and supporting base. Parameters: l = 10 mm, w = 0.35 mm, l_t = 3.5 mm. The total length of the metallic housing is 30 mm. The dimension of WR3-band rectangular waveguides used in simulation is 0.86 mm × 0.43 mm. The loss tangent of alumina substrate is about tan δ = 0.001. The conductivity of gold is σ = 4.1 × 10^7 S/m. The metallic housing is made by aluminum with a conductivity of σ = 3.8 × 10^7 S/m

Two standard WR3-band rectangular waveguides with a dimension of 0.86 mm × 0.43 mm are used for measurement. To achieve a satisfactory matching condition between the rectangular waveguide and the SINRD waveguide, two alumina tapers with a length of l_t = 3.5 mm are added at both ends of the SINRD waveguide. HFSS is used to carry out the calculation of transmission performances of the designed SINRD waveguide. The simulated electric field distribution at 260 GHz is given in Figure 3.9, which shows that the field can be well confined near the guiding core.

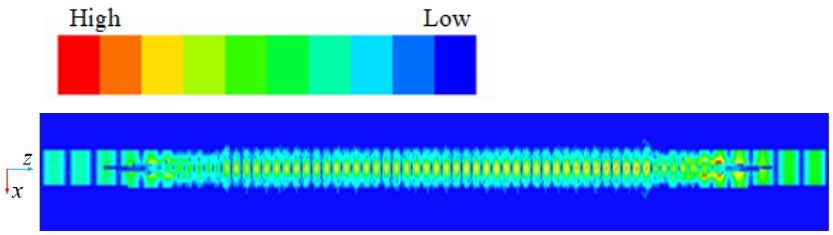

(a)

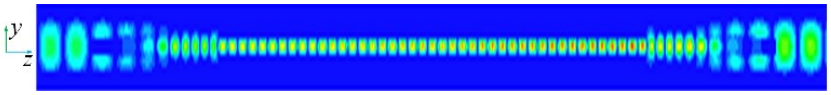

(b)

Figure 3.9 Simulated electric field distributions at 260 GHz along the propagation direction. (a) At *xoz* plane (E-plane), (b) at *yoz* plane (H-plane)

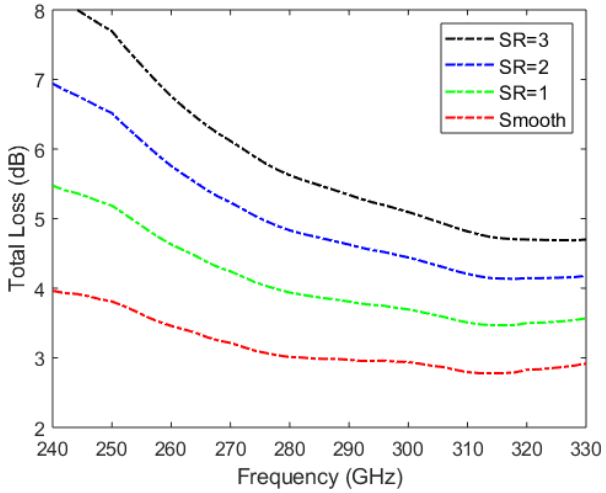

Figure 3.10 Simulated transmission performance of the designed SINRD waveguide with length of l = 10 mm under different surface roughness

As studied in [193], the conductor loss of a rough metallic waveguide can be twice that of a smooth one. It is necessary to investigate the surface roughness effect on SINRD waveguide in the THz band. The surface roughness can be modeled by the well-known Hurry's snowball model [193], [194], and then its influence on the transmission performance of SINRD waveguide can be evaluated by simulation in HFSS. The simulated transmission performance of the presented SINRD waveguide under different surface ratio (*SR*) indicating different surface roughness conditions is given in Figure 3.10, which indicates that polishing alumina substrate (reducing *SR*) could help reducing the transmission loss of SINRD waveguide.

3.3 Experiment

The presented SINRD waveguide is fabricated at Poly-Grames research center. Standard lithography is used to pattern the metallic coating. To avoid the undesired metallization of air holes, the metal is first deposited at surfaces of hosting substrate before being drilled, as shown in Figure 3.11. The air-hole perforation and the layout including the tapers are cutting by using a laser micromachining. The SINRD waveguide is placed into a designed two-piece aluminum housing and aligned using dowel pins. A photograph of the as-fired alumina-based prototype is shown in Figure 3.12 (a). The S-parameters are measured using a PNA-X network analyzer and a pair of VDI frequency extenders, as shown in Figure 3.13. A standard short-open-load-through (SOLT) calibration method is used.

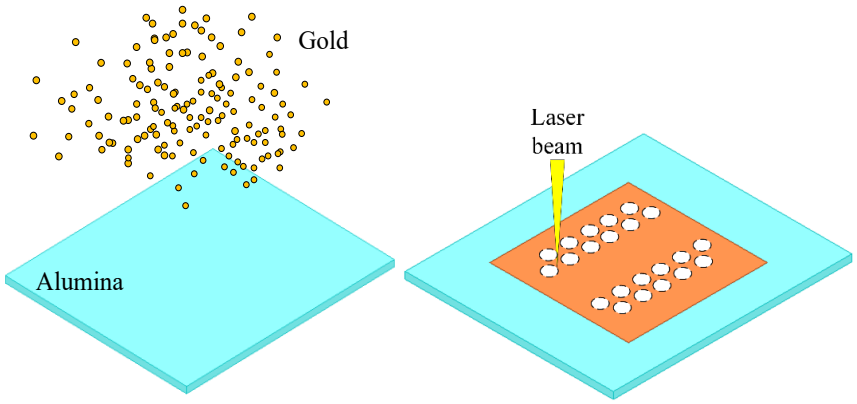

(a) (b)

Figure 3.11 Fabrication process. (a) Metallization of hosting substrate (alumina), (b) laser drilling with a desired or designed air-hole pattern

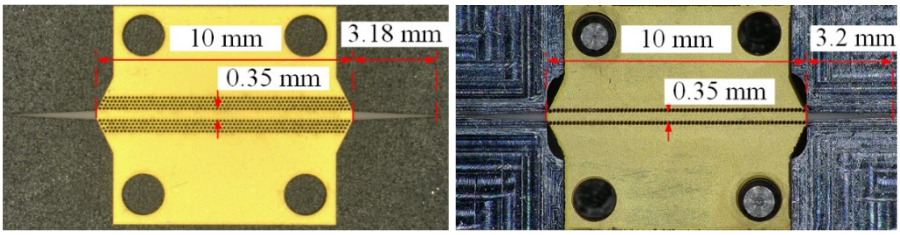

(a) (b)

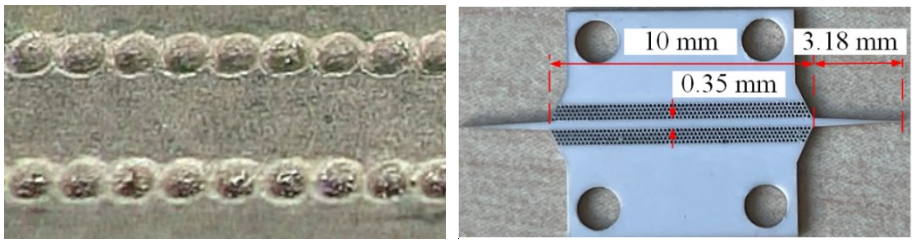

(c) (d)

Figure 3.12 Photographs of the as-fired alumina-based devices under test. (a) SINRD waveguide, (b) SIW, (c) metallized via holes of the SIW waveguide, (d) SIDW

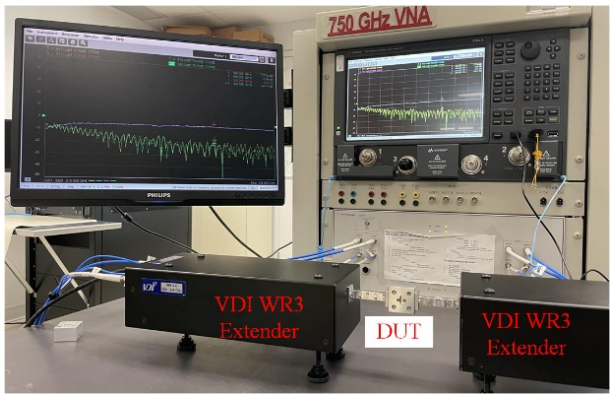

Figure 3.13 Measurement set-up of the device-under-test (DUT) in WR3-band using a PNA-X and VDI extenders

The measured results are shown in Figure 3.14. The presented device works well in the WR3-band with an average measured insertion loss of 3.5 dB from 240 GHz to 330 GHz, and of maximum 4.8 dB at 270 GHz. The conductor loss, dielectric loss, and feeding loss are all included. The measured S_{21} in green line is averagely smaller than the simulated one in black line because of surface roughness. As studied, reducing the surface roughness of SINRD waveguide can improve the transmission loss. An SINRD waveguide build on a polished alumina substrate was fabricated and measured. The measured results in red line are given in Figure 3.14. A polished substrate surface can reduce the transmission loss of the SINRD waveguide by 0.5 dB on average (difference between red and green solid lines) with an increased cost.

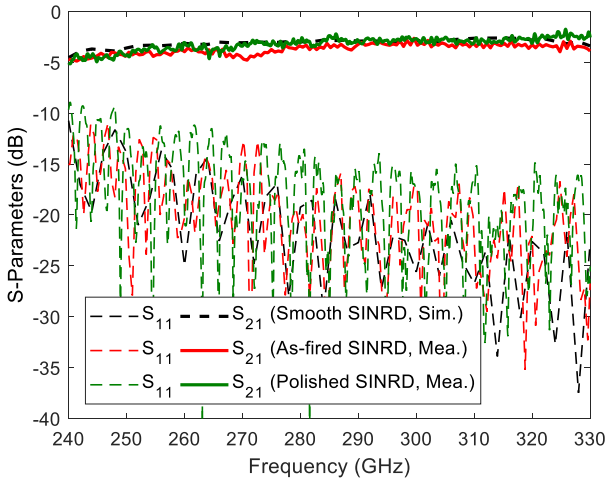

Figure 3.14 Transmission performance of the designed SINRD waveguides in Figure 3.12 (a)

Without polishing the substrate surface, the SINRD waveguide performs better than the SIW waveguide. An SIW waveguide with the same dimension of the SINRD waveguide built on an as-fired alumina substrate is fabricated, as shown in Figure 3.12 (b). Only one row of metalized via holes at each side of guiding core to simulate the metal walls of rectangular waveguide is needed to completely confine the EM waves. The fabrication of the SIW is similar to that of the SINRD waveguide, but with the additional step of metalizing via holes, as shown in Figure 3.12 (c). A metallic housing similar to the one in Figure 3.8 (b) but with differently oriented transitions enclosing the matching tapers is redesigned for measurement. The measured results are given in Figure 3.15. A noticeable discrepancy about 2.5 dB between the measured (average of -5.5 dB) and simulated S_{21} (average of -3 dB) is observed for the SIW, which is related to the surface roughness, especially the metalized via holes. The metalized-via-free SINRD waveguide has a more guaranteed transmission performance and a lower cost than the SIW.

SINRD waveguide has a higher total loss than its non-metalized counterpart (SIDW) which is free from conductor loss. An as-fired alumina-based SIDW is fabricated, as shown in Figure 3.12 (d). A comparison in measured insertion loss between SINRD, SIW and SIDW (operating in E_{11}^{x} mode) is given in Figure 3.16. As suggested, the

SIDW has the best transmission performance among the three, especially at the lower frequency end where the SINRD and SIW are suffering from conductor loss near the cut-off frequency zone or the rough metalized via holes. Even though the loss performance becomes comparable to that of the SIDW with frequency increases, the SINRD waveguide will work at the multimode zone. Specific designs, such as mode suppressors aiming to suppress undesired high-order modes, are needed, which complicates the circuit design. Therefore, the SINRD waveguide is not superior to the SIDW in the discontinuity-free circuits. It does provide more guaranteed transmission performance for integrated circuits and systems. In integrated circuit design where discontinuities are inevitable, besides the SIW with numerous metalized via holes/walls, the presented SINRD waveguide is capable of EM waves confinement by a pair of metal layers deposited on the same dielectric substrate or provided by other layers in multi-layer integrated circuits and systems, then resulting in a hybrid metallo-dielectric waveguide architecture [195] which maintains an excellent degree of freedom in circuit developments with a reasonable compromise between the overall size, fabrication complexity and transmission performance.

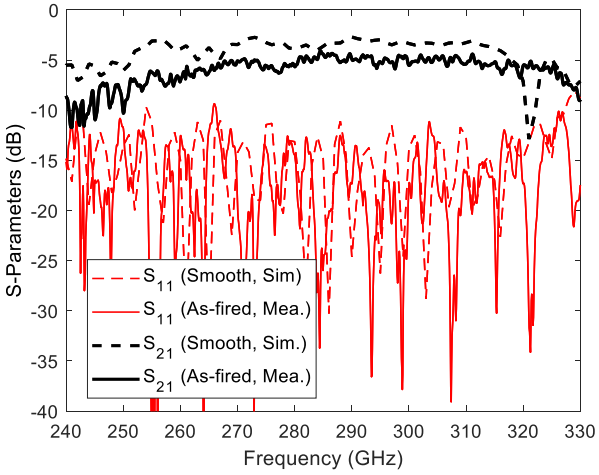

Figure 3.15 Transmission performance of the designed SIW in Figure 3.12 (b).

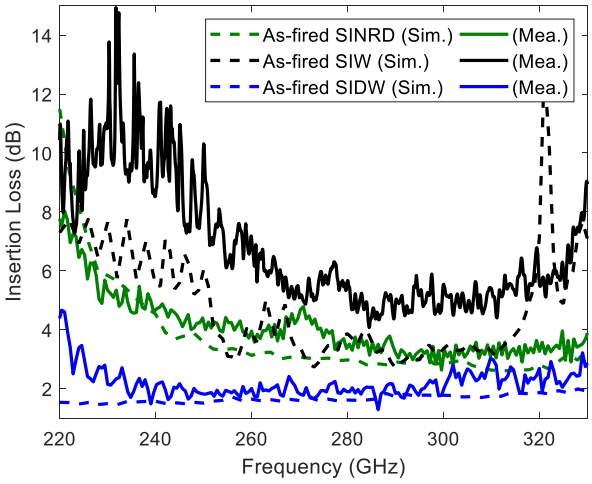

Figure 3.16 Total loss of the SINRD waveguide, SIW and SIDW

3.4 Conclusion

In this work, an SINRD waveguide is studied and demonstrated in the WR3-band. Design guidelines for SINRD waveguides are discussed. The operating band of the desired non-radiative LSM_{01} mode is approximately predetermined by the hosting substrate, namely the thickness and the permittivity. Other two flexibly selected structural parameters, air-hole perforation pattern and core width, can adjust the transmission performance. Increasing the core width can decrease the cut-off frequency of the LSM_{01} mode, as well as the undesired higher order LSE_{21} mode. Decreasing the air-hole perforation ratio slightly moves the LSM_{01} mode forwards, however, possibly brings the undesired TE_1 mode in the band of interest. We have found that adjusting the core width is more efficient and practical than adjusting perforation pattern. The narrower the core, the wider the bandwidth, but the higher the loss and the looser the field confinement. Further, we have found that a polished alumina substrate can incrementally improve transmission performance at the expense of increased cost. In addition, compared to the SIWs, the SINRD waveguides have a more guaranteed transmission performance, a simpler manufacturing process and a lower cost, which is critical in THz integrated circuits and systems.

CHAPTER 4 ARTICLE 2: VERTICALLY STACKED DOUBLE-LAYER SUBSTRATE-INTEGRATED NONRADIATIVE DIELECTRIC WAVEGUIDES FOR THZ APPLICATIONS

Chun-Mei Liu and Ke Wu

Published in *IEEE Microwave and Wireless Technology Letters*, vol. 33, no. 6, pp.791-794

Publication date: April 24, 2023

Abstract: Non-radiative dielectric (NRD) waveguides have been studied and exploited to address the leakage issue in dielectric waveguides (DWs) used by discontinuities. With the proliferation of substrate integration technologies, planarized substrate-integrated non-radiative dielectric (SINRD) waveguides have emerged, which are found to be more suitable for terahertz (THz) integrated circuits and systems. However, in the making of SINRD waveguides, a process-related conflict may arise between the air-hole perforation of a hosting substrate and its essential residual metallic coating on the perforated region. In this work, a solution to this problem using a multi-layer topology is formulated, where the size difference between entrance and exit of the drilled air holes is reduced. Moreover, the exposed metallic coating over both sides of the multi-layer SINRD waveguide is well preserved. Therefore, a dense air-hole perforation is allowed when needed. In this letter, a vertically stacked double-layer guiding structure is presented, studied, and experimentally verified, which demonstrates the interesting features of this technique.

Index Terms: Double-layer, laser drilling, non-radiative dielectric (NRD) waveguide, substrate-integrated NRD (SINRD) waveguide, substrate-integration technologies, terahertz (THz) techniques, vertically stacked.

4.1 Introduction

Non-radiative dielectric (NRD) waveguides have shown an intriguing potential for THz applications thanks to their low conductor loss while working in the non-radiative LSM_{01} mode and to their ability of guiding electromagnetic waves at discontinuities without metallized via holes [170], [174]. Additionally, the simplicity of NRD waveguides is set to loosen stringent requirements for THz manufacturing processes. With the proliferation of substrate integration technologies such as the substrate-integrated waveguide (SIW) and substrate-integrated circuits (SICs), the planarized NRD waveguides, namely the substrate-integrated non-radiative dielectric (SINRD) waveguides, were developed for integrated circuits and systems [176]. By deliberately punching a hosting substrate with air holes to lower its effective permittivity, a guiding channel can be created through the contrast in permittivity between the unperforated and perforated regions.

Even though the feature of planarity is attractive, there are some metallization issues with laser drilling or any other etching methods when punching holes in a metallized substrate to form an SINRD waveguide. To avoid the metallization of air holes, the metal should be deposited on the surfaces of the hosting substrate, and the metalized hosting substrate is then drilled with a designated or desired perforation pattern. As shown in Figure 4.1 (a), a laser beam first hits the top metallic coating then penetrates the substrate. When the laser beam goes through the substrate, the accumulated overheating would affect the adjacent area. In this case, the metallic coating near the holes' edge will be inadvertently ablated.

No leftover of metallic debris around the perforated region after a common laser drilling for the case of a dense air-hole perforation would result in a substrate-integrated image guide (SIIG) [166], [184] with metallized at the top side of the guiding core, as shown in Figure 4.1 (b). Unfortunately, this process leads to a failure of the SINRD waveguide as its parallel metallic layers that sandwich the guiding core are the key to achieve the desired non-radiative performance. As such, the drilling diameter of the air holes would be shrunk during fabrication to avoid an SINRD waveguide failure, resulting in a narrower non-radiative bandwidth.

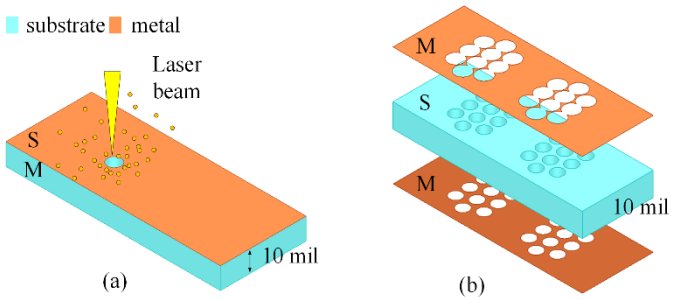

Figure 4.1 (a) Manufacturing process and (b) 3D view of 10-mil single-layer SINRD waveguide

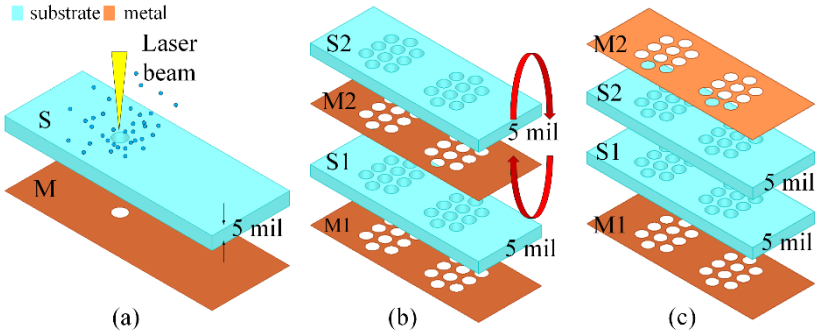

Figure 4.2 Manufacturing process of vertically stacked double-layer SINRD waveguide. (a) Penetrating through two backside metallized 5-mil substrates separately, (b) flipping over one of the substrates and assembly the two layers together, (c) 3D view

Another issue is the processing-related inverted trapezoid-shaped air hole, which is commonly seen with laser-drilling and other etching techniques. This vertical asymmetry within SINRD waveguides may generate leakage in the form of a transversal parallel plate waveguide (PPW) mode, which is detrimental to the longitudinal wave guidance. Generally, the diameter of drilled air holes decreases as penetration depth increases, which leads to inconsistent perforation patterns on the top and back sides of the hosting substrate. This difference becomes more pronounced for thicker substrates. Although this discrepancy can be reduced by using a high-precision deep reactive ion etching (DRIE), the available substrate materials are rather limited [152].

This imperfection in air holes can be improved or mitigated by using a multi-layer topology with a simple vertical stacking. In this case, the air-hole perforation pattern

can be made more flexible. The two metallic layers of the multi-layer SINRD waveguide are formed by two thin substrates with backside metallization. Since the laser beam always goes through the substrate from the top to back, the metallic coating at the backside of substrate will not be affected by the overheating of the laser beam, as shown in Figure 4.1 (b). In this work, a back-to-back vertically stacked double-layer WR3-band SINRD waveguide is investigated and experimentally verified. The effects of the potential air layer between the two layers are analytically evaluated.

4.2 Double-layer SINRD waveguide

The fabrication process of the proposed double-layer SINRD waveguide is illustrated in Figure 4.2. The first two steps involve metallizing the backside of the two substrates and bilaterally perforating them to create a guiding channel. Then, by flipping over one of the substrates (S2) and assembling the two layers together with the two metallized sides exposed, one can have an SINRD waveguide within a certain bandwidth determined by the total thickness of the double-layer structure and the effective permittivity of the perforated region. The meshed metallic layers act as the metal plates in the NRD waveguide as long as each is electrically self-connected.

The presented double-layer waveguide also helps to preserve good structural symmetry in the SINRD waveguide. As mentioned earlier, due to the nature of laser drilling, the diameter of air holes decreases as the depth increases. For the double-layer waveguide, the two thinner substrates are perforated separately, leading to a smaller difference in the entrance and exit of the air holes. Thus, one could obtain a more symmetrical waveguide cross section. In addition, the substrate outside the guiding core can be densely perforated without worrying about the top metallic layer being machined off. The challenge of developing a double-layer waveguide lies in the bonding of these two layers. A commercial adhesive layer may be required. However, for THz applications, adding a lossy adhesive layer in the middle would significantly increase the dielectric loss of the SINRD waveguide. In this work, the two layers are directly stacked and compressed by a two-piece metallic housing. A potential air layer might exist, as shown

in Figure 4.3 (a). Thus, it is necessary to study the effect of the air layer on the transmission performance of the double-layer SINRD waveguide.

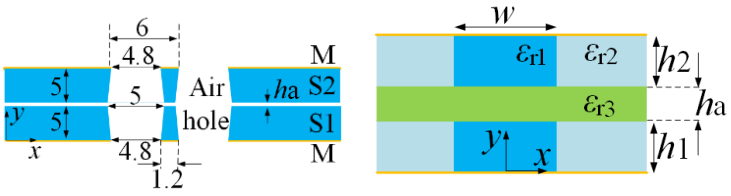

(a) (b)

Figure 4.3 (a) Side view and (b) equivalent model of perforated double-layer substrate. Unit in mil

An equivalent model is used for analysis. The perforated region can be represented by an unperforated substrate with a lower effective (equivalent) permittivity, as shown in Figure 4.3 (b). For the double-layer waveguide with a potential air layer, one needs to separately study the fields in the air and dielectric regions then match the tangential field components at the interfaces. After applying the boundary conditions at the interfaces ($y = h_1$ and $h_1 + h_a$ planes), β_y in the different regions should satisfy (4-1)

$$\frac{\beta_{y1,2}}{\varepsilon_{r1,2}} \tan \beta_{y1,2} h_1 = \frac{\beta_{y3}}{\varepsilon_{r3}} \cot \beta_{y3} \frac{h_a}{2}$$
$$\beta_{x1}^2 + \beta_{y1}^2 + \beta_z^2 = \omega^2 \mu \varepsilon_1$$
$$\beta_{x2}^2 + \beta_{y2}^2 + \beta_z^2 = \omega^2 \mu \varepsilon_2$$
$$\beta_{x3}^2 + \beta_{y3}^2 + \beta_z^2 = \omega^2 \mu \varepsilon_3 \quad (4\text{-}1)$$

for the first four modes with a local maximum horizontal electric field at $y = h_1 + h_a/2$ plane. Combining the transcendental equations for β_x obtained from the boundary conditions at the dielectric interfaces $x = \pm w/2$ planes [194], the dispersion curves of the double-layer SINRD waveguide can be determined.

In this work, two alumina substrates with a thickness of $h_1 = h_2 = 5$ mil and $\varepsilon_{r1} = 9.8$ are used to form the double-layer SINRD waveguide in the WR3-band. To avoid the

higher-order PPW TE_1 mode in the band of interest, the effective permittivity of the perforated region should be smaller than ε_{r2} = 3.2 [56]. In our laboratories, the manufacturing tolerance of the micromachining process can be controlled within 1 mil for the two-piece metallic housing containing the double-layer SINRD waveguide. Therefore, the thickness of the air layer between two substrate layers is set as h_a = 1 mil for investigation. The dispersion curves of the double-layer SINRD waveguide with a width of w = 14 mil are given in Figure 4.4. The comparison between single- and double-layer SINRD waveguides suggests that a potential thin air layer would hardly affect the frequency response of the double-layer SINRD waveguide. The simulated transverse electric field patterns of the LSM_{01} mode of those two SINRD waveguides are carried out by HFSS and plotted in Figure 4.5.

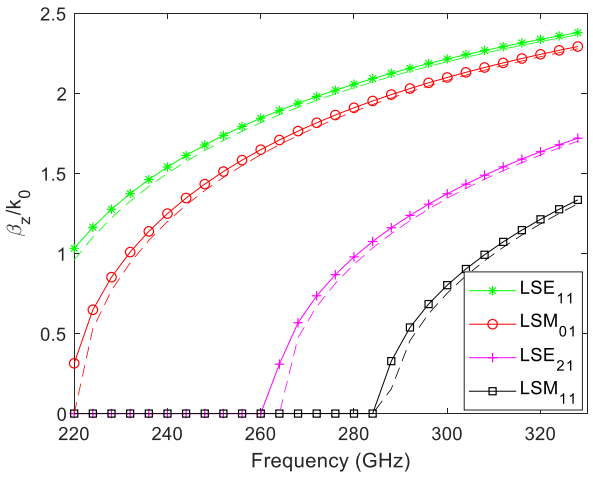

Figure 4.4 Dispersion curves of SINRD waveguides, single-layer (dashed lines) and double-layer with air layer (solid lines with symbols). $h_1 = h_2$ = 10 mil, w = 14 mil, ε_{r1} = 9.8, ε_{r2} = 3.2, ε_{r3} = 1, h_a = 1 mil

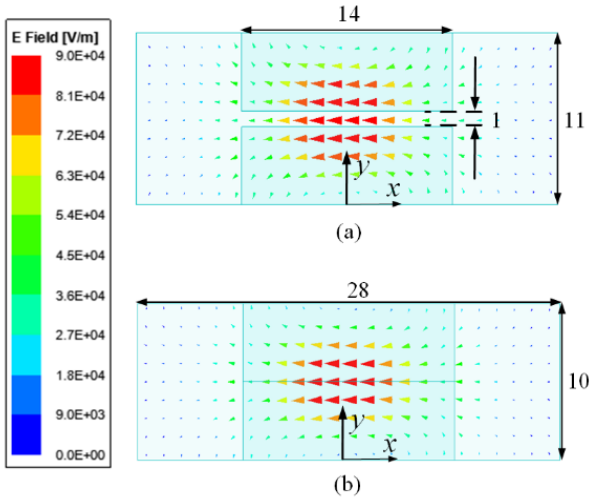

Figure 4.5 Transverse electric field patterns of LSM_{01} mode of (a) double-layer and (b) single-layer SINRD waveguides at 300 GHz. Unit in mil

However, the increase in the total thickness of SINRD waveguide caused by this potential air layer does lead to the early appearance of the PPW TE_1 mode, as shown in Figure 4.6. Since there is no conflict between the metallic coating and the air-hole perforation pattern, the effect of air layer can be compensated by densely perforating the substrate to lower the effective ε_r outside the guiding core. The analytical loss behavior of the two SINRD waveguides is given in Figure 4.7.

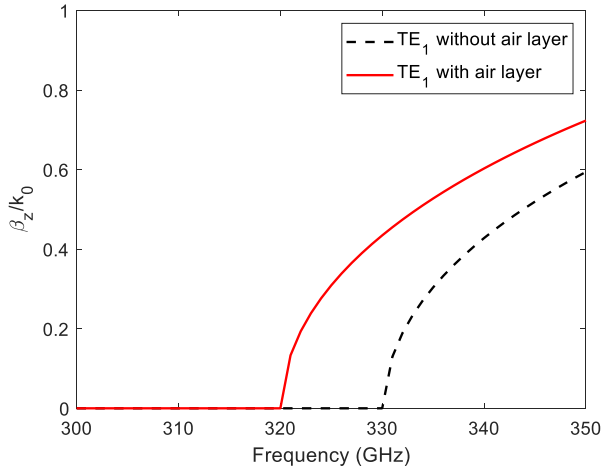

Figure 4.6 Air layer effect on higher-order PPW TE_1 mode

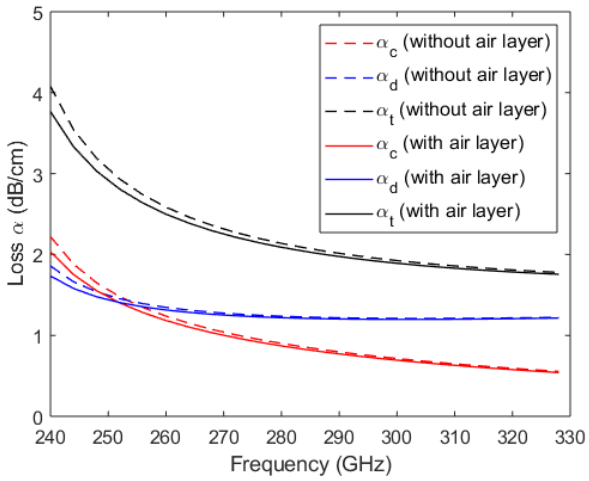

Figure 4.7 Air layer effect on loss behavior of LSM_{01} mode. Loss tangent of alumina is tan $\delta = 0.001$, and conductivity of gold is $\sigma = 4.1 \times 10^7$ S/m

4.3 Experiment

A double-layer WR3-band SINRD waveguide is fabricated and measured with the designated two alumina substrates. The air-hole perforation pattern is shown in Figure 4.3 (a). Based on the effective medium theory [189], for the LSM_{01} mode with the electric field perpendicular to the air hole axial, the effective permittivity of the perforated region is approximately $\varepsilon_{r2} = 3.2$. The simulation model of the double-layer SINRD waveguide is given in Figure 4.8. Two tapers at the ends of the SINRD waveguide are used for matching with standard rectangular waveguides [120], [196]. The SINRD waveguide is then placed into a designed two-piece metallic housing for testing. Two metal blocks with a vertical gap of 10 mil and a width of 40 mil are integrated with the metallic housing, as shown in Figure 4.8 (b), which helps compress the two alumina layers. The loss tangent of alumina is set as tan $\delta = 0.001$. Gold with a conductivity of $\sigma = 4.1 \times 10^7$ S/m is used for the metallic coating.

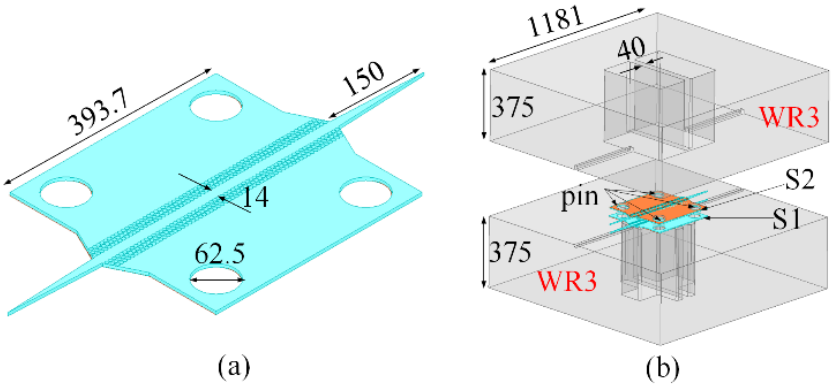

Figure 4.8 Simulation model of double-layer SINRD waveguide. (a) The bottom layer of SINRD waveguide, (b) metallic housing with two 5-mil alumina layers inside for testing. Unit in mil

The photograph of the fabricated prototype is given in Figure 4.9. The metallization is finished by standard lithography process, and the air-hole perforation and the layout cutting are finished by laser drilling. A PNA-X analyzer with a pair of VDI WR3-band frequency extenders is used to obtain the transmission performance. The measured results in Figure 4.10 suggest that the measured average insertion loss is around 5 dB. This loss includes material losses (dielectric loss and conductor loss), mismatching loss and radiation loss from the open apertures of the two transitions integrated with the metallic housing.

A discrepancy between measurements and simulations exists. In this work, two pins at the diagonal corners of the metallic housing were used to align the two alumina layers. The two holes for alignment in the two alumina layers were made larger than the pins for easy mounting. Thus, a misalignment between the two layers could occur, which may excite the fundamental zero cut-off frequency PPW mode and produce unwanted leakage, then deteriorate the non-radiative performance of SINRD waveguide. A high-precision alignment method is required to improve the performance of the double-layer SINRD waveguide. The roughness of the dielectric tapers and the two metallic layers also affects the transmission performance of the SINRD waveguide.

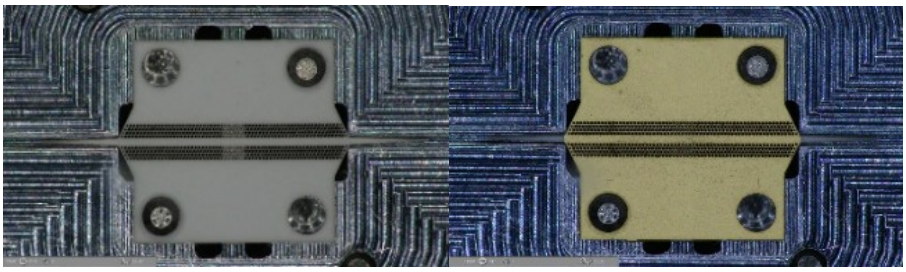

Figure 4.9 Prototype of the proposed double-layer SINRD waveguide, bottom layer (left) and top layer (right)

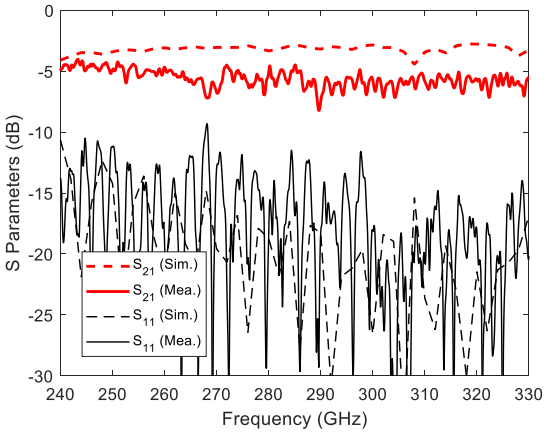

Figure 4.10 Transmission performance of the proposed double-layer SINRD waveguide

4.4 Conclusion

In this work, a vertically stacked double-layer substrate-integrated non-radiative dielectric (SINRD) waveguide is proposed and studied. Two alumina substrates with a thickness of 5 mil are used to construct the WR3-band SINRD waveguide. Compared with its single-layer counterpart, the double-layer waveguide has a guaranteed metallic covering on both sides, which is essential for non-radiative performance. A dense air-hole perforation is allowed, resulting in a more flexibility in the design of the SINRD waveguide. The simulation shows that the double-layer SINRD waveguide can operate well in the WR3-band. The measured results show that a high-precision alignment method is required during the assembly process.

CHAPTER 5 ARTICLE 3: SUBSTRATE-INTEGRATED HYBRID METALLO-DIELECTRIC WAVEGUIDE ARCHITECTURE FOR MILLIMETER-WAVE AND TERAHERTZ APPLICATIONS

Chun-Mei Liu, Louis-Philippe Carignan, Shaoqiu Xiao, Yejun He, and Ke Wu

Published in *IEEE Transaction on Microwave Theory and Techniques*, vol. 71, no. 9, pp.3958-3967

Publication date: March 06, 2023

Abstract: In millimeter-wave (mmW) and terahertz (THz) applications, the transmission behavior along circuit structures and components such as radiation and leakage losses are critical for their overall performances. It is imperative to develop low-loss interconnect and transmission techniques that should be used for the construction of building circuit blocks and elements. In this work, a hybrid metallo-dielectric (MD) waveguide architecture is proposed and studied for the first time. The scheme is made of mixed substrate-integrated dielectric waveguide (SIDW) and substrate-integrated non-radiative dielectric (SINRD) waveguide, which are respectively deployed for the design of specific building parts in consideration of respective transmission properties of the two waveguides. A back-to-back WR3-band prototype based on this hybrid scheme is investigated theoretically and validated experimentally. The hybrid MD waveguide architecture with SINRD is found to outperform the hybrid MD waveguide architecture with substrate-integrated waveguide (SIW) in terms of transmission performance and manufacturing complexity because of the advantageous features of metallized-via-free structure. The presented hybrid MD waveguide architecture shows its potential for developing low-loss highly integrated mmW and THz circuits and systems.

Index Terms: Hybrid metallo-dielectric waveguide, millimeter-wave (mmW), substrate-integrated dielectric waveguide (SIDW), substrate-integrated non-radiative dielectric (SINRD) waveguide, terahertz (THz).

5.1 Introduction

Dielectric waveguide (DW) has been well known for its great potential for the development of RF/wireless communications and sensing systems thanks to its attractive loss properties free from conductors when operating over millimeter-wave (mmW) and terahertz (THz) bands [120]. Solid-core DW structures [131], [132], [133], [144], [149], [183], which demand for a simpler manufacturing process, are good candidates for integrated circuits and systems. Ultra-low-loss transmission can basically be achieved by deploying low-loss dielectric materials. Furthermore, the overall transmission loss can be reduced by optimizing the geometry and dimension of a DW cross-sectional profile. In [122], [123], [124], a dielectric ribbon waveguide with polymer coating was developed. In [152], substrate-integrated dielectric waveguide (SIDW) was studied and characterized, which resembles substrate-integrated image guide (SIIG) [166] without a metallic grounding. The SIDW geometry is self-supported by its bilateral air-hole perforated region. The SIDW is still subject to a potential leakage like other DW structures, which stems from any transmission discontinuities due to its open geometric nature.

In understanding the detrimental nature of waveguide discontinuities, one may adopt smoothing transmission topologies, which is one straightforward way to reduce the effects of discontinuities, thus mitigating inherent radiation leakage losses. When space is limited, smooth transitions or discontinuities are impractical. Shielded waveguides, such as substrate integrated waveguide (SIW), can be used jointly with discontinuities. Such a hybrid architecture, schematically shown at Figure 5.1 (a) can yield a compact structure. Metallized via fences can suppress some undesired modes and improve transmission performance, but at the expense of increased topological complexity and metallic loss. On the other hand, a dielectric waveguide surrounded by a lower permittivity cladding is known to suffer less loss in bend region [197].

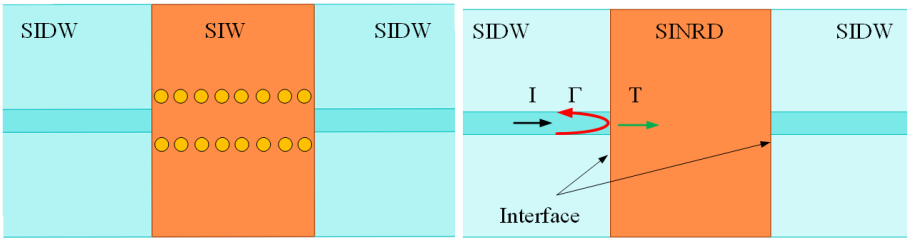

(a) (b)

Figure 5.1 (a) Existing hybrid waveguide architecture consisting of SIDW and SIW, (b) scheme of the proposed hybrid waveguide architecture consisting SIDW and SINRD waveguide

Non-radiative dielectric (NRD) waveguide [170], [171], [174] provides an alternative solution for the above-described leakage problem in connection with DW geometries. More recently, substrate-integrated non-radiative dielectric (SINRD) waveguide based on a synthesis of the original non-planar topology in planar form, emerges as an interesting alternative [176], [177], [187], [188], which can be realized by using a planar circuit board (PCB) technology and other planar processing techniques. The SINRD waveguide is promising for mmW and THz integrated systems due to its high tolerance and resilience to sharp discontinuities as well as its resulting planar geometric structure.

However, the total loss of an SINRD waveguide is generally higher than that of its SIDW counterpart because of its metallic coatings or plates involved in its formation and more confined field pattern within the lossy dielectric material. SINRD-based architecture generally suffers from a relatively high conductor loss. Interestingly, it can be anticipated that a straightforward solution of hybrid waveguides in Figure 5.1 (b) should be attractive, which is set to combine the merits of each of those waveguides in a waveguide architecture [195]. This hybridization presents a reasonable compromise of transmission loss and circuit design through blending those DW variants altogether.

The key of the hybrid waveguide architecture is an effective transmission over the interface between SIDW and SINRD in Figure 5.1 (b). In this work, the feasibility of the proposed hybrid waveguide architecture is validated by studying the mode compatibility between the E_{11}^{x} mode of SIDW and the non-radiative LSM_{01}^{x} mode of SINRD waveguide. Then this work devises and presents a straight back-to-back

substrate-integrated hybrid metallo-dielectric (SIHMD) waveguide architecture composed of SIDW and SINRD waveguides.

5.2 Feasibility of substrate-integrated hybrid metallo-dielectric waveguide

5.2.1 SIDW and SINRD waveguide

A general SIDW topology is described in Figure 5.2 (a). By metallizing the substrate surface as shown in Figure 5.2 (b), one can have an SINRD waveguide within a certain bandwidth. In this work, alumina substrate with $\varepsilon_r = 9.8$ and thickness of $h = 0.254$ mm is used for WR3-band demonstration. Its cross-section should be appropriately considered and designed to confine the guided electromagnetic fields. The width of the guiding channel is initially set to $w = 0.3$ mm. Air-hole perforation is applied over the bilateral section next to the guiding channel to reduce the dielectric permittivity of the hosting substrate. Even though it resembles a photonic bandgap structure [198], [199], their nature of operation is completely different.

In this work, equivalent models in Figure 5.2 (c) and (d) are used to characterize the SIDW and SINRD waveguide. In this way, the SIDW and SINRD are simplified as a composite guide consisting of an unperforated dielectric guiding channel of rectangular cross-section and its surrounding materials with an air-perforation-induced lower equivalent homogeneous or effective permittivity. According to [120], [170], the dispersion curves of SIDW and SINRD can be obtained. As shown in Figure 5.3, both the SIDW and SINRD waveguides of interest are set to work in the WR3-band. The SIDW supports the fundamental E_{11}^{x} and E_{11}^{y} modes whereas the SINRD supports the non-radiative LSE_{11}^{x} and LSM_{01}^{x} modes.

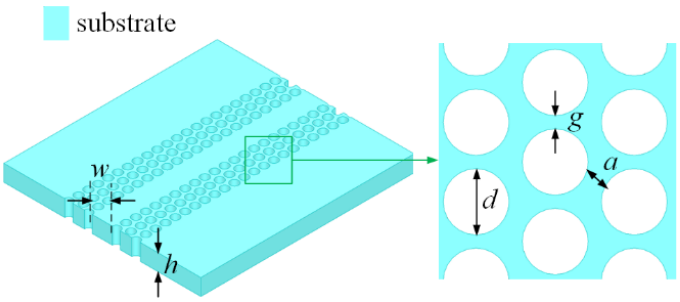

(a)

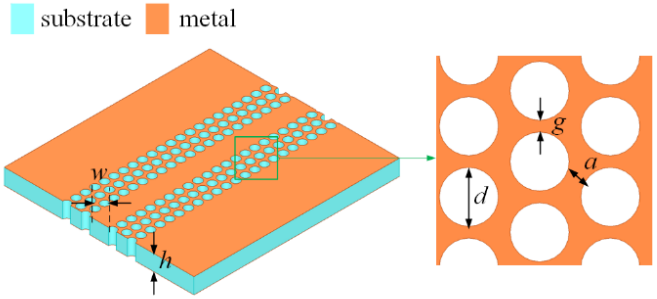

(b)

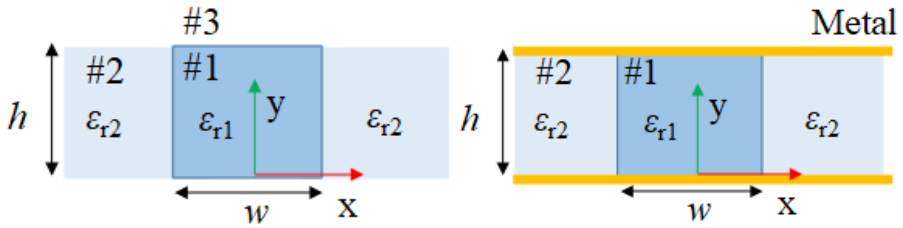

(c) (d)

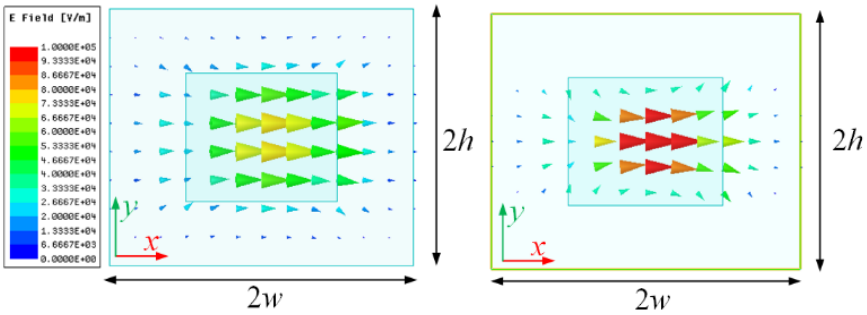

(e) (f)

Figure 5.2 Structures of (a) SIDW and (b) SINRD waveguide, equivalent models of (c) SIDW and (d) SINRD waveguide, simulated transverse electric field patterns of (e) E_{11}^{x} mode and (f) of LSM_{01}^{x} mode

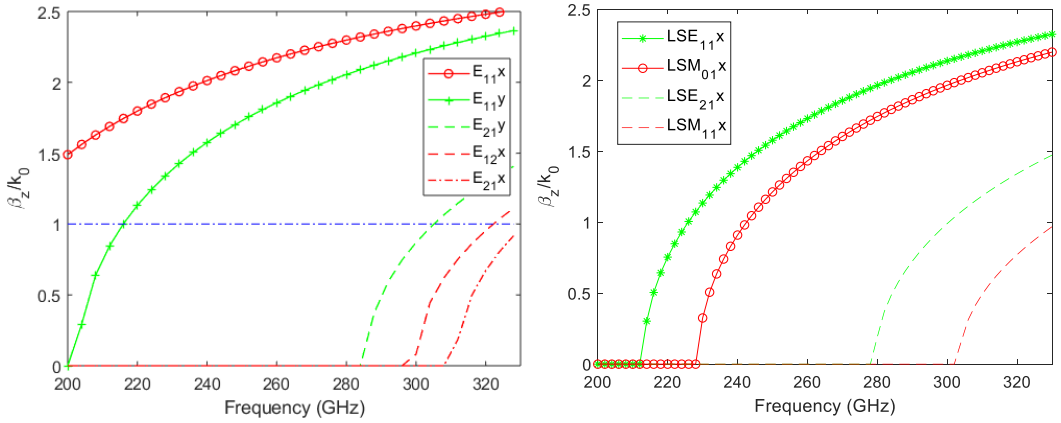

(a) (b)

Figure 5.3 Dispersion curves of (a) SIDW and (b) SINRD waveguide. Parameters: h = 0.254 mm, w = 0.3 mm, ε_{r1} = 9.8, ε_{r2} = 3.2

5.2.2 Substrate-integrated hybrid metallo-dielectric waveguide

The feasibility of a hybrid waveguide architecture consisting of both waveguides can be evaluated in a straightforward manner. As discussed in [120], while cascading two different types of waveguides to achieve efficient power coupling and signal transmission, three conditions should generally be satisfied, namely field matching, phase velocity matching, and impedance matching.

According to field equations (5-1) and (5-2) in Appendice B, one can figure out that the E_{11}^x mode of SIDW and the LSM_{01}^x mode of SINRD waveguide have similar transverse electric field patterns, as depicted in Figure 5.2 (e) and (f). The phase velocities of the E_{11}^x mode and the LSM_{01}^x mode are plotted in Figure 5.4 (a), showing a good matching condition. According to (5-3) in Appendice B, the wave impedances of those two modes are also plotted in Figure 5.4 (b). In this case, they are found to converge toward each other as frequency increases, which indicates the possibility of a good impedance matching between the two waveguides.

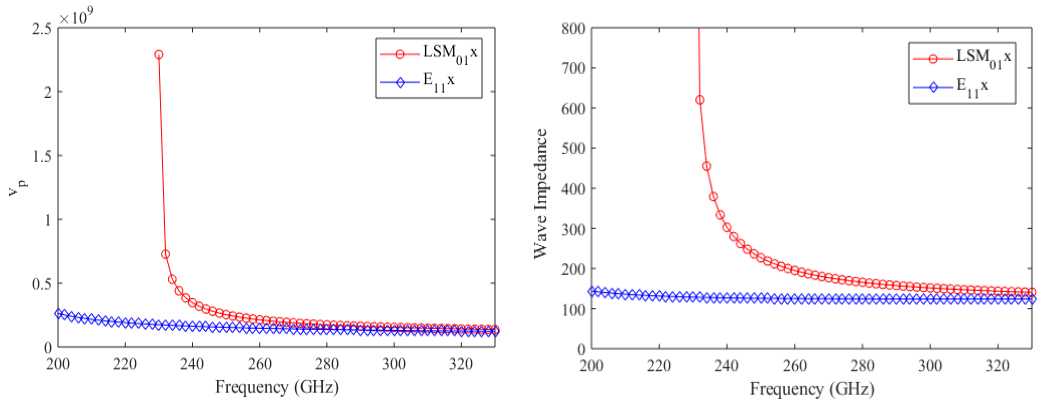

(a) (b)

Figure 5.4 (a) Phase velocities of SIDW and SINRD waveguide, (b) wave impedances of SIDW and SINRD waveguide

The structure of the substrate-integrated hybrid metallo-dielectric (SIHMD) waveguide architecture is shown in Figure 5.5 (a). The SIDW is directly connected to an SINRD waveguide without resorting to any geometrical adjustment and compensation. The simulated result is given in Figure 5.5 (b). As indicated, power or signal can be effectively coupled from the SIDW to the SINRD waveguide. The operating band starts from 260 GHz with a maximum loss of 0.3 dB. The bandwidth of the SIHMD waveguide architecture is mainly decided by that of the SINRD waveguide. As suggested in Figure 5.3 (b), the cut-off frequency of the LSM_{01}^{x} mode of the given SINRD waveguide is 230 GHz. The upper end of the SINRD waveguide is determined by the cut-off frequency of the first higher-order parallel-plate waveguide (PPW) mode of the dielectric-loaded parallel-plate waveguide. For the given SINRD waveguide, the first higher-order PPW mode propagating in region #2 with $\varepsilon_{r2} = 3.2$ appears at 340 GHz [56]. Theoretically, the appearance of the higher-order PPW mode can be moved backwards by decreasing the effective permittivity of region #2. However, decreasing ε_{r2} by increasing the density of air holes would adversely fragile the structure.

The average insertion loss of the proposed SIHMD waveguide architecture, mainly caused by impedance mismatch, is about 0.15 dB over the bandwidth from 260 GHz – 330 GHz. Both the phase velocity and the wave impedance of the E_{11}^{x} mode converge with those of the LSM_{01}^{x} mode as frequency increases, which results in a better impedance match. The field distribution of the SIHMD waveguide architecture is plotted in Figure 5.5 (c) and (d).

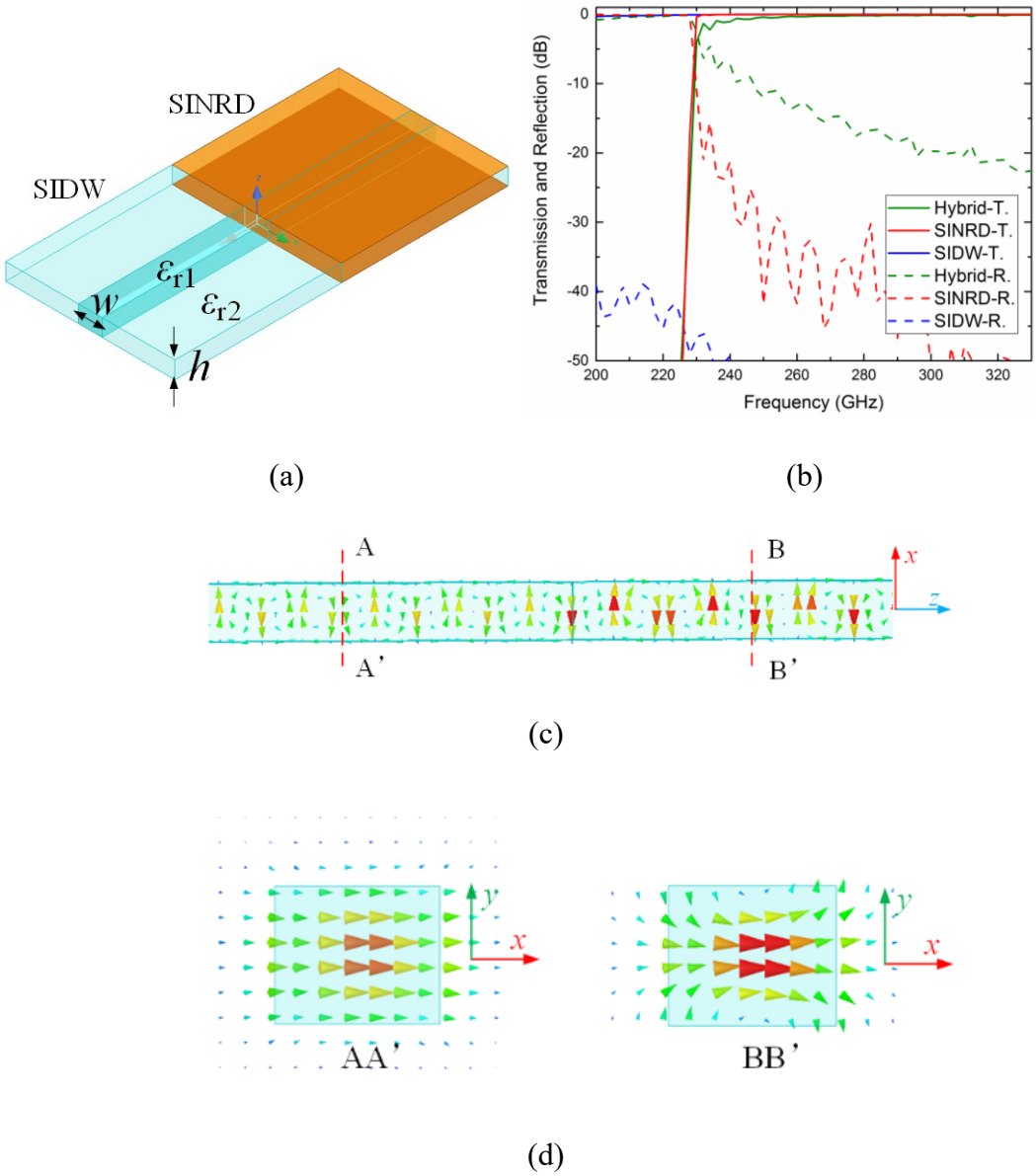

(a) (b)

(c)

(d)

Figure 5.5 (a) Equivalent model of SIHMD waveguide, (b) transmissions, (c) electric field distributions of SIHMD waveguide architecture at the *xoz* plane. (d) E_x^{11} mode at AA' (left) and LSM_x^{01} mode at BB' (right). Parameters: h = 0.254 mm, w = 0.3 mm, ε_{r1} = 9.8, and ε_{r2} = 3.2

5.3 Back-to-back SIHMD waveguide

5.3.1 Proposed SIHMD waveguide architecture consisting of SIDW and SINRD

A back-to-back SIHMD waveguide architecture consisting of SIDW and SINRD for the WR3-band is demonstrated. Its layout is sketched in Figure 5.6 (a). An alumina substrate with a thickness of h = 0.254 mm is used to develop the SIHMD waveguide architecture prototype with a length of l = 10 mm and a width of w = 0.3 mm. In this work, a fabricated prototype with the SINRD waveguide length of l_n = 1.75 mm is demonstrated and experimentally verified.

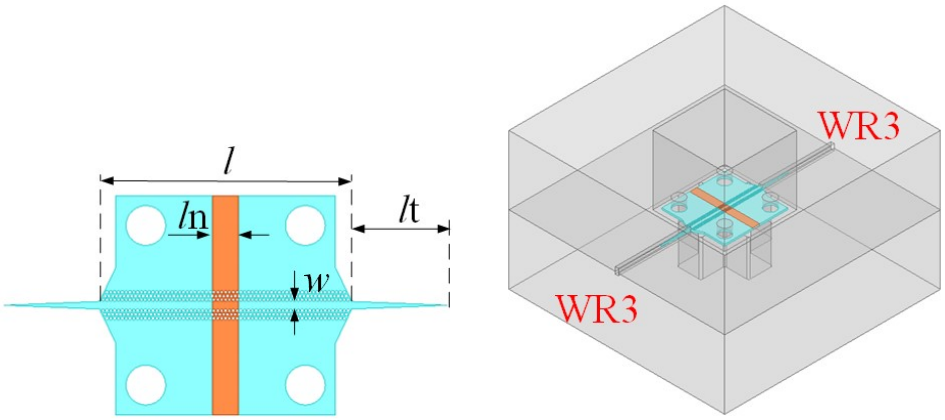

(a) (b)

Figure 5.6 (a) Layout of the proposed back-to-back SIHMD waveguide architecture, (b) metallic housing used to support the waveguide under testing. Parameters: l = 10 mm, w = 0.3 mm, l_t = 3.5 mm, l_n = 1.75 mm

The periodicity of air hole perforation p = 0.15 mm considered here is smaller than the operating guided wavelength to avoid the electromagnetic band gap in the band of interest. The diameter of the air hole is set as d = 0.125 mm. The wall thickness between two adjacent air holes is a = g = 0.025 mm, reaching the manufacturing limit of our laser drilling system in the Poly-Grames Research Center. Approximate values of the permittivity of the given perforated substrate are around ε_{r2} = 3.2 for the horizontal polarization by using the characteristic equations formulated and examined in [189].

The same air-hole perforation pattern is used throughout the SIHMD waveguide architecture.

Table 5.1 Parameters of demonstrated SIHMD waveguide architecture

Symbol	Description	Quantity
w	width of guiding core	0.3 mm
h	thickness of hosting substrate	0.254 mm
d	diameter of air hole	0.125 mm
a/g	thickness of wall between adjacent holes	0.025 mm
ε_{r1}	relative permittivity of the hosting substrate	9.8
ε_{r2}	effective relative permittivity in region #2 used in equivalent models	3.2
l	total length of the demonstrated SIHMD	10 mm
l_t	length of the taper for matching	3.5 mm
l_n	length of SINRD waveguide	1.75 mm
σ	conductivity of gold in simulation	4.1×10^7 S/m
tan δ	loss tangent of alumina in simulation	0.001

The dimension of WR3-band rectangular waveguide used in simulation is 0.86 mm × 0.43 mm.

The tan δ of the alumina substrate is 0.001 in simulation. The conductivity of the gold metallic coatings is set to $\sigma = 4.1 \times 10^7$ S/m in our HFSS simulations without considering potential surface roughness. A metallic housing is required for the measurement of the SIHMD waveguide, as shown in Figure 5.6 (b). To maintain the field pattern of the SIDW, the metal is removed underneath and above the SIDW sections. The substrate is bilaterally extended and suspended within the metallic housing. The SIHMD waveguide is tapered with length of $l_t = 3.5$ mm at both ends for impedance matching between the air-filled standard rectangular waveguide and the

SIDW. The standard WR3-band rectangular waveguides (0.86 mm × 0.43 mm) are rotated to excite the horizontally polarized modes. The electromagnetic wave can successfully propagate through the SIDW-SINRD-SIDW architecture in Figure 5.7.

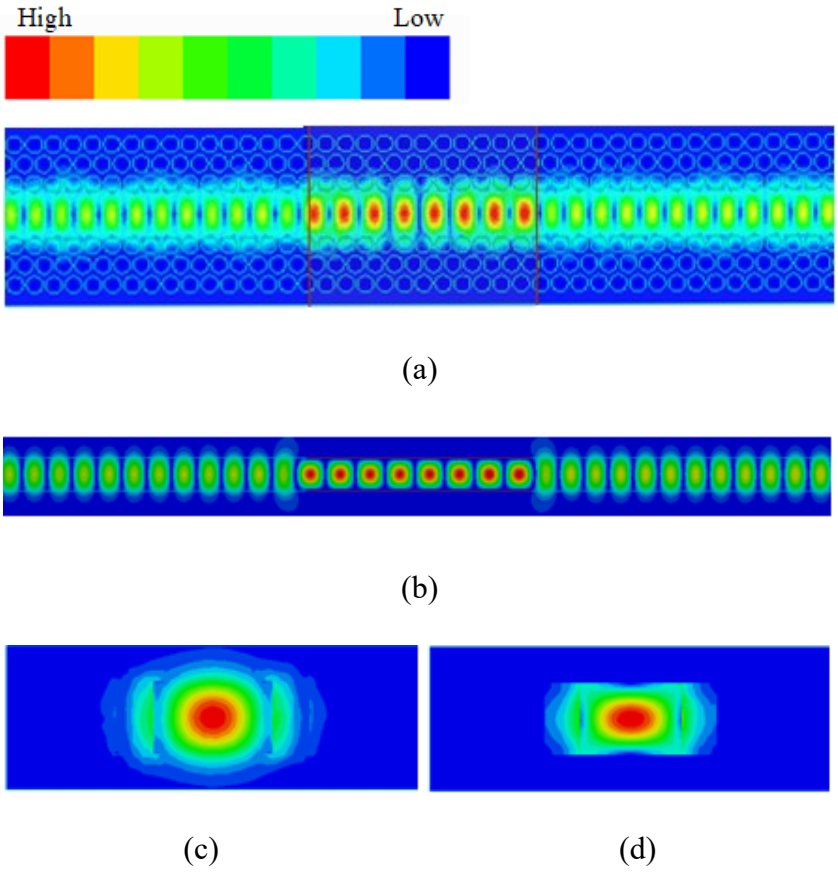

Figure 5.7 Simulated electric field distributions of the proposed back-to-back SIHMD waveguide architecture at 280 GHz. (a) Top view, (b) side view, (c) cross section of SIDW, E_{11}^{x} mode, (d) cross section of SINRD waveguide, LSM_{01}^{x} mode

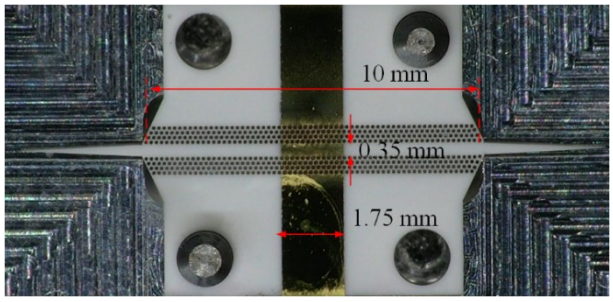

Figure 5.8 Photograph of the presented back-to-back SIHMD waveguide architecture under microscope

The fabricated prototype of the demonstrated SIHMD waveguide architecture is shown in Figure 5.8. Air-hole perforation was performed by a laser micromachining. The taper length is l_t = 3.35 mm, a value smaller than the designed counterpart since the tip has been burned during the manufacturing process. The metallic coatings were obtained by standard lithography before the air-hole perforation to avoid unwanted metal deposition into air holes.

S-parameters were measured using a PNA-X with VDI frequency extenders. Short-open-load-through (SOLT) calibration was performed up to the edges of the metallic support. Figure 5.9 shows the comparison between the measured results (solid lines) and full-wave simulation results (dashed lines). The average insertion loss is around 2.4 dB, which shows a good agreement with the simulated result (2.2 dB).

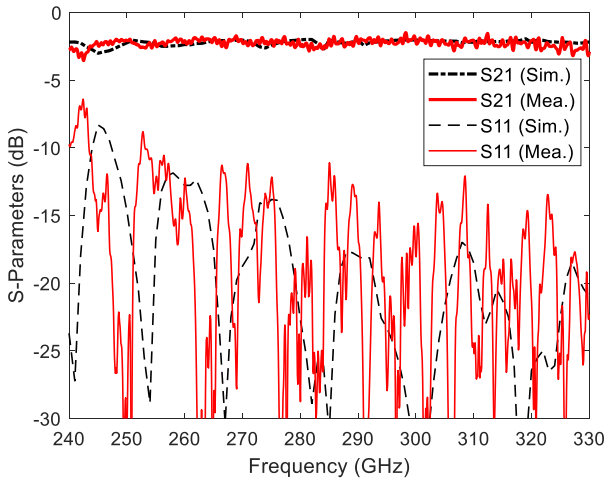

Figure 5.9 Simulated and measured results of the presented back-to-back SIHMD waveguide architecture

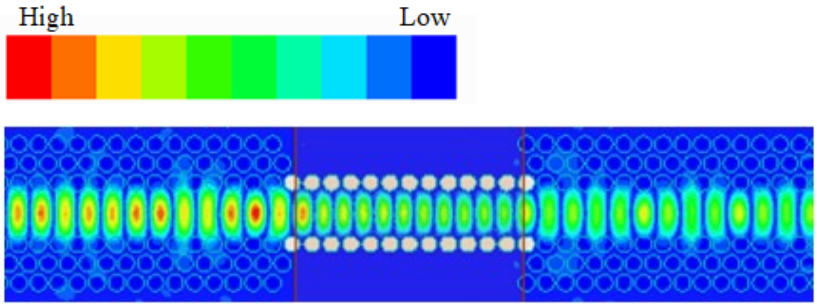

(a)

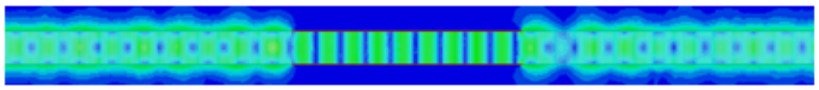

(b)

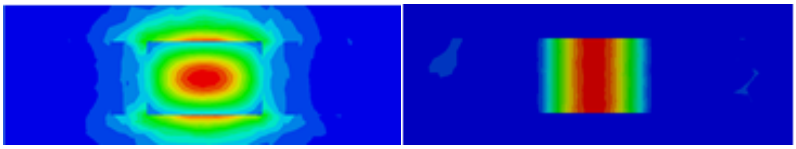

(c) (d)

Figure 5.10 Simulated electric field distributions of the traditional back-to-back SIHMD waveguide architecture (SIDW and SIW) at 280 GHz. (a) Top view, (b) side view, (c) cross section of the SIDW, E_{11}^{y} mode, (d) cross section of the SIW waveguide, TE_{10}^{z} mode

5.3.2 Comparison with SIHMD waveguide architecture consisting of SIDW and SIW

As mentioned earlier, the traditional SIHMD waveguide architecture consisting of SIW is also capable of confining electromagnetic waves at discontinuities. A comparison between the two SIHMD waveguide architectures is given here. The length of the SIW is selected to be the same as the SINRD waveguide in the proposed SIHMD scheme. No transition is added between two involved waveguides for each hybrid waveguide architecture. The coupling efficiency between the SIDW and SIW can be guaranteed because of the mode compatibility between the E_{11}^{y}/ E_{11}^{x} mode and the TE_{10}^{z}/TE_{01}^{z} mode if the SIW has two continuous metallized walls. For the given SIDW-SIW-SIDW in Figure 5.10, the operating mode is the E_{11}^{y} mode in SIDW and the TE_{10}^{z} mode in SIW with two rows of metallized via holes. Simulated electric field distribution is carried out by using of HFSS package. Obviously, the electromagnetic wave can successfully propagate through the SIDW-SIW-SIDW architecture. A metallic housing similar to that in Figure 5.6 (b) but with differently oriented transitions is fabricated to measure the back-to-back SIDW-SIW-SIDW architecture. The measured results are plotted in Figure 5.11.

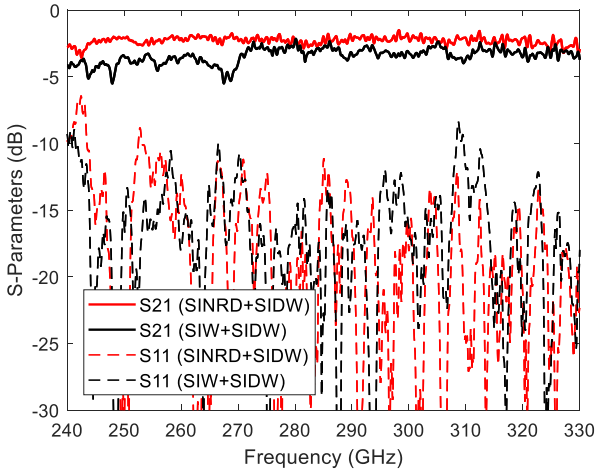

Figure 5.11 Comparison between the measured S-parameters of two SIHMD waveguide architectures

The transmission coefficient of the proposed SIHMD waveguide architecture is 1 dB better on average. Compared the SIHMD of SIDW and SIW, where the manufacturing process of metallized via holes could introduce more fabrication complexity, the presented SIHMD of SIDW and SINRD is preferred with its superior performance. Note that the mode operating in SIDW of the proposed SIHMD waveguide architecture is the E_{11}^{x} mode to ensure the excited mode in SINRD is the non-radiative LSM_{01}^{x} mode. Otherwise, the E_{11}^{y} mode in SIDW could excite the TE_{10}^{z} mode of the SINRD which actually works as an H-guide [178], [200]. Again, additional measures are required to confine electromagnetic waves over the discontinuities since H-guide does not have this feature, leading to design complexity.

5.4 Discussion

A parametric study based on HFSS simulations is given in this section to examine the influence of geometrical and substrate parameters on transmission properties of the proposed waveguide architecture. The SINRD waveguide and the SIDW are set to share the same width, which simplifies our analysis. The equivalent model used in this investigation is shown in Figure 5.12 (a).

5.4.1 Core width

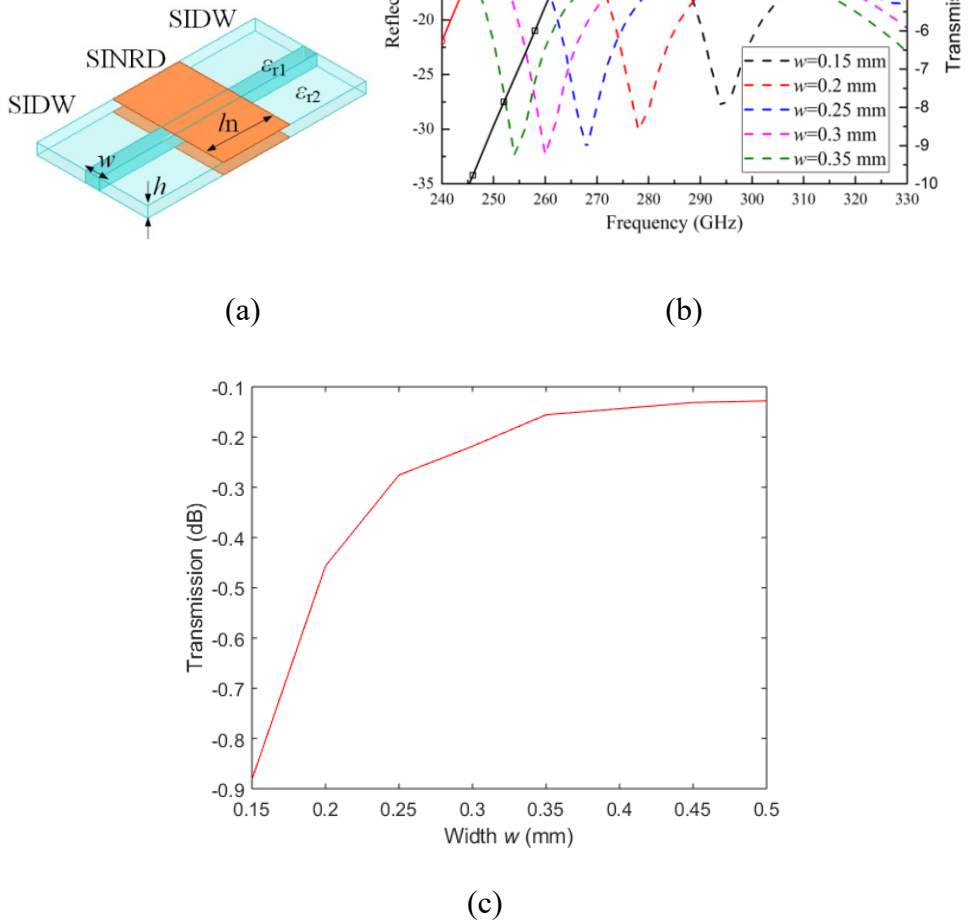

Figure 5.12 (a) Equivalent model of the proposed back-to-back SIHMD waveguide architecture, (b) transmissions and reflections of the back-to-back SIHMD waveguide architecture with different SINRD width, (c) transmission of the back-to-back SIHMD waveguide architecture with different widths at 330 GHz. Parameters: h = 0.254 mm, w = 0.3 mm, l_n = 0.254 mm, ε_{r1} = 9.8, ε_{r2} = 3

The frequency response of the SIHMD waveguide architecture with different waveguide width is shown in Figure 5.12 (b). The operating band is upshifted after increasing the waveguide width. Also, the transmission coefficient increases with

increasing waveguide width, as shown in Figure 5.12 (c), however at the expense of a narrower bandwidth, as shown in Figure 5.13 (a).

5.4.2 Effective permittivity of perforated region

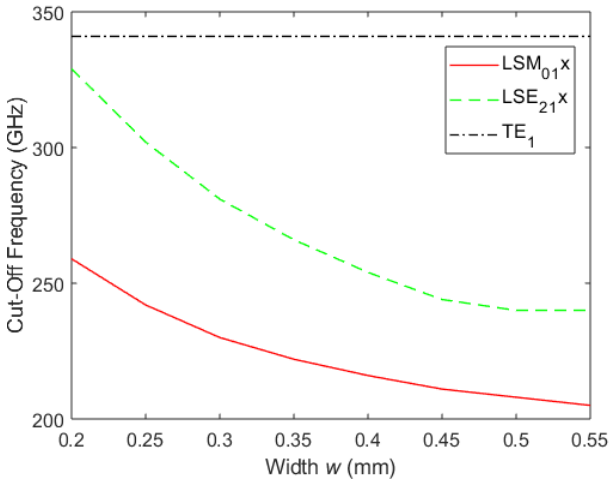

(a)

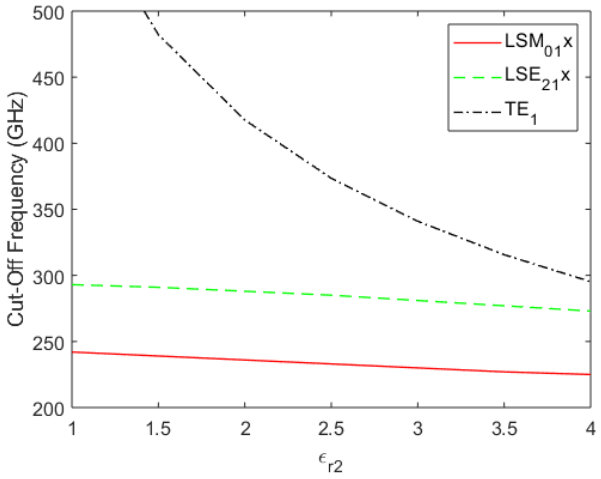

(b)

Figure 5.13 (a) Width effect and (b) ε_{r2} effect on frequency response

In consideration of the structure feasibility of SINRD waveguide, the diameter of air holes has been reduced to 0.1 mm during fabrication, leading to a value of ε_{r2} larger than the expected one. Increasing ε_{r2} will push the related higher-order PPW TE_1 mode into the band of interest, leading to a narrow non-radiative bandwidth. In practical

applications, the bandwidth of LSM_{01}^{x} mode is terminated by either the higher-order LSE_{21}^{x} mode or the PPW mode, whichever appears first. As shown in Figure 5.13 (b), the ε_{r2} hardly affects the bandwidth of the LSM_{01}^{x} mode.

5.4.3 SINRD waveguide

It is necessary to point out the effect of SINRD waveguide parameters, namely the length and the roughness in our case, on the performance of the hybrid waveguide architecture. As shown in Figure 5.14 (a), the length of the SINRD waveguide section hardly affects the transmission performance as long as the material losses are excluded.

One needs to carefully decide the extent of the SINRD waveguide section since it could affect the overall loss performance of the proposed SIHMD waveguide architecture. The loss performance of both waveguides with the same dimensions and materials is analytically calculated based on their field distributions [120], [170] and the data sheet of given materials. It suggests that the SINRD waveguide has a higher loss (in turn SIHMD waveguide architecture) as shown in Figure 5.14 (b). First, the SINRD waveguide is not a conductor-loss-free structure because of the finite conductivity of metallic coatings. In addition, the SINRD waveguide typically has a higher dielectric loss because its field is more concentrated within the lossy dielectric core. As shown in Figure 5.2 (e) and (f), the field extends slightly to the region #3 for the SIDW whereas the field is completely confined between the two metallic coatings for the SINRD waveguide. Therefore, one should balance the system performance for specific scenarios. For example, while the space is not limited, smooth transition is allowed and SIDW is preferred. While discontinuities are densely distributed, involving SINRD waveguide can dramatically reduce the propagation path, thus the associated transmission loss.

Next, the conductivity effect is examined on the transmission performance of SINRD waveguide. According to Figure 5.14 (c), reducing the conductivity slightly reduces the conductor loss. This phenomenon can be explained as follows. The dominant electric field component of the LSM_{01}^{x} mode is parallel to the two parallel metal coatings and

is essentially close to zero near the metal coatings because of boundary conditions. Therefore, the transmission performance of the SINRD waveguide is not that sensitive to the surface roughness while operating in the LSM_{01}^{x} mode.

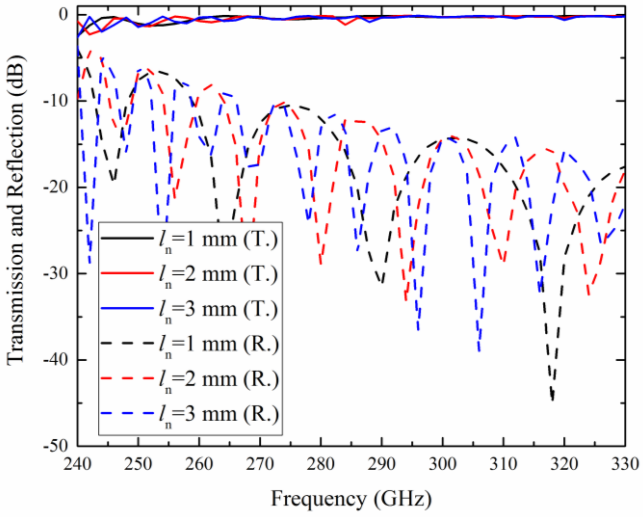

(a)

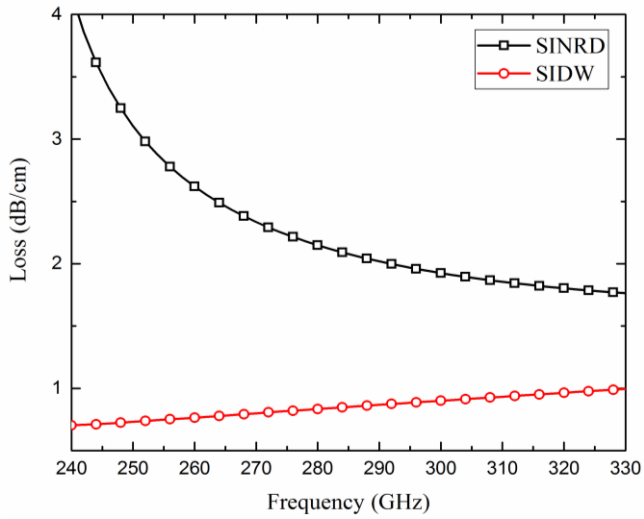

(b)

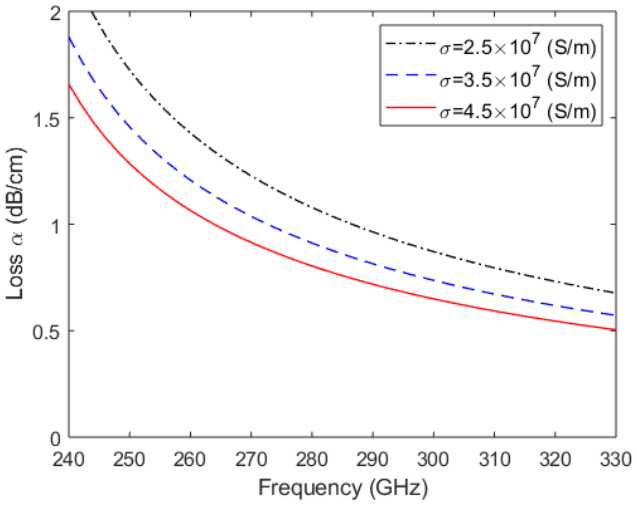

(c)

Figure 5.14 (a) Transmissions and reflection of SIHMD waveguide architectures with different SINRD length (w = 0.3 mm), (b) loss comparison between the SIDW and the SINRD waveguide, (c) conductivity effect on the conductor loss of SINRD waveguide

5.5 Conclusion

This work presents a hybrid waveguide architecture consisting of the SIDW and the SINRD waveguide, namely the SIHMD waveguide architecture. The presented SIHMD waveguide architecture has been analyzed by full-wave simulations, and experimentally verified in WR3-band. The simulated average insertion loss is 2.2 dB for a back-to-back experimental prototype involving the material losses, feeding loss, and reflection loss. The loss caused by the two interfaces between the SIDW and the SINRD waveguide is average 0.3 dB in total, as observed from the simulated transmission coefficient of the back-to-back SIHMD waveguide architecture. The proposed scheme shows a great potential in future mmW and THz applications.

CHAPTER 6 ARTICLE 4: HYBRID METALLO-DIELECTRIC WAVEGUIDE ARCHITECTURE FOR COMPACT LOW-LOSS THZ APPLICATIONS

Chun-Mei Liu, Louis-Philippe Carignan, annd Ke Wu

Published in *IEEE Microwave Wireless Technology Letters*, vol. 34, no. 5, pp.486-489

Publication date: April 01, 2024

Abstract: A hybrid metallo-dielectric waveguide (HMDW) architecture is studied and applied to the reduction of transition sizes over discontinuities, in turn the overall dimension of circuits and systems. The scheme is made of mixed dielectric waveguide (DW) and non-radiative dielectric (NRD) waveguide, which are respectively deployed for the design of specific building parts in consideration of respective transmission properties of the two waveguides. NRD waveguide with metallic covers is used over discontinuities, which allows for suppressing potential radiation and leakage effects, whereas DW is adopted along discontinuity-free segments to maintain a minimum transmission loss. A back-to-back guiding structure with four 90° bends covered by metal layers is demonstrated and experimentally validated in WR3-band. The simulated and measured insertion losses are comparable to their straight counterpart. With the NRD, the bend radius can be reduced by a factor of about 10, which enables the development of an extremely compact dielectric waveguide THz system. The presented metal-via-free HMDW can be implemented in high-density integrated low-loss circuits and systems, which is critical in THz manufacturing process.

Index Terms—Compact bend, dielectric waveguide, hybrid waveguide architecture, integrated terahertz (THz) circuits and systems, low-loss, manufacturing simplicity, metalized-via-free, non-radiative dielectric (NRD) waveguide.

6.1 Introduction

Terahertz frequency band (0.1 - 10 THz) has become one of the most studied topics since the past decade thanks to its great potential for high-speed and high-capacity wireless communication, sensing, imaging, and spectroscopic systems [201], [202]. Dielectric waveguides (DWs) exhibit a great potential in the development of THz circuits and systems due to the absence of conductor loss [120], [123], [133], [136], [203], [204]. Solid-core DWs with lateral dimensions comparable to the guided wavelength are preferable for highly integrated systems while considering the system compactness and the loss performance [120], [131]. Materials such as high-resistivity silicon (HR-Si) were applied to construct THz waveguides [129], [132], [144], [149], [151], [158]. However, channels and components are required to be sparsely distributed to avoid crosstalk. Moreover, dielectric transitions should be made as smooth as possible to reduce radiation and leakage because of their open boundary conditions, leading to a bulky size.

Metallized via holes/walls applied to the development of a substrate-integrated waveguide (SIW) technology are generally placed around discontinuities to prevent leakage [127], [205], [206], [207]. However, SIWs [96], [170], [208], which have been studied and used extensively in microwave/millimeter-wave components and systems, may not be practical in THz band circuits and systems because of manufacturing complexity and high conductor loss related to the metallized via holes/walls.

Non-radiative dielectric (NRD) waveguides can also confine electromagnetic (EM) waves at discontinuities[170], [171]. By simply adding two parallel metal plates to sandwich a dielectric core, undesired radiation leakage can be suppressed within a certain bandwidth, which allows for accommodating sharp discontinuities. Even though, NRD waveguides have a higher total loss than that of pure dielectric guides because of the two metal plates, especially at THz band [209]. A hybrid waveguide architecture [210], which can inherit the merits of DW and NRD, is beneficial to achieve a compact low-loss long interconnection in circuits and systems with more flexibility.

For instance, by using dielectric guides at discontinuity-free sections to minimize the conductor loss and switching to NRD at discontinuities such as sharp bends shown in Figure 6.1 to reduce the radiation leakage, one can obtain a very compact circuit with an optimized loss performance. The juxtaposition between NRD and DW constitutes the proposed hybrid metallo-dielectric waveguide (HMDW) architecture that offers a tradeoff between transmission performance and space efficiency.

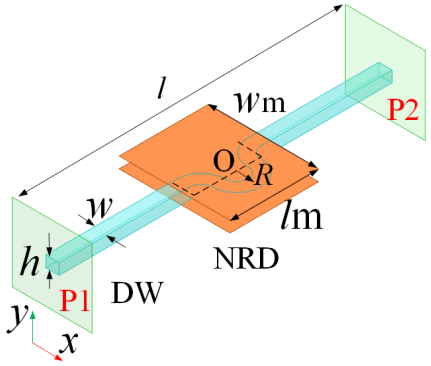

Figure 6.1 Discontinuity-tolerant hybrid metallo-dielectric waveguide architecture. Two parallel metal sheets are added over the discontinuity to avoid radiation leakage. Here, w = 0.3 mm, h = 0.254 mm, l_m = 1 mm, w_m = 2.5 mm, R = 0.2 mm, l = 3 mm

6.2 Hybrid metallo-dielectric waveguide

6.2.1 DW and NRD waveguide

For WR3-band demonstration, an alumina substrate with ε_r = 9.8 and a thickness of h = 0.254 mm is selected. A dielectric waveguide width of w = 0.3 mm is used to confine waves and to maintain a reasonable bandwidth. The dispersion diagram of the desired E_{11}^x mode of the DW [131], [190] and the LSM_{01}^x mode of NRD [170] is plotted at Figure 6.2. The transverse electric field patterns are plotted at Figure 6.3. The mode compatibility between the E_{11}^x of DW and the LSM_{01}^x mode of NRD has been verified in a previous work [170], [210]. An effective coupling from one to another through the junction with this mode compatibility can be guaranteed. For demonstration, a back-to-back straight hybrid metallo-dielectric waveguide (HMDW) with an NRD area of $l_m \times w_m$ = 1 mm × 2.5 mm (Figure 6.1 without bends) was simulated using HFSS. The

simulated results in Figure 6.4 suggest that the EM waves can propagate through the HMDW with an average insertion loss of 0.3 dB (without considering material loss) from 270 to 290 GHz.

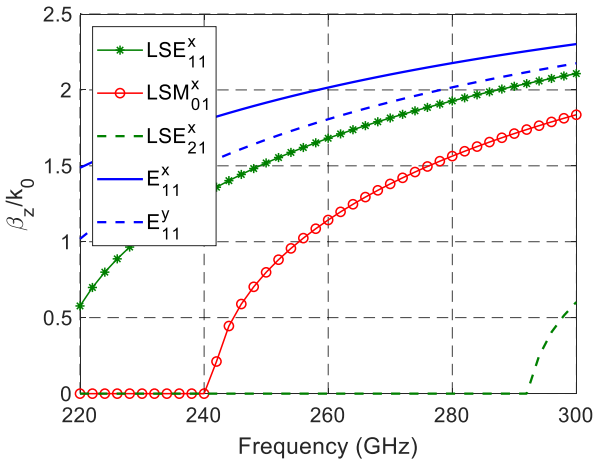

Figure 6.2 Dispersion diagram of DW and NRD waveguides: E_{11}^x and E_{11}^y modes of DW; LSE_{11}^x, LSM_{01}^x and LSE_{21}^x modes of NRD waveguide

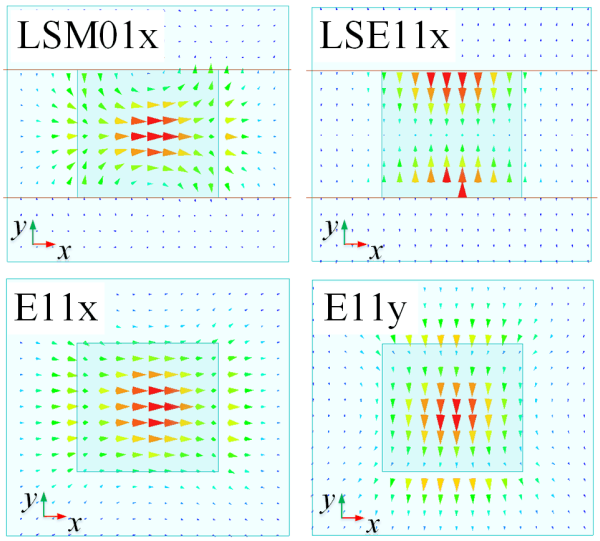

Figure 6.3 Transverse electric field patterns of the modes of interest for DW and NRD waveguide

6.2.2 Discontinuity-tolerant compact low-loss guiding

The back-to-back guiding structure, shown at Figure 6.1, that includes four 90° bends with a radius (from the bend origin to the middle of dielectric guiding) of R = 0.2 mm (about 0.19 wavelength at the center frequency of 280 GHz) is studied. For R = 0.2 mm, it can be shown at Figure 6.5 that the LSM_{01} mode is mostly converted to LSE_{11} after a single 90° bend. Thus, pairs of 90° bends are required to retrieve the LSM_{01} mode at the exit of NRD bend, and four of them were used to facilitate the measurement. Alternatively, a mode suppressor [190], [191] would be required to maintain the LSM_{01} mode throughout NRD bend. Extensive studies of mode conversion and mode suppression are outside the scope of this work and will be discussed in future. A pair of metal layers with an area of $l_m \times w_m$ = 1 mm × 2.5 mm have sandwiched the four bends to form an NRD guide.

On one hand, the use of metal should be reduced as much possible in the NRD to minimize conductor loss. On the other hand, for the case of HMDW with bends, a small portion of EM waves in LSE_{11} mode propagates inside the NRD bends and eventually radiates out through the two interfaces between the NRD section and DW, leading to spurious radiation. Therefore, the length of the NRD waveguide should be optimized to ensure no spurious radiation occurs in the band of interest. Mode suppressors could be used when necessary. However, it is outside the scope of this work.

The results of the simulation shown at Figure 6.4 show that the EM waves in E_{11}^{x} mode can propagate through four bends with a maximum insertion loss of 0.5 dB from 272 to 288 GHz. The cross-section of the electric field distributions over the bend at 280 GHz is shown at Figure 6.6. It indicates that radiation leakage can be significantly reduced after adding the two metal layers. The bandwidth limitation, obtained from the S parameters at Figure 6.4, is related to two inherent properties of the HMDW architecture: mode conversion of NRD bend, and mode selectivity of HMDW. As shown in Figure 6.5, after propagating through a 360° bend with a radius of R = 0.2 mm, about a half of LSM_{01}^{x} mode converts to LSE_{11}^{x} mode at 260 and 300 GHz.

However, this part of EM waves in LSE_{11}^{x} mode cannot be coupled to the DW because of the mode incompatibility. As shown in Figure 6.3, the LSE_{11}^{x} mode has a dominant transverse electric field component E_y with a minimum at the dielectric core center, which is not compatible with the fundamental $E_{11}^{x/y}$ modes of DW. Consequently, the LSE_{11}^{x} mode will be reflected at the DW- NRD interface. By using NRD over the bends, one can obtain a very compact structure at the expense of some bandwidth. Mode suppressors can be used to extend the bandwidth and will be discussed in future.

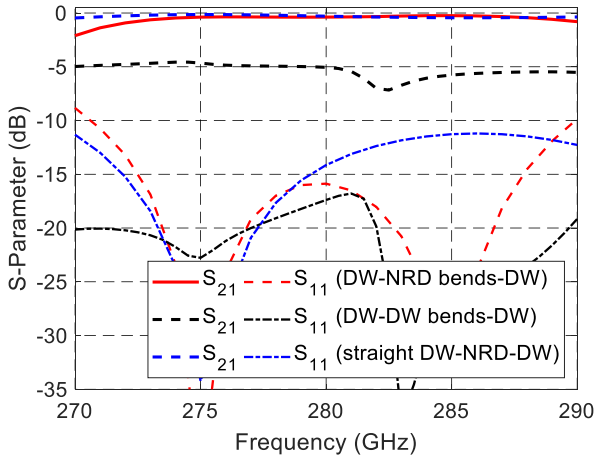

Figure 6.4 Simulated performance of the back-to-back guide shown at Figure 6.1 with and without metal layers over bends and the standard straight guide, for comparison

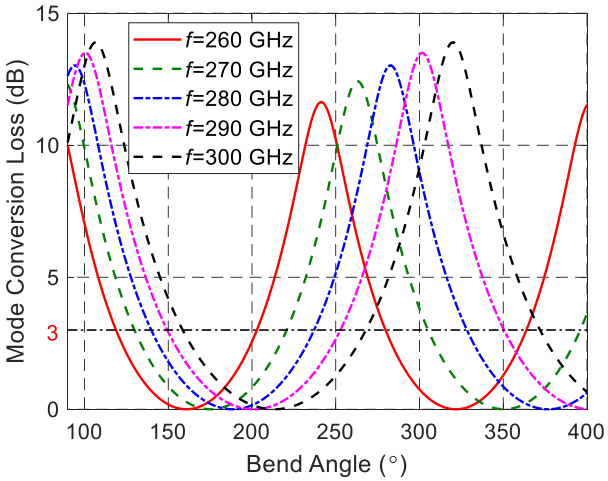

Figure 6.5 Mode conversion loss of LSM_{01} mode to LSE_{11} over sharp bend with metallic patch on the bends and with a radius of R = 0.2 mm [171]

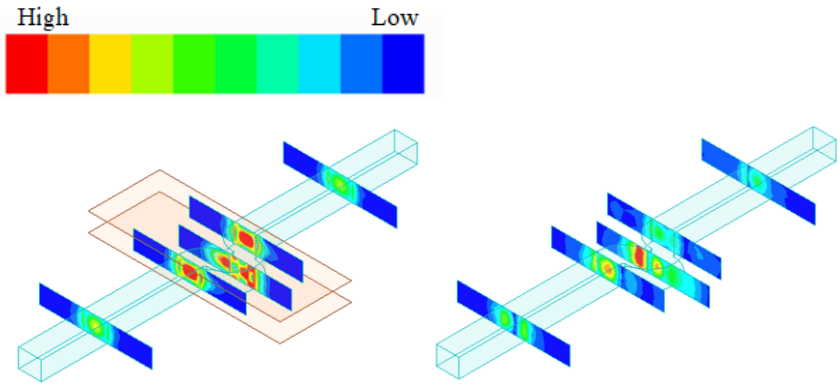

Figure 6.6 Cross-section electric field distribution at 280 GHz with two metal layers (left) and without metal layers (right) over the four 90° bends

6.3 Experiment

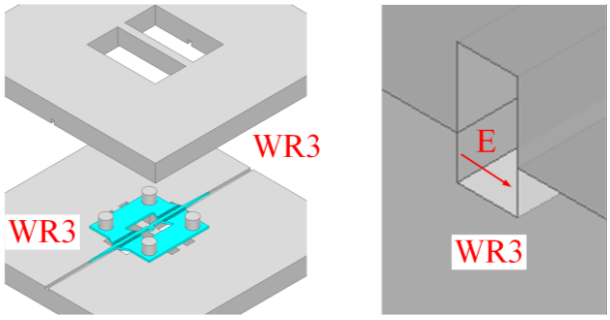

Figure 6.7 Simulation model of the back-to-back guiding waveguide (in blue) with four 90° bends placed on the base of the designed two-piece aluminum housing (in grey). The loss tangent of alumina substrate is set at tan $\delta = 0.001$ in simulation. The conductivity of aluminum is $\sigma = 3.8 \times 10^7$ S/m

A back-to-back alumina-based guiding structure was designed and fabricated. As shown at Figure 6.7, the guiding channel is bilaterally supported by perforated substrate arms realized by laser cutting, similar to that described in [195], at two ends, and then placed on the base of a two-piece metallic housing designed for testing. Tapers at the alumina DW ends act as transitions between the air-filled rectangular waveguide and the DW. The layout in Figure 6.8 (a) and (b) is obtained by laser drilling. The metallic (aluminum) housing in Figure 6.8 (c) was fabricated by CNC milling. Two trenches were created to enclose the two fragile alumina tapers. Dowel pins located at corners

of the metallic housing are used for alignment. The metal above and underneath the two straight DW sections is removed to ensure that the straight sections are free from conductor loss. Above and underneath the four bends, the metal is left, as the metal layers of NRD waveguide, to avoid radiation, as detailed above.

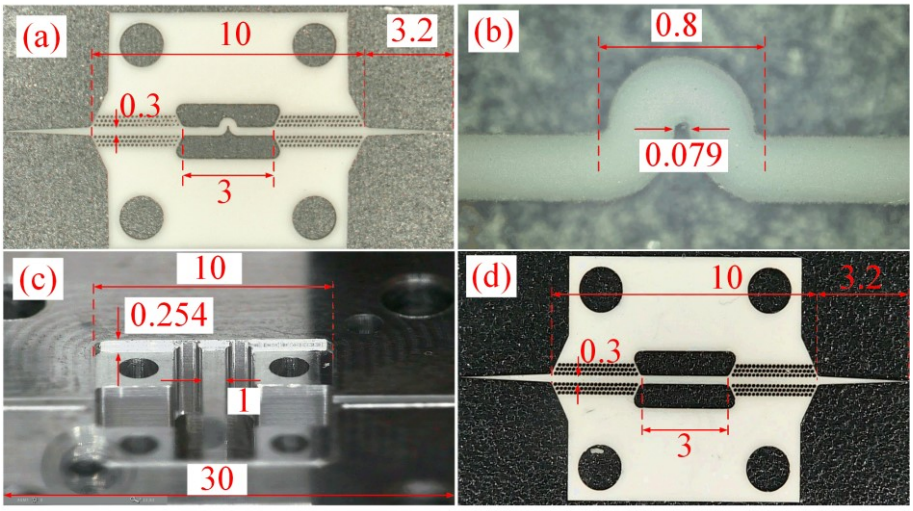

Figure 6.8 Photograph of the alumina based guiding structure with bends, (b) picture of bends, (c) two pieces of the aluminum housing, base and cover, (d) photograph of the standard back-to-back straight waveguide. Unit in mm

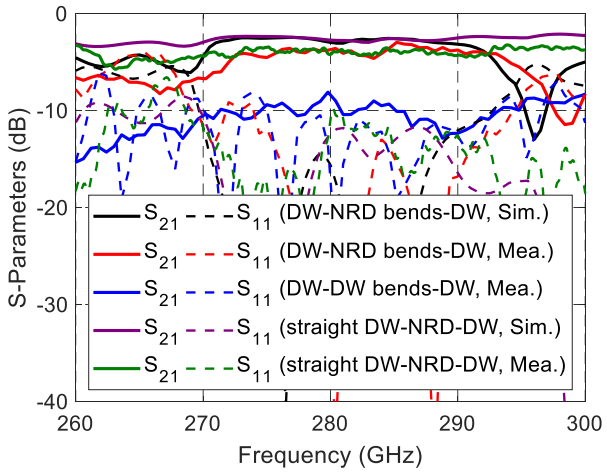

Figure 6.9 Comparison between measured and simulated results of the back-to-back guide with four 90° bends with/without metallic covering and standard back-to-back straight guide

A PNA-X network analyzer with a pair of VDI frequency extenders is used for measuring S-parameters. A short-open-load-through (SOLT) calibration brings the reference plane at the edge of the metallic waveguide. The measured results show a fair agreement with the simulated results, as depicted at Figure 6.9. The measured averaged insertion loss is 4 dB (3.2 dB in simulation carried by HFSS) from 272 to 292 GHz, with a minimum of 3.15 dB at 286 GHz and a maximum of 5 dB at 272 GHz, which consists of material losses, reflection loss from interfaces and feeding loss. The measured reflection coefficient is less than -10 dB within the bandwidth. For comparison, the circuit without two metallic covering over the bends has an average loss of 10 dB. A back-to-back straight waveguide shown in Figure 6.8 (d) is fabricated and measured with the same metallic housing in Figure 6.8 (c). The measured averaged insertion loss indicated by green solid line in Figure 6.9 is 4 dB from 260 to 300 GHz. The measured insertion loss of the waveguide with bends is comparable with that of the straight one from 272 to 292 GHz (from 270 to 288 GHz for the simulation), which suggests that the four bends covered by metal layers are considered non-radiative in this frequency band.

6.4 Conclusion

This work presents a hybrid metallo-dielectric waveguide (HMDW) architecture for THz system compactness. A non-radiative dielectric (NRD) waveguide is used over sharp discontinuities such as bends to suppress radiation leakage and a dielectric waveguide (DW) is used at discontinuity-free sections to maintain low-loss performance. Thanks to the nature of NRD waveguide, the dielectric bend radius can be reduced by a factor of about 10 within a certain bandwidth, without significantly sacrificing S-parameter performances. Compact low-loss power dividers, couplers and other components based on the HMDW architecture are feasible. Compared to the traditional methods of suppressing the radiation or leakage effects over discontinuities by using metalized via hole/walls and fully metallic shielding or dielectric cladding, the presented method is easier to implement, which can significantly relax stringent requirements for THz design and manufacturing processes and cost. The use of mode suppressors to cancel out the unwanted LSE_{11} mode will be considered in a future work.

CHAPTER 7 ARTICLE 5: CROSSTALK AND LEAKAGE SUPPRESSION BY MODE SELECTIVITY AND CONVERSION IN TERAHERTZ HYBRID METALLO-DIELECTRIC WAVEGUIDE CROSSOVER AND INTERSECTIONS

Chun-Mei Liu, Louis-Philippe Carignan, and Ke Wu

Published in *IEEE Transaction on Microwave Theory and Techniques*, vol. 72, no. 12, pp. 6943-6955

Publication date: June 18, 2024

Abstract: Hybrid metallo-dielectric waveguide (HMDW) crossover is proposed and presented in this work. Two parallel metal plates over two intersecting dielectric waveguides (DWs) area create a non-radiative dielectric (NRD) waveguide intersection that is harnessed to avoid the inherent radiation/leakage loss effect of such open dielectric waveguide discontinuities. Straight DW sections far from the intersection are set to minimize conductor loss free from any metal plates. Furthermore, crosstalk can be significantly reduced due to the mode conversion over the NRD waveguide intersection and the mode selectivity of the HMDW architecture. The proposed HMDW crossover has a lower structural insertion loss (material losses are excluded) of 0.37 dB from 275 GHz to 295 GHz, whereas DW crossover and NRD crossover have 1.5 dB of insertion loss. The HMDW architecture is applied to a 10 mm back-to-back alumina-based waveguide with four orthogonal dielectric strips. The metal plates of NRD covering all intersections with a designed width can prevent the EM waves from propagating to four orthogonal dielectric strips. The fabricated prototype has a measured insertion loss about 5.5 dB from 262 GHz to 286 GHz (4.8 dB in simulation from 262 GHz to 288 GHz). While the hybrid waveguide has a higher loss than its dielectric counterpart, it allows multiple orthogonal guides to cross-pass, providing an alternative solution for integrated systems where intersecting paths are inevitable. Its structural simplicity is beneficial to THz manufacturing.

Index Terms: Crossover, crosstalk reduction, dielectric waveguides (DWs), hybrid metallo-dielectric waveguides (HMDWs), leakage reduction, mode conversion, mode selectivity, non-radiative dielectric (NRD) waveguides, terahertz (THz).

7.1 Introduction

Crossovers are one of the vital transmission structures and components used in constructing integrated circuits, interconnects, and systems. Directly intersecting orthogonal paths generally lead to a high level of crosstalk, which adversely influences signal integrity and causes additional loss. A simple approach is to redirect one of the paths out of the circuit layer in question to avoid directly intersecting the other path [211]. To electrically connect transmission paths at different layers, metallic walls or via holes are required [212], [213], [214]. Coupling methods are available for guiding electromagnetic (EM) waves from one layer to another [56], [215], [216], [217]. However, these out-of-plane approaches significantly escalate manufacturing complexity and costs. Additionally, turns or interconnects in a transmission path out of and into the current circuit layer generally introduce unwanted radiation leakage, transmission reflection, and path loss.

Numerous solutions have been derived and reported to improve the isolation of coplanar crossovers [218], [219], [220], [221]. Inserting via holes near a coupling window can reduce the crosstalk of its related waveguide crossover, but typically at the expense of the performance of the orthogonal guide, such as bandwidth [222]. Substrate-integrated waveguide (SIW) filtering crossovers exhibit high isolation performance based on intrinsic common-mode (CM) suppression [223], [224], [225], [226], [227]. Although adjustable frequency response can be achieved by controlling resonant frequencies and mutual couplings, the sophisticated topologies adversely challenge the THz manufacturing process. Moreover, SIWs may essentially not be used in THz circuits and systems because of potential high manufacturing costs and high conductor losses associated with the process of metallic via holes or walls [209].

Although dielectric waveguides (DWs) are excellent candidates due to their conductor loss-free properties [120], [131], [132], [133], [136], [147], [153], their applications in THz integrated circuits and systems are limited because of their open boundary conditions. This fundamental DW property is responsible for any radiation loss or

leakage once signal transmission path encounters waveguide discontinuities. For example, DW crossovers suffer from large crosstalk and radiation leakage, thus leading to a non-negligible insertion loss. Multimode-interference couplers have been applied to reduce the crosstalk of DW crossovers thanks to their self-image effects [228][229][230][231][232]. Reducing the coupling window by locally narrowing the width of the orthogonal waveguide can reduce crosstalk but consequently affects the transmission performance of the orthogonal waveguide.

Non-radiative dielectric (NRD) waveguides were proposed [170][171][233] to mitigate radiation leakage issues of DWs discontinuities. Discontinuities, such as crossovers, could be made to be non-radiative over a certain bandwidth determined by the spacing between the two parallel metal plates of the NRD waveguides. Meanwhile, NRD waveguides exhibit relatively low conductor loss while operating in the second non-radiative longitudinal-section magnetic (LSM) mode, that is the LSM_{01} mode, making the LSM_{01} mode favorable for THz applications where conductor loss may become dominant. However, NRD waveguide crossovers may also experience high crosstalk. Mode suppressors [182], [191] could reduce the crosstalk by suppressing the coupled longitudinal-section electric (LSE) mode, that is the LSE_{11} mode, which is realized by appropriately inserting vertical metallized walls in the middle of the dielectric strips.

In this work, a hybrid metallo-dielectric waveguide (HMDW) crossover and intersection are proposed and demonstrated. Section 7.2 presents the principle of HMDW crossover using a NRD junction and DW arms, including mode analysis of DW and NRD waveguide, mode conversion of NRD junction and mode selectivity of HMDW architecture. Section 7.3 discusses asymmetrical and symmetrical HMDW crossovers. Section 7.4 presents a two-port waveguide with intersections, where the same principle used for the crossover is applied to reduce the leakage into orthogonal arms. Section 7.5 presents the measurement results of the two-port prototype. Section 7.6 discusses the obtained results. Section 7.7 concludes the manuscript.

7.2 Principle of HMDW crossover

The principle of operation of the HMDW crossover is illustrated in Figure 7.1. Sandwiching the intersection of two DWs with two parallel metal plates to form an NRD waveguide intersection, can significantly reduce radiation leakage within a

certain bandwidth. Discontinuity-free sections are exposed to air to minimize conductor loss associated with the presence of metal plates. The propagation of electromagnetic (EM) waves along the hybrid through guide from port 1 (P1) to port 2 (P2) is guaranteed thanks to the mode compatibility between the LSM_{01}^{x} mode of NRD guide and the fundamental E_{11}^{x} mode of DW, which has been experimentally validated in [195]. The HMDW crossover brings about a reduction in crosstalk. Mode conversion happens over the NRD waveguide intersection, resulting in a coupled LSE_{11}^{z} mode in the orthogonal NRD guide. The mode incompatibility between the LSE_{11}^{z} mode of the orthogonal NRD guide and the fundamental modes of the orthogonal DW reduces the leakage into port 3/4 (P3/4), thus improving the isolation between the two intersecting guides. Here, the HMDW crossover is demonstrated from 275 GHz to 295 GHz, within WR3-band (225 GHz to 335 GHz).

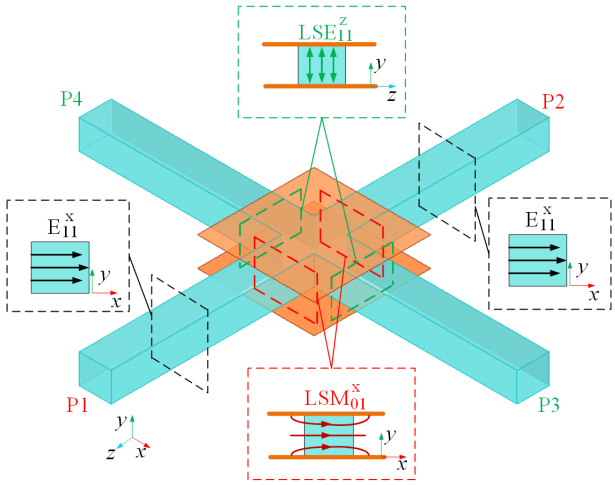

Figure 7.1 Hybrid metallo-dielectric waveguide (HMDW) crossover. Schematics of electric fields for LSM_{01}^{x} of the through NRD guide and E_{11}^{x} mode of the through DW and LSE_{11}^{z} mode of the orthogonal NRD guide are given

7.2.1 Modes of DW and NRD waveguide

The modes supported by DWs are divided into E_{mn}^{x} and E_{mn}^{y} modes [120]. The superscript x and y represent the electric field polarization and subscript *m* and *n* represent the order of mode along *x*- and *y*-axes, respectively. In this work, low-loss

alumina substrate with ε_r = 9.8, a thickness of h = 0.254 mm and a width of w = 0.28 mm is used for WR3-band demonstration. Cut-off frequencies and dispersion curves can be approximated using [131]. The given DW supports the fundamental $E_{11}^{x/y}$ mode in the WR3-band, as depicted in Figure 7.2. Higher order mode E_{21}^{y} mode is not guided in the band of interest.

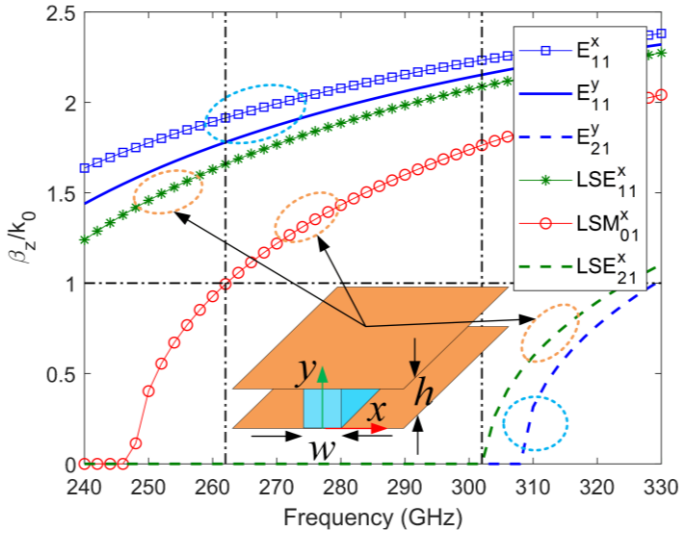

Figure 7.2 Dispersion curves of E_{11}^{x}, E_{11}^{y} and E_{21}^{y} modes of DW; LSE_{11}^{x}, LSM_{01}^{x} and LSE_{21}^{x} of NRD waveguide with h = 0.254 mm, w = 0.28 mm and ε_r = 9.8. Inset: schematic of NRD waveguide. Dispersion curves circled by blue dashed circles are for DW, circled by orange dashed circles are for NRD waveguide

For waveguides inhomogeneously filled with dielectric slab, it is convenient to define the Hertzian potential normal to the air-dielectric interface to find the hybrid modes satisfying the boundary condition along the dielectric interface [234]. For the NRD waveguide in Figure 7.2, one can define a magnetic-type Hertzian potential Ψ_x^h for longitudinal-section electric (LSE^x) modes with no electric field component normal to the interface and an electric-type Hertzian potential Ψ_x^e for longitudinal-section magnetic (LSM^x) modes with no magnetic field component normal to the interface. The superscript x represents the vector direction of potential function. The first two non-radiative modes of NRD waveguide are the LSE_{11}^{x} and LSM_{01}^{x} modes. Their cut-off frequencies can be obtained by numerically solving the transcendent equations, after

applying the boundary conditions of perfect electrical conductors and of the air-dielectric interfaces at $x = \pm w/2$ along y-z plane [234]. The LSM_{01}^{x} mode starts from 246 GHz but the bandwidth near cut-off frequency is discarded because of high conductor loss [20] and poor matching between NRD and DW [195]. The bandwidth of the LSM_{01}^{x} mode thus starts from 262 GHz (4.8 % above the LSM_{01}^{x} cut-off frequency) and extends to 302 GHz, the cut-off frequency of the LSE_{21}^{x} mode.

Within the 262-302 GHz band, mode conversion between LSM_{01} and LSE_{11} might occur, thus generally introducing additional loss and potentially degrading the signal integrity of the system. Here, the mode conversion between the LSM_{01} and LSE_{11} modes at the NRD waveguide intersection is one of the two keys of developing proposed HMDW crossover. The other key is the mode selectivity of the HMDW architecture.

7.2.2 Mode conversion of NRD waveguide intersection

For the NRD waveguide intersection shown in Figure 7.3 inset, two bilateral coupling windows along the through guide from P1 to P2 are created at the four-port cross junction. The orthogonal guide P3-P4 lying along the x-axis supports the LSE^{z} and LSM^{z} mode. The cut-off frequencies and dispersion curves of the LSE_{11}^{z} and LSM_{01}^{z} modes of the orthogonal guide are essentially the same as those of the through guide. Both the LSE_{11}^{z} and LSM_{01}^{z} modes could be excited with a proper excitation at the four-port junction. The electric field components of LSM_{01}^{x} mode in P1 -P2 NRD waveguide sections (except the intersection) can be given by (7-2) in the Appendice C. The field components of the LSE_{11}^{z} and LSM_{01}^{z} modes, in the NRD straight waveguide portions (excluding the junction), are given by (7-5) and (7-6) in the Appendice C. The E_y component of the LSM_{01}^{x} mode excited at P1 can excite the LSE_{11}^{z} mode in the orthogonal waveguide arms. The E_z component at the junction can excite LSM_{01}^{z} mode in the orthogonal waveguide arms, i.e., the ones containing P3 and P4. In fact, the LSM_{01}^{x} mode in the through guide can excite various modes at the discontinuities. Mode expansion would be needed to obtain the amplitude of the various modes [192].

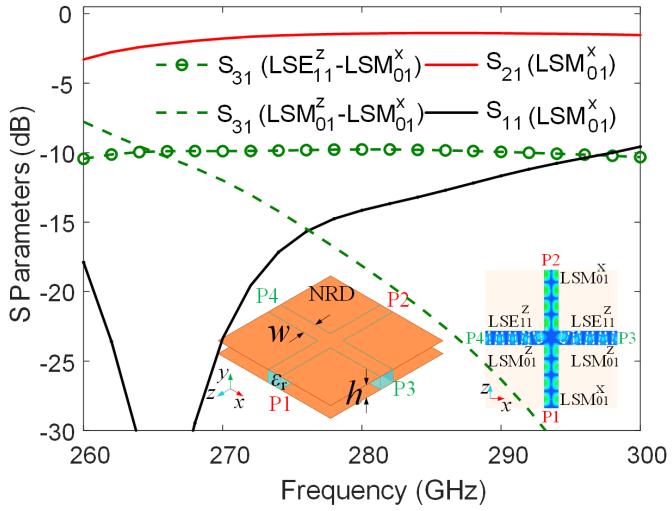

Figure 7.3 Simulated performance of NRD waveguide junction. Inset: schematic of the NRD waveguide junction (center) and simulated electric field at 280 GHz (right). LSM_{01}^{x} mode is assigned at P1

Deriving the theory of the four-port junction is outside the scope of the manuscript. It will be discussed elsewhere. ANSYS HFSS is used for full-wave simulations. An ideal model without considering material and feeding losses is used to study the losses caused by the structure. Multi-mode wave ports are assigned at all four ports to obtain mode conversion. The wave ports have a dimension of $2w \times h$ to fully cover the extending field outside the dielectric core. As shown in Figure 7.3, the average insertion loss from P1 to P2 (red line) is 1.65 dB from 262 GHz to 300 GHz, with a maximum of 2.75 dB at 262 GHz, due to a leakage into unwanted ports P3/4. Two modes are received at P3/4, namely, the LSE_{11}^{z} and LSM_{01}^{z} modes. The coupling between the LSM_{01}^{x} and the LSE_{11}^{z} modes is about -10 dB within the frequency band from 262 GHz to 300 GHz. The coupling between the LSM_{01}^{x} and LSM_{01}^{z} modes decreases with increasing frequency.

7.2.3 Mode selectivity of HMDW

The mode selectivity of the HMDW architecture is the other key aspect for realizing the proposed crossover. On one hand, the mode compatibility between the E_{11}^{x} mode

of the DW and the LSM_{01}^{x} mode of the NRD guide is essential for wave transmission through the interconnection between the through DW and the through NRD guide [210], as shown in Figure 7.4 (a). Wave ports are assigned at P1, P3 and C. C is a reference plane near the intersection. Wave port at C has a dimension of $2w \times h$, whereas wave port at P1/3 has a dimension of $4w \times 4h$. Material losses are excluded in the simulation. The LSM_{01}^{x} mode of the NRD guide can propagate through the interface between the two dissimilar waveguides with an average insertion loss of 0.26 dB from 262 GHz to 300 GHz, with maximum of 0.6 dB at 264 GHz, and then excite the E_{11}^{x} mode in the DW, and vice versa. The S_{11} is of the order of -15 dB, but could be improved by widening the width of dielectric core and introducing parasitic impedance matching structures.

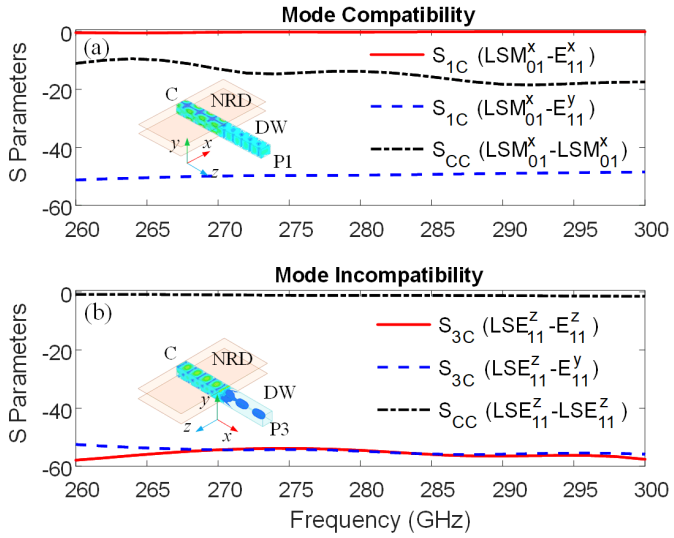

Figure 7.4 Mode selectivity of HMDW architecture. (a) Mode compatibility between LSM_{01}^{x} mode and E_{11}^{x} mode, inset: electric field distribution inside HMDW architecture when LSM_{01}^{x} mode propagates along NRD guide, (b) mode incompatibility between LSE_{11}^{z} mode and $E_{11}^{z/y}$ mode, inset: electric field distribution inside HMDW architecture when LSE_{11}^{z} mode propagates in NRD guide

On the other hand, the mode incompatibility between the coupled LSE_{11}^{z} mode of the orthogonal NRD guide and the fundamental modes of the orthogonal DW enhances the independence of the two intersecting guides. According to [192], it is difficult to couple

EM waves in the LSE_{11} mode of the NRD guide into the DW. From (7-5) and (7-7), the transverse electric field of the LSE_{11}^{z} mode is E_y component. For the orthogonal DW guide, the fundamental E_{11}^{z} mode has a dominant E_z component. The LSE_{11}^{z} mode cannot excite the E_{11}^{z} mode. Meanwhile, the LSE_{11}^{z} mode cannot excite the degenerate E_{11}^{y} mode in the orthogonal DW guide because of the mode pattern orthogonality. Consequently, the mode incompatibility of the HMDW architecture prevents the coupled LSE_{11}^{z} mode from propagating to P3/4. Instead, the LSE_{11}^{z} mode is reflected back to C as indicated by S_{CC} in Figure 7.4 (b). Therefore, by creating a mode selective interface, resulting an HMDW architecture, the leakage associated with the coupled LSE_{11}^{z} mode can be suppressed.

7.3 HMDW crossover

Here, we first investigate the asymmetrical HDMW to evaluate the insertion loss reduction of the through guide. Then a symmetrical HMDW crossover is studied.

7.3.1 Asymmetrical HMDW crossover

A schematic representation of the asymmetrical HMDW crossover is shown in Figure 7.5 (a). Material losses are excluded in the simulation. A fraction of EM waves (Ic) leaks into the orthogonal guide and mode conversion occurs. Once the leaking EM waves in the coupled LSE_{11}^{z} mode reach the bilateral interfaces between the DW and NRD guide along the orthogonal guide, they are reflected back (R_c) to the intersection due to the mode incompatibility. This significantly reduces the crosstalk associated with the coupled LSE_{11}^{z} mode. In simulation, wave ports are assigned at P1/2/3/4. Wave port at P1/2 has a dimension of $2w \times h$, whereas wave port at P3/4 has a dimension of $4w \times 4h$.

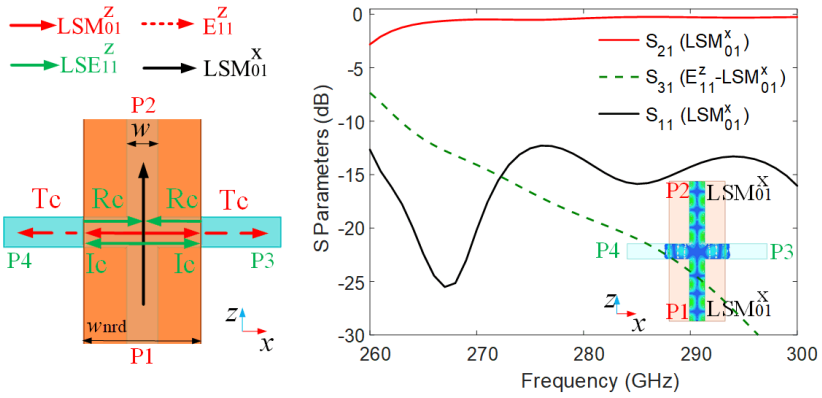

(a)

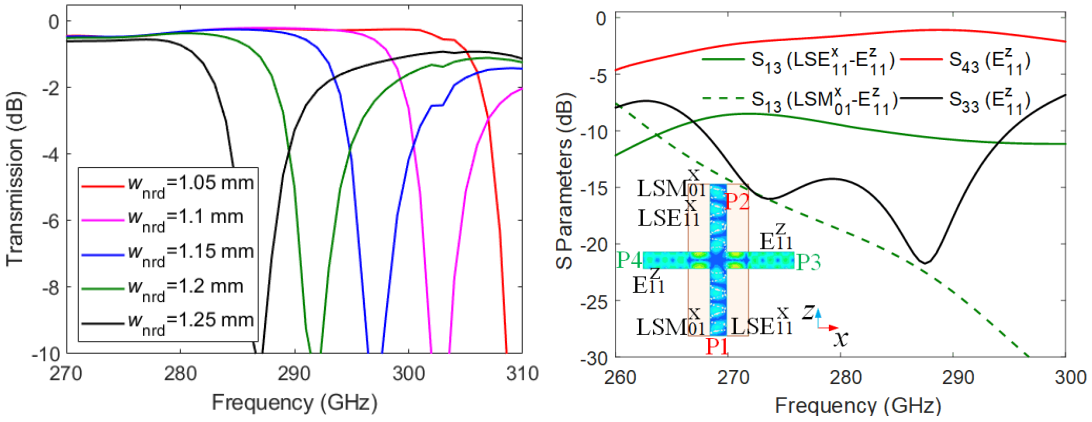

(b) (c)

Figure 7.5 (a) Simulated performance of the asymmetrical hybrid metallo-dielectric waveguide (AHMDW) crossover, inset: simulated electric field at 280 GHz when P1 is excited by LSM_{01}^{x} mode. (b) transmission performance of the through guide versus NRD stub length (orthogonal NRD guide length), (c) simulated performance when P3 is excited by E_{11}^{z} mode, inset: simulated electric field at 280 GHz

The average insertion loss from P1 to P2 is 0.37 dB from 268 GHz to 300 GHz (average of 1.5 dB for the NRD waveguide and DW crossovers), with a maximum of 0.54 dB at 268 GHz (maximum of 1.95 at 268 GHz for NRD waveguide and DW crossovers), which includes reflection loss and the unsuppressed crosstalk associated with LSM_{01}^{z} mode. The orthogonal HMDW works as a pair of open stubs for the through guide. The length of the orthogonal NRD guide should be carefully designed to avoid the presence

of a stopband in the band of interest [235], [236], as shown in Figure 7.5 (b). From 260 GHz to 268 GHz, the insertion loss from P1 to P2 is higher than 0.5 dB. As suggested by the green dashed line in Figure 7.3, the coupled LSM_{01}^{z} mode becomes dominant in the frequency band from 260 GHz to 268 GHz. The coupled EM waves in LSM_{01}^{z} mode pass through the interfaces between the NRD and DW, propagate in the orthogonal DW in E_{11}^{z} mode (Tc in Figure 7.5 (a)), resulting in high crosstalk from P1 to P3/4 and thus causing high insertion loss from P1 to P2.

For the asymmetric HMDW crossover with hybrid waveguide architecture only applied to the orthogonal guide, leakage from P3/4 to P1/2 still happens. The E_{11}^{z} mode in the orthogonal DW converts to the LSM_{01}^{z} mode in the orthogonal NRD guide, then excites the LSE_{11}^{x} and LSM_{01}^{x} modes in the through NRD guide, leading to high crosstalk, as shown in Figure 7.5 (c). Hybrid waveguide architecture needs to be applied to the through guide to reduce the leakage from P3/4 to P1/2.

7.3.2 Symmetrical HMDW crossover

The results of the symmetrical HMDW crossover are shown in Figure 7.6. A pair of parallel metal layers with w_{nrd} = l_{nrd} = 1 mm sandwich the dielectric waveguide intersection. The E_{11}^{x} mode is assigned at P1 in the simulation. All material losses are excluded in simulation. The symmetrical HMDW crossover has an average insertion loss of 0.37 dB from 275 GHz to 300 GHz, with maximum value of 0.86 dB at 275 GHz, from P1 to P2. The crosstalk from P1 to P3/4 is less than -20 dB from 275 to 300 GHz. A relatively poor transmission from P1 to P2 in the frequency band from 260 GHz to 275 GHz is related to a high crosstalk from P1 to P3/4 (green solid line in Figure 7.6 (b)) and a poor HMDW transmission (blue solid line in Figure 7.6 (b)) caused by impedance mismatch (blue dashed line in Figure 7.6 (b)) between the DW and the NRD guide at the lower operating frequency end [195]. Improving the matching condition of the HMDW architecture through parasite structures can enhance the performance of the hybrid waveguide crossover at the lower frequency end and moderately increase the

bandwidth. Any attempt to suppress the coupled LSM_{01}^{z} mode to further enlarge the bandwidth will simultaneously affect the performance of the orthogonal guide.

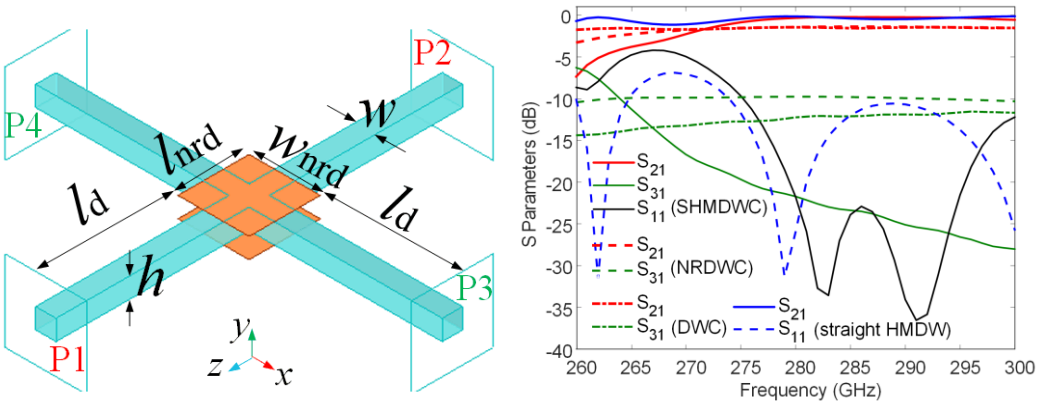

(a) (b)

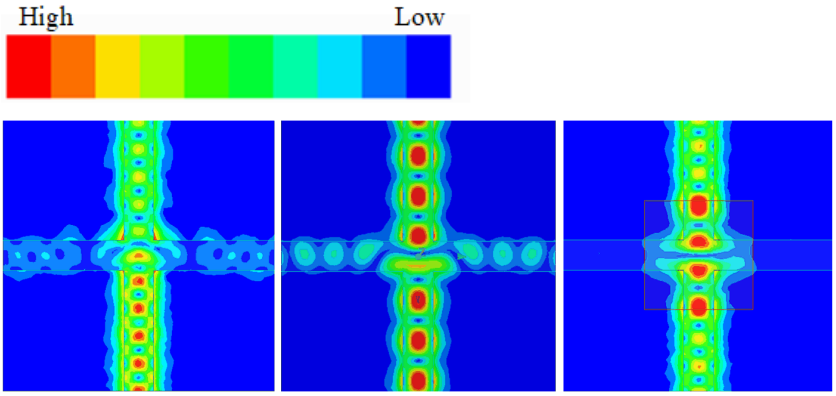

(c)

Figure 7.6 Simulation of the symmetric HMDW crossover. (a) Model, (b) performance, (c) electric field of DWC (left, P1 is excited by E_{11}^{x} mode), NRDWC (middle, P1 is excited by LSM_{01}^{x} mode) and the proposed HMDWC (right, P1 is excited by E_{11}^{x} mode)) at 280 GHz. Symmetrical HMDW crossover is called SHMDWC in Figure 7.6 (b) legend for short, DW crossover is called DWC, NRD waveguide crossover is called NRDWC

The performance of a DW crossover and an NRD crossover with the same waveguide width is given in Figure 7.6 (b) for comparison. It suggests that the NRD waveguide and DW crossovers are subject to a level of crosstalk of about 10 dB and 12 dB within the band of interest. The insertion loss is about 1.5 dB. Compared to DW and NRD

waveguide crossover, the insertion loss from P1 to P2 has been reduced by 1.13 dB with the hybrid waveguide architecture. The simulated electric field distributions of DW crossover, NRD waveguide crossover and the proposed hybrid crossover are plotted in Figure 7.6 (c) for reference.

The performance of a straight hybrid waveguide without intersection is given in Figure 7.6 (b) for reference. The proposed hybrid crossover has a comparable transmission performance to the straight HMDW, suggesting that the intersection introduces a negligible loss from P1 to P2. It is worth mentioning that the HMDW crossover has a higher loss than a straight dielectric waveguide without discontinuity since the HMDW architecture itself has certain reflection losses and radiation losses [195]. Nevertheless, the HMDW crossover offers a simple alternative solution when intersecting multiple path becomes inevitable in a system.

7.3.3 Simulation model of symmetrical HMDW crossover with material losses and feeding losses

When the material losses are considered, the transmission improvement realized by hybrid waveguide architecture would be degraded because NRD waveguide has a higher loss than DW. The dielectric loss of DW can be approximated with the use of [120] by assuming that most waves are confined inside the dielectric core. The loss of NRD waveguide can be calculated with the use of [209]. As shown in Figure 7.7, the NRD waveguide has a higher dielectric loss and additional conductor loss than the DW. The surface roughness of metal layers would further increase the NRD insertion loss.

The prototype of the proposed crossover with supporting structure and feeding structure is shown at the left of Figure 7.8 (a). Alumina with $\varepsilon_r = 9.8$, thickness of $h = 0.254$ mm and tan $\delta = 0.001$ is used in simulations. Conductivity of gold layers over the intersection is set as $\sigma = 4.1\times10^7$ S/m. Surface roughness is not considered. The crossover with width of $w = 0.28$ mm is suspended by perforated arms (air hole perforation is the same as that in [209]) at four ends. Taper with a designed length of l_t

= 3.5 mm is added at each end to smoothly couple the EM waves from rectangular waveguide into dielectric. A two-piece aluminum housing is designed for supporting the alumina piece during measurement, as shown at the right of Figure 7.8 (a). Four trenches with a length of 10 mm at four sides of housing are machined to enclose the fragile matching tapers. The trenches are made to fit with standard WR3-band rectangular waveguide with dimensions of 0.86 mm × 0.43 mm at one end (Figure 7.8 (b)), and to achieve a good match at the other end [132]. Conductivity of the aluminum housing is set as $\sigma = 3.8 \times 10^7$ S/m in the simulation. A DW crossover (without metal layers over the intersection) is simulated for comparison.

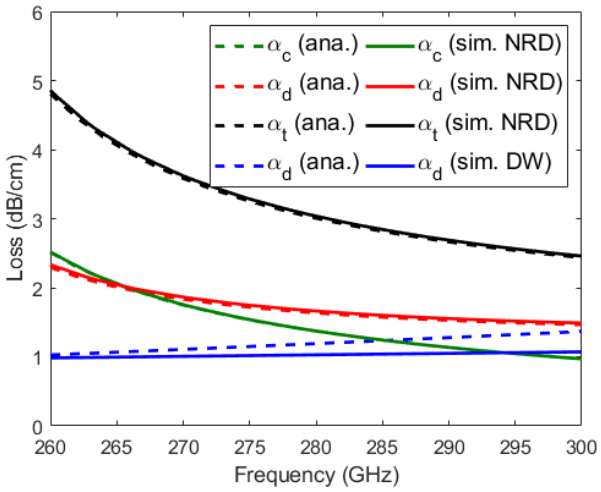

Figure 7.7 Loss of DW and NRD waveguide with a cross-section with $h = 0.254$ mm, $w = 0.28$ mm and $\varepsilon_r = 9.8$. The loss tangent of alumina is set as $\tan \delta = 0.001$, conductivity of metal layers (gold) is set as $\sigma = 4.1 \times 10^7$ S/m. The letters c, d and t refer to conductor, dielectric and total losses, respectively

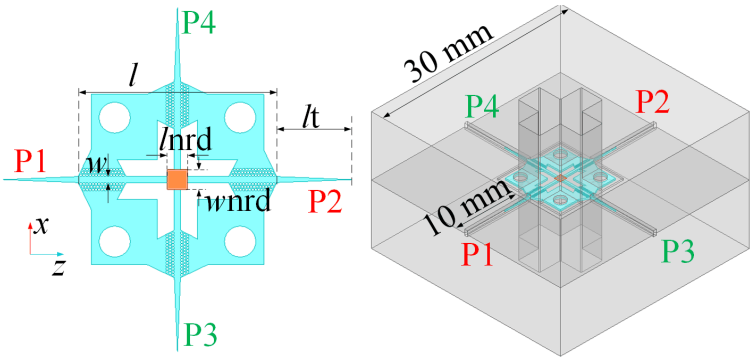

(a)

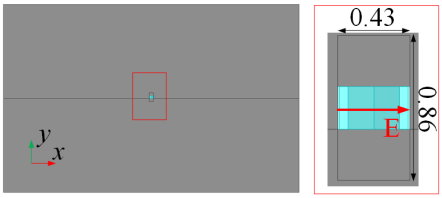

(b)

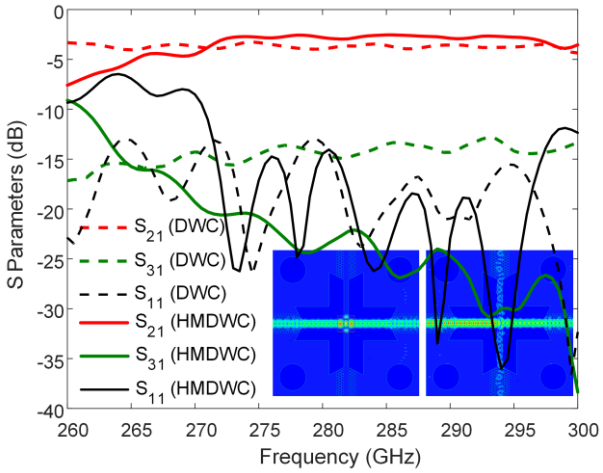

(c)

Figure 7.8 (a) Simulation model of the proposed crossover with supporting and feeding structure, (b) details of feeding port of the aluminum housing, unit in mm, (c) simulated performance, inset: simulated electric field of the crossover with (left) and without (right) metal layers over intersection when P1 is excited at 280 GHz

Comparison between the proposed hybrid waveguide crossover and DW crossover in Figure 7.8 (c) suggests that the crosstalk from P1 to P3/4 has been reduced from order

of -13 dB to -21 dB after adding two metal layers over the intersection .The electric field of the crossover with/without metal layers are given as inset of Figure 7.8 (c), suggesting that the EM wave can be well guided in the through guide from P1 to P2 with assistance of metal layers.

7.4 Alternative validation strategy: two-port device with intersection

To measure the crosstalk from P1 to P3/4, well preformed twists are required, which would increase the measurement complexity and uncertainty. Instead of measuring all four ports, the proposed topology for reducing crosstalk can be verified by measuring the performance of the transmission performance of the through guide if the orthogonal guide is properly terminated. In this section, the two ports of the orthogonal guide are left unterminated and the orthogonal guide is tapered at two ends. Meanwhile, to ensure the transmission improvement is visible in experiment, multiple intersections are introduced.

7.4.1 Unterminated tapered orthogonal waveguide arms

If the two intersecting guides were independent, the terminations of the orthogonal guide would not affect performance the through guide. For example, leaving the two ports of the orthogonal guide unterminated, as shown at the left of Figure 7.9 (a), would not affect the performance of the through guide when the two intersecting guides are independent. However, in Figure 7.9 (b), represented by the solid blue line, two ripples on S_{21} are observed. Although the dominant crosstalk from P1 to P3/4 associated to the LSE_{11}^{z} mode is suppressed by the interfaces between NRD and DW, a small portion of crosstalk in the LSM_{01}^{z} mode is coupled into the orthogonal DW guide and is eventually reflected back from the truncated end of the DW to the NRD intersection, thereby affecting the performance of the through guide. For the case of the hybrid crossover where the two intersecting guides are dependent, properly terminating the orthogonal guide is needed.

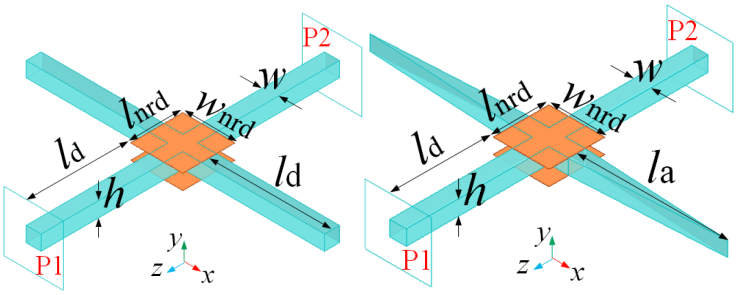

(a)

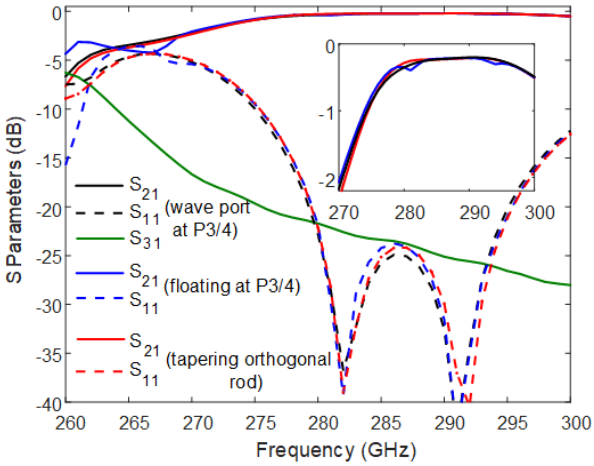

(b)

Figure 7.9 (a) Simulation model of the proposed crossover with P3/4 unloaded (left) and with the orthogonal dielectric rod tapered at two ends (right), (b) performance of the through guide from P1 to P2 with the orthogonal dielectric guide loaded with wave ports, unloaded and tapered. h = 0.254 mm, w = 0.28 mm, l_{nrd} = w_{nrd} = 1 mm, l_d = 2 mm, l_a = 2 mm. E_{11}^x mode is assigned

Instead of using the wave ports at P3/4 to measure the remaining crosstalk, one could taper the orthogonal dielectric guide at two ends, as shown at the right of Figure 7.9 (a) to radiate the EM waves. The coupled LSM_{01}^z mode in the orthogonal NRD guide converts to the E_{11}^z mode in the orthogonal DW guide. By tapering the orthogonal dielectric strip, the coupled EM waves in E_{11}^z mode can be eventually radiated because the narrow dielectric strip is not able to guide the mode [192], [234]. The two dielectric tapers function as two dielectric rod antennas [237][238][239][240]. As a result, the

two ripples on the S_{21} curve vanish. In summary, leaving the orthogonal guide unterminated and then tapering it at both ends hardly affects the performance (transmission and reflection) of the through guide of the proposed HMDW crossover, thereby facilitating the measurements.

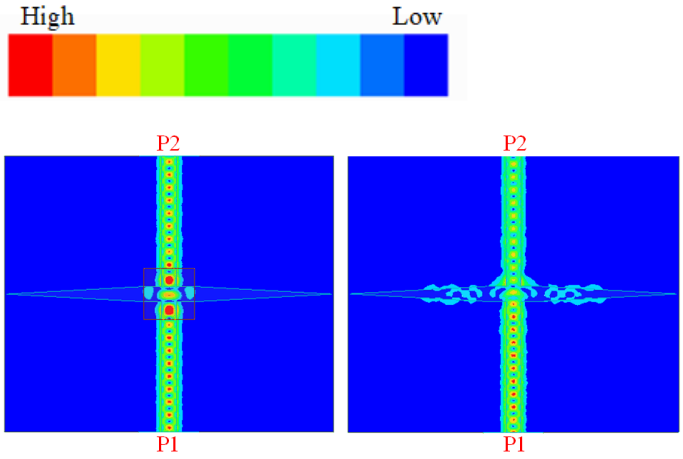

Figure 7.10 Electric field distributions of two-port device intersected with tapered orthogonal dielectric rod with (left) and without (right) two metal plates at the intersection at 280 GHz. E_{11}^{x} mode is assigned at P1

The average insertion loss of the two-port device with single intersection is 0.33 dB from 275 GHz to 300 GHz, with a maximum value of 0.88 dB at 275 GHz. It includes reflection loss caused by the mismatch between the through DW and the through NRD guide, reflection loss caused by the intersection itself and radiation loss radiated by two bilateral tapered orthogonal dielectric rods (residual crosstalk caused by the coupled LSM_{01}^{z} mode). The simulated field distributions are plotted in Figure 7.10, suggesting that the leakage into the orthogonal dielectric strip can be significantly reduced by applying the HMDW architecture over the intersection.

7.4.2 Two-port device with four intersections

The performance improvement achieved by the hybrid waveguide architecture is mitigated when considering material losses in THz band. To better observe the performance improvement, four identical and evenly distributed intersections are

cascaded and introduced as depicted in Figure 7.11 (a). The distance of *dis* = 0.75 mm between adjacent intersections is optimized by simulation to avoid transmission zeros in the frequency band of interest. All four orthogonal NRD strips are terminated by tapered dielectric rods with a length of l_a = 2 mm. A pair of parallel gold plates with a conductivity of $\sigma = 4.1 \times 10^7$ S/m and with dimensions of l_{nrd} = 3.25 mm and w_{nrd} = 1 mm cover all intersections. The two-port device is bilaterally supported by perforated arms. Two tapers with a designed length of l_t = 3.5 mm are added for impedance matching between the DW and the air-filled rectangular waveguide. A two-piece aluminum housing is designed for measurements, as shown in Figure 7.11 (b). Two trenches are machined inside the aluminum housing to enclose the two matching tapers. The dimension of feeding ports is the same as that given in Figure 7.8 (b). Conductivity of the aluminum housing is set to $\sigma = 3.8 \times 10^7$ S/m in the simulation. Surface roughness is not included at this stage.

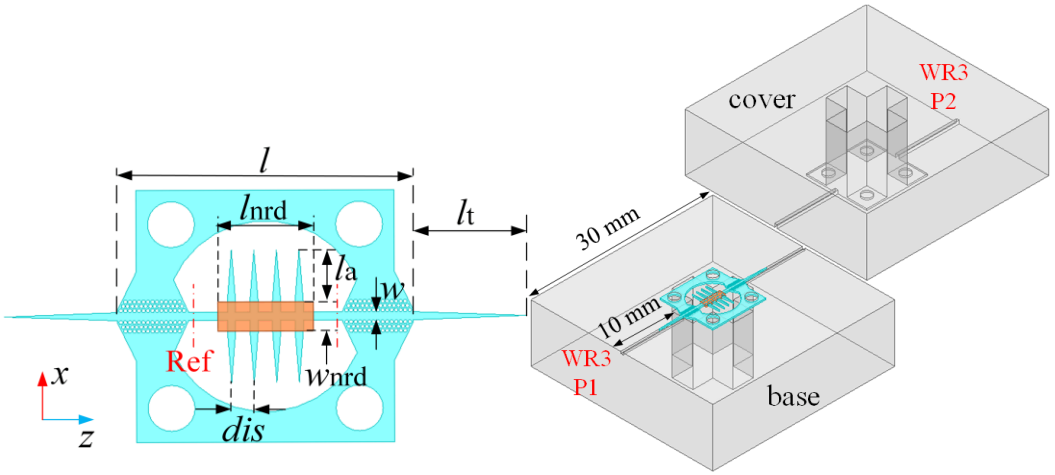

(a) (b)

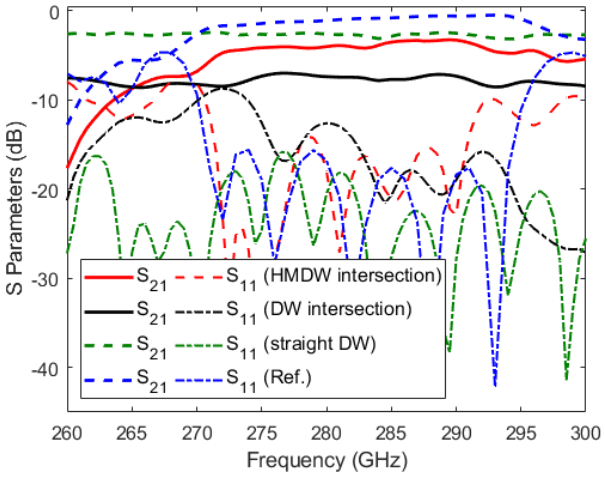

(c)

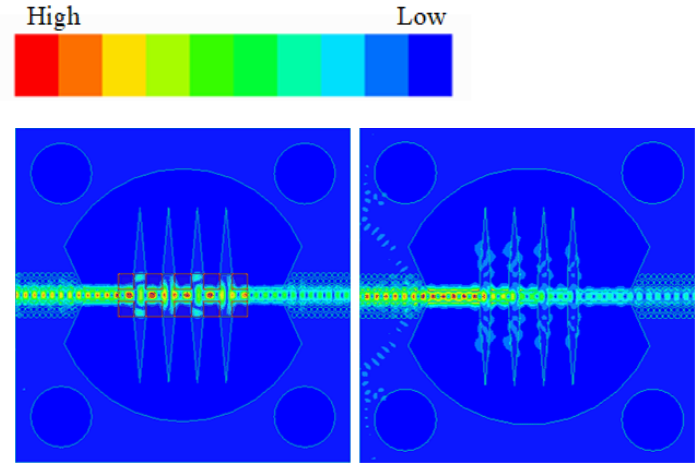

(d)

Figure 7.11 (a) Simulation model of the presented back-to-back device with four intersections with metal plate covering, (b) exploded view of aluminum housing for enclosing the fragile alumina structure, (c) simulated transmission performance, (d) electric field of the two-port device with four cascading intersections covered by two metal layers (left) and not covered (right) at 280 GHz. The blue dashed line is the transmission between two reference planes indicted with red dot-dashed line in Figure 7.11 (a) without considering material losses. Four intersections only introduce 0.5 – 1.7 dB of structural loss (including leakage and reflection loss) from 272 GHz to 295 GHz with the assistance of metal layers

The simulated results in Figure 7.11 (c) show that the two-port device with four intersections has an average insertion loss of 4.1 dB from 272 GHz to 295 GHz, with a maximum of 4.7 dB at 272 GHz and a minimum of 3.3 dB at 289 GHz. Compared to the transmission performance of a straight two-port DW without intersection (green dashed line in Figure 7.11 (c)), introducing four intersections adds an extra loss of 1 - 2.3 dB including reflection loss, leakage loss associated with the coupled LSM_{01}^{z} mode and the conductor loss of the two metal layers. The device exhibits better transmission performance at the higher frequency end than at the lower frequency end. Indeed, the leakage into the orthogonal tapered dielectric rods, caused by the coupled LSM_{01}^{z} mode, decreases with increasing frequency, as indicated by the green solid line in Figure 7.8 (c). Also, the conductor loss of the NRD guide in the LSM_{01}^{x} mode decreases as frequency increases, as shown in Figure 7.7 [209].

For its DW counterpart (without metal layers covering) the through guide with four intersections has an insertion loss about 7.5 dB from 272 to 295 GHz, with a maximum of 8.55 dB at 293 GHz and a minimum of 7 dB at 276.5 GHz. The simulated electric field plotted in Figure 7.11 (d) shows that it is difficult for EM waves to leak into the eight vertically oriented tapered dielectric rods, thanks to the presence of the two metal layers.

7.5 Fabrication and measurement

The two-port device with four intersections was fabricated by laser drilling at Poly-Grames Research Center, as shown in Figure 7.12 (a). The actual dimensions of the fabricated prototype are given in Figure 7.12 (b). A two-piece aluminum housing for measurements was fabricated by CNC milling, and the cover is shown in Figure 7.12 (c). Two metal blocks, each with a width of 1.13 mm and a length of 3.35 mm, and a gap of 0.254 mm between them, serving as the metal layers of NRD guide, were integrated into the aluminum housing. To avoid any spurious mode of a vertically unsymmetrical NRD guide (related to a potential asymmetrical air gaps between the dielectric core and the two metal surfaces offered by the two metal blocks integrated

into the aluminum housing) [241], the alumina substrate is pre-metallized with gold at the NRD section, as shown in Figure 7.12 (a). The two-port device was then placed into the designed aluminum housing and aligned with dowel pins at corners, as shown in Figure 7.12 (d). The two fragile tapers for matching were enclosed by the trenches inside the aluminum housing. The measured dimensions of the fabricated prototype are listed in Table 7.1. Simulated model is modified based on the measured dimensions.

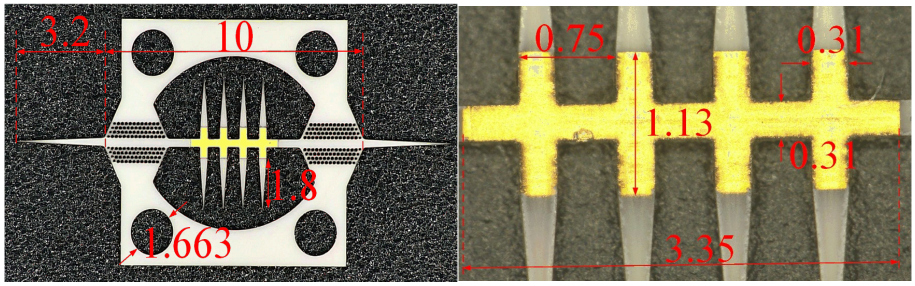

(a) (b)

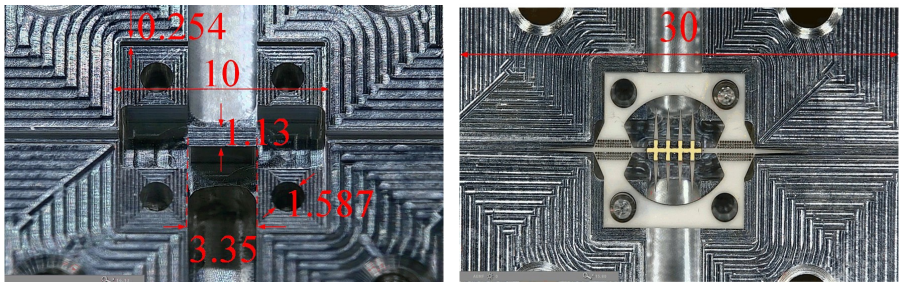

(c) (d)

Figure 7.12 (a) Experimental prototype of two-port device with four intersections, (b) dimension details, (c) cover of aluminum housing for measurement, (d) assembled with the base of aluminum housing. Unit in mm

Table 7.1 Important parameters of proposed HMDW with four intersections

Symbol	Description	Measured value
w	width of center unperforated dielectric core	0.31 mm
w_{nrd}	width of metal blocks (metal layers) covering four intersections	1.13 mm

l_{nrd}	length of metal blocks (metal layers) covering four intersections	3.35 mm
l_a	length of orthogonal dielectric tapers	1.8 mm
dis	distance between two adjacent intersections	0.75 mm
l	length of the through guide	10 mm
l_t	length of the matching tapers	3.2 mm
tan δ	loss tangent of alumina	0.001*
σ_{Al}	conductivity of aluminum housing	1.1×10^7 S/m*

*these values where obtained by curve fitting.

The surface roughness can significantly decrease the conductivity of the metal, and then increase the conductor loss of the guide when it is comparable to the skin depth [186][242]. The surface roughness of the aluminum housing was measured by a DekTak surface profiler, shown in Figure 7.13 as inset. The roughness is about 100 nm which is comparable to the skin depth at the band of interest (for example, 148.5 nm for 280 GHz). A straight rectangular metallic waveguide (aluminum) with a designed dimension of 0.86 × 0.43 mm is made by CNC machining with a manufacturing tolerance of 12 um and measured to evaluate the losses introduced by the aluminum housing. The results in Figure 7.13 indicate that an effective conductivity of σ_{Al} = 1.1 $\times10^7$ S/m can fit the insertion loss introduced by the aluminum housing in the band of interest. Understanding the exact causes of insertion loss introduced by the metallic waveguide (impurity, tolerances, metal-to-metal contact, offsets, etc.) is outside the scope of the work.

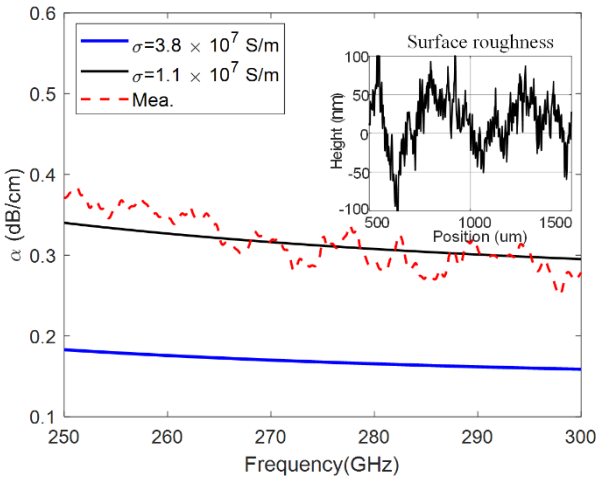

Figure 7.13 Comparison between measured losses (dashed red) and analytical losses (based on perturbation method in [56]) of aluminum rectangular waveguide with a designed dimension of 0.86 mm × 0.43 mm

The surface roughness profile of the alumina was evaluated with a DekTak surface profiler, as shown in Figure 7.14. It suggests that the surface roughness is much larger than the skin depth in the band of interest. Huray surface roughness model [234] in HFSS, is used to evaluate the additional losses related to the surface roughness of metallic coating on substrate. The two parameters in the surface roughness model dialog box are set as a = 0.5 um (radius of a spherical nodule) and surface ratio (SR) = 1.18. The SR is selected based on the measured surface profile in Figure 7.14 [243]. Simulated results are plotted in Figure 7.15. The operating frequency band is slightly shifted to lower frequency band from 262 GHz to 288 GHz (the designated band from section III is from 272 GHz to 295 GHz) due to manufacturing tolerances of the laser cutting process resulting in an increase in the actual size of the fabricated prototype. The average insertion loss is about 4.8 dB in band, with a maximum of 5.5 dB at 288 GHz and a minimum of 4.2 dB at 278 GHz.

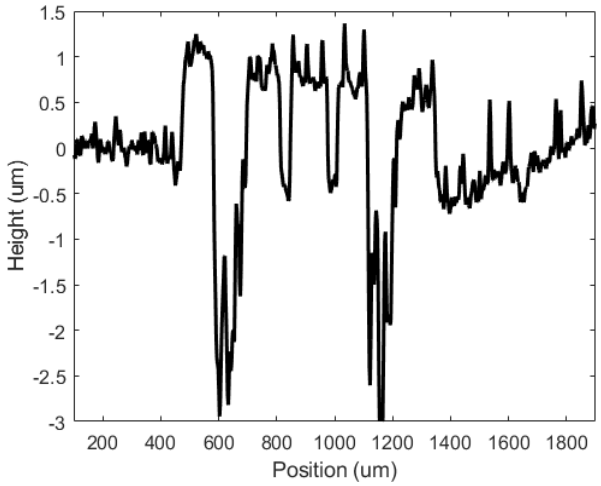

Figure 7.14 Measured surface roughness profile of alumina substrate

A PNA-X network analyzer N5247A, with a pair of WR3-band Virginia Diodes Inc., (VDI) frequency extenders, was used to measure the S-parameters, with a short-open-load-through (SOLT) calibration. The measured results are given in Figure 7.15. The measured average insertion loss is around 5.5 dB from 262 GHz to 286 GHz.

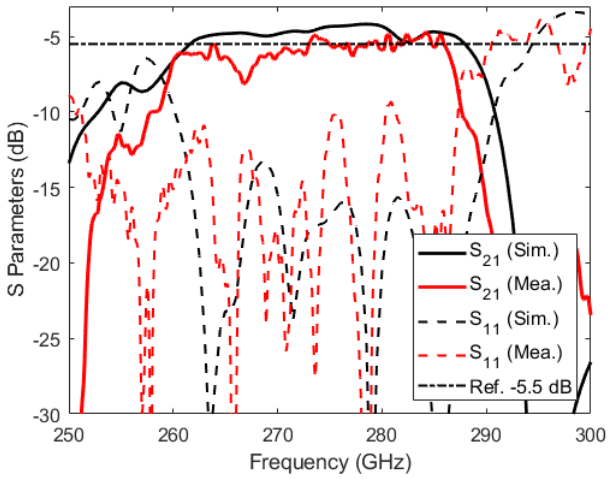

Figure 7.15 Simulated and measured results of two-port device with four intersections covered by metal layers. Simulated results are based on a modified model with the measured size of the fabricated prototype in Figure 7.12

7.6 Discussion

Due to the tolerance of the laser cutting, the dielectric waveguide is fabricated wider, resulting in all modes moving lower in frequency. The wider metal layers also cause

unexpected transmission zero moving lower in frequency. As discussed in Figure 7.5 (b), the reflected EM waves from the interfaces at the orthogonal guide would affect the transmission of the through guide. As the same for the hybrid two-port device with four orthogonal dielectric rods, the reflected EM waves from the interfaces at the orthogonal dielectric rods would affect the transmission of the two-port device. In the designed prototype, the width w_{nrd} = 1 mm of the metal layers is selected to avoid the unwanted transmission zero in the band of interest. Transmission zero appears at 295 GHz (out of the band of interest from 252 GHz to 288 GHz for the practical prototype) in both simulation and measurement of the experimental prototype with w_{nrd} = 1.13 mm. A parametric study on the width of NRD is shown in Figure 7.16. It shows that the transmission zero moves lower in frequency, from 294 GHz to 280 GHz when increasing NRD width from 1.13 mm to 1.27 mm.

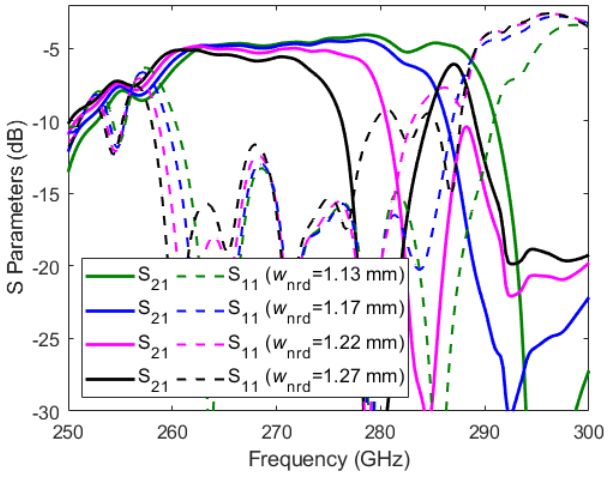

Figure 7.16 Effect of width of the metal layers on the performance of the two-port device

From Figure 7.15, one can notice a spurious at 266.8 GHz. It will be shown next that this spurious is caused by misalignment between the gold metal layer and the aluminum housing. Indeed, the aluminum housing is rotated 90 degrees for measuring with the VDI extenders, which causes the alumina circuit to slightly move in the housing, as illustrated in Figure 7.17 (a). The offset off_x shown on the left side Figure 7.17 (b)

causes spurious transmissions. The effect of the offset off_x is shown in Figure 7.18 (a). The results indicate that a transmission spurious appears at 264 GHz when off_x is 0.381 mm. The horizontal offset off_z has a minor effect on the two-port device transmission performance, as shown in Figure 7.18 (b). The effect of the tilt, illustrated in Figure 7.17 (b, right) is studied in Figure 7.19. The laser cutting can also lead to an imperfect matching taper, as shown in Figure 7.20. However, this effect is minor on the S parameters. Overall, the lateral offset and the tilt of the alumina circuit, in addition to surface roughness have the most important effects on the S parameters.

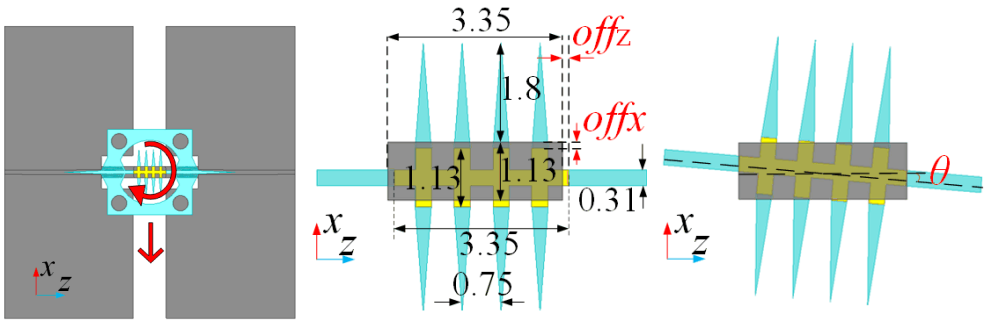

(a) (b)

Figure 7.17 (a) Schematic of a potential displacement of alumina circuit inside the aluminum housing, (b) potential offset or rotation between the alumina circuit and the aluminum housing during measurement. Unit in mm

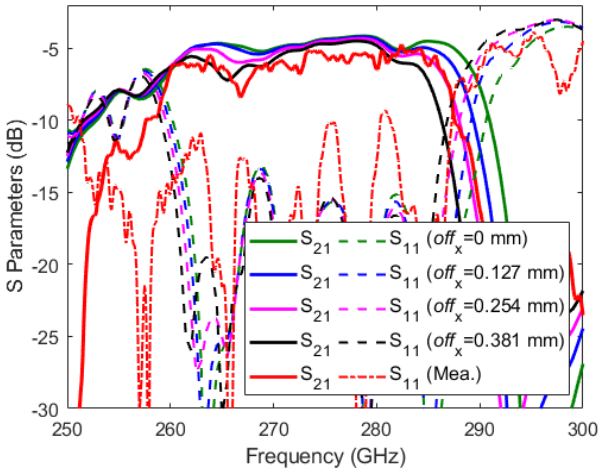

(a)

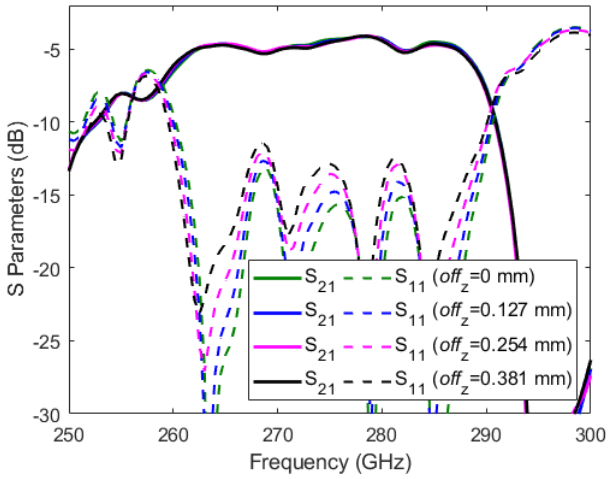

(b)

Figure 7.18 Offset effect of the alumina circuit in the aluminum housing on the simulated performance of the two-port device. (a) off_x, (b) off_z

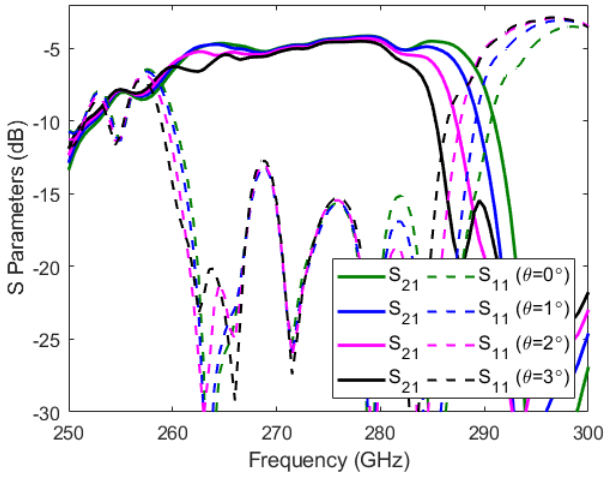

Figure 7.19 Tilt effect of the alumina circuit with respect to the aluminum housing on the simulated performance of the two-port device

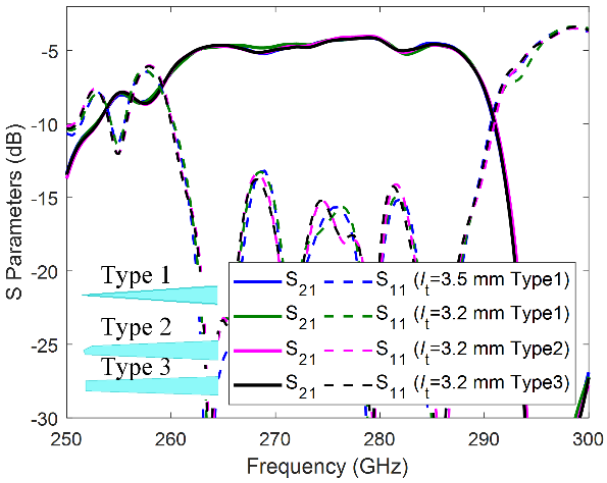

Figure 7.20 Effect of imperfect matching taper of the alumina circuit on the simulated performance of the two-port device

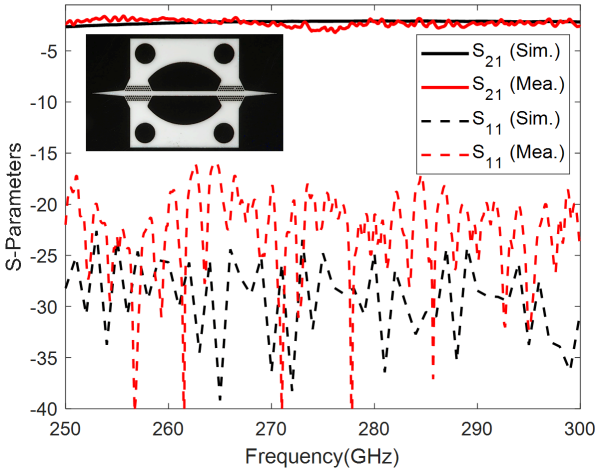

Figure 7.21 Simulated and measured results of two-port straight dielectric waveguide operating in E_{11}^{y} mode. $\varepsilon_r = 9.8$ and $\tan\delta = 0.001$ are used for alumina in the simulation

A back-to-back straight dielectric waveguide without intersections is fabricated and measured as a reference. The measured insertion loss is about 2.46 dB (about 2.2 dB in simulation with considering the surface roughness of the aluminum housing) in the frequency band from 250 GHz to 300 GHz, as given in Figure 7.21, with a maximum of 3.4 dB at 276 GHz. This enables us to confirm the loss tangent of the alumina circuit of $\tan\delta = 0.001$ and $\varepsilon_r = 9.8$ in simulation can well predict the performance of the

dielectric waveguide. The roughness caused by the laser drilling has been taken into account.

According to Figure 7.18 (a) and Figure 7.19, the bilateral offset and the tilt of alumina circuit can explain the spurious frequency response at 266.8 GHz and the transmission degradation after 286 GHz. However, the measured transmission is 0.7 dB lower than the simulated one. One possible factor is the non-ideal cross-section fabricated by laser drilling. Indeed, the bottom part of the circuit is slightly narrower than the top, due to the laser beam profile, giving a trapezoid shaped cross-section rather than an ideal rectangular shaped one. A 1 mil (0.0254 mm) narrower of width of dielectric strip at the backside would increase the conductor loss of NRD waveguide [209]. The asymmetry introduces an additional radiation loss. The simulated results are plotted in Figure 7.22. The blue solid line representing the transmission of the two-port circuit with trapezoid shaped cross section is lower than that of the green dashed line. The difference is more pronounced at lower frequency end because of the conductor loss of the NRD waveguide [209]. The simulation model, considering the non-ideal cross section of dielectric strip and the potential misalignment, reproduces well the S_{21} measurement, as shown in Figure 7.22.

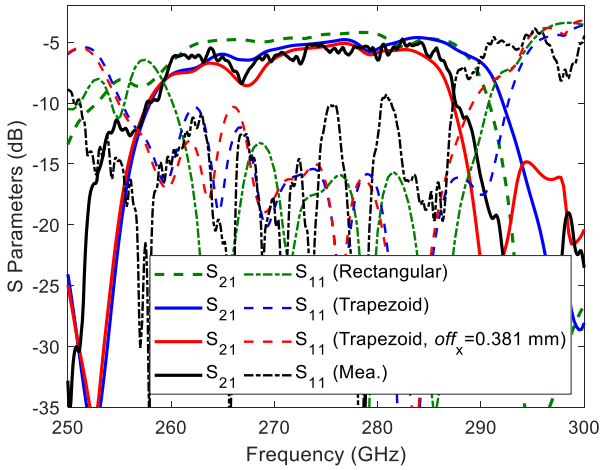

Figure 7.22 Comparison between the simulated results of the two-port device with rectangular and trapezoid shaped cross section and measured results

7.7 Conclusion

The proposed hybrid metallo-dielectric waveguide (HMDW) crossover in this work is beneficial for low-loss compact THz circuits and systems. Non-radiative dielectric (NRD) waveguide, allowing for discontinuities, is used at intersections to eliminate radiation leakage or loss. Dielectric waveguides (DWs) are used at discontinuity-free sections to minimize conductor loss. Furthermore, the HMDW architecture enhances the independence of two intersecting transmission paths by leveraging the mode conversion at the NRD waveguide intersection and the mode selectivity of the HMDW architecture. The proposed hybrid structure has been applied to a two-port device with four intersections. The application of the NRD waveguide at the intersection markedly improves the transmission performance by preventing the EM waves from leaking into orthogonal guiding structures. The simple principle and structure of the proposed HMDW crossover and intersection facilitate its implementation, which is critical for the fabrication of high-density integrated THz circuits and systems. Although the hybrid waveguide architecture would introduce extra conductor losses because of the present of metal layers, it allow flexibly intersecting multiple transmission paths, enabling simple and clean circuit layouts.

CHAPTER 8 CONCLUSION AND FUTURE WORK

8.1 Conclusion

The hybrid waveguide solution that combines the advantages of various waveguide types shows great promise for the development of low-loss, compact THz integrated circuits and systems. In this work, I proposed and demonstrated a hybrid metallo-dielectric waveguide architecture consisting of NRD waveguides and DWs. This innovative approach facilitates the design of compact circuits while leveraging the advantages of both waveguide types, ultimately enhancing performance in THz applications.

- In Chapter 3, I have designed, fabricated, and measured an SINRD waveguide constructed from an as-fired alumina substrate with a thickness of 0.254 mm. Air-filled rectangular WR3-band waveguides were employed to excite the LSM_{01} mode of the SINRD waveguide. To ensure proper impedance matching, two tapers were incorporated on either side of the SINRD waveguide, facilitating a seamless connection to the 10-mm-long rectangular waveguides. The SINRD waveguide demonstrated an average measured loss of approximately 3.5 dB across the band of interest, which includes contributions from conductor loss, dielectric loss, and feeding loss. Notably, the conductor loss of the SINRD waveguide decreases with increasing operating frequency, and polishing surface could further reduce conductor loss. For comparative analysis, an SIDW and an SIW were also designed and fabricated using the same material and measured within the same frequency band. Theoretically, the SIW exhibits a loss performance comparable to that of the SINRD waveguide; however, the metallization process for through air holes increases the cost and introduces additional uncertainties in performance. Measurement results indicate that the SINRD waveguide achieves more favorable transmission performance overall. Conversely, when compared to the SIDW, the SINRD waveguide exhibits higher losses due to the presence of two lossy metal layers. The demonstrated 10-mm-length SIDW recorded a measured loss of 1.8 dB.

- During the fabrication of the single-layer SINRD waveguide, a process-related

conflict arises between the air-hole perforation of the hosting substrate and the essential residual metallic coating within the perforated regions. Laser drilling is employed to intentionally create these perforations. The perforated areas exhibit a lower effective dielectric constant than the unperforated core, which facilitates the confinement of EM waves within the unperforated guiding core. A greater disparity in dielectric constants leads to a wider non-radiative bandwidth. However, achieving dense air-hole perforations compromises the structural integrity, increasing the risk of SINRD failure due to unintended ablation of the metal layer caused by laser overheating. To address this conflict, Chapter 4 proposed a double-layer SINRD waveguide. This design involved drilling two half-height alumina substrates separately while preserving the metal layer on the backside of each. The two layers were then stacked with their metallized side exposed. Theoretical analyses and simulations indicated that thin air gap between the two layers does not significantly degrade the transmission performance of the LSM_{01} mode. However, a discrepancy between simulation and measurement was observed, which can be attributed to misalignment between the two layers. Therefore, a high-precision alignment method is essential to minimize leakage and enhance overall performance.

- The study presented in Chapter 3 demonstrates that the SINRD waveguide exhibits higher loss compared to the SIDW. To optimize performance, it is advantageous to combine the SINRD waveguide and SIDW in the design of specific components, resulting in the substrate-integrated hybrid metallo-dielectric (SIHMD) waveguide, as discussed in Chapter 5. When integrating two different waveguides, coupling efficiency is a critical factor. Generally, long transitions are required to ensure a smooth transfer of EM waves from one guide to another, minimizing strong reflections. However, this can introduce additional path losses that may diminish the benefits of the hybrid design. Coupling between the SINRD waveguide and SIDW has been investigated. The LSM_{01} mode from the SINRD section can successfully traverse the interface

between the two waveguides with an average insertion loss of 0.15 dB across the frequency range of 260 to 330 GHz. A back-to-back SIHMD waveguide, measuring 10 mm in length, has been designed, fabricated, and measured. This configuration includes a short SINRD section approximately 5.5 guide wavelengths long at 300 GHz (1.75 mm), sandwiched between two SIDW sections. The measured average insertion loss of the back-to-back hybrid waveguide is approximately 2.4 dB, accounting for material losses, feeding losses, and insertion losses at the two interfaces. Although this hybrid waveguide exhibits slightly higher loss than the SIDW (1.8 dB), it significantly outperforms the SINRD waveguide, which has a loss of 3.5 dB.

- The hybrid waveguide architecture has been effectively employed in low-loss, compact circuits, with an initial focus on minimizing bend radius, as discussed in Chapter 6. NRD waveguides were implemented in the bending regions to prevent radiation leakage, while DWs were utilized in straight sections free from discontinuities to reduce conductor loss. The use of NRD waveguides allows for a reduction in bend radius by a factor of approximately 10. In contrast, EM waves struggle to propagate through DW bends with the same radius (0.19 λ_g at 280 GHz). This hybrid waveguide design facilitates the development of compact circuits and systems. However, the operational bandwidth of the hybrid bends is constrained due to mode conversion occurring at the NRD bends and the inherent mode selectivity in the hybrid waveguide structure.

- In Chapter 7, the proposed hybrid waveguide architecture has been leveraged to enhance crossover performance. Unlike the focus in Chapter 6, the mode conversion between the LSE_{11} and LSM_{01} modes of the NRD waveguide becomes crucial for minimizing crosstalk between two intersecting DWs. Another key aspect of this improvement is the mode selectivity inherent to the hybrid waveguide design. At the intersection of the two DWs, parallel metal layers were incorporated to create an NRD junction, which not only reduces

radiation loss but also mitigates crosstalk. At this NRD junction, mode conversion occurs; specifically, the LSM_{01} mode in the through guide can excite both the LSE_{11} and LSM_{01} modes in the orthogonal guide, leading to considerable crosstalk. The coupled LSE_{11} mode in the orthogonal guide is predominant, while the coupled LSM_{01} mode diminishes with increasing frequency. By utilizing the hybrid waveguide architecture, I can effectively suppress the coupled LSE_{11} mode in the orthogonal guide due to mode incompatibility. This results in a reduction of structural loss at the crossover by 1 dB compared to conventional DW and NRD crossovers. The proposed method is particularly advantageous in scenarios where multiple intersections are closely packed.

8.2 Future work

This Ph. D. work presents a hybrid solution for THz integrated circuits and systems. The proposed hybrid waveguide technology and its associated applications are set to emerge as significant areas of research. While the performance of the hybrid waveguide presented here is promising, practical implementations will likely require further efforts in the following aspects:

Hybrid metallo-dielectic waveguide divider

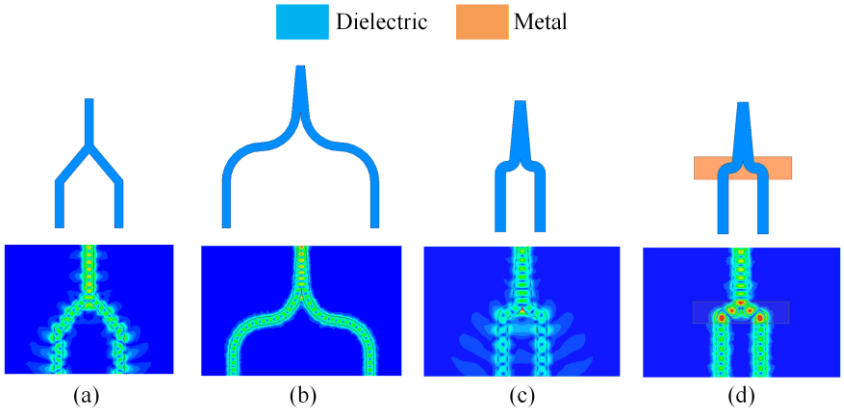

Figure 8.1 Structures (top) and electric field distributions (bottom) of dividers. (a) Y-shape dielectric waveguide (DW) divider, (b) DW divider with smooth bend transition, (c) compact DW divider, (d) hybrid metallo-dielectric waveguide (HMDW) divider

For NRD bends with very small bending radii, a pair of 90° bends are required to retrieve the LSM_{01} mode within certain bandwidth. We can find its applications in the design of compact dividers, as shown in Figure 8.1. It is necessary to emphasize that, when space allows and low-loss materials are used, DW dividers with smooth bends are preferred.

Mode suppressor

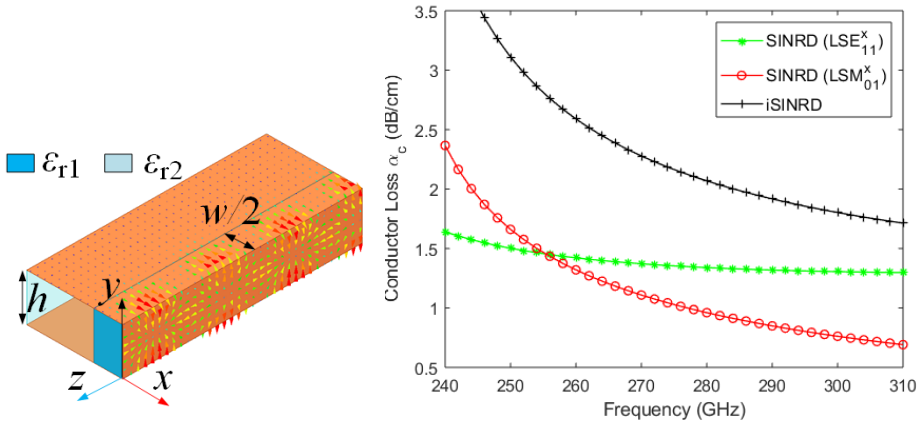

(a) (b)

Figure 8.2 (a) Image SINRD waveguide, (b) conductor loss of SINRD waveguide and iSINRD waveguide

Further research into effective mode management strategies is essential for optimizing mode conversion in complex configurations, particularly within densely packed circuits. This research should focus on designing specialized mode suppressors to mitigate the LSE_{11} mode in NRD bends, thereby increasing the bandwidth of hybrid bends. Inserting a vertical metal plane in the middle dielectric strip of SINRD waveguide can suppress the LSE_{11} mode without changing the cut-off frequency of the LSM_{01} mode, resulting in an image SINRD waveguide, as shown in Figure 8.2 (a). However, the inserted metal plane results in an increase in conductor loss, as shown in Figure 8.2 (b). Moreover, the surface roughness of metallized sidewall can dramatically degrade the transmission performance. New types of mode suppressors should be developed.

As the LSM_{01} mode has dominant transverse current J_t on the metal surfaces, etching a pair of transverse slots at both the top and bottom metal plates, as shown in Figure 8.3, will not affect the transmission performance of LSM_{01} mode. However, the LSE_{11} mode

cannot propagate through the locally exposed dielectric core, nor can the higher-order LSE_{21} mode. By doing so, the slotted SINRD waveguide only supports the non-radiative LSM_{01} mode. Compared to the iSINRD waveguide, the slotted SINRD waveguide is easier to fabricate because of its metallized-wall-free structure. Meanwhile, the low loss performance of SINRD waveguide while operating in the LSM_{01} mode remains.

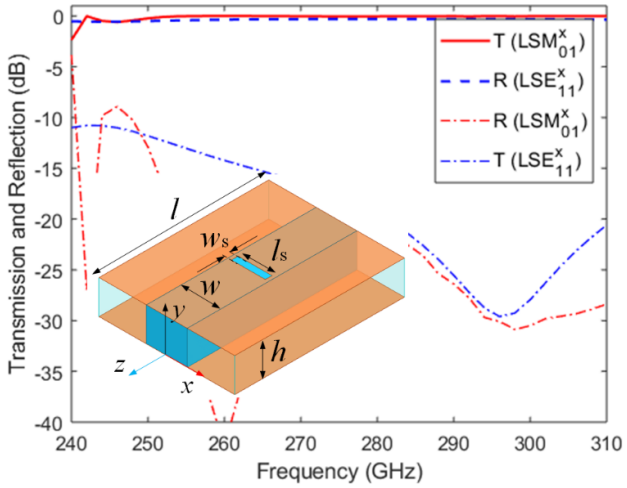

Figure 8.3 LSE_{11} mode suppressor based on mode selectivity

Mode suppressor in bend applications

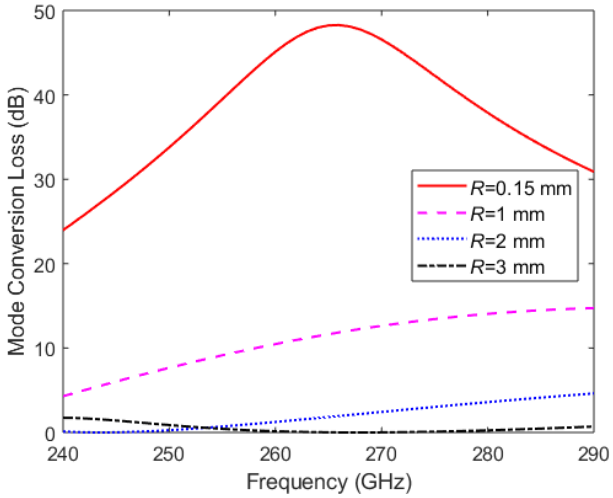

Figure 8.4 Mode conversion of NRD 90° bend

90° bends are essential in integrated circuits and systems for rerouting field propagation directions. However, mode conversion between the LSE_{11} and LSM_{01} modes occur within NRD bends, reducing the overall efficiency of circuits and systems. While

increasing the bend radius, as shown in Figure 8.4, can mitigate this mode conversion, it compromises the compactness and performance advantages that NRD waveguides offer.

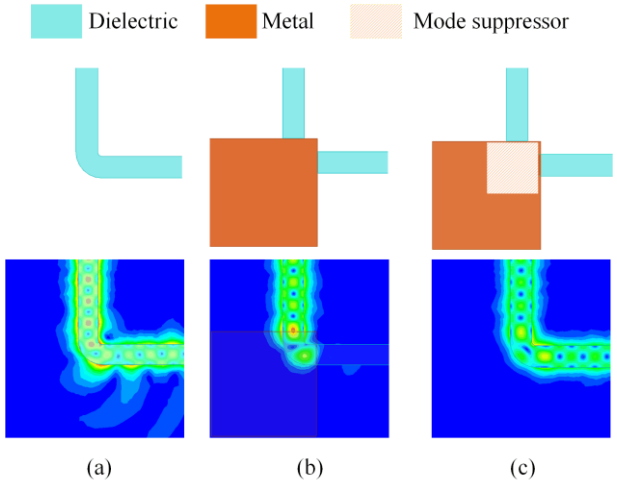

Figure 8.5 Structures (top) and electric field distributions (bottom) of 90° bends. (a) DW bend, (b) HMDW bend without mode suppressor, (c) HMDW bend with mode suppressor

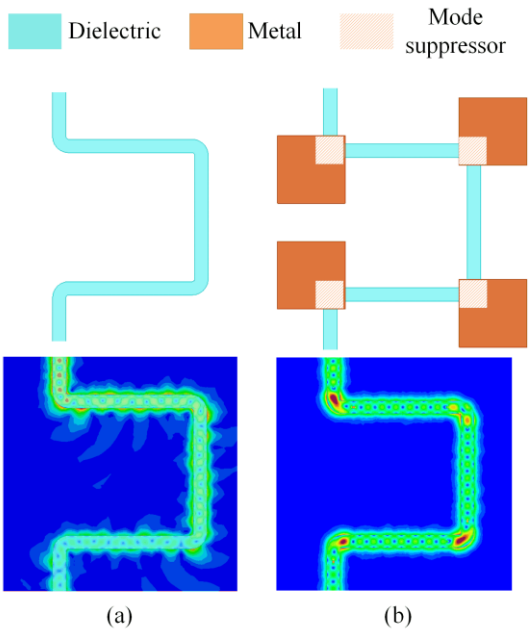

Figure 8.6 Routing EM waves (a) with DW bends and (b) with NRD bends

A mode suppressor is essential for maintaining the LSM_{01} mode, ensuring effective coupling of EM waves to the DW at the exit of a 90° NRD waveguide bend, as illustrated in Figure 8.5. By utilizing NRD waveguides over sharp bends, radiation

leakage can be effectively minimized. The mode suppressor guarantees the preservation of the LSM01 mode throughout the NRD waveguide bends, facilitating the smooth propagation of EM waves within the hybrid waveguide structure. Moreover, NRD waveguide bends can accommodate various radii, offering design flexibility. Since NRD waveguides occupy only a small portion of the overall waveguiding structure, as depicted in Figure 8.6, additional conductor losses associated with the metal layers of the NRD waveguide are unlikely to significantly impact overall power dissipation. This hybrid waveguide architecture demonstrates clear advantages in compact systems where components are densely integrated, enhancing performance while minimizing footprint.

Flexible interconnecting in large-scale integration

In large-scale integration, effectively interconnecting multiple modules is essential for optimizing performance and ensuring reliability. Traditional out-of-planar routing can introduce discontinuities, leading to signal loss and distortion, which is particularly problematic in high-fidelity applications such as communication systems. Additionally, direct in-planar connections often result in significant crosstalk between intersecting waveguides, compromising signal integrity and degrading overall system performance.

Hybrid metallo-dielectric waveguides (HMDWs) offer a promising solution to these challenges by enhancing isolation between intersecting waveguides. By utilizing HMDWs, we can substantially improve the flexibility and effectiveness of interconnects within large-scale integration systems, as illustrated in Figure 8.7. This approach effectively addresses the limitations of traditional routing methods. As demonstrated in Figure 8.8, the incorporation of NRD junctions allows each transmission path to operate almost independently, further reducing interference and enhancing system performance. This innovative strategy not only mitigates the issues of signal degradation and crosstalk but also enables the design of more robust and efficient integrated systems, paving the way for advancements in a variety of high-performance applications.

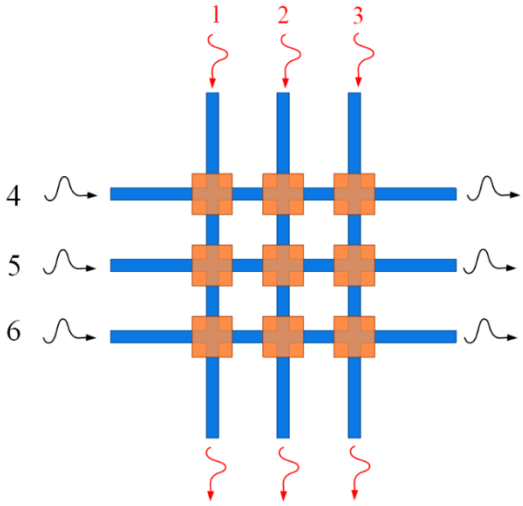

Figure 8.7 Flexible routing between multiple modules

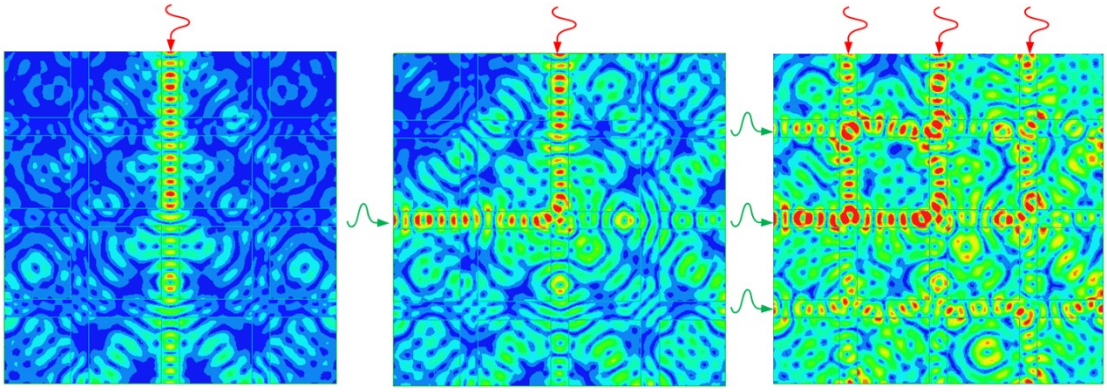

(a)

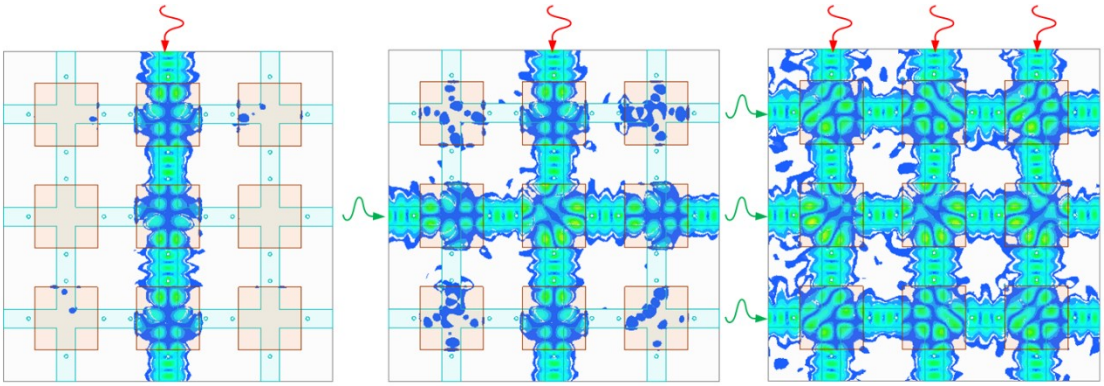

(b)

Figure 8.8 Electric field distributions of multiple (a) DW crossovers, (b) NRD waveguide crossovers

Advanced manufacturing process

The development of precise and reliable fabrication methods is crucial for ensuring the integrity and performance of hybrid waveguide structures. This includes optimizing laser drilling processes and refining alignment techniques. Furthermore, exploring alternative materials with enhanced dielectric properties and lower loss tangents could significantly improve the overall performance of the waveguides. This may involve investigating advanced fabrication technologies, such as 3-D printing as shown in Figure 8.9, to further enhance waveguide performance.

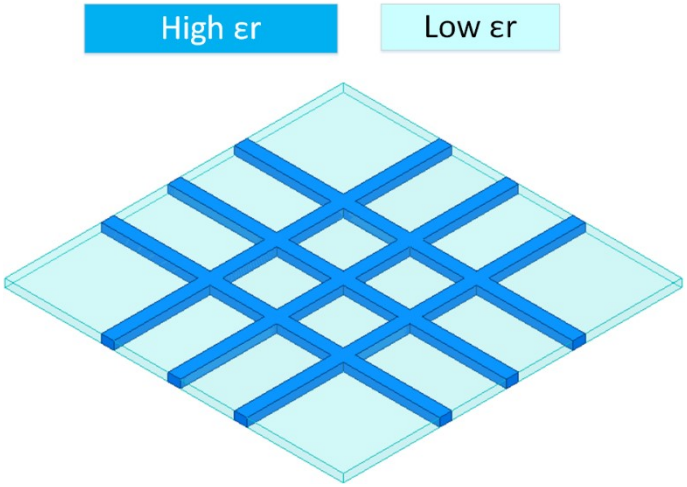

Figure 8.9 3-D printing custommizable substrate

REFERENCES

[1] D. Grischkowsky, I. N. Duling, J. C. Chen, and C. C. Chi, "Electromagnetic shock waves from transmission lines," *Phys Rev Lett*, vol. 59, no. 15, pp. 1663–1666, 1987, doi: 10.1103/PhysRevLett.59.1663.

[2] M. Y. Frankel, S. Gupta, J. A. Valdmanis, and G. A. Mourou, "Terahertz attenuation and dispersion characteristics of coplanar transmission lines," *IEEE Trans Microw Theory Tech*, vol. 39, no. 6, pp. 910–916, 1991, doi: 10.1109/22.81658.

[3] A. Grimault-Jacquin, B. Tissafi, E. Perret, and F. Aniel, "Consideration to minimize losses in terahertz coplanar waveguide on indium phosphide," *Microw Opt Technol Lett*, vol. 54, no. 1, pp. 213–219, Jan. 2012, doi: 10.1002/mop.26448.

[4] J. Zhang, S. Alexandrou, and T. Y. Hsiang, "Attenuation characteristics of coplanar waveguides at subterahertz frequencies*," IEEE Trans Microw Theory Tech,* vol. 53, no. 11, pp. 3281–3287, Nov. 2005, doi: 10.1109/TMTT.2005.857124.

[5] H.-J. Cheng, J. F. Whitaker, T. M. Weller, and L. P. B. Katehi, "Terahertz-bandwidth characteristics of coplanar transmission lines on low permittivity substrates," 1994.

[6] L. Cao, A. S. Grimault-Jacquin, N. Zerounian, and F. Aniel, "Design and VNA-measurement of coplanar waveguide (CPW) on benzocyclobutene (BCB) at THz frequencies," *Infrared Phys Technol*, vol. 63, pp. 157–164, Mar. 2014, doi: 10.1016/j.infrared.2013.12.023.

[7] M. Moallem, J. East, and K. Sarabandi, "A broadband, micromachined rectangular waveguide to cavity-backed coplanar waveguide transition using impedance-taper technique," *IEEE Trans Terahertz Sci Technol*, vol. 4, no. 1, pp. 49–55, Jan. 2014, doi: 10.1109/TTHZ.2013.2293876.

[8] K. W. Goossen and R. B. Hammond, "Modeling of picosecond pulse propagation in microstrip interconnections on integrated circuits," *IEEE Trans Microw Theory Tech*, vol. 37, no. 3, pp. 469–478, 1989, doi: 10.1109/22.21616.

[9] H. Roskos *et al.*, "Propagation of picosecond electrical pulses on a silicon-based microstrip line with buried cobalt silicide ground plane," *Appl Phys Lett*, vol. 58, no. 23, pp. 2604–2606, 1991, doi: 10.1063/1.104836.

[10] J. Gondermann, E. G. Stein von Kamienski, H. G. Roskos, and H. Kurz, "Al-SiO2-Al sandwich microstrip lines for high-frequency on-chip interconnects,"

IEEE Trans Microw Theory Tech, vol. 41, no. 12, pp. 2087–2091, 1993, doi: 10.1109/22.260691.

[11] H.-M. Heiliger, M. Nagel, H. G. Roskos, H. Kurz, F. Schnieder, and W. Heinrich, "Thin-film microstrip lines for MM and sub-MM/wave on-chip interconnects," in *1997 IEEE MTT-S International Microwave Symposium Digest*, Denver: IEEE, Jun. 1997, pp. 421–424. doi: 10.1109/MWSYM.1997.602823.

[12] H. M. Heiliger *et al.*, "Low-dispersion thin-film microstrip lines with cyclotene (benzocyclobutene) as dielectric medium," *Appl Phys Lett*, vol. 70, no. 17, pp. 2233–2235, Apr. 1997, doi: 10.1063/1.118849.

[13] M. Nagel, P. Haring Bolivar, M. Brucherseifer, H. Kurz, A. Bosserhoff, and R. Büttner, "Integrated THz technology for label-free genetic diagnostics," *Appl Phys Lett*, vol. 80, no. 1, pp. 154–156, Jan. 2002, doi: 10.1063/1.1428619.

[14] F. Schnieder and W. Heinrich, "Model of thin-film microstrip line for circuit design," *IEEE Trans Microw Theory Tech*, vol. 49, no. 1, pp. 104–110, 2001, doi: 10.1109/22.899967.

[15] M. B. Byrne *et al.*, "Terahertz vibrational absorption spectroscopy using microstrip-line waveguides," *Appl Phys Lett*, vol. 93, no. 18, 2008, doi: 10.1063/1.3013349.

[16] A. Hassona, V. Vassilev, A. U. Zaman, V. Belitsky, and H. Zirath, "Compact low-loss chip-to-waveguide and chip-to-chip packaging concept using EBG structures," *IEEE Microwave and Wireless Components Letters*, vol. 31, no. 1, pp. 9–12, Jan. 2021, doi: 10.1109/LMWC.2020.3034772.

[17] C. H. Li and T. Y. Chiu, "Low-loss single-band, dual-band, and broadband mm-Wave and (bub-)THz interconnects for THz SoP heterogeneous system integration," *IEEE Trans Terahertz Sci Technol*, vol. 12, no. 2, pp. 130–143, Mar. 2022, doi: 10.1109/TTHZ.2021.3128596.

[18] A. M. Eblabla, X. Li, D. J. Wallis, I. Guiney, and K. Elgaid, "GaN on low-resistivity silicon THz high-Q passive device technology," *IEEE Trans Terahertz Sci Technol*, vol. 7, no. 1, pp. 93–97, Jan. 2017, doi: 10.1109/TTHZ.2016.2618751.

[19] A. Eblabla, D. J. Wallis, I. Guiney, and K. Elgaid, "Novel shielded coplanar waveguides on GaN-on-low resistivity Si substrates for MMIC applications," *IEEE Microwave and Wireless Components Letters*, vol. 25, no. 7, pp. 427–429, Jul. 2015, doi: 10.1109/LMWC.2015.2429120.

[20] M. Ur Rehman, S. Ravichandran, A. O. Watanabe, S. Erdogan, and M. Swaminathan, “Characterization of ABF/glass/ABF substrates for mmWave applications,” *IEEE Trans Compon Packaging Manuf Technol*, vol. 11, no. 3, pp. 384–394, Mar. 2021, doi: 10.1109/TCPMT.2021.3061485.

[21] V. Sukumaran, T. Bandyopadhyay, V. Sundaram, and T. Rao, “Low-cost thin glass interposers as a superior alternative to silicon and organic interposers for packaging of 3-D ICs,” *IEEE Trans Compon Packaging Manuf Technol*, vol. 2, no. 9, pp. 1426–1433, 2012, doi: 10.1109/TCPMT.2012.2204392.

[22] H. Akahoshi *et al.*, “Fine line circuit manufacturing technology with electroless copper plating,” *IEEE Transactions on Components, Packaging, and Manufacturing Technology: Part A*, vol. 18, no. 1, pp. 127–135, Mar. 1995, doi: 10.1109/95.370746.

[23] M. Ur Rehman, L. N. V. Kumar, and M. Swaminathan, “Characterization of microstrip line and SIW on ABF in glass interposers for mmWave applications,” *IEEE Trans Compon Packaging Manuf Technol*, vol. 13, no. 9, pp. 1520–1523, Sep. 2023, doi: 10.1109/TCPMT.2023.3305459.

[24] N. Aslani-Amoli *et al.*, “Characterization of alumina ribbon ceramic substrates for 5G and mm-Wave applications,” *IEEE Trans Compon Packaging Manuf Technol*, vol. 12, no. 9, pp. 1432–1445, Sep. 2022, doi: 10.1109/TCPMT.2022.3196663.

[25] N. Aslani-Amoli *et al.*, “Transmission lines on alumina ribbon ceramic substrate material for 30 to 170 GHz wireless applications,” in *Proceedings - Electronic Components and Technology Conference*, Institute of Electrical and Electronics Engineers Inc., 2021, pp. 2272–2278. doi: 10.1109/ECTC32696.2021.00356.

[26] C. Kim, H. Kim, E. J. Moon, D. R. Peters, H. Vanselous-Barrett, and S. Seok, “5G mmWave patch antenna array on extremely low loss alumina ribbon ceramic substrates for antenna-in-packaging (AiP),” in *2023 IEEE 73rd Electronic Components and Technology Conference (ECTC)*, IEEE, May 2023, pp. 492–497. doi: 10.1109/ECTC51909.2023.00088.

[27] A. Treizebré, T. Akalin, and B. Bocquet, “Planar excitation of Goubau transmission lines for THz BioMEMS,” *IEEE Microwave and Wireless Components Letters*, vol. 15, no. 12, pp. 886–888, Dec. 2005, doi: 10.1109/LMWC.2005.859976.

[28] T. Akalin, A. Treizebré, and B. Bocquet, “Single-wire transmission lines at terahertz frequencies,” *IEEE Trans Microw Theory Tech*, vol. 54, no. 6, pp. 2762–2767, Jun. 2006, doi: 10.1109/TMTT.2006.874890.

[29] D. Gacemi *et al.*, “Confinement of THz surface waves on the subwavelength size metal waveguide,” *Appl Phys A Mater Sci Process*, vol. 109, no. 4, pp. 993–995, Dec. 2012, doi: 10.1007/s00339-012-7363-y.

[30] A. K. Horestani *et al.*, “Metamaterial-inspired bandpass filters for terahertz surface waves on goubau lines,” *IEEE Trans Terahertz Sci Technol*, vol. 3, no. 6, pp. 851–858, Nov. 2013, doi: 10.1109/TTHZ.2013.2285556.

[31] L. Dazhang *et al.*, “On-chip terahertz Goubau-line waveguides with integrated photoconductive emitters and mode-discriminating detectors,” *Appl Phys Lett*, vol. 95, no. 9, 2009, doi: 10.1063/1.3216579.

[32] T. Schaich, D. Molnar, A. Al Rawi, and M. Payne, “Analytic modelling of a planar Goubau line with circular conductor,” *Sci Rep*, vol. 10, no. 1, Dec. 2020, doi: 10.1038/s41598-020-77703-w.

[33] G. Goubau, “Surface waves and their application to transmission lines,” *J Appl Phys*, vol. 21, no. 11, pp. 1119–1128, 1950, doi: 10.1063/1.1699553.

[34] G. Goubau, “Single-conductor surface-wave transmission lines,” *Proceedings of the IRE*, vol. 39, no. 6, pp. 619–624, 1951, doi: 10.1109/JRPROC.1951.233782.

[35] G. Goubau, “Open wire lines,” *IEEE Trans Microw Theory Tech*, vol. 4, no. 4, pp. 197–200, Oct. 1956, doi: 10.1109/TMTT.1956.1125062.

[36] M. J. King and J. C. Wiltse, “Surface-wave propagation on coated or uncoated metal wires at millimeter wavelengths,” *IRE Transactions on Antennas and Propagation*, vol. 10, no. 3, pp. 246–254, 1962, doi: 10.1109/TAP.1962.1137859.

[37] J. Cabello-Sánchez, H. Rodilla, V. Drakinskiy, and J. Stake, “Multiline TRL calibration standards for S-parameter measurement of planar Goubau lines from 0.75 THz to 1.1 THz,” in *IEEE MTT-S International Microwave Symposium Digest*, Institute of Electrical and Electronics Engineers Inc., Aug. 2018, pp. 879–882. doi: 10.1109/MWSYM.2018.8439138.

[38] J. Cabello-Sanchez, V. Drakinskiy, J. Stake, and H. Rodilla, “Terahertz planar Goubau line components on thin suspended silicon substrate,” in *International Conference on Infrared, Millimeter, and Terahertz Waves, IRMMW-THz*, IEEE Computer Society, 2022. doi: 10.1109/IRMMW-THz50927.2022.9896069.

[39] J. Cabello-Sanchez, V. Drakinskiy, J. Stake, and H. Rodilla, “Capacitively-coupled resonators for terahertz planar-Goubau-line filters,” *IEEE Trans Terahertz Sci Technol*, vol. 13, no. 1, pp. 58–66, Jan. 2023, doi: 10.1109/TTHZ.2022.3220599.

[40] J. Cabello-Sánchez, V. Drakinskiy, J. Stake, and H. Rodilla, “A corrugated planar-Goubau-line termination for terahertz waves,” *IEEE Microwave and Wireless Technology Letters*, vol. 33, no. 6, pp. 643–646, Feb. 2023, doi: 10.1109/lmwt.2023.3239984.

[41] J. Cabello-Sánchez, V. Drakinskiy, J. Stake, and H. Rodilla, “A capacitive-gap coupled terahertz planar-Goubau-line power divider,” *IEEE Trans Terahertz Sci Technol*, vol. 13, no. 6, pp. 698–703, Nov. 2023, doi: 10.1109/TTHZ.2023.3303849.

[42] R. Mendis and D. Grischkowsky, “Undistorted guided-wave propagation of subpicosecond terahertz pulses,” *Opt Lett*, vol. 26, no. 11, p. 846, Jun. 2001, doi: 10.1364/OL.26.000846.

[43] R. Menais and D. Grischkowsky, “THz interconnect with low-loss and low-group velocity dispersion,” *IEEE Microwave and Wireless Components Letters*, vol. 11, no. 11, pp. 444–446, Nov. 2001, doi: 10.1109/7260.966036.

[44] M. Nagel, P. H. Bolivar, and H. Kurz, “Modular parallel-plate THz components for cost-efficient biosensing systems,” *Semicond Sci Technol*, vol. 20, no. 7, Jul. 2005, doi: 10.1088/0268-1242/20/7/019.

[45] R. Mendis and D. M. Mittleman, “Comparison of the lowest-order transverse-electric (TE_1) and transverse-magnetic (TEM) modes of the parallel-plate waveguide for terahertz pulse applications,” *Opt Express*, vol. 17, no. 17, p. 14839, Aug. 2009, doi: 10.1364/OE.17.014839.

[46] V. Astley, K. S. Reichel, J. Jones, R. Mendis, and D. M. Mittleman, “Terahertz multichannel microfluidic sensor based on parallel-plate waveguide resonant cavities,” *Appl Phys Lett*, vol. 100, no. 23, Jun. 2012, doi: 10.1063/1.4724204.

[47] M. Wächter, M. Nagel, and H. Kurz, “Metallic slit waveguide for dispersion-free low-loss terahertz signal transmission,” *Appl Phys Lett*, vol. 90, no. 6, 2007, doi: 10.1063/1.2472544.

[48] J. S. Jo, T. I. Jeon, and D. R. Grischkowsky, “Prototype 250 GHz bandwidth chip to chip electrical interconnect, characterized with ultrafast optoelectronics,” *IEEE Trans Terahertz Sci Technol*, vol. 3, no. 4, pp. 453–460, 2013, doi: 10.1109/TTHZ.2013.2251930.

[49] T. I. Jeon and D. Grischkowsky, “Direct optoelectronic generation and detection of sub-ps-electrical pulses on sub-mm-coaxial transmission lines,” *Appl Phys Lett*, vol. 85, no. 25, pp. 6092–6094, Dec. 2004, doi: 10.1063/1.1839645.

[50] F. David, M. Chatras, C. Dalmay, L. Lapierre, L. Carpentier, and P. Blondy, "Surface-micromachined rectangular micro-coaxial lines for sub-millimeter-wave applications," *IEEE Microwave and Wireless Components Letters*, vol. 26, no. 10, pp. 756–758, Oct. 2016, doi: 10.1109/LMWC.2016.2604867.

[51] J. C. Wiltse, "Surface-wave propagation on a single metal wire or rod at millimeter-wave and terahertz frequencies," in *IEEE MTT-S International Microwave Symposium Digest*, 2006, pp. 970–973. doi: 10.1109/MWSYM.2006.249880.

[52] K. Wang and D. M. Mittleman, "Metal wires for terahertz wave guiding," *Nature*, vol. 432, no. 7015, pp. 376–379, Nov. 2004, doi: 10.1038/nature03040.

[53] E. A. J. Marcatili and R. A. Schmeltzer, "Hollow metallic and dielectric waveguides for long distance optical transmission and lasers," *Bell System Technical Journal*, vol. 43, no. 4, pp. 1783–1809, Jul. 1964, doi: 10.1002/j.1538-7305.1964.tb04108.x.

[54] R. W. McGowan, G. Gallot, and D. Grischkowsky, "Propagation of ultrawideband short pulses of terahertz radiation through submillimeter-diameter circular waveguides," *Opt Lett*, vol. 24, no. 20, p. 1431, Oct. 1999, doi: 10.1364/OL.24.001431.

[55] X. Tang *et al.*, "Elliptical hollow fiber with inner silver coating for linearly polarized terahertz transmission," *IEEE Photonics Technology Letters*, vol. 25, no. 4, pp. 331–334, 2013, doi: 10.1109/LPT.2013.2238525.

[56] D. M. Pozar, *Microwave Engineering*, 4th ed. JohnWiley & Sons, Inc., 2011.

[57] O. Mitrofanov, R. James, F. A. Fernández, T. K. Mavrogordatos, and J. A. Harrington, "Reducing transmission losses in hollow THz waveguides," *IEEE Trans Terahertz Sci Technol*, vol. 1, no. 1, pp. 124–132, Sep. 2011, doi: 10.1109/TTHZ.2011.2159547.

[58] M. Miyagi and K. Shojiro, "Design theory of dielectric-coated circular metallic waveguides for infrared transmission," *Journal of Lightwave Technology*, vol. 2, no. 2, pp. 116–126, 1984, doi: 10.1109/JLT.1984.1073590.

[59] Christos Themistos, B. M. Azizur Rahman, Muttukrishnan Rajarajan, Kenneth T. V. Grattan, B. Bowden, and J. A. Harrington, "Characterization of silver/polystyrene (PS)-coated hollow glass waveguides at THz frequency," *Journal of Lightwave Technology*, vol. 25, no. 9, pp. 2463–2468, Sep. 2007, doi: 10.1063/1.3013445.

[60] B. Bowden, J. A. Harrington, and O. Mitrofanov, “Silver/Polystyrene coated hollow glass waveguides for the transmission of THz radiation,” in *2007 Conference on Lasers and Electro-Optics (CLEO)*, IEEE, May 2007, pp. 1–2. doi: 10.1109/CLEO.2007.4452817.

[61] B. Bowden, J. A. Harrington, and O. Mitrofanov, “Low-loss modes in hollow metallic terahertz waveguides with dielectric coatings,” *Appl Phys Lett*, vol. 93, no. 18, 2008, doi: 10.1063/1.3013585.

[62] A. Aming and B. M. A. Rahman, “Design and characterization low-loss Modes in dielectric-coated hollow-core waveguides at THz frequency,” *Journal of Lightwave Technology*, vol. 36, no. 13, pp. 2716–2722, Jul. 2018, doi: 10.1109/JLT.2018.2820690.

[63] C. M. Bledt, J. E. Melzer, and J. A. Harrington, “Fabrication and characterization of improved Ag/PS hollow-glass waveguides for THz transmission,” *Appl Opt*, vol. 52, no. 27, pp. 6703–6709, Sep. 2013, doi: 10.1364/AO.52.006703.

[64] B.-S. Sun, X.-L. Tang, Y.-W. Shi, K. Iwai, and M. Miyagi, “Optimal design for hollow fiber inner-coated by dielectric layers with surface roughness,” *Opt Lett*, vol. 36, no. 17, p. 3461, Sep. 2011, doi: 10.1364/OL.36.003461.

[65] S. Liu *et al.*, “Transmission and confocal imaging characteristics of bendable ABS/Ag-coated hollow waveguide at low THz band,” *IEEE Trans Terahertz Sci Technol*, vol. 13, no. 3, pp. 193–199, May 2023, doi: 10.1109/TTHZ.2023.3263628.

[66] B. M. A. Rahman, A. Quadir, H. Tanvir, and K. T. V. Grattan, “Characterization of plasmonic modes in a low-loss dielectric-coated hollow core rectangular waveguide at terahertz frequency,” *IEEE Photonics J*, vol. 3, no. 6, pp. 1054–1066, 2011, doi: 10.1109/JPHOT.2011.2173326.

[67] Y.-W. Shi *et al.*, “Cyclic olefin polymer-coated silver hollow glass waveguides for the infrared,” *Appl Opt*, vol. 37, no. 33, p. 7758, Nov. 1998, doi: 10.1364/AO.37.007758.

[68] Y.-W. Shi, K. Ito, L. Ma, T. Yoshida, Y. Matsuura, and M. Miyagi, “Fabrication of a polymer-coated silver hollow optical fiber with high performance,” *Appl Opt*, vol. 45, no. 26, p. 6736, Sep. 2006, doi: 10.1364/AO.45.006736.

[69] M. Navarro-Cía, J. E. Melzer, J. A. Harrington, and O. Mitrofanov, “Silver-coated teflon tubes for waveguiding at 1–2THz,” *J Infrared Millim Terahertz Waves*, vol. 36, no. 6, pp. 542–555, Jun. 2015, doi: 10.1007/s10762-015-0157-5.

[70] James A. Harrington, Roshan George, and Pal Pedersen, “Hollow polycarbonate waveguides with inner Cu coatings for delivery of terahertz radiation,” SPIE Press, 2004. doi: 10.1364/OPEX.12.005263.

[71] R. J. George and J. A. Harrington, “New coatings for metal-dielectric hollow waveguides,” in *Fiber and Integrated Optics*, I. Gannot, Ed., SPIE Press, Mar. 2002, pp. 129–134. doi: 10.1117/12.463804.

[72] I. Stil, A. Fontana, B. Lefranc, and A. Navarrini, “Low loss WR10 waveguide across 70-116 GHz,” in *22nd International Symposium on Space Terahertz Technology*, Tokyo, Apr. 2012.

[73] J. Q. Ding, Y. Zhao, and S. C. Shi, “A full WR-3 band and low-loss 90° waveguide twist based on CNC,” *IEEE Trans Terahertz Sci Technol*, vol. 10, no. 1, pp. 93–96, Jan. 2020, doi: 10.1109/TTHZ.2019.2951064.

[74] C. D. Lopez, D. Montofre, V. Desmaris, A. Henkel, and V. Belitsky, “Ultra-wideband 90° waveguide twist for THz applications,” *IEEE Trans Terahertz Sci Technol*, vol. 13, no. 1, pp. 67–73, Jan. 2023, doi: 10.1109/TTHZ.2022.3213468.

[75] A. R. Kerr, C. Litton, G. Petencin, D. Koller, and M. Shannon, “ALMA Memo 585 Loss of gold plated waveguides at 210-280 GHz,” 2009.

[76] C. E. Collins *et al.*, “W-band measurements of 100 μm height micro-machined air-filled rectangular waveguides,” in *1997 IEEE MTT-S International Microwave Symposium Digest*, IEEE, pp. 1439–1442. doi: 10.1109/MWSYM.1997.596600.

[77] C. E. Collins *et al.*, “A new micro-machined millimeter-wave and terahertz snap-together rectangular waveguide technology,” *IEEE Microwave and Guided Wave Letters*, vol. 9, no. 2, pp. 63–65, 1999, doi: 10.1109/75.755047.

[78] X. Shang, M. Ke, Y. Wang, and M. J. Lancaster, “WR-3 band waveguides and filters fabricated using SU8 photoresist micromachining technology,” *IEEE Trans Terahertz Sci Technol*, vol. 2, no. 6, pp. 629–637, 2012, doi: 10.1109/TTHZ.2012.2220136.

[79] W. R. McGrath, C. Walker, M. Yap, and Y. C. Tai, “Silicon micromachined waveguides for millimeter-wave and submillimeter-wave frequencies,” *IEEE Microwave and Guided Wave Letters*, vol. 3, no. 3, pp. 61–63, 1993, doi: 10.1109/75.205665.

[80] Y. Li, P. Kirby, and J. Papapolymerou, “Silicon micromachined W-band folded and straight waveguides using DRIE technique,” in *2006 IEEE MTT-S*

International Microwave Symposium Digest, IEEE, 2006, pp. 1915–1918. doi: 10.1109/MWSYM.2006.249790.

[81] B. Beuerle, J. Campion, U. Shah, and J. Oberhammer, "A very low loss 220-325 GHz silicon micromachined waveguide technology," *IEEE Trans Terahertz Sci Technol*, vol. 8, no. 2, pp. 248–250, Mar. 2018, doi: 10.1109/TTHZ.2018.2791841.

[82] K. M. K. H. Leong *et al.*, "WR1.5 silicon micromachined waveguide components and active circuit integration methodology," *IEEE Trans Microw Theory Tech*, vol. 60, no. 4, pp. 998–1005, Apr. 2012, doi: 10.1109/TMTT.2012.2184296.

[83] T. J. Reck, C. Jung-Kubiak, J. Gill, and G. Chattopadhyay, "Measurement of silicon micromachined waveguide components at 500-750 GHz," *IEEE Trans Terahertz Sci Technol*, vol. 4, no. 1, pp. 33–38, Jan. 2014, doi: 10.1109/TTHZ.2013.2282534.

[84] A. Gomez-Torrent, U. Shah, and J. Oberhammer, "Compact silicon-micromachined wideband 220-330-GHz turnstile orthomode transducer," *IEEE Trans Terahertz Sci Technol*, vol. 9, no. 1, pp. 38–46, Jan. 2019, doi: 10.1109/TTHZ.2018.2882745.

[85] P. L. Kirby, D. Pukala, H. Manohara, I. Mehdi, and J. Papapolymerou, "Characterization of micromachined silicon rectangular waveguide at 400 GHz," *IEEE Microwave and Wireless Components Letters*, vol. 16, no. 6, pp. 366–368, Jun. 2006, doi: 10.1109/LMWC.2006.875593.

[86] A. Pavolotsky, D. Meledin, C. Risacher, M. Pantaleev, and V. Belitsky, "Micromachining approach in fabricating of THz waveguide components," *Microelectronics J*, vol. 36, no. 7, pp. 683–686, Jul. 2005, doi: 10.1016/j.mejo.2005.04.041.

[87] V. Desmaris, D. Meledin, A. Pavolotsky, R. Monje, and V. Belitsky, "All-metal micromachining for the fabrication of sub-millimetre and THz waveguide components and circuits," *Journal of Micromechanics and Microengineering*, vol. 18, no. 9, Sep. 2008, doi: 10.1088/0960-1317/18/9/095004.

[88] C. D. Joye, J. P. Calame, M. Garven, and B. Levush, "UV-LIGA microfabrication of 220 GHz sheet beam amplifier gratings with SU-8 photoresists," *Journal of Micromechanics and Microengineering*, vol. 20, no. 12, Dec. 2010, doi: 10.1088/0960-1317/20/12/125016.

[89] J. R. Stanec and N. S. Barker, "Fabrication and integration of micromachined submillimeter-wave circuits," *IEEE Microwave and Wireless Components*

Letters, vol. 21, no. 8, pp. 409–411, Aug. 2011, doi: 10.1109/LMWC.2011.2158411.

[90] A. Del Campo and C. Greiner, "SU-8: A photoresist for high-aspect-ratio and 3D submicron lithography," *Journal of Micromechanics and Microengineering*, vol. 17, no. 6, Jun. 2007, doi: 10.1088/0960-1317/17/6/R01.

[91] Y. S. Liao and Y. T. Chen, "Precision fabrication of an arrayed micro metal probe by the laser-LIGA process," *Journal of Micromechanics and Microengineering*, vol. 15, no. 12, pp. 2433–2440, Dec. 2005, doi: 10.1088/0960-1317/15/12/027.

[92] M. D'Auria *et al.*, "3-D printed metal-pipe rectangular waveguides," Sep. 01, 2015, *Institute of Electrical and Electronics Engineers Inc.* doi: 10.1109/TCPMT.2015.2462130.

[93] A. Von Bieren, E. De Rijk, J. P. Ansermet, and A. Macor, "Monolithic metal-coated plastic components for mm-wave applications," in *International Conference on Infrared, Millimeter, and Terahertz Waves, IRMMW-THz*, IEEE Computer Society, Nov. 2014. doi: 10.1109/IRMMW-THz.2014.6956222.

[94] B. Zhang and H. Zirath, "Metallic 3-D printed rectangular waveguides for millimeter-wave applications," *IEEE Trans Compon Packaging Manuf Technol*, vol. 6, no. 5, pp. 796–804, May 2016, doi: 10.1109/TCPMT.2016.2550483.

[95] D. Deslandes and K. Wu, "Accurate modeling, wave mechanisms, and design considerations of a substrate integrated waveguide," *IEEE Trans Microw Theory Tech*, vol. 54, no. 6, pp. 2516–2526, Jun. 2006, doi: 10.1109/TMTT.2006.875807.

[96] K. Wu, Y. J. Cheng, T. Djerafi, and W. Hong, "Substrate-integrated millimeter-wave and terahertz antenna technology," in *Proceedings of the IEEE*, Institute of Electrical and Electronics Engineers Inc., 2012, pp. 2219–2232. doi: 10.1109/JPROC.2012.2190252.

[97] J. Xu, Z. N. Chen, X. Qing, and W. Hong, "140-GHz planar SIW slot antenna array with a large-via-fence dielectric loading in LTCC," in *2012 6th European Conference on Antennas and Propagation (EUCAP)*, IEEE, Mar. 2012, pp. 3542–3545. doi: 10.1109/EuCAP.2012.6206389.

[98] H. J. Tang, W. Hong, G. Q. Yang, and J. X. Chen, "Silicon based THz antenna and filter with MEMS process," in *2011 International Workshop on Antenna Technology (iWAT)*, IEEE, Mar. 2011, pp. 148–151. doi: 10.1109/IWAT.2011.5752383.

[99] H. J. Tang, G. Q. Yang, J. X. Chen, W. Hong, and K. Wu, “Millimeter-wave and terahertz transmission loss of CMOS process-based substrate integrated waveguide,” in *2012 IEEE/MTT-S International Microwave Symposium Digest*, IEEE, Jun. 2012, pp. 1–3. doi: 10.1109/MWSYM.2012.6259786.

[100] A. Bhutani *et al.*, “Sub-THz substrate integrated waveguide signal transitions in backend-of-line of a silicon process,” in *18th European Conference on Antennas and Propagation, EuCAP 2024*, Institute of Electrical and Electronics Engineers Inc., 2024. doi: 10.23919/EuCAP60739.2024.10501393.

[101] A. Bhutani, M. Kaynak, E. Bekker, and T. Zwick, “200–330-GHz substrate-integrated waveguide in BEOL of a SiGe BiCMOS process,” *IEEE Microwave and Wireless Technology Letters*, vol. 33, no. 9, pp. 1258–1261, Sep. 2023, doi: 10.1109/LMWT.2023.3283304.

[102] R. K. Pokharel *et al.*, “200 GHz-band low-loss half-mode SIW CMOS interconnects and transmission lines for sub-terahertz frequency band applications,” in *IEEE MTT-S International Microwave Symposium Digest*, Institute of Electrical and Electronics Engineers Inc., 2023, pp. 497–500. doi: 10.1109/IMS37964.2023.10188034.

[103] S. K. Thapa *et al.*, “Experimental study on transition loss of on-chip SIW interconnects and transmission lines using two de-embedding reference planes in 200 GHz band frequency,” in *2024 IEEE/MTT-S International Microwave Symposium - IMS 2024*, IEEE, Jun. 2024, pp. 694–697. doi: 10.1109/IMS40175.2024.10600291.

[104] M. S. Mahani and G. W. Roberts, “A mmWave folded substrate integrated waveguide in a 130-nm CMOS process,” *IEEE Trans Microw Theory Tech*, vol. 65, no. 8, pp. 2775–2788, Aug. 2017, doi: 10.1109/TMTT.2017.2661259.

[105] M. Bertrand *et al.*, “Substrate Integrated Waveguides for mm-wave Functionalized Silicon Interposer,” in *IEEE MTT-S International Microwave Symposium Digest*, Institute of Electrical and Electronics Engineers Inc., Aug. 2018, pp. 875–878. doi: 10.1109/MWSYM.2018.8439287.

[106] G. Gentile *et al.*, “Silicon-filled rectangular waveguides and frequency scanning antennas for mm-Wave integrated systems,” *IEEE Trans Antennas Propag*, vol. 61, no. 12, pp. 5893–5901, 2013, doi: 10.1109/TAP.2013.2281518.

[107] G. Gentile *et al.*, “Silicon filled integrated waveguides,” *IEEE Microwave and Wireless Components Letters*, vol. 20, no. 10, pp. 536–538, Oct. 2010, doi: 10.1109/LMWC.2010.2063420.

[108] A. Krivovitca, U. Shah, O. Glubokov, and J. Oberhammer, “Micromachined silicon-core substrate-integrated waveguides at 220-330 GHz,” *IEEE Trans Microw Theory Tech*, vol. 68, no. 12, pp. 5123–5131, Dec. 2020, doi: 10.1109/TMTT.2020.3022060.

[109] W. T. Khan, C. A. Donado Morcillo, A. C. Ulusoy, and J. Papapolymerou, “Characterization of liquid crystal polymer from 110 GHz to 170 GHz,” in *2014 IEEE Radio and Wireless Symposium (RWS)*, IEEE, Jan. 2014, pp. 157–159. doi: 10.1109/RWS.2014.6830138.

[110] M. Yi *et al.*, “Surface roughness modeling of substrate integrated waveguide in D-band,” *IEEE Trans Microw Theory Tech*, vol. 64, no. 4, pp. 1209–1216, Apr. 2016, doi: 10.1109/TMTT.2016.2535290.

[111] S. Li, M. Yi, S. Pavlidis, H. Yu, M. Swaminathan, and J. Papapolymerou, “Investigation of surface roughness effects for D-band SIW transmission lines on LCP substrate,” in *IEEE Radio and Wireless Symposium, RWS*, IEEE Computer Society, Mar. 2017, pp. 121–124. doi: 10.1109/RWS.2017.7885963.

[112] G. Acri *et al.*, “BenzoCycloButene-based in-package substrate integrated waveguides for sub-THz applications,” in *2020 50th European Microwave Conference, EuMC 2020*, Institute of Electrical and Electronics Engineers Inc., Jan. 2021, pp. 41–44. doi: 10.23919/EuMC48046.2021.9338003.

[113] M. Ur Rehman, A. Watanabe, S. Ravichandran, and M. Swaminathan, “Substrate integrated waveguides in glass interposers for mm Wave applications,” in *IEEE MTT-S International Microwave Symposium Digest*, Institute of Electrical and Electronics Engineers Inc., Jun. 2021, pp. 339–341. doi: 10.1109/IMS19712.2021.9574832.

[114] N. Aslani-Amoli *et al.*, “Ultralow-Loss Substrate-Integrated Waveguides in Alumina Ribbon Ceramic Substrates for 75-170 GHz Wireless Applications,” *IEEE Microwave and Wireless Technology Letters*, vol. 33, no. 10, pp. 1415–1418, Oct. 2023, doi: 10.1109/LMWT.2023.3304949.

[115] M. Bertrand *et al.*, “Integrated waveguides in nanoporous alumina membrane for millimeter-wave interposer,” *IEEE Microwave and Wireless Components Letters*, vol. 29, no. 2, pp. 83–85, Feb. 2019, doi: 10.1109/LMWC.2018.2887193.

[116] J. M. de Saxcé *et al.*, “E-band vertically aligned carbon nanotubes-based air-filled waveguide,” *IEEE Microwave and Wireless Technology Letters*, vol. 33, no. 4, pp. 395–398, Apr. 2023, doi: 10.1109/LMWT.2022.3227946.

[117] F. Parment, A. Ghiotto, T.-P. Vuong, J.-M. Duchamp, and K. Wu, “Air-filled SIW transmission line and phase shifter for high-performance and low-cost U-band integrated circuits and systems.”

[118] S. Sinha, H. Trischler, I. Ocket, and E. Schaffler, “D-band air-filled substrate integrated waveguide (AFSIW) and broadband stripline to AFSIW launcher embedded in multi-layer PCBs,” *IEEE Microwave and Wireless Technology Letters*, vol. 33, no. 6, pp. 795–798, May 2023, doi: 10.1109/lmwt.2023.3267769.

[119] M. ur Rehman, L. N. V. Kumar, S. Erdogan, and M. Swaminathan, “Air-filled SIWs using laminate dielectrics on glass substrate for D-band applications,” *IEEE Trans Compon Packaging Manuf Technol*, vol. 14, no. 1, pp. 98–105, Jan. 2024, doi: 10.1109/TCPMT.2024.3351789.

[120] C. Yeh and F. Shimabukuro, *The Essence of Dielectric Waveguides*. New York: NY, USA: Springer, 2008.

[121] R. Mendis and D. Grischkowsky, “Plastic ribbon THz waveguides,” *J Appl Phys*, vol. 88, no. 7, pp. 4449–4451, 2000, doi: 10.1063/1.1310179.

[122] C. Yeh, F. Shimabukuro, P. Stanton, V. Jamnejad, W. Imbriale, and F. Manshadi, “Communication at millimetre–submillimetre wavelengths using a ceramic ribbon,” *Nature*, vol. 404, no. 6778, pp. 584–588, Apr. 2000, doi: 10.1038/35007036.

[123] C. Yeh, F. I. Shimabukuro, and J. Chu, “Dielectric ribbon waveguide: an optimum configuration for ultra-low-loss millimeter/submillimeter dielectric waveguide,” *IEEE Trans Microw Theory Tech*, vol. 38, no. 6, pp. 691–702, Jun. 1990, doi: 10.1109/22.130962.

[124] C. Yeh, F. Shimabukuro, and P. H. Siegel, “Low-loss terahertz ribbon waveguides,” *Appl Opt*, vol. 44, no. 28, p. 5937, Oct. 2005, doi: 10.1364/AO.44.005937.

[125] J. A. Hejase, P. R. Paladhi, and P. P. Chahal, “Terahertz characterization of dielectric substrates for component design and nondestructive evaluation of packages,” *IEEE Trans Compon Packaging Manuf Technol*, vol. 1, no. 11, pp. 1685–1694, Nov. 2011, doi: 10.1109/TCPMT.2011.2163632.

[126] X. Yang and P. Chahal, “THz ribbon waveguides using polymer-ceramic nanocomposites,” in *2012 IEEE 62nd Electronic Components and Technology Conference*, IEEE, May 2012, pp. 225–230. doi: 10.1109/ECTC.2012.6248832.

[127] X. Yang and P. P. Chahal, “On-wafer terahertz ribbon waveguides using polymer-ceramic nanocomposites,” *IEEE Trans Compon Packaging Manuf*

Technol, vol. 5, no. 2, pp. 245–255, Feb. 2015, doi: 10.1109/TCPMT.2015.2390611.

[128] J. A. Byford and P. Chahal, "Ultra-wideband hybrid substrate integrated ribbon waveguides using 3D printing," in *2016 IEEE MTT-S International Microwave Symposium (IMS)*, IEEE, May 2016, pp. 1–4. doi: 10.1109/MWSYM.2016.7540071.

[129] J. A. Byford and P. Chahal, "Demonstration of substrate integrated ribbon waveguide using 3-D printing," *IEEE Trans Compon Packaging Manuf Technol*, vol. 9, no. 1, pp. 146–155, Jan. 2019, doi: 10.1109/TCPMT.2018.2885637.

[130] K. Y. Park, N. Wiwatcharagoses, and P. Chahal, "Wafer-level integration of micro-lens for THz focal plane array application," in *2013 IEEE 63rd Electronic Components and Technology Conference*, IEEE, May 2013, pp. 1912–1919. doi: 10.1109/ECTC.2013.6575839.

[131] E. A. J. Marcatili, "Dielectric rectangular waveguide and directional coupler for integrated optics," *Bell System Technical Journal*, vol. 48, no. 7, pp. 2071–2102, Sep. 1969, doi: 10.1002/j.1538-7305.1969.tb01166.x.

[132] A. Malekabadi, S. A. Charlebois, D. Deslandes, and F. Boone, "High-resistivity silicon dielectric ribbon waveguide for single-mode low-loss propagation at F/G-bands," *IEEE Trans Terahertz Sci Technol*, vol. 4, no. 4, pp. 447–453, 2014, doi: 10.1109/TTHZ.2014.2322513.

[133] B. Yu, Y. Liu, Y. Ye, J. Ren, X. Liu, and Q. J. Gu, "High-efficiency micromachined sub-THz channels for low-cost interconnect for planar integrated circuits," *IEEE Trans Microw Theory Tech*, vol. 64, no. 1, pp. 96–105, Jan. 2016, doi: 10.1109/TMTT.2015.2504443.

[134] B. Yu, Y. Liu, Y. Ye, X. Liu, and Q. J. Gu, "Low-loss and broadband G-band dielectric interconnect for chip-to-chip communication," *IEEE Microwave and Wireless Components Letters*, vol. 26, no. 7, pp. 478–480, Jul. 2016, doi: 10.1109/LMWC.2016.2574837.

[135] Bo Yu, Yuhao Liu, Xing Hu, Xiaoxin Ren, Xiaoguang Liu, and Qun Jane Gu, "Micromachined sub-THz interconnect channels for planar silicon processes," in *2014 IEEE MTT-S International Microwave Symposium (IMS2014)*, IEEE, Jun. 2014, pp. 1–3. doi: 10.1109/MWSYM.2014.6848632.

[136] B. Yu *et al.*, "Ortho-mode sub-THz interconnect channel for planar chip-to-chip communications," *IEEE Trans Microw Theory Tech*, vol. 66, no. 4, pp. 1864–1873, Apr. 2018, doi: 10.1109/TMTT.2017.2779496.

[137] A. M. Marconnet *et al.*, “Microfabricated silicon high-frequency waveguide couplers and antennas,” *IEEE Trans Electron Devices*, vol. 56, no. 5, pp. 721–729, 2009, doi: 10.1109/TED.2009.2015415.

[138] J. W. Holloway, L. Boglione, T. M. Hancock, and R. Han, “A fully integrated broadband sub-mmWave chip-to-chip interconnect,” *IEEE Trans Microw Theory Tech*, vol. 65, no. 7, pp. 2373–2386, Jul. 2017, doi: 10.1109/TMTT.2017.2660491.

[139] J. W. Holloway, G. C. Dogiamis, and R. Han, “Innovations in terahertz interconnects: high-speed data transport over fully electrical terahertz waveguide links,” *IEEE Microw Mag*, vol. 21, no. 1, pp. 35–50, Jan. 2020, doi: 10.1109/MMM.2019.2945139.

[140] Q. J. Gu, “THz interconnect: the last centimeter communication,” *IEEE Communications Magazine*, vol. 53, no. 4, pp. 206–215, Apr. 2015, doi: 10.1109/MCOM.2015.7081096.

[141] X. Ding, H. Yu, S. Sabbaghi, and Q. J. Gu, “Design and analysis of a mode-coupler-based multimode multidrop Si dielectric waveguide channel for Sub-THz/THz interconnect,” *IEEE Trans Microw Theory Tech*, vol. 72, no. 1, pp. 111–123, Jan. 2024, doi: 10.1109/TMTT.2023.3290189.

[142] X. Ding, H. Yu, S. Sabbaghi, and Q. J. Gu, “G-band mode-coupler-based Si dielectric waveguide for multidrop sub-THz interconnect,” *IEEE Microwave and Wireless Technology Letters*, vol. 33, no. 6, pp. 647–650, Feb. 2023, doi: 10.1109/lmwt.2023.3239624.

[143] Q. J. Gu, “Sub-THz/THz interconnect, complement to electrical and optical interconnects: addressing fundamental challenges related to communication distances,” *IEEE Solid-State Circuits Magazine*, vol. 12, no. 4, pp. 20–32, Sep. 2020, doi: 10.1109/MSSC.2020.3021836.

[144] H. T. Zhu *et al.*, “Low-loss, thermally insulating, and flexible rectangular dielectric waveguide for sub-THz - signal coupling in superconducting receivers,” *IEEE Trans Terahertz Sci Technol*, vol. 10, no. 2, pp. 190–199, Mar. 2020, doi: 10.1109/TTHZ.2019.2963688.

[145] H. T. Zhu *et al.*, “Low-cost narrowed dielectric microstrip line-a three-layer dielectric waveguide using PCB technology for millimeter-wave applications,” *IEEE Trans Microw Theory Tech*, vol. 65, no. 1, pp. 119–127, Jan. 2017, doi: 10.1109/TMTT.2016.2613527.

[146] C. S. Sun, X. C. Li, H. B. Zhan, and K. Ning, “A low-loss and high-bandwidth hollow rectangular dielectric waveguide for sub-THz applications,” *IEEE Trans Microw Theory Tech*, 2024, doi: 10.1109/TMTT.2024.3382399.

[147] N. Ranjkesh, M. Basha, A. Taeb, A. Zandieh, S. Gigoyan, and S. Safavi-Naeini, “Silicon-on-glass dielectric waveguide-part I: For millimeter-wave integrated circuits,” *IEEE Trans Terahertz Sci Technol*, vol. 5, no. 2, pp. 268–279, Mar. 2015, doi: 10.1109/TTHZ.2015.2399693.

[148] N. Ranjkesh, A. Taeb, N. Ghafarian, S. Gigoyan, M. A. Basha, and S. Safavi-Naeini, “Millimeter-wave suspended silicon-on-glass tapered antenna with dual-mode operation,” *IEEE Trans Antennas Propag*, vol. 63, no. 12, pp. 5363–5371, Dec. 2015, doi: 10.1109/TAP.2015.2493164.

[149] N. Ranjkesh, M. Basha, A. Taeb, and S. Safavi-Naeini, “Silicon-on-glass dielectric waveguide-part II: For THz applications,” *IEEE Trans Terahertz Sci Technol*, vol. 5, no. 2, pp. 280–287, Mar. 2015, doi: 10.1109/TTHZ.2015.2397279.

[150] N. Ranjkesh, S. Gigoyan, H. Amarloo, M. Basha, and S. Safavi-Naeini, “Broadband single-mode THz suspended silicon-on-glass waveguide,” *IEEE Microwave and Wireless Components Letters*, vol. 28, no. 3, pp. 185–187, Mar. 2018, doi: 10.1109/LMWC.2018.2797524.

[151] N. Ranjkesh, H. Amarloo, S. Gigoyan, N. Ghafarian, M. A. Basha, and S. Safavi-Naeini, “1.1 THz U-silicon-on-glass (U-SOG) waveguide: a low-loss platform for THz high-density integrated circuits,” *IEEE Trans Terahertz Sci Technol*, vol. 8, no. 6, pp. 702–709, Nov. 2018, doi: 10.1109/TTHZ.2018.2868462.

[152] W. Gao *et al.*, “Characteristics of effective-medium-clad dielectric waveguides,” *IEEE Trans Terahertz Sci Technol*, vol. 11, no. 1, pp. 28–41, Jan. 2021, doi: 10.1109/TTHZ.2020.3023917.

[153] N. Shibata, Y. Uemura, Y. Kawamoto, L. Yi, M. Fujita, and T. Nagatsuma, “Silicon dielectric diplexer module for 600-GHz-band frequency-division multiplexing wireless communication,” *IEEE Trans Terahertz Sci Technol*, vol. 12, no. 4, pp. 334–344, Jul. 2022, doi: 10.1109/TTHZ.2022.3167946.

[154] M. Tsuji, S. Suhara, H. Shigesawa, and K. Takiyama, “Submillimeter guided-wave experiments with dielectric rib waveguides,” *IEEE Trans Microw Theory Tech*, vol. 29, no. 6, pp. 547–552, Jun. 1981, doi: 10.1109/TMTT.1981.1130390.

[155] H. Lees, M. Sakaki, D. Headland, N. Benson, J. C. Balzer, and W. Withayachumnankul, “Single-mode rib waveguide for the terahertz range using 3D printed alumina,” in *2023 48th International Conference on Infrared,*

Millimeter, and Terahertz Waves (IRMMW-THz), IEEE, Sep. 2023, pp. 1–2. doi: 10.1109/IRMMW-THz57677.2023.10299283.

[156] H. T. Zhu and Q. Xue, "Determination of propagation constant of terahertz dielectric ridge waveguide using noncontact measurement approach," *IEEE Trans Instrum Meas*, vol. 66, no. 8, pp. 2118–2128, Aug. 2017, doi: 10.1109/TIM.2017.2685118.

[157] W. V. McLevige, T. Itoh, and R. Mittra, "New waveguide structures for millimeter-wave and optical integrated circuits," *IEEE Trans Microw Theory Tech*, vol. 23, no. 10, pp. 788–794, Oct. 1975, doi: 10.1109/TMTT.1975.1128684.

[158] H. T. Zhu, Q. Xue, J. N. Hui, and S. W. Pang, "Design, fabrication, and measurement of the low-loss SOI-based dielectric microstrip line and its components," *IEEE Trans Terahertz Sci Technol*, vol. 6, no. 5, pp. 696–705, Sep. 2016, doi: 10.1109/TTHZ.2016.2585345.

[159] T. Itoh, "Inverted strip dielectric waveguide for millimeter-wave integrated circuits," *IEEE Trans Microw Theory Tech*, vol. 24, no. 11, pp. 821–827, Nov. 1976, doi: 10.1109/TMTT.1976.1128967.

[160] A. G. Engel and L. P. B. Katehi, "Low-loss monolithic transmission lines for submillimeter and terahertz frequency applications," *IEEE Trans Microw Theory Tech*, vol. 39, no. 11, pp. 1847–1854, 1991, doi: 10.1109/22.97485.

[161] L. P. B. Katehi, "Novel transmission lines for the submillimeter-wave region," *Proceedings of the IEEE*, vol. 80, no. 11, pp. 1771–1787, 1992, doi: 10.1109/5.175254.

[162] T. Takano and J. Hamasaki, "Propagating modes of a metal-clad-dielectric-slab waveguide for integrated optics," *IEEE J Quantum Electron*, vol. 8, no. 2, pp. 206–212, Feb. 1972, doi: 10.1109/JQE.1972.1076923.

[163] L. Hahn, T. Pfahler, T. Bader, G. Gold, M. Vossiek, and C. Carlowitz, "3D-printed dielectric image lines towards chip-to-chip interconnects for subTHz-applications," in *2024 IEEE International Conference on Microwaves, Communications, Antennas, Biomedical Engineering and Electronic Systems (COMCAS)*, IEEE, Jul. 2024, pp. 1–5. doi: 10.1109/COMCAS58210.2024.10666228.

[164] R. M. Knox, "Dielectric waveguide microwave integrated circuits-an overview," *IEEE Trans Microw Theory Tech*, vol. 24, no. 11, pp. 806–814, 1976, doi: 10.1109/TMTT.1976.1128965.

[165] S. Shindo and T. Itanami, “Low-loss rectangular dielectric image line for millimeter- wave integrated circuits,” *IEEE Trans Microw Theory Tech*, vol. 26, no. 10, pp. 747–751, 1978, doi: 10.1109/TMTT.1978.1129480.

[166] A. Patrovsky and K. Wu, “Substrate integrated image guide (SIIG) - a planar dielectric waveguide technology for millimeter-wave applications,” *IEEE Trans Microw Theory Tech*, vol. 54, no. 6, pp. 2872–2879, 2006, doi: 10.1109/TMTT.2006.875461.

[167] M. Moradi, M. S. Sharawi, and K. Wu, “Analytical model of guided waves in periodically perforated dielectric structure and its applications to terahertz substrate-integrated image guide (SIIG),” *IEEE Trans Microw Theory Tech*, vol. 71, no. 10, pp. 4236–4246, Oct. 2023, doi: 10.1109/TMTT.2023.3260445.

[168] M. Moradi, M. S. Sharawi, and K. Wu, “Exploring low-loss wideband substrate-integrated image guides (SIIG) for terahertz applications,” *IEEE Trans Terahertz Sci Technol*, vol. 14, no. 1, pp. 1–12, Jan. 2024, doi: 10.1109/TTHZ.2023.3332303.

[169] R. M. Knox, P. P. Toulios, and J. Q. Howell, “Radiation losses in curved dielectric image waveguides of rectangular cross section,” in *1973 IEEE G-MTT International Microwave Symposium*, IEEE, 1973, pp. 25–27. doi: 10.1109/GMTT.1973.1123078.

[170] T. Yoneyama and S. Nishida, “Nonradiative dielectric waveguide for millimeter-wave integrated circuits,” *IEEE Trans Microw Theory Tech*, vol. 29, no. 11, pp. 1188–1192, Nov. 1981, doi: 10.1109/TMTT.1981.1130529.

[171] T. Yoneyama, H. Tamaki, and S. Nishida, “Analysis and measurements of nonradiative dielectric waveguide bends,” *IEEE Trans Microw Theory Tech*, vol. 34, no. 8, pp. 876–882, Aug. 1986, doi: 10.1109/TMTT.1986.1133460.

[172] F. Kuroki, H. Ohta, and T. Yoneyama, “Transmission characteristics of NRD guide as a transmission medium in THz frequency band,” in *2005 Joint 30th International Conference on Infrared and Millimeter Waves and 13th International Conference on Terahertz Electronics*, IEEE, pp. 331–332. doi: 10.1109/ICIMW.2005.1572547.

[173] T. Yoneyama, N. Tozawa, and S. Nishida, “Loss measurements of nonradiative dielectric waveguide (special papers),” *IEEE Trans Microw Theory Tech*, vol. 32, no. 8, pp. 943–946, Aug. 1984, doi: 10.1109/TMTT.1984.1132804.

[174] T. Yoneyama, M. Yamaguchi, and S. Nishida, “Bends in nonradiative dielectric waveguides,” *IEEE Trans Microw Theory Tech*, vol. 30, no. 12, pp. 2146–2150, 1982, doi: 10.1109/TMTT.1982.1131398.

[175] Y. Cassivi and K. Wu, “Substrate integrated circuits concept applied to the nonradiative dielectric guide,” in *IEE Proceedings: Microwaves, Antennas and Propagation*, Dec. 2005, pp. 424–433. doi: 10.1049/ip-map:20045089.

[176] F. Xu and K. Wu, “Substrate integrated nonradiative dielectric waveguide structures directly fabricated on printed circuit boards and metallized dielectric layers,” *IEEE Trans Microw Theory Tech*, vol. 59, no. 12 PART 1, pp. 3076–3086, Dec. 2011, doi: 10.1109/TMTT.2011.2168969.

[177] Y. Cassivi and K. Wu, “Substrate integrated nonradiative dielectric waveguide,” *IEEE Microwave and Wireless Components Letters*, vol. 14, no. 3, pp. 89–91, 2004, doi: 10.1109/LMWC.2004.824808.

[178] C. Di Nallo, F. Frezza, A. Galli, P. Lampariello, and A. A. Oliner, “Properties of NRD-guide and H-guide higher-order modes: physical and nonphysical ranges,” *IEEE Trans Microw Theory Tech*, vol. 42, no. 12, pp. 2429–2434, 1994, doi: 10.1109/22.339777.

[179] T. Yoneyama, “Millimeter-wave transmitter and receiver using the nonradiative dielectric waveguide,” in *IEEE MTT-S International Microwave Symposium Digest*, IEEE, pp. 1083–1086. doi: 10.1109/MWSYM.1989.38910.

[180] Jifu Huang, K. Wu, F. Kuroki, and T. Yoneyama, “Computer-aided design and optimization of NRD-guide mode suppressors,” *IEEE Trans Microw Theory Tech*, vol. 44, no. 6, pp. 905–910, Jun. 1996, doi: 10.1109/22.506450.

[181] K. Wu and Liang Han, “Hybrid integration technology of planar circuits and NRD-guide for cost-effective microwave and millimeter-wave applications,” *IEEE Trans Microw Theory Tech*, vol. 45, no. 6, pp. 946–954, Jun. 1997, doi: 10.1109/22.588607.

[182] Y. Sugawara, N. Nakaminami, N. Ishii, and K. Ito, “Proposal of image NRD waveguide and radiation from its end,” *Electronics and Communications in Japan, Part I: Communications (English translation of Denshi Tsushin Gakkai Ronbunshi)*, vol. 84, no. 3, pp. 56–64, 2001, doi: 10.1002/1520-6424(200103)84:33.3.CO;2-F.

[183] H. Amarloo, N. Ranjkesh, and S. Safavi-Naeini, “Terahertz silicon–BCB–quartz dielectric waveguide: An efficient platform for compact THz systems,” *IEEE Trans Terahertz Sci Technol*, vol. 8, no. 2, pp. 201–208, Mar. 2018, doi: 10.1109/TTHZ.2017.2788202.

[184] A. Patrovsky and K. Wu, “Substrate integrated image guide array antenna for the upper millimeter-wave spectrum,” *IEEE Trans Antennas Propag*, vol. 55, no. 11 I, pp. 2994–3001, 2007, doi: 10.1109/TAP.2007.908558.

[185] D. Wang, F. Fesharaki, and K. Wu, “Longitudinally uniform transmission lines with frequency-enabled mode conversion,” *IEEE Access*, vol. 6, pp. 24089–24109, Apr. 2018, doi: 10.1109/ACCESS.2018.2830352.

[186] D. Wang and K. Wu, “Mode-selective transmission line-part II: Excitation scheme and experimental verification,” *IEEE Trans Compon Packaging Manuf Technol*, vol. 11, no. 2, pp. 260–272, Feb. 2021, doi: 10.1109/TCPMT.2020.3043633.

[187] P. Mondal and K. Wu, “Single mode operation of substrate integrated non-radiative dielectric waveguide and an excitation scheme of LSE11 mode,” *IEEE Microwave and Wireless Components Letters*, vol. 23, no. 8, pp. 418–420, 2013, doi: 10.1109/LMWC.2013.2271294.

[188] J. Dallaire and K. Wu, “Complete characterization of transmission losses in generalized nonradiative dielectric (NRD) waveguide,” *IEEE Trans Microw Theory Tech*, vol. 48, no. 1, pp. 121–125, Jan. 2000, doi: 10.1109/22.817480.

[189] A. V. Subashiev and S. Luryi, “Modal control in semiconductor optical waveguides with uniaxially patterned layers,” *Journal of Lightwave Technology*, vol. 24, no. 3, pp. 1513–1522, Mar. 2006, doi: 10.1109/JLT.2005.863280.

[190] J. Attari, T. Djerafi, and K. Wu, *Planar orthogonal mode transducer based on orthogonal LSM10 and TE10 modal fields of co-layered image SINRD (iSINRD) and SIW guides*. Nuremberg: Proceedings of the 43rd European Microwave Conference, 2013.

[191] J. Attari, T. Djerafi, and K. Wu, “A compact 94 GHz image substrate integrated non-radiative dielectric (iSINRD) waveguide cruciform coupler,” *IEEE Microwave and Wireless Components Letters*, vol. 23, no. 10, pp. 533–535, 2013, doi: 10.1109/LMWC.2013.2279102.

[192] R. F. Harrington, *Time Harmonice Electricmagnetic Filed*. JohnWiley & Sons, Inc., 2001.

[193] P. G. Huray *et al.*, “Fundamentals of a 3-D ‘snowball’ model for surface roughness power losses,” *IEEE Electromagn Compat Mag*, vol. 9, no. 2, pp. 62–65, 2020, doi: 10.1109/MEMC.2020.9133247.

[194] D. G. Dudley *et al.*, “Foundations for Microwave Engineering,” 2001. [Online]. Available: www.copyright.com.

[195] C. Liu and K. Wu, “Substrate-integrated hybrid metallo-dielectric waveguide for millimeter-wave and terahertz applications,” in *IEEE MTT-S International*

Microwave Symposium Digest, Institute of Electrical and Electronics Engineers Inc., 2022, pp. 359–362. doi: 10.1109/IMS37962.2022.9865393.

[196] R. Klopfenstein, "A transmission line taper of improved design," *Proceedings of the IRE*, vol. 44, no. 1, pp. 31–35, Jan. 1956, doi: 10.1109/JRPROC.1956.274847.

[197] D. C. Lugo, J. Wang, and T. M. Weller, "Analytical and experimental study of multilayer dielectric rod waveguides," *IEEE Trans Microw Theory Tech*, vol. 69, no. 4, pp. 2088–2097, Apr. 2021, doi: 10.1109/TMTT.2021.3056433.

[198] K. Tsuruda, M. Fujita, and T. Nagatsuma, "Extremely low-loss terahertz waveguide based on silicon photonic-crystal slab," *Opt Express*, vol. 23, no. 25, p. 31977, Dec. 2015, doi: 10.1364/oe.23.031977.

[199] H. Mosallaei and Y. Rahmat-Samii, "Photonic band-gap (PBG) versus effective refractive index: a case study of dielectric nanocavities," in *IEEE Antennas and Propagation Society International Symposium. Transmitting Waves of Progress to the Next Millennium. 2000 Digest. Held in conjunction with: USNC/URSI National Radio Science Meeting (Cat. No.00CH37118)*, IEEE, pp. 338–341. doi: 10.1109/APS.2000.873831.

[200] F. Tischer, "Properties of the H-guide at microwaves and millimeter waves," in *WESCON/58 Conference Record*, Institute of Electrical and Electronics Engineers, pp. 4–12. doi: 10.1109/WESCON.1958.1150192.

[201] D. M. Mittleman, "Perspective: Terahertz science and technology," *J Appl Phys*, vol. 122, no. 23, Dec. 2017, doi: 10.1063/1.5007683.

[202] K. Sengupta, T. Nagatsuma, and D. M. Mittleman, "Terahertz integrated electronic and hybrid electronic–photonic systems," Dec. 01, 2018, *Nature Publishing Group*. doi: 10.1038/s41928-018-0173-2.

[203] J. Weinzierl, Ch. Fluhrer, and H. Brand, "Dielectric waveguides at submillimeter wavelengths," in *1998 IEEE Sixth International Conference on Terahertz Electronics Proceedings. THZ 98. (Cat. No.98EX171)*, IEEE, pp. 166–169. doi: 10.1109/THZ.1998.731707.

[204] C. Yeh, F. Shimabukuro, P. Stanton, V. Jamnejad, W. Imbriale, and F. Manshadi, "Communication at millimetre–submillimetre wavelengths using a ceramic ribbon," *Nature*, vol. 404, no. 6778, pp. 584–588, Apr. 2000, doi: 10.1038/35007036.

[205] A. G. Engel, N. I. Dib, and L. P. B. Katehi, “Characterization of a shielded transition to a dielectric waveguide,” *IEEE Trans Microw Theory Tech*, vol. 42, no. 5, pp. 847–854, May 1994, doi: 10.1109/22.293534.

[206] N. K. Das, “Methods of suppression or avoidance of parallel-plate power leakage from conductor-backed transmission lines,” *IEEE Trans Microw Theory Tech*, vol. 44, no. 2, pp. 169–181, 1996, doi: 10.1109/22.481565.

[207] A. Sain and K. L. Melde, “Impact of ground via placement in grounded coplanar waveguide interconnects,” *IEEE Trans Compon Packaging Manuf Technol*, vol. 6, no. 1, pp. 136–144, Jan. 2016, doi: 10.1109/TCPMT.2015.2507121.

[208] K. Liu, P. Wu, and J. Zhang, “Wideband RWG-SIW interconnection with improved integration for millimeter-wave/terahertz application,” *IEEE Microwave and Wireless Components Letters*, vol. 32, no. 7, pp. 835–838, Jul. 2022, doi: 10.1109/LMWC.2022.3153137.

[209] C. M. Liu, L. P. Carignan, and K. Wu, “Substrate-integrated nonradiative dielectric (SINRD) waveguide for THz integrated circuits and systems,” *IEEE Trans Terahertz Sci Technol*, vol. 13, no. 5, pp. 454–463, Sep. 2023, doi: 10.1109/TTHZ.2023.3299155.

[210] C. M. Liu, L. P. Carignan, S. Xiao, Y. He, and K. Wu, “Substrate-integrated hybrid metallo-dielectric waveguide architecture for millimeter-wave and terahertz applications,” *IEEE Trans Microw Theory Tech*, vol. 71, no. 9, pp. 3958–3967, Sep. 2023, doi: 10.1109/TMTT.2023.3249047.

[211] Tzyy-Sheng Horng, “A rigorous study of microstrip crossovers and their possible improvements,” *IEEE Trans Microw Theory Tech*, vol. 42, no. 9, pp. 1802–1806, 1994, doi: 10.1109/22.310591.

[212] G. E. Ponchak and E. M. Tentzeris, “Finite ground coplanar waveguide (FGC) low loss, low coupling 90-degree crossover junctions,” in *IEEE Transactions on Advanced Packaging*, Aug. 2002, pp. 385–392. doi: 10.1109/TADVP.2002.805314.

[213] D. Packiaraj, K. J. Vinoy, P. Nagarajarao, M. Ramesh, and A. T. Kalghatgi, “Miniaturized defected ground high isolation crossovers,” *IEEE Microwave and Wireless Components Letters*, vol. 23, no. 7, pp. 347–349, Jul. 2013, doi: 10.1109/LMWC.2013.2263219.

[214] S. Y. Eom, A. Batgerel, and L. Minz, “Compact broadband microstrip crossover with isolation improvement and phase compensation,” *IEEE Microwave and Wireless Components Letters*, vol. 24, no. 7, pp. 481–483, 2014, doi: 10.1109/LMWC.2014.2303163.

[215] A. Abbosh, S. Ibrahim, and M. Karim, “Ultra-wideband crossover using microstrip-to-coplanar waveguide transitions,” *IEEE Microwave and Wireless Components Letters*, vol. 22, no. 10, pp. 500–502, 2012, doi: 10.1109/LMWC.2012.2218586.

[216] A. B. Guntupalli, T. Djerafi, and K. Wu, “Ultra-compact millimeter-wave substrate integrated waveguide crossover structure utilizing simultaneous electric and magnetic coupling,” in *2012 IEEE/MTT-S International Microwave Symposium Digest*, IEEE, Jun. 2012, pp. 1–3. doi: 10.1109/MWSYM.2012.6259540.

[217] A. M. Abbosh and M. E. Bialkowski, “Design of compact directional couplers for UWB applications,” *IEEE Trans Microw Theory Tech*, vol. 55, no. 2, pp. 189–194, Feb. 2007, doi: 10.1109/TMTT.2006.889150.

[218] W. Liu, Z. Zhang, Z. Feng, and M. F. Iskander, “A compact wideband microstrip crossover,” *IEEE Microwave and Wireless Components Letters*, vol. 22, no. 5, pp. 254–256, 2012, doi: 10.1109/LMWC.2012.2190270.

[219] Y. Chen and S. P. Yeo, “A symmetrical four-port microstrip coupler for crossover application,” *IEEE Trans Microw Theory Tech*, vol. 55, no. 11, pp. 2434–2438, 2007, doi: 10.1109/TMTT.2007.908675.

[220] Y. C. Chiou, J. T. Kuo, and H. R. Lee, “Design of compact symmetric four-port crossover junction,” *IEEE Microwave and Wireless Components Letters*, vol. 19, no. 9, pp. 545–547, Sep. 2009, doi: 10.1109/LMWC.2009.2027054.

[221] F. Lin, Q. X. Chu, and S. W. Wong, “Dual-band planar crossover with two-section branch-line structure,” *IEEE Trans Microw Theory Tech*, vol. 61, no. 6, pp. 2309–2316, 2013, doi: 10.1109/TMTT.2013.2261084.

[222] M. Jost, R. Reese, H. Maune, and R. Jakoby, “In-plane hollow waveguide crossover based on dielectric insets for millimeter-wave applications,” in *2017 IEEE MTT-S International Microwave Symposium (IMS)*, IEEE, Jun. 2017, pp. 188–191. doi: 10.1109/MWSYM.2017.8059015.

[223] S. S. Hesari and J. Bornemann, “Substrate integrated waveguide crossover formed by orthogonal TE<inf>102</inf> resonators,” in *2017 47th European Microwave Conference (EuMC)*, IEEE, Oct. 2017, pp. 17–20. doi: 10.23919/EuMC.2017.8230788.

[224] S. Q. Han, K. Zhou, J. D. Zhang, C. X. Zhou, and W. Wu, “Novel substrate integrated waveguide filtering crossover using orthogonal degenerate modes,” *IEEE Microwave and Wireless Components Letters*, vol. 27, no. 9, pp. 803–805, Sep. 2017, doi: 10.1109/LMWC.2017.2734842.

[225] L. Sun, H. W. Deng, Y. F. Xue, J. M. Zhu, and S. B. Xing, “Compact-balanced BPF and filtering crossover with intrinsic common-mode suppression using single-layered SIW cavity,” *IEEE Microwave and Wireless Components Letters*, vol. 30, no. 2, pp. 144–147, Feb. 2020, doi: 10.1109/LMWC.2020.2965530.

[226] W. L. Zhan, J. X. Xu, X. L. Zhao, B. J. Hu, and X. Y. Zhang, “Substrate integrated waveguide multi-channel filtering crossover with extended channel number and controllable frequencies,” *IEEE Transactions on Circuits and Systems II: Express Briefs*, vol. 67, no. 12, pp. 2858–2862, Dec. 2020, doi: 10.1109/TCSII.2020.2982409.

[227] K. Zhou and K. Wu, “Wide-stopband substrate-integrated waveguide filtering crossovers with flexibly allocated channel frequencies and bandwidths,” *IEEE Trans Microw Theory Tech*, vol. 69, no. 7, pp. 3264–3274, Jul. 2021, doi: 10.1109/TMTT.2021.3067886.

[228] H. Chen and A. W. Poon, “Low-loss multimode-interference-based crossings for silicon wire waveguides,” *IEEE Photonics Technology Letters*, vol. 18, no. 21, pp. 2260–2262, Nov. 2006, doi: 10.1109/LPT.2006.884726.

[229] H. Xu and Y. Shi, “Dual-mode waveguide crossing utilizing taper-assisted multimode-interference couplers,” *Opt Lett*, vol. 41, no. 22, p. 5381, Nov. 2016, doi: 10.1364/ol.41.005381.

[230] C. Sun, Y. Yu, and X. Zhang, “Ultra-compact waveguide crossing for a mode-division multiplexing optical network,” *Opt Lett*, vol. 42, no. 23, p. 4913, Dec. 2017, doi: 10.1364/ol.42.004913.

[231] Y. Zhang, A. Hosseini, X. Xu, D. Kwong, and R. T. Chen, “Ultralow-loss silicon waveguide crossing using Bloch modes in index-engineered cascaded multimode-interference couplers,” *Opt Lett*, vol. 38, no. 18, p. 3608, Sep. 2013, doi: 10.1364/ol.38.003608.

[232] W. Chang *et al.*, “Ultracompact dual-mode waveguide crossing based on subwavelength multimode-interference couplers,” *Photonics Res*, vol. 6, no. 7, p. 660, Jul. 2018, doi: 10.1364/prj.6.000660.

[233] C. M. Liu, L. P. Carignan, and K. Wu, “Hybrid metallo-dielectric waveguide architecture for compact low-loss THz applications,” *IEEE Microwave and Wireless Technology Letters*, vol. 34, no. 5, pp. 486–489, May 2024, doi: 10.1109/LMWT.2024.3380445.

[234] R. E. Collin, *Field Theory of Guided Waves*. IEEE Press, 2015.

[235] T. Yoneyama, S. Fujita, and S. Nishida, “Insulated nonradiative dielectric waveguide for millimeter-wave integrated circuits,” in *MTT-S International Microwave Symposium Digest*, MTT005, 1983, pp. 302–304. doi: 10.1109/MWSYM.1983.1130892.

[236] J. A. G. Malherbe and J. C. Olivier, “A bandstop filter constructed in coupled nonradiative dielectric waveguide,” *IEEE Trans Microw Theory Tech*, vol. 34, no. 12, pp. 1408–1412, Dec. 1986, doi: 10.1109/TMTT.1986.1133556.

[237] S. Kobayashi, R. Mittra, and R. Lampe, “Dielectric tapered rod antennas for millimeter-wave applications,” *IEEE Trans Antennas Propag*, vol. 30, no. 1, pp. 54–58, Jan. 1982, doi: 10.1109/TAP.1982.1142758.

[238] J. P. Pousi, D. V. Lioubtchenko, S. N. Dudorov, and A. V. Räisänen, “High permittivity dielectric rod waveguide as an antenna array element for millimeter waves,” *IEEE Trans Antennas Propag*, vol. 58, no. 3, pp. 714–719, Mar. 2010, doi: 10.1109/TAP.2009.2039314.

[239] N. Ghassemi and K. Wu, “Planar dielectric rod antenna for gigabyte chip-to-chip communication,” *IEEE Trans Antennas Propag*, vol. 60, no. 10, pp. 4924–4928, 2012, doi: 10.1109/TAP.2012.2207359.

[240] A. A. Generalov, J. A. Haimakainen, D. V. Lioubtchenko, and A. V. Raisanen, “Wide band mm-and sub-mm-wave dielectric rod waveguide antenna,” *IEEE Trans Terahertz Sci Technol*, vol. 4, no. 5, pp. 568–574, 2014, doi: 10.1109/TTHZ.2014.2342503.

[241] F. Kuroki, K. Yamaoka, M. Yamaguchi, and T. Yoneyama, “Mode coupling phenomenon in high permittivity NRD guide with asymmetrically remained small air gap,” in *IEEE MTT-S International Microwave Symposium Digest, 2003*, IEEE, pp. 2053–2056. doi: 10.1109/MWSYM.2003.1210564.

[242] G. Mendez-Jeronimo, S. C. Sejas-Garcia, and R. Torres-Torres, “Modeling and parameter extraction for the metal surface roughness loss effect on substrate integrated waveguides from S-parameters,” *IEEE Trans Microw Theory Tech*, vol. 66, no. 2, pp. 875–882, Feb. 2018, doi: 10.1109/TMTT.2017.2765328.

[243] S. H. Hall and H. L. Heck, *Advanced Signal Integrity for High-Speed Digital Designs*. Hoboken, NJ: USA: Wiley, 2009.

APPENDICES

Appendice A

According to [56], the conductor loss can be given by using perturbation method.

$$\alpha_c = \frac{P_c}{2P_0} \tag{3-1}$$

$$P_0 = \frac{1}{2} Re\left(\iint \vec{E} \times \vec{H}^* \, ds\right) \tag{3-2}$$

$$P_c = \frac{R_s}{2} \int_C \left|\vec{J_s}\right|^2 dl \tag{3-3}$$

$$R_s = \sqrt{\frac{\omega\mu_0}{2\sigma}} \tag{3-4}$$

$$\vec{J_s} = \vec{n} \times \vec{H}_{surface} \tag{3-5}$$

, where ω is angular frequency, μ_0 and σ are the permeability and the conductivity of the metal surface.

The dielectric loss of SINRD is given by

$$\alpha_d = \frac{P_d}{2P_0} \tag{3-6}$$

$$P_d = \frac{1}{2} \omega\varepsilon_0 tan\delta \iint \vec{E}^2 \, ds) \tag{3-7}$$

, where tan δ is the loss tangent of dielectric material.

As studied in [192], besides TE^z/TM^z modes supported by dielectric-loaded waveguide, hybrid combinations of TE^z and TM^z modes might be required to satisfy all boundary conditions in some cases. Thus, it is more convenient to specify the electric potential or magnetic potential function along the normal direction of the dielectric interface, here along x-axis, as Ψ_x^e and Ψ_x^h for the LSM and LSE modes, respectively. Then all related

field components of LSM mode can be obtained by solving wave equations [192]

$$E_x = -j\frac{1}{\omega\mu\varepsilon}\left(k^2 + \frac{\partial^2}{\partial x^2}\right)\Psi_x^e$$

$$E_y = -j\frac{1}{\omega\mu\varepsilon}\frac{\partial^2}{\partial x\partial y}\Psi_x^e$$

$$E_z = -j\frac{1}{\omega\mu\varepsilon}\frac{\partial^2}{\partial x\partial z}\Psi_x^e$$

$$H_x = 0$$

$$H_y = \frac{1}{\mu}\frac{\partial\Psi_x^e}{\partial z}$$

$$H_z = -\frac{1}{\mu}\frac{\partial\Psi_x^e}{\partial y} \tag{3-8}$$

For the LSM modes, the field components in dielectric core (R1) and perforated region (R2) are given by

$$E_x = \begin{cases} A_1\dfrac{\left({k_1}^2 - {\beta_{x1}}^2\right)}{j\omega\mu\varepsilon_1}\cos(\beta_{x1}x)\sin\left(\beta_y y\right)e^{-j\beta_z z} & \text{R1} \\ A_2\dfrac{\left({k_2}^2 + {\beta_{x2}}^2\right)}{j\omega\mu\varepsilon_2}e^{-\beta_{x2}x}\sin\left(\beta_y y\right)e^{-j\beta_z z} & \text{R2} \end{cases}$$

$$E_y = \begin{cases} -A_1\dfrac{\beta_{x1}\beta_y}{j\omega\mu\varepsilon_1}sin(\beta_{x1}x)cos\left(\beta_y y\right)e^{-j\beta_z z} & \text{R1} \\ -A_2\dfrac{\beta_{x2}\beta_y}{j\omega\mu\varepsilon_2}e^{-\beta_{x2}x}cos\left(\beta_y y\right)e^{-j\beta_z z} & \text{R2} \end{cases}$$

$$E_z = \begin{cases} A_1\dfrac{\beta_{x1}\beta_z}{j\omega\mu\varepsilon_1}sin(\beta_{x1}x)\sin\left(\beta_y y\right)e^{-j\beta_z z} & \text{R1} \\ A_2\dfrac{\beta_{x2}\beta_z}{j\omega\mu\varepsilon_2}e^{-j\beta_{x2}x}\sin\left(\beta_y y\right)e^{-j\beta_z z} & \text{R2} \end{cases}$$

$$H_x = 0$$

$$H_y = \begin{cases} A_1\dfrac{\beta_z}{\mu}cos(\beta_{x1}x)\sin\left(\beta_y y\right)e^{-j\beta_z z} & \text{R1} \\ A_2\dfrac{\beta_z}{\mu}e^{-\beta_{x2}x}\sin\left(\beta_y y\right)e^{-j\beta_z z} & \text{R2} \end{cases}$$

$$H_z = \begin{cases} -A_1 \dfrac{\beta_y}{\mu} cos(\beta_{x1} x) cos(\beta_y y) e^{-j\beta_z z} & \text{R1} \\ -A_2 \dfrac{\beta_y}{\mu} e^{-\beta_{x2} x} cos(\beta_y y) e^{-j\beta_z z} & \text{R2} \end{cases}$$

(3-9)

$$A_2 = A_1 \cos(\beta_{x1} \frac{w}{2}) e^{\beta_{x2} \frac{w}{2}}$$

(3-10)

After, by applying the boundary conditions at the dielectric interfaces between different regions, one can obtain the transcendental equation

$$\beta_{x1} \tan\left(\beta_{x1} \frac{w}{2}\right) = \pm \beta_{x2}$$

$$\beta_{x1}{}^2 + \beta_y{}^2 + \beta_z{}^2 = \omega^2 \mu \varepsilon_1$$

$$-\beta_{x2}{}^2 + \beta_y{}^2 + \beta_z{}^2 = \omega^2 \mu \varepsilon_2$$

$$\beta_y = \frac{n\pi}{h}$$

(3-11)

The dispersion curves can be found by numerically solving β_z in (3-11). The power flow of the LSM_{01} mode is given by

$$P_0 = A_1{}^2 \frac{\beta_z}{\mu} \frac{k_1{}^2 - \beta_{x1}{}^2}{\omega \mu \varepsilon_1} \frac{h}{2} \left(\frac{w}{4} + \frac{\sin(\beta_{x1} w)}{4\beta_{x1}} \right) + A_2{}^2 \frac{\beta_z}{\mu} \frac{k_2{}^2 + \beta_{x2}{}^2}{\omega \mu \varepsilon_2} \frac{h}{2} \frac{e^{-\beta_{x2} w}}{2\beta_{x2}}$$

(3-12)

The power dissipated in loss dielectric material per unit is obtained by

$$P_d = {A_1}^2 \omega \varepsilon_1 tan\delta_1 \frac{1}{(\omega\mu\varepsilon_1)^2}\frac{h}{2}\left\{\left(\frac{w}{4}+\frac{\sin(\beta_{x1}w)}{4\beta_{x1}}\right)({k_1}^2-{\beta_{x1}}^2)^2 + \left(\frac{w}{4}-\frac{\sin(\beta_{x1}w)}{4\beta_{x1}}\right)\left((\beta_{x1}\beta_y)^2+(\beta_{x1}\beta_z)^2\right)\right\} + {A_2}^2 \omega \varepsilon_2 tan\delta_2 \frac{1}{(\omega\mu\varepsilon_2)^2}\frac{h}{2}\frac{e^{-\beta_{x2}w}}{2\beta_{x2}}\left((\beta_{x2}\beta_y)^2+(\beta_{x2}\beta_z)^2 + ({k_2}^2+{\beta_{x2}}^2)^2\right)$$

(3-13)

The power dissipated in metallic plates per unit is given by

$$P_l = 2R_s\left(\frac{\beta_{x1}}{\mu}\right)^2\left\{{A_1}^2\left(\frac{w}{4}+\frac{sin(\beta_{x1}w)}{4\beta_{x1}}\right)+{A_2}^2\frac{e^{-\beta_{x2}w}}{2\beta_{x2}}\right\}$$

(3-14)

Appendice B

The dominant transverse field of the E_{11}^x mode of SIDW is given by

$$E_x = \begin{cases} A_1\dfrac{({k_1}^2-{\beta_{x1}}^2)}{j\omega\mu\varepsilon_1}\cos(\beta_{x1}x)\sin(\beta_{y1}y)e^{-j\beta_z z} & \text{region \#1} \\ A_2\dfrac{({k_1}^2+{\beta_{x2}}^2)}{j\omega\mu\varepsilon_2}e^{-\beta_{x2}x}e^{-\beta_{y2}y}e^{-j\beta_z z} & \text{region \#2} \\ A_3\dfrac{({k_1}^2+{\beta_{x3}}^2)}{j\omega\mu\varepsilon_3}e^{-\beta_{x3}x}e^{-\beta_{y3}y}e^{-j\beta_z z} & \text{region \#3} \end{cases}$$

(5-1)

For the LSM_{01}^x mode of SINRD waveguide, the dominant transverse field is given by [170]

$$E_x = \begin{cases} B_1\dfrac{({k_1}^2-{\beta_{x1}}^2)}{j\omega\mu\varepsilon_1}\cos(\beta_{x1}x)\sin(\beta_y y)e^{-j\beta_z z} & \text{region \#1} \\ B_2\dfrac{({k_1}^2+{\beta_{x2}}^2)}{j\omega\mu\varepsilon_2}e^{-\beta_{x2}x}\sin(\beta_y y)e^{-j\beta_z z} & \text{region \#2} \end{cases}$$

(5-2)

where c and ω are, respectively, the free space speed of light and radian frequency, k_1 is the propagation constant in region #1 in Figure 5.2 (c) and (d), w and h are, respectively, the width and the height of the SIDW core, m and n are the orders of modes, and ε_{r1}, ε_{r2} and ε_{r3} are respectively the relative permittivity of regions #1, #2 and #3, $\beta_{x/y,\ 1/2/3}$ is the propagation constant along x/y-axis at region #1/2/3. β_z is the propagation constant along the z direction. $A/B_{1,2,3}$ is the amplitude of electric fields for the corresponding mode at region #1, 2, 3.

For the SIDW operating in the E_{11}^{x} mode and the SINRD waveguide operating in the LSM_{01}^{x} mode, the wave impedance is given by

$$Z_w = \frac{E_t}{H_t} = \frac{k_1^2 - \beta_{x1}^2}{\omega \varepsilon_1 \beta_z} \tag{5-3}$$

Appendice C

For the LSM^{x} mode, the related field components can be obtained by solving wave equations [192]

$$E_x = -j\frac{1}{\omega\mu\varepsilon}\left(k^2 + \frac{\partial^2}{\partial x^2}\right)\Psi_x^e$$

$$E_y = -j\frac{1}{\omega\mu\varepsilon}\frac{\partial^2}{\partial x \partial y}\Psi_x^e$$

$$E_z = -j\frac{1}{\omega\mu\varepsilon}\frac{\partial^2}{\partial x \partial z}\Psi_x^e$$

$$H_x = 0$$

$$H_y = \frac{1}{\mu}\frac{\partial \Psi_x^e}{\partial z}$$

$$H_z = -\frac{1}{\mu}\frac{\partial \Psi_x^e}{\partial y} \tag{7-1}$$

The electric field of the LSM_{01}^{x} (propagating along $-z$ axis) mode of NRD dielectric core is given by

$$E_x = \frac{(k^2 - \beta_x^2)}{j\omega\mu\varepsilon_1}\cos(\beta_x x)\sin(\beta_y y)e^{j\beta_z z}$$
$$E_y = \frac{\beta_x\beta_y}{j\omega\mu\varepsilon}\cos(\beta_x x)\cos(\beta_y y)e^{j\beta_z z}$$
$$E_z = \frac{\beta_x\beta_z}{j\omega\mu\varepsilon}\sin(\beta_x x)\sin(\beta_y y)e^{j\beta_z z}.$$

(7-2)

For the LSE^x mode, the related field components can be obtained by solving wave equations [192]

$$E_x = 0$$
$$E_y = -\frac{1}{\varepsilon}\frac{\partial}{\partial z}\Psi_x^h$$
$$E_z = \frac{1}{\varepsilon}\frac{\partial}{\partial y}\Psi_x^h$$
$$H_x = -j\frac{1}{\omega\mu\varepsilon}\left(k^2 + \frac{\partial^2}{\partial x^2}\right)\Psi_x^h$$
$$H_y = -j\frac{1}{\omega\mu\varepsilon}\frac{\partial^2}{\partial x\partial y}\Psi_x^h$$
$$H_z = -j\frac{1}{\omega\mu\varepsilon}\frac{\partial^2}{\partial x\partial z}\Psi_x^h$$

(7-3)

The electric field of the LSE$_{11}^x$ (propagating along $-z$ axis) mode of NRD dielectric core is given by

$$E_y = \frac{\beta_z}{\varepsilon}\cos(\beta_x x)\cos(\beta_y y)e^{j\beta_z z}$$
$$E_z = \frac{\beta_y}{\varepsilon}\cos(\beta_x x)\sin(\beta_y y)e^{j\beta_z z}$$

(7-4)

The electric field components of the LSE$_{11}^z$ (propagating along -x axis) and LSM$_{01}^z$ (propagating along -x axis) modes are given by the same way

$$E_x = \frac{\beta_y}{\varepsilon} e^{j\beta_x x} \sin(\beta_y y)\cos(\beta_z z)$$
$$E_y = \frac{\beta_z}{\varepsilon} e^{j\beta_x x} \cos(\beta_y y)\cos(\beta_z z)$$

(7-5)

and

$$E_x = \frac{\beta_x \beta_z}{j\omega\mu\varepsilon} e^{j\beta_x x} \sin(\beta_y y)\sin(\beta_z z)$$
$$E_y = \frac{\beta_x \beta_y}{j\omega\mu\varepsilon} e^{j\beta_x x} \cos(\beta_y y)\cos(\beta_z z)$$
$$E_z = \frac{(k^2 - {\beta_z}^2)}{j\omega\mu\varepsilon} e^{j\beta_x x} \sin(\beta_y y)\cos(\beta_z z).$$

(7-6)

The dominant transverse electric field component of $E_{11}^{y/z}$ (propagating along -*x* axis) mode is given by [120]

$$E_{y,z} = \frac{(k^2 - {\beta_{y,z}}^2)}{j\omega\mu\varepsilon} e^{j\beta_x x} \sin(\beta_{y,z} y, z)\cos(\beta_{z,y} z, y)$$

(7-7)

where ω is radian frequency, k is the propagation constant in dielectric core, w and h are, respectively, the width and the height of the dielectric core, and ε and μ are permittivity and permeability of dielectric core, respectively, $\beta_{x/y/z}$ is the propagation constant along *x/y/z*-axis at dielectric core. $A/B/C/D_{y,z}$ is the amplitude of electric fields for the corresponding mode.

Appendice D List of Publication

Journal papers:

[J1] **Chun-Mei Liu,** Louis-Philippe Carignan, and Ke Wu, "Crosstalk and leakage suppression by mode selectivity and conversion in terahertz hybrid metallo-dielectric waveguide crossover and intersections," ***IEEE Trans. Microw. Theory Techn.,*** vol. 72, no. 12, pp. 6943-6955, Jun. 2024.

[J2] **Chun-Mei Liu,** Louis-Philippe Carignan, and Ke Wu, "Hybrid metallo-dielectric waveguide architecture for compact low-loss THz circuits," ***IEEE Microw. Wireless Technol. Lett.,*** vol. 34, no. 5, pp. 486-489, May 2024.

[J3] **Chun-Mei Liu,** Louis-Philippe Carignan, Shaoqiu Xiao, Yejun He and Ke Wu, "Substrate-integrated hybrid metallo-dielectric waveguide architecture for millimeter-wave and terahertz applications," ***IEEE Trans. Microw. Theory Techn.***, vol. 71, no. 9, pp. 3958-3967, Sep. 2023.

[J4] **Chun-Mei Liu,** Louis-Philippe Carignan and Ke Wu, "Substrate-Integrated non-radiative dielectric (SINRD) waveguide for THz integrated circuits and systems," ***IEEE Trans. Terahertz Sci. Technol***., vol. 13, no. 5, pp. 454-463,Sep. 2023.

[J5] **Chun-Mei Liu** and Ke Wu, "Vertically stacked double-layer substrate-integrated non-radiative dielectric waveguides for THz applications," ***IEEE Microwave Wireless Technol. Lett,*** vol. 33, no. 6, pp. 791-794, Jun. 2023.

[J6] **Chun-Mei Liu,** Shaoqiu Xiao, Desong Wang and Ke Wu, "Wideband via-loaded cylindrical open-ended SIW cavity antenna," ***IEEE Open Journal of Antennas and Propagation***, vol. 2, pp. 1001-1019, Sep. 2021.

[J7] **Chun-Mei Liu,** Shaoqiu Xiao and Ke Wu, "Miniaturized cylindrical open-ended SIW cavity antenna and its dual-band applications," ***IEEE Trans. Antenna Propag.***, vol. 69, no. 8, pp. 4390-4400, Jan. 2021.

Conference papers:

[C1] **Chun-Mei Liu** and Ke Wu, "Crosstalk reduction enabled by hybrid metallo-dielectric waveguide architecture," ***European Microwave Week (EuMW) 2024***.

[C2] **Chun-Mei Liu** and Ke Wu, "Wideband wide-angle beam-scanning SIW cavity-backed patch antenna array," ***2022 IEEE AP-S/URSI***.

[C3] **Chun-Mei Liu** and Ke Wu, "Substrate-integrated hybrid metallo-dielectric waveguide for millimeter-wave and terahertz applications," ***2022 IEEE International Microwave Symposium (IMS)***.

[C4] **Chun-Mei Liu** and Ke Wu, "Aperture-shared X/Ka-band cylindrical open-ended SIW cavity antenna," ***2021 IEEE 19th International Symposium on Antenna Technology and Applied Electromagnetics (ANTEM)***.